UNIVERSITY OF CALGARY

**New technologies for unconventional reservoir characterization: Seismic inversion, focal-time estimation, and signal processing to improve reservoir imaging**

by

Ronald McKenzie Weir

A THESIS

SUBMITTED TO THE FACULTY OF GRADUATE STUDIES

IN PARTIAL FULFILLMENT OF THE REQUIREMENTS FOR THE

DEGREE OF DOCTOR OF PHILOSOPHY

GRADUATE PROGRAM IN GEOLOGY AND GEOPHYSICS

CALGARY, ALBERTA

APRIL, 2020

## Abstract

Seismic data, comprising both passively and actively recorded data, have long been used for resource evaluation and geohazard assessments. Unconventional resource extraction, such as Alberta's Duvernay play, requires a multifaceted approach to optimize reservoir development and to mitigate geohazards such as induced seismicity. Frequently, hydraulic fracture stimulation programs do not go as planned; fractures occur out of zone, depart from the predicted models, and, in some cases, induce felt seismic events (induced by hydraulic fracturing operations). From the Fox Creek, Alberta study area are well log data, multicomponent seismic reflection data, and microseismic data recorded from a permanent near-surface passive recording array. For this study, an industry partner provided two multicomponent seismic reflection surveys, as well as two co-located passive microseismic surveys. The Microseismic Industry Consortium (MIC) supplied microseismic data from the Tony Creek dual microseismic experiment (ToC2ME); an anonymous industry contributor contributed a second passive survey. Technologies developed in this thesis enable more accurate positioning of microseismic hypocenters by incorporating seismic reflection data. Signal-processing techniques used in seismic reflection processing are employed in this thesis to enhance the detection quality and quality of induced seismic events. Structural interpretation provides a framework of vital information to map and understand the relationship between geological structure and induced seismic events. Constraints obtained from full-waveform inversion provide detailed information about the properties of the Duvernay Formation itself, such as brittle and ductile facies. Accurate microseismic hypocenter determination in the context of seismic analysis identifies which structural elements and reservoir facies control the direction and size of induced fractures and which faults may be responsible for induced seismicity. Hypocenters are accurately located and plotted in depth and are associated with faults mapped from the reflected seismic. This analysis highlights what geological conditions, faults, lithology, and structure are dominant factors with respect to hydraulic fracture propagation and induced seismicity. The results of this research will aid in the design of hydraulic fracture completion programs and geohazard (induced seismic event) mitigation.

## Preface

The research presented here is conducted under the supervision of Dr. D. Lawton, Dr. David Eaton, and Dr. L. Lines at the University of Calgary within the Consortium for Research in Elastic Wave Exploration Seismology (CREWES) research group, as well as Dr. David W. Eaton within the MIC. The PhD thesis is composed in a manuscript-based format based on two published papers, two expanded abstracts, and one paper pending publication. I am the primary author of these five publications. I am the first author of the papers in Chapters 2 and 3, published in the journals *Interpretation* and *The Leading Edge*, respectively. The research compiled in Chapter 6 is in preparation for peer review, with the intent of submitting it to *Interpretation* for publication.

Chapter 2 is published as follows: Weir, R.M., D.W Eaton, L.R Lines, D.C Lawton, and E Ekpo, 2018. Inversion and interpretation of seismic-derived rock properties in the Duvernay play. Interpretation, 6, SE1-SE14[1]. The seismic reflection data used are three-component, three-dimensional (3D/3C) seismic data provided by industry and are co-located with a passive seismic array active before, during, and after hydraulic fracture stimulation. The seismic analysis consists of structural mapping followed by joint inversion to calculate lithological properties within the Duvernay Formation.

Chapter 3 is published as follows: Weir, R., L R. . Lines, D. Lawton, T Eyre, D Eaton, "Application of structural interpretation and simultaneous inversion and reservoir characterization of the Duvernay Formation, Fox Creek, Alberta, 2018, The Leading Edge, Volume 3 38, Issue 2, February 2019." The seismic reflection data are 3D/3C seismic data and

[1] SEG Interpretation, TLE, and Expanded abstracts open access policy*:" Authors may reuse all or part of their papers published with SEG in a thesis or dissertation that authors write and are required to submit to satisfy criteria of degree-granting institutions."* https://seg.org/Publications/Policies-and-Permissions/Open-Access-Policy

are co-located with a second passive seismic array active during fracture stimulation. The interpretation methodology used in Chapter 3 is similar to that used for Chapter 2, but there are significant geological differences. T. Eyre (2019) incorporated this work into a *Science Advances* publication, whereby aseismic creep caused by hydraulic fracture stimulation was proposed as an earthquake-triggering mechanism.

Chapter 4 is published as an expanded abstract for the 2019 GeoConvention: Weir, R, L. Lines, D. Lawton, D. Eaton, A Poulin. Can continuously recorded seismic data be improved with signal processing? This research came about as a result of experience I have in seismic signal processing for seismic reflection data, where signal processing is routinely applied to reduce noise and enhance the signal. The seismic detection software Repeating Earthquake Detector, Python (REDPy), run by Rebecca Salvage on the signal-processed data, uses the same parameters as used on the raw microseismic data. With the microseismic data used here, all of the seismic event detection algorithms are initially applied on the raw data. The results of using signal processing are shown here, showing significant improvement in the quality and quantity of microseismic events before and after processing. Given the sheer data volume of detected seismic events, the seismic event detection is not expected to be ready for final publication until the summer of 2020.

Chapter 5 is a new method for hypocenter depth determination derived as a result of collaboration among myself, D. Eaton., A. Poulin, and N. Igonin. The collaboration is the result of a discussion regarding the difficulties in determining hypocenter depth from passive seismic data. Current depth-determination methods use one-dimensional (1D) velocity models that do not account for anisotropy or variations in structure These 1-D methods often produce erroneous depth results, sometimes clustering seismic events around velocity boundaries in the 1D model.

After working on a multicomponent data set that was co-located with the passive seismic array (ToC2ME), I suggested using the compressional (P)-wave and shear (S)-wave velocity data derived from the multicomponent P-wave reflection and converted S-wave reflection registration instead of a 1D velocity model. A completely new and more accurate method to depth-convert passive seismic events comes from collaboration of this idea. A. Poulin developed the code, and I provided the depth-converted data, as well as a method for reconciling the reflection and passive seismic data. This work is published as an expanded Society of Exploration Geophysicists (SEG) abstract in the 2018 convention archives and was presented at the 2018 SEG conference in Houston, Texas: Ronald Weir, A. Poulin, Nadine Igonin, David W. Eaton, L. Lines, D. Lawton, (2018). "Focal-time Method." It is also published as a peer-reviewed paper in *Geophysics*, with A. Poulin as the primary author and myself as the second author. This method for focal-time estimation can be deployed, in a more general sense, in areas where reflection data are available, such as areas prone to naturally occurring earthquakes.

Chapter 6 is written with the intent of submission for publication in early 2020. It is the field development application of the new methods developed in earlier chapters of the thesis. This chapter integrates the work from Chapters 2, 3, and 5, showing a method whereby microseismic data and passive seismic data are integrated into a comprehensive seismic interpretation. Subtle fault features are observed in the seismic mapping between major strike-slip faults originating within the Precambrian basement. A geological model is proposed to explain these observations based on the concept of transcurrent faulting. This model provides a viable explanation for both the nature of the observed hydraulic fracture patterns and the associated induced earthquakes occurring in the shallower horizons. Incorporating these results into future field development can reduce risk, increase the efficiency of well design, and reduce capital requirements for future development of the Duvernay Formation.

## Acknowledgments

Sponsors of the MIC are sincerely thanked for their support of this initiative. I also thank the sponsors of CREWES for their financial support of this study. The microseismic data are acquired using the BuriedArray method under license from Microseismic, Inc. This work is supported by funding for the Natural Sciences and Engineering Research Council (NSERC) / Chevron Industrial Research Chair in Microseismic System Dynamics. I sincerely thank TGS Canada Corp for providing multicomponent 3D seismic data for this study, as well as an anonymous company for the use of the microseismic catalog in the northern project area. This work is also funded by NSERC through grants CRDPJ 461179-13, CRDPJ 474748-14, IRCPJ/485692-2014, and IRCSA 485691. I thank Divestco for providing digital LAS curves. I thank the SEG Earl D. and Reba C. Griffin Memorial Scholarship for its financial contribution to this research.

I am grateful to Mike Moussallem at Signature Seismic, Inc. for giving me access to its seismic-processing system for data processing and to Lona Gregory-Brown for assisting in setting up the processing flow. I thank CGG for providing the InsightEarth software, as well as the use of HampsonRussell Geoview software. I thank Seisware for interpretation and mapping software and geoLOGIC Systems for the geoSCOUT software. I am grateful to Marco Venieri for geological insight and input with respect to the geomechanics of the Duvernay Formation.
I finally thank Don Lawton and Larry Lines, who supervised me through the graduate studies program, and David Eaton for his guidance and direction. Thank you to the staff and students in CREWES for their support, as well as the staff and students in MIC. Thanks to Kevin Hall for audiovisual, computer, and software support, as well as pretty much anything else related to seismic data. Thanks to Catherine Hubbell and Faye Nicholson in the Department of Geoscience

for navigating me through all the various administrative items associated with being a graduate student.

## Dedication

I am grateful to Dr. Laurence Lines (Larry), my graduate studies co-supervisor and friend, who passed away in the fall of 2019. He served as my advisor, co-author, and examiner throughout my graduate studies program. He was also present as a support when I went through a time of personal difficulty, making sure I had the support I needed to complete my studies.

He was always present at my presentations and available for proofreading, edits, and an informal coffee meeting or lunch. When life seemingly became overwhelming, he had the ability to put things back into perspective, often with his sense of humor or a baseball analogy.

I will miss Larry and will always think of him as a scholar and a family man. I will remember his contribution to science and his dedication to his students.

## Table of Contents

## List of Tables

**List of Figures and Illustrations**

## List of Symbols, Abbreviations, and Nomenclature

| Symbol/abbreviation | Definition |
|---|---|
| $\alpha$ | P-wave velocity (m/s) |
| $\beta$ | S-wave velocity (m/s) |
| $\gamma$ | $V_P/V_S$, P-wave to S-wave velocity ratio |
| $\theta$ | angle of incidence |
| $\lambda$ | Lamé parameter lambda (Pa) |
| $\mu$ | Lamé parameter mu (shear Modulus, Pa) |
| $\rho$ | density (kg/m$^3$) |
| $\Delta$ | change in |
| $\Delta t_M$ | change in time, seismic event/earthquake arrival |
| $\Delta t_P$ | difference in P-wave arrival time |
| $\Delta t_S$ | difference in S-wave arrival time |
| 1D | one-dimensional |
| 2D | two-dimensional |
| 3D | three-dimensional |
| 3D/3C | three-dimensional, three-component |
| 5D | five-dimensional |
| AER | Alberta Energy Regulator |
| AVA | amplitude versus angle |
| AVO | amplitude versus offset |
| CF | characteristic function |
| CPU | central processing unit |
| CREWES | Consortium for Research in Elastic Wave Exploration Seismology |
| *BRI* | Brittleness index |
| *E* | Young’s Modulus (GPa) |
| FEF | fault enhancement–filtered |
| Focal-time | The Focal Time method for hypocenter determination |
| GB | gigabyte |
| GHz | gigahertz |
| $G_P$ | Green’s function, P-wave travel path |
| $G_S$ | Green’s function, S-wave travel path |
| H1 | geophone horizontal channel |
| H2 | geophone horizontal channel orthogonal to H1 |
| Hz | cycles per second |
| LAS | Log ASCII Standard file format |
| LTA | long-term average |
| LMR | Lamé parameters lambda ($\lambda$), mu ($\mu$), and rho ($\rho$) |
| $L_P$ | length of the P-wave ray travel path (m) |
| $L_S$ | length of the S-wave ray travel path (m) |
| MFA | matched filter analysis |
| MIC | Microseismic Industry Consortium |
| $M_W$ | seismic moment magnitude, Nm |
| MHz | mega (million) cycles per second |

| | |
|---|---|
| NGL | natural gas liquid |
| NSERC | Natural Sciences and Engineering Research Council |
| $N(t)$ | noise as a function of time |
| PC | personal computer |
| PP-PS | P-wave reflection and converted S-wave reflection |
| *PR* | Poisson's Ratio |
| P-P | P-wave to P-wave reflection |
| P-S | P-wave to S-wave reflection |
| P-wave | compressional wave |
| RAM | random access memory |
| REDPy | Repeating Earthquake Detector, Python |
| RNA | random noise attenuation |
| S-wave | shear wave |
| SEG | Society of Exploration Geophysicists |
| SEG Y | SEG file format |
| STA | short-term average |
| $SH_{max}$ | maximum horizontal stress |
| $t_0$ | origin time |
| $t_P$ | P-wave arrival time (ms) |
| $t_S$ | S-wave arrival time (ms) |
| $t_{PP}$ | two-way reflection time, P-wave reflected (ms) |
| $t_{PS}$ | two-way reflection time, S-wave reflected (ms) |
| TOC | total organic carbon (%) |
| ToC2ME | Tony Creek dual microseismic experiment |
| V | geophone vertical channel |
| $V_P$ | P-wave velocity (m/s) |
| $V_S$ | S-wave velocity (m/s) |
| $V_P/V_S$ | P- to S-wave velocity ratio |
| $W_P$ | source wavelet, P-wave |
| $W_S$ | source wavelet, S-wave |
| $x_R$ | receiver location |
| $x_S$ | event location |
| $z'$ | event focal depth |
| $Z_P$ | P-wave impedance (kg/m$^3$)(m/s) |
| $Z_S$ | S-wave impedance (kg/m$^3$)(m/s) |
| Z | vertical component, used interchangeably with V |

*Geological formations*

| | |
|---|---|
| 2WS | Second White Speckled Shale |
| Colo | Colorado group |
| Wab | Wabamun Formation |
| Ireton | Ireton Formation |
| SWH | Swan Hills Formation |
| Gill | Gilwood member, Watt Mountain Formation |
| ~Prec | Precambrian basement (approximation) |

# Chapter 1

# Introduction

## 1.0 Objectives

The use of reflection seismic data has a significant impact on the economics of oil and gas extraction as a means of risk reduction. In an exploration role, it can high-grade structures, define faults and traps, and is used as a direct hydrocarbon detection tool. In a development role, it is used to define areas suitable for development in a given basin. Reflection seismic is used as a structural guide to direct the orientation of horizontal well bores. The use of three dimensional multicomponent data, 3-D/3-C, enables the extraction of petrophysical attributes relevant to field development. 3-D/3-C seismic data is a powerful tool in the identification of faults, contributing a structural analysis to field development.

Passive seismic data (microseismic) is used to monitor seismic activity during the course of a hydraulic fracture stimulation operation. It determines the position and depth of the induced seismic events[2], as well as monitors undesirable seismic events such as large magnitude (felt) earthquakes, or fractures occurring above and below the treatment zone. Microseismic monitoring serves to provide information with respect to hydrocarbon development in adjoining areas.

---

[2] In this thesis, induced seismic events are defined to be anthropomorphic in origin, the result of human activity

In the compilation of this thesis, methods were developed to combine these two aspects of seismic analysis. These include a method to combine the passive and active data to derive an accurate depth for induced seismic events, and a method to interpret the results using both types of seismic data. In addition, data processing methods commonly applied to reflection are applied to passive seismic, significantly increasing the quantity and quality of identified passive seismic events.

The data presented in this thesis is centered in an active hydrocarbon exploitation project, near Fox Creek, Alberta This thesis presents results acquired in an active hydrocarbon exploitation area, combining reflection seismic, microseismic, signal processing and 3-D visualization. An explanation for the mechanism fracture propagation and induced (felt) seismicity in terms of deep seated basement faults and Riedel[3] shear faulting (Davis, et al., 2000). The analysis presents a significant departure from previous reservoir fracture models, where the reservoir is assumed to be homogeneous and *SHmax* dominates the fracture propagation direction; that the reservoir acts as a homogeneous block of material, and *SHmax* is the dominant feature in fracture propagation. Here, I show that the large induced seismic (felt) events are reactivated basement faults, and that the fracture propagation is dominated by re-activating pre-existing faulting such as Riedel shear zones near strike-slip faults. .

[3] Riedel and transcurrent faulting refer to the oblique shear deformation that occur as a result of strike-slip movement, Davis et al. 2000.

### 1.1 Overview

Hydraulic fracturing is used extensively in the development of unconventional reservoirs. The hydraulic fracturing method typically starts with drilling a well vertically to the target formation and then turning the wellbore horizontally through the tight, hydrocarbon-bearing (King, 2011). The horizontal section of the wellbore is perforated over discrete intervals and is injected with water, chemicals, and proppant in what is called hydraulic fracture stimulation or "fracking." The combination of high-pressure water, chemicals, and proppant (usually sand) opens up microfractures within the reservoir (CAPP, Hydraulic Fracturing, 2019). The function of the proppant is to hold the newly formed fractures open; otherwise, the stimulated reservoir rock would collapse once the pressure is reduced during flowback. Along with creating new fractures, fracture stimulation connects existing fracture networks within the reservoir, enabling oil and gas to flow from tight reservoirs.

The Duvernay Formation is the subject of study in this thesis, with the results of two horizontal hydraulic fracture treatment programs evaluated. The Duvernay Formation is a hydrocarbon play in active development in western Alberta, utilizing horizontal drilling, hydraulic fracture stimulation, and microseismic monitoring. This unconventional play is comprised of a bituminous / argillaceous carbonate deposited adjacent to several large Leduc reef complexes The Duvernay has an effective porosity of 6 - 7 % and an average total organic carbon (TOC) content of up to 4.5% (Chopra, 2017). The Duvernay was deposited as basin fill sediments between the stratigraphically equivalent Leduc Formation platform and reefs. The sediments, consistent of fine grained organic rich sediments, varying in lithology as described by Knapp (2017), and Dunn

(2012). . It is correlative with the lower Leduc Formation and is believed to be the source rock for the conventional Leduc, Nisku, and Wabamun oil pools in Alberta (Dunn 2012). During the Devonian, the growth of Leduc reefs was terminated by sea level rise, during which the reef-building organisms were ultimately unable to keep up with the rising sea level and drowned. The Leduc and Duvernay Formations are both overlain by the quartz-rich Ireton Formation, which forms a cap rock and seal for the oil reservoirs. Figure 1.1 shows the location of the study area within Alberta, the treatment well locations with the passive recording array, the downhole recording configuration, and generalized Devonian stratigraphic column. Within the stratragraphic column, the Duvernay is colored red, the Leduc Formation and Gilwood member are highlighted in yellow. The Gilwood member is a significant seismic marker, a channel incised into the Muskeg formation. The mapping of the Gilwood channel aids greatly in recognizing the structural evolution of the environment affecting the Duvernay Formation deposition and diagenesis.

The depositional environment of the Duvernay Formation varied enormously depending on where it was situated with respect to the Leduc reef. Factors which affected the deposition were tides, climate, storms and sea level changes. Inter-reef areas were protected from waves and tides, so that sediments were deposited in a low energy environment. In the subsurface, five lithofacies have been identified from cores (Dunn and Schmidt, 2012): argillaceous mudstones, bioturbated limestones, organic rich siliceous mudstones, siliceous organic-rich mudstone and mixed siliceous mudstones.

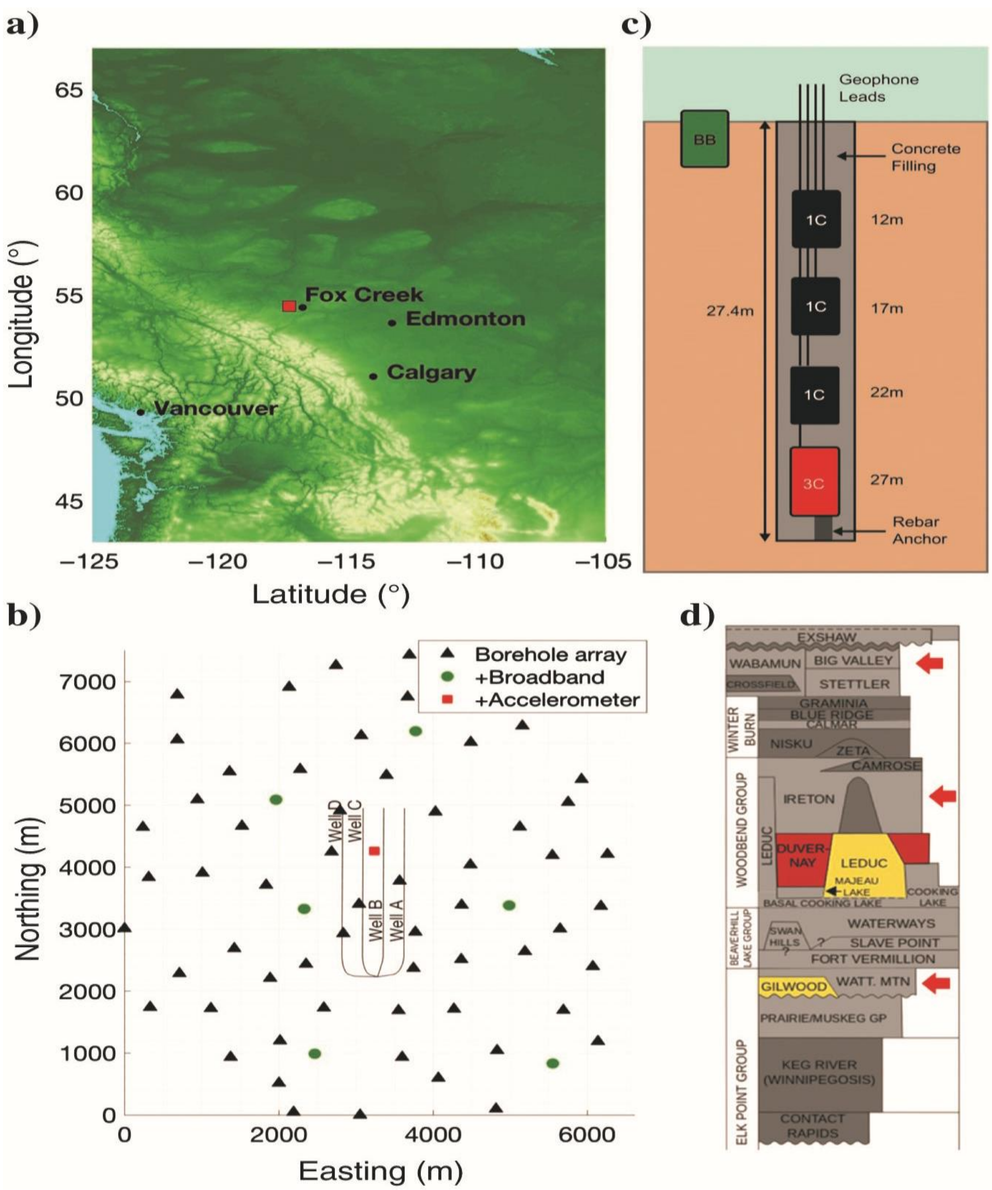


Figure 1.1. A location map highlighting the study area within the province of Alberta. (a.) The area is near Fox Creek, Alberta, (b) displays the horizontal well treatment program with the microseismic recording array. (c) is the downhole recording configuration, and (d) is the generalized stratigraphic column for the Devonian age in Alberta. The formations of interest highlighted in red (Duvernay) and yellow (Leduc). (adapted from Core Labs Stratigraphic Correlation Chart

Seismic information plays an integral part in the development of unconventional reservoirs such as the Duvernay Formation in Alberta, Canada. Two types of seismic data are analyzed in this thesis: seismic reflection data, acquired using active seismic dynamite near the surface, and passive seismic data, recorded continuously to "listen" for seismic events such as induced earthquakes occurring at reservoir depth (microseismic events). For wellbore placement, seismic reflections are converted to depth and are used to determine well placement and trajectory. Emerging technologies such as simultaneous inversion, structural mapping, and microseismic analysis are routinely used as key components in deriving a complete reservoir picture (Chopra et al., 2017; Weir et al., 2018). These inversion methods deliver lithologic properties such as P-wave velocity, S-wave velocity, and density, from which petrophysical properties such as Young's Modulus, Poisson's Ratio, and Brittleness index are calculated.

Horizontal well treatment programs (hydraulic fracture stimulation) are monitored by a passive seismic recording array situated on the near surface (Eaton, 2018). This array records seismic events such as perforation shots background seismicity, induced fractures, and induced earthquakes. Data recording occurs before, during, and after the well treatment program. The passive seismic recording is processed to catalog seismic events and to determine the epicenter (surface projection) and hypocenter (seismic event depth). Analyzing the depth and pattern of the microseismic fracture propagation serves as a method to characterize the reservoir by interpreting the fault patterns. The lateral extent of the fracture stimulation is tracked, and insights are obtained as to the mechanism by which fractures propagate. A challenge exists in determining the optimal method to develop a reservoir by well placement while avoiding geohazards such as induced seismicity. Technologies developed and discussed in this thesis are used to advance reservoir characterization and include simultaneous inversion (Weir et al., 2018), a new method to determine hypocenter depth (Poulin et al, 2019) , improvements in signal processing (Weir et al., 2019), and a method to integrate passive seismic data with reflection data to provide a comprehensive geological interpretation.

### 1.11 Poststack inversion

The concept of seismic inversion dates back to R. Lindseth and the Seislog® inversion (Lindseth, 1979). Seismic reflection data are inherently band-limited (Lines and Newrick, 2004), so the ability to recover subsurface impedance values is data-limited. As part of normal seismic processing, seismic data are stacked to approximate a zero-offset reflection and to reduce noise (Margrave, 2005). Stacked seismic data processing makes the assumption that all the seismic traces that focus on a common midpoint can be summed to increase the signal to noise ratio, and form a reflection seismic section that assumes all raypaths are vertical, and hence zero incidence. The seismic data used for poststack inversion is the common midpoint stack, where the individual traces that focus on a common midpoint are summed together, or “stacked.’ Sonic well log data are used to add a low-frequency (0 to 12 Hz) component to seismic data, resulting in a more accurate subsurface impedance profile. The resulting inversion is a representation of the acoustic impedance profile in the subsurface. By adding the low-frequency component, a more accurate subsurface acoustic impedance is defined. By using the sonic log, as shown in Figure 1.2, the low-frequency component of the seismic data is recovered. The sonic log (or sonic/density logs) is resampled, tied to the reflection data by means of a synthetic seismogram.

The blocked log is perturbed at each and every trace in the survey until there is a match. The resulting output is the acoustic impedance inversion. A limitation of this type of inversion is that it is a combined sonic and density response and cannot isolate density or velocity effects. An anomaly caused by a coal bed may be indistinguishable from a gas sand. Poststack inversion is also subject to the same resolution issues with respect to the thickness of the target interval at one-fourth to one-eighth of a wavelength (Lines and Newrick, 2004, Widess, 1973).

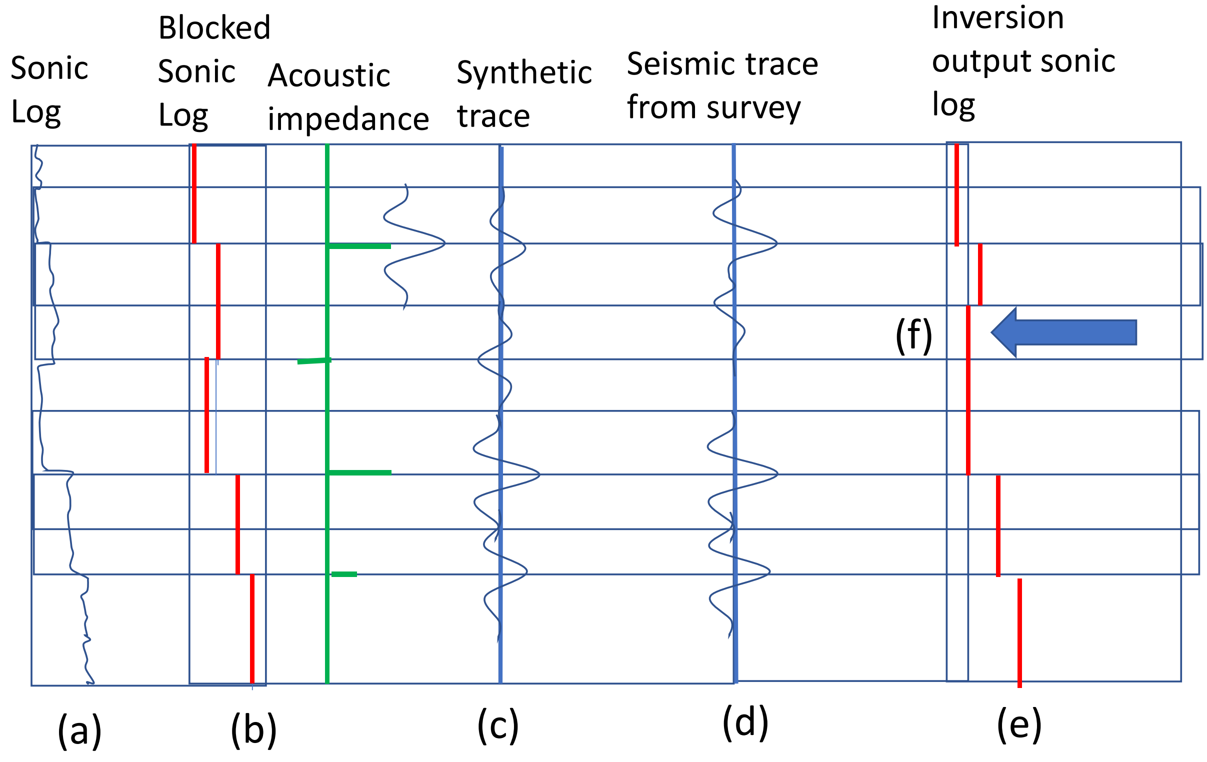


**Figure 1.2.** A simplified model-based inversion workflow. (a) The original sonic or acoustic impedance log. (b) The sonic log block model derived from the sonic log. (c) The reflection coefficient generated from the block model. (c) Where the synthetic data are tied to the seismic survey. (d) An arbitrary trace from the survey. (e) The block model from (b) perturbed to match the data. In this example, (e) is the final inversion output. (f) The layer that is modified to match the seismic trace (blue arrow).

### 1.12 Amplitude versus offset

Amplitude versus offset (AVO) is a technique where nonzero incidence seismic reflection data is used to determine the physical properties of the subsurface. With AVO analysis, the amplitude behavior is investigated as a function of source receiver offset or incidence angle, the traces that were stacked for the zero-offset seismic section are investigated individually for their angle dependence. AVO came about as a recognition of the offset-dependent reflectivity within seismic reflection data. Initially, AVO analysis was used as a method for direct gas detection in the subsurface (Ostrander, 1984), where gas sands were observed to have a demonstrable increase in amplitude with offset. It became a routine practice to distinguish strong anomalies generated by low-impedance events such as coal beds from gas zones (Lines and Newrick, 2004). Hydrocarbon maturity windows for early use of AVO analysis were described by Chiburis et al. (1993), where prestack seismic data were used as a direct hydrocarbon indicator. Equations 1.1 and 1.2 were used based on petrophysical parameters to generate forward models and predict the offset reflection dependence of reservoirs as a function of fluid content. Using AVO, the interpreter was able to distinguish lithology changes from fluid changes; some of the observed “bright spots” in the stack data were confirmed to be generated by the presence of hydrocarbons and to be distinguishable from lithology-generated anomalies such as coal beds. . This amplitude-versus-angle (AVA) strategy is used as an interpretation tool to determine fluid content or rock properties. Figure 1.3 is a diagram of how an incident P-wave reflects a P-wave and converts to S-waves.

Aki and Richards (2002) discussed the following relationships for energy partitioning at an interface. P-wave to P-wave reflection (P-P) and P-wave to S-wave reflection (P-S) can be expressed as a function of incidence angle or, more conveniently, as a function of $\theta$, where $\theta$ is the incidence angle:

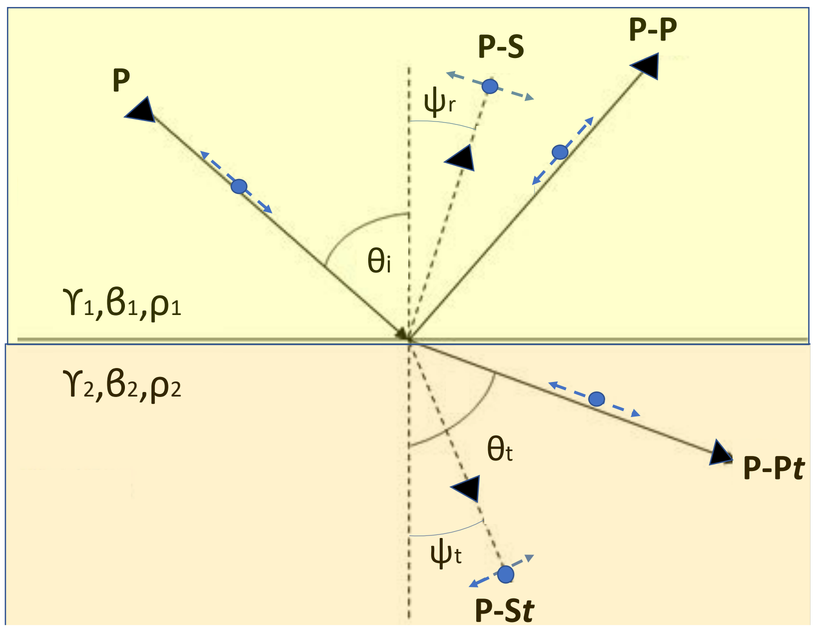


**Figure 1.3.** A display of an incident P-wave reflecting, refracting, and partially converting to an S-wave. The reflectivity is a function of the incidence angle and is determined by contrasts from $V_P$, $V_S$, and ρ *(*P-wave velocity, S-wave velocity, and density, respectfully*).* θ is the incidence, reflection, and refracted P-wave angle, and ψ is the S-wave reflected and refracted angle.

$$R_{ps}(\theta) = \frac{1}{2}\left(\frac{\Delta\rho}{\rho}\right) + 2\gamma\left[\frac{\Delta\rho}{\rho} + 2\frac{\Delta V_S}{V_S}\right]\theta^2 \qquad (1.1)$$

where $\theta$ is the P-P incidence angle in radians and:

$$V_P = \frac{1}{2}[V_{P1} + V_{P2}], \qquad V_S = \frac{1}{2}[V_{S1} + V_{S2}], \qquad \rho = \frac{1}{2}[\rho_1 + \rho_2]$$

$\gamma = \frac{V_S}{V_P}$. Values for $V_S$ and $V_P$ (S- and P-wave velocity, respectfully) are generally taken as the average value over the region of interest.

$$\Delta V_P = V_{P2} - V_{P1}, \qquad \Delta V_S = V_{S2} - V_{S1}, \qquad \Delta\rho = \rho_2 - \rho_1$$

Fatti's version of the Aki-Richards equation is (Fatti et al., 1994):

$$R_{PP}(\theta) = c_1 R_P + c_2 R_S + c_3 R_D \qquad (1.2)$$

where

$$c_1 = 1 + \tan^2\theta, \qquad c_2 = -8\gamma^2 \sin^2\theta, \qquad c_3 = -\frac{1}{2}\tan^2\theta + 2\gamma^2 \sin^2\theta$$

$$R_P = \frac{1}{2}\left[\frac{\Delta\rho}{\rho} + \frac{\Delta V_P}{V_P}\right], \qquad R_S = \frac{1}{2}\left[\frac{\Delta\rho}{\rho} + \frac{\Delta V_S}{V_S}\right], \qquad R_D = \frac{\Delta\rho}{\rho}$$

These equations form the basis to estimate P-P and P-S derived from sonic, shear, and density logs.

The choice for using a linearized inversion method (CGG Geoview) is based on the following considerations:

-At present, the Zoeppritz (Zoeppritz, 1919) equations are very complex, and are difficult to implement for practical applications (Zhang et al., 2016), linear approximations are sufficient given that the analysis is for incident angles well below critical, and the general band limited nature of our reflection seismic data is well suited to a model based “blocked” inversion..

-Geoview Commercial software is configured to processes large prestack data volumes, .uses advanced graphics, and has the I/O capability to pass data to and from other platforms.

-Computational efficiency, non-linear methods can be computationally expensive, and are not readily available for 3-D/3-C datasets.

-All of the offsets for inversion were intentionally limited to a maximum incident angle of 38°, linear approximations are quite effective in our application, the objective to image relative differences in the Duvernay Formation in the calculated impedance volumes.

**1.13 Simultaneous and joint inversion**

Combining impedance inversion with AVO results in a process called simultaneous inversion, where prestack seismic data are combined with subsurface log data, with the P and S wave, and density are calculated (Hampson and Russell, 2005). The converted wave response depends only on the in shear ($\Delta Vs$) contrasts and density ($\Delta\rho$), which is much simpler than the P-P response, where the response is dependent on $\Delta Vp$, $\Delta Vs$ and $\Delta\rho$ (Gray, 2003). Synthetic data as well as converted wave data from Long Lake, Alberta as examples. Without the shear wave data, the it is difficult to resolve accurate density values. Inversion tests were also performed using synthetic and VSP data (Mahmoudian and Margrave, 2007). The shear wave data contributed a greater portion to the density value than the compressional velocity. The Blackfoot field study (synthetic data) and a field study in the Red Deer area on a walkout VSP were processed as comparison examples between different inversion algorithms. AVO inversion, by its very nature, requires the use of a damped singular value decomposition to stabilize the AVO inversion. The density solution is very sensitive to noise in the AVO inversion, hence the need for a stability factor (thereby reducing resolution). In the simplest of terms, the converted wave data provides a direct shear wave response from the subsurface. This data is independent of the P wave reflected and adds additional information to the inversion. Given that the objective of the inversions presented here is to derive petrophysical properties such as Young's Modulus, and Poisson's' Ratio (calculated using $Vp$, $Vs$ and $\rho$), an accurate density estimate is crucial.

Ideally in a 3-D seismic acquisition program the source points (dynamite shots) and receivers (geophones) are distributed evenly, with an even distribution of near and offsets for each common midpoint. The surface projection of the common mid-point is referred to as a "bin," the objective of seismic processing is to ensure all of the bins are equivalent, with an even distribution of offsets. In the real world, there are surface obstructions, roads, railways, wells, and so on which make it all but impossible to even out the bin distribution by field acquisition alone. The process of interpolation (Trad, 2005) fills in the missing acquisition data and normalizes the AVO trace distribution for each surface bin, and subsurface common midpoint. This process is essential to prepare data for simultaneous and joint inversion.

This simultaneous inversion is model-based, using conjugate gradients to calculate an optimal solution. This inversion is constrained by well log data and defined seismic horizons. This inversion process has been applied to single-component data using offset dependency to extract S-wave data, with calculations based on approximations to the Zoeppritz equations (Lines and Newrick, 2004).

Joint inversion uses multicomponent data, with the S-wave data (converted from P-wave to S-wave upon reflection) recorded in conjunction with the P-wave data. This inversion is model-based and requires well logs, P-P and P-S data, and seismic interpretation (Weir et al., 2018). Five-component seismic data interpolation normalizes the prestack data by calculating an even distribution of traces in bins the prestack P-P and P-S recorded data (Trad, 2009). Interpolation addresses the problem of offset and bin distribution in the prestack domain, improving by regularizing the offset distribution and normalizing the bins to the bin center. Rock parameters are calculated from this inversion such as Young's Modulus, Poisson's Ratio, and brittleness. These are used for detailed petroleum reservoir characterization. Combining these data with structural interpretation can lead to the identification of geohazards, "sweet spots" in the petroleum reservoir, and a way to plan well trajectories, such as with areas subject to induced seismicity.

In order to interpret the inversion results, stratal slices are created from the inversion volumes. The Swan Hills Formation seismic reflector served as a reference and slices from 2 to 16 ms are created above the Swan Hills Formation. The 8 ms stratal slice is selected for display, the slices are very similar to the 6, 10 and 12 ms time slices derived from the same data set, a function of the band limited nature of the seismic method. A seismic wavelet is displayed in one of the outcrop photographs to illustrate the relationship between seismic resolution and bed thickness. The velocity and density contrast between the Ireton Formation shale and the

Duvernay Formation is relatively small, especially compared with the strong peak associated with the Swan Hills Formation reflection; it does not have a strong peak or trough uniquely associated with it, rather the pick sits on the side of a trough when correlated in the synthetic seismogram. The Duvernay Formation does not have an observed “tuning” effect, as observed in a shallow gas sand; rather, there is substantial side lobe effect form the Shan Hills reflector. The inversion operator, using wavelet extraction mitigates this problem by compressing the wave form to a spike within the resampled (blocked model, Russell and Hampson, 1991).

**1.14 Microseismic recording**

Microseismic recording for the petroleum industry was first performed by the El Paso Natural Gas Company in 1973 (Power et al., 1976). Microseismic recording has since been deployed over a number of varied settings such as the hot dry rock experiment by Whetten et al. (1987) and in geothermal applications such as the monitoring of geysers . Microseismic recording came into common use around 1997 (Zinno, 2011) using both downhole and surface arrays. Microseismic monitoring usage has been documented for many unconventional plays such as the Montney Formation (Eaton et al., 2013), the Duvernay Formation (Eaton et al., 2018), the Barnett Shale Formation (Wu et al., 2016), and the Fayetteville Formation (Hobro et al., 2016), as well as for the Marcellus, Bakken, and Haynesville Shales (Duncan et al., 2013), the tight sand fields and the unconventional oil fields of the Austin Chalk Formation (Phillips et al., 1998), and the Eagle Ford Shale (Inamdar et al., 2010).

Seismic events have been detected as P- and S-wave arrivals in a time-series geophone recording; placing these events in depth requires the use of a velocity model (Lomax et al., 2000;

Lomax et al., 2009). During hydraulic fracture stimulation (fracking), microseismic events are recorded on continuously recorded multichannel/multicomponent acquisition arrays. For the microseismic recording used in these studies, the data were acquired before, during, and after hydraulic fracturing using a near-surface array. In this thesis, data are used in their original (raw) form with minimal signal processing applied. Seismic events are detected using a variety of methods, which are then converted to hypocenters using a 1D time-depth model. In order to improve event detection, processes commonly used in seismic reflection data are deployed here. The result is an improvement in the signal-to-noise ratio and a significant increase in the number of events detected.

### 1.15 Microseismic event detection methods

Matched filter analysis (MFA) is a method used for detecting microseismic events (Caffagni et al., 2016). MFA correlates a template waveform against a continuous data stream to detect similar occurrences. Several seismic events are manually picked as template events, called “parent” events. These events are correlated against the continuous data to detect occurrences that match the parent events. The quality of the “child” events are dependent on the quality of the identified parent event for each cluster and are affected by the signal-to-noise ratio of the input data. Beamforming (Verdon et al., 2017) generates P- and S-wave travel-time lookup tables from identified events. From these events, a search is performed across the array using short-term average (STA) and long-term average (LTA), a time shift is calculated, and the aligned tracs are stacked.

STA/LTA (Eaton, 2018) calculates the average values of the absolute amplitude of the seismic signal in two moving time windows. When the STA/LTA ratio exceeds a threshold greater than a preset value, a seismic event is cataloged. New methods for event detection are currently being evaluated, such as differential kurtosis (Paes and Eaton, 2017). Kurtosis is used with STA/LTA ratio to detect seismic events. The method is to sum the energy in a collection of geophones in a localized area. The signal delay between geophones between nearby stations is used to confirm the specific event.

**1.16 Microseismic depth determination**

Improvement in focal depth determination has been realized as a newly developed technology developed and described here as the “focal-time method.” Rather than using a 1D model to determine the hypocenter locations, a 3D P-P and P-S velocity volume is derived from a co-located multicomponent 3D survey calibrated to well control. The velocity volume used in this method takes into account velocity anisotropy and variations in subsurface structure and is constrained by nearby well control to convert arrival times to subsurface depths. Vertical transverse isotropy (VTI) is generally the result of bedding plane deposition, where the P and S velocity differ in horizontal and vertical directions (Ogiesoba et al. 2003). Azimuthal anisotropy is a condition where the seismic velocities vary as a function of the direction parallel to the bedding planes, or azimuthal direction (i.e. degrees from North). These variations may be caused by fracturing in the rock, reducing the velocity in the direction orthogonal to the fracture network. A 1-D velocity model cannot account for VTI, or variations in structure, whereas the focal-time method does. This results in accurately positioned hypocenters, which are combined with the P-P/P-S seismic volume and are displayed in the same 3D-rendered interpretation environment. With these data, geological insights are obtained as to the nature and propagation of fracture and induced seismic events. In case studies, risks associated with reservoir development include induced seismic events (felt earthquakes) and fracture propagation occurring in an unexpected manner and without easy explanation by a simple homogeneous reservoir model.

### 1.17 Microseismic data preparation

Seismic reflection processing such as deconvolution filtering and scaling is routinely applied to seismic data to reduce noise and enhance the signal (Margrave, 2005). This processing improves the information available for interpretation of seismic events. This same processing is applied to the continuously recorded data for microseismic event recording, resulting in a marked improvement in the signal-to-noise ratio over the raw data. The tests are performed using event detection such as STA/LTA ratio and kurtosis; a marked improvement is shown in the number of events. The intent of this work is to provide a method whereby event-picking algorithms (i.e., STA/LTA ratio and MFA) are provided with a set of data with improved signal-to-noise ratio. The signal processing used here is specifically tailored to the bandwidth of the P- and S-wave arrivals, removing signals and noise with frequencies outside this bandwidth.

### 1.18 Integrated interpretation

The final step in interpretation is to ascribe geological meaning to the seismic data. Risk reduction is a primary component of why seismic data, both continuous and reflection, are acquired. Risks for reservoir quality are assessed through inversion (brittle, ductile), risks for induced earthquakes are assessed by characterizing basement faults, and risks associated with fracture propagation are assessed through detailed fault and facies mapping. Within this thesis I consider a fracture to be on opening in the host rock, in a hydraulic fracture operation this often is a tensile crack opening (Eaton, 2018). Conversely a fault is considered to have movement of one plane with respect to another; strike-slip, compressional, tensional, or compensated linear-vector dipole (knopoff et al., 1970).

Although somewhat speculative, basement heat flow can be correlated with deep-seated basement faults. The hypothesis is that the increased heat flow may alter thermal maturity in localized areas and create overmature (dry gas) reservoirs. This may explain why dry gas is produced in areas mapped to be in the regional condensate window.

## 1.2 Thesis organization

This thesis comprises two published case studies (Chapters 2 and 3) and two expanded abstracts (Chapters 4 and 5) that use the technology developed during the course of this research. Chapter 6 combines research from the previous chapters and outlines methods using technologies developed in this thesis as applied to risk reduction, encompassing both economic and geohazard risks. Chapter 7 summarizes the research developed here and discusses how these new concepts contribute to geoscience.

### 1.21 Interpretation and inversion—Tony Creek dual microseismic experiment

Chapter 2 is a paper published in the SEG journal *Interpretation* that describes the use of simultaneous inversion for multicomponent seismic data in a case study. The intent of this work is to investigate the role of reservoir parameters such as Young's Modulus and Poisson's Ratio and determine the influence these have had on fracture propagation. The role of geological structure is also investigated, considering its role with respect to hydraulic fracture performance and induced seismicity. In this seismic-mapping project, seismic reflection data are correlated to the local geology using well log–generated synthetic seismograms. This is followed by PP-PS registration, in which the converted S-wave reflection section is tied to the P-wave seismic reflection section. Synthetic seismograms establish a time-depth relationship, identifying several key formations. Fault correlations are performed by observing matching vertical displacements in the seismic data and time slices and by observing the lateral displacement in the deep markers. Significant lateral variations are observed in the Duvernay Formation with respect to Poisson's Ratio, Young's Modulus, and Brittleness index, indicating the reservoir to be highly variable in geomechanical properties.

**1.22 Interpretation and inversion—Bigstone North**

Chapter 3 is a paper published in SEG's *The Leading Edge.* The methodology is similar to that deployed in Chapter 2, highlighting the Duvernay Formation in a different structural setting. The behavior of the hydraulic fracture propagation differs significantly from the adjoining Toc2ME area, the mapping of both structure and inversion attributes are investigated to explain these differences. The research uses multi-component 3-D seismic data to produce a structural interpretation, and integrate seismic inversion attributes such as Young's Modulus, Poisson`s Ratio, and Brittleness into the seismic interpretation. Hydraulic fracturing operations caused an induced event (a felt earthquake) , followed by several aftershocks. The 3D/3C Bigstone North seismic reflection dataset relates directly to the seismic survey ties of ToC2ME to the south, with several square kilometers of overlapping coverage. Although the fracture stimulation programs are within 10 km of each other, there are significant geological differences between the two areas.

### 1.34 Application of deconvolution to continuously recorded passive seismic data

The intent for the research in Chapter 4 is to demonstrate how the raw signal recorded during a microseismic survey can be improved by using established signal processing techniques commonly applied to reflection seismic processing This realization came about from earlier work in reflection data field testing where field processing were used in real time for raw field data evaluation. Often, a field shot record during the test sequence would be devoid of observable reflection events, a single pass of deconvolution would bring out these events so they could be easily observed. Applying these processes to continuously recorded (microseismic data) is observed to produce similar results; continuously recorded seismic records seemingly devoid of events in their raw state are observed to have visible seismic events. The effect of pre-processing is evaluated on three different automatic event picking algorithms, and the improvements to seismic auto picking methods are evaluated.

### 1.35 Focal-time method

Chapter 5 describes a new method for focal-time/depth estimation (hypocenter depth determination), that I co-developed. This method was originally published as an SEG expanded abstract and given as an oral presentation at the 2018 SEG meeting in Anaheim, California. The focus of this chapter is to demonstrate how this new technique, the `focal-time method, is used and applied to an existing microseismic catalog, showing how it can improve the depth solution over previous model-based methods. The new method uses the interpreted P- and S-wave seismic events to derive a velocity field over the 3D volume in both the P- and S-wave domains. This new method implicitly accounts for vertical and horizontal anisotropy, as well as variations in geological structure. These data are used to locate the microseismic events into equivalent times and depths within the seismic volume. This is a departure from previous methods using a 1D velocity model based either on well logs or on a layer cake model. This method is used to determine hypocenter depths in the same manner that the seismic reflection data are converted to depth. These microseismic hypocenter events are used as a key component of the seismic interpretation and mapping.

### 1.35 Integrated interpretation—Using microseismic to derisk the Duvernay

In Chapter 6, microseismic events are incorporated into the seismic volume (generated from the work in Chapter 5), and an interpretation is derived using fault mapping, reservoir characterization, and microseismic hypocenters. This chapter proposes a method whereby accurately positioned hypocenters (from focal-time), seismic inversion, (E,PR, BRI, from inversion), and structural interpretation (strike-slip and Riedel shear faulting) are incorporated into a comprehensive reservoir description. The interpretation workflow incorporates all of the reflection and microseismic data into a 3D visualization workstation, allowing the use of microseismic hypocenters as an independent component of the seismic interpretation. An explanation of microseismic fracture propagation is proposed, as well as a mechanism where induced seismicity is triggered. The emphasis is on de-risking the Duvernay Formation, taking into account induced seismicity, variations in structure, and lithology.

### 1.3 Main thesis contributions

New technologies, findings, and methods developed in this thesis are as follows:

- A new method is developed to determine the depth of microseismic events. The focal-time method replaces 1D velocity modeling with a velocity volume derived from a reflection survey, thereby accounting for anisotropy and subsurface structure.
- A new way of applying established signal-processing methods to continuous data for signal enhancement and event detection. This results in a significant increase in the number of detected events, and a potential reduction in the uncertainty of passive seismic event picks.
- A geological interpretation to explain why hydraulic propagation occurs in the manner observed and how fault and geological facies are the important factors.
- An explanation as to how and why large-magnitude seismic events (induced earthquakes) can occur based on deep-seated faults at depths significantly shallower than the treatment interval[4].
- A workflow designed to mitigate risk and potentially improve the economics of Duvernay Formation unconventional field development.

---

[4] The work in Chapter 3 of this thesis is an integral part of the publication Eyre et al., The role of aseismic slip in hydraulic-fracturing induced seismicity, Science Advances 28 Aug 2019: Vol. 5, no. 8.

# Chapter 2[5]

# Inversion and interpretation of seismic-derived rock properties in the Duvernay play, Tony Creek dual microseismic experiment

## 2.1 Summary

This chapter summarizes the development of an interpretive seismic workflow that incorporates multicomponent seismic inversion, guided by structural mapping, for characterizing low-permeability unconventional reservoirs. The workflow includes the determination of a calibrated time-depth relationship, generation of seismic-derived structural maps, poststack inversion, AVO analysis, and PP-PS joint inversion. The subsequent interpretation procedure combines structural and inversion results with seismic-derived lithologic parameters such as Young's Modulus, Poisson's Ratio, and Brittleness index. I applied this workflow to a 3D multicomponent seismic data set from the Duvernay play in the Kaybob area in Alberta, Canada. Subtle faults are discernible using isochron maps, horizontal time slices, and seismic stratal slices. Fault detection software is also used to aid in the delineation of structural discontinuities. I show that seismic-derived attributes, coupled with structural mapping, can be used to map reservoir facies and, thus, to highlight zones that are most favorable for hydraulic fracture stimulation. By imaging structural discontinuities and pre-existing zones of weakness, seismic mapping also contributes to an improved framework for understanding induced seismicity risk.

---

[5] Published in the SEG journal *Interpretation,* 2018, 6, SE1-SE14.

## 2.2 Introduction

Unconventional plays represent resource fairways, including those characterized by low-permeability, organic-rich rock formations, that are not economically producible by conventional drilling and completion methods. Low-permeability unconventional plays, such as the Duvernay Formation in the Western Canadian Sedimentary Basin, are now routinely developed with multiple horizontal wells drilled from a single surface location and are completed using hydraulic fracturing technology to enhance permeability and enable economic rates of hydrocarbon production (e.g., Dusseault and McLennan, 2011). Figure 2.1 shows the placement of the project area within the Western Canadian Sedimentary Basin, the thermal maturity regions, and the general stratigraphic column. In planning an unconventional drilling program, well logs, cores, and seismic data can provide valuable information for horizontal well placement and the design of hydraulic fracture stages. Parez and Marfurt (2015) described the importance of applying seismic to provide estimates of lithologic parameters such as Young's Modulus, Poisson's Ratio, and brittleness. Prior to the widespread development of unconventional resource plays, Pennington (2001) introduced seismic imaging as a primary tool to deliver statistical constraints for reservoir development within an emerging framework of reservoir geophysics. In contrast to traditional approaches for seismic exploration, Pennington (2001) emphasized how the calibration of 3D seismic models using well data, combined with rock-physics relationships, could be used to differentiate between competing

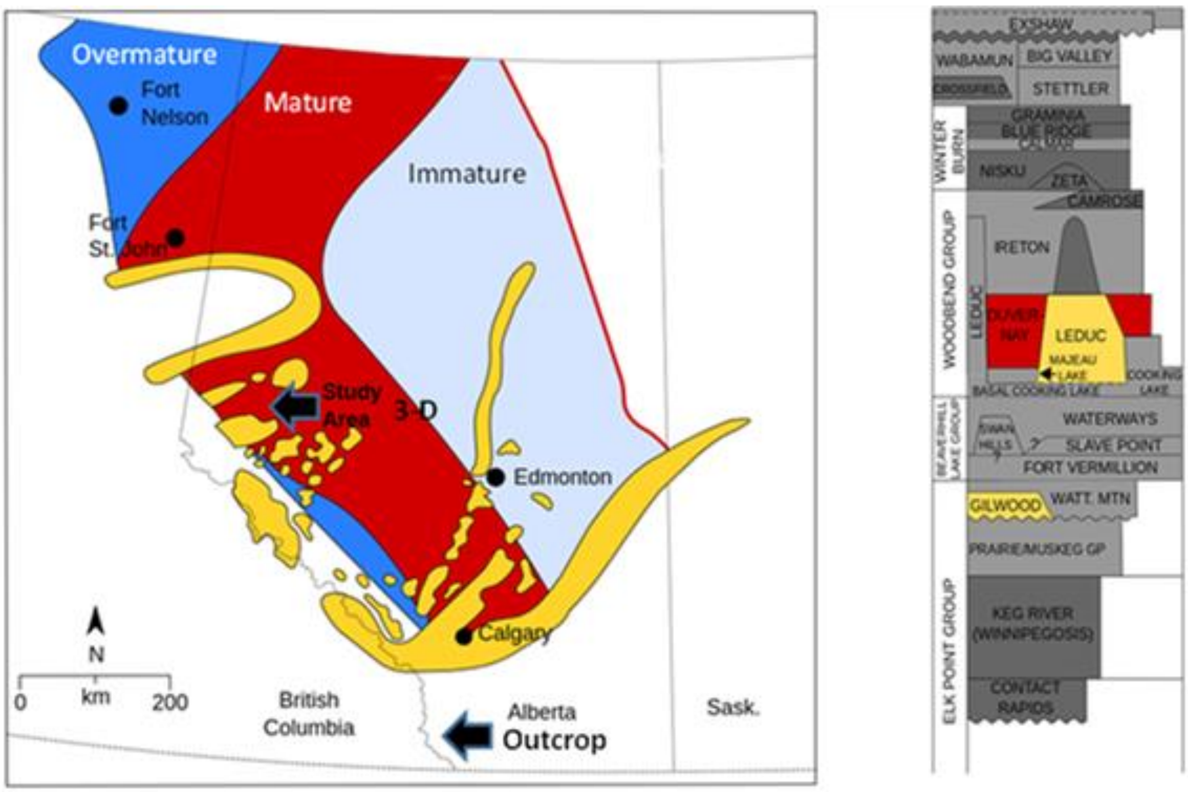


**Figure 2.1.** Hydrocarbon maturity windows for the Duvernay petroleum system (modified from Creaney and Allan [1990]), showing location of the study area. The stratigraphic column on the right (adapted from Core Labs Stratigraphic Correlation Chart [2017) shows Middle and Upper Devonian regional stratigraphic nomenclature, highlighting several units that are discussed in this thesis.

reservoir models on the basis of lithologic character, fluid content, and in-situ conditions such as pore (over) pressure. Dommisse (2013) applied similar concepts to unconventional reservoirs and demonstrated how stratal slicing can be a powerful technique for seismic reservoir characterization. By focusing on lateral spatial variability in the seismic expression of various reservoir facies, Dommisse (2013) argued that stratal slicing can overcome bandwidth-related limitations in vertical seismic resolution.

Goodway et al. (2010) described methods built on the use of AVO analysis to differentiate ductile shale reservoirs from brittle reservoirs in the Barnett Shale of Texas. Lambda, mu, and rho (LMR) parameters were derived from well logs and were cross-plotted and compared with data derived from seismic inversion. Trends that emerged from this approach demonstrated that variations in rock properties, often attributed to the brittle behavior of reservoir rocks, exhibit coherent patterns that reflect reservoir quality. When seismic-derived LMR attributes are back-projected onto a seismic section, trends in brittleness are observed and can be mapped spatially within a seismic volume. Perez and Marfurt (2015) showed that this technique can be useful to extract mineralogical content of rocks. The importance of fault mapping was highlighted by Refayee et al. (2016) in a Utica Shale example. Parameters such as dip, similarity, and curvature were extracted from the seismic data and incorporated into an interpretive model. A "fault enhancement–filtered" (FEF) seismic volume was derived from the seismic cube (similar to semblance) and was used to map major faults and image fracture networks. Refayee et al. (2016) proposed that sweet spots within in the reservoir are defined by areas of enhanced natural fractures and are mappable within the seismic volume.

Meek et al. (2013) highlighted the advantages of a multidisciplinary reservoir geophysics approach by combining results from microseismic monitoring, structural attribute analysis, and seismic petrophysics. Comparison of recorded microseismic events with curvature anomalies and other seismic-derived attributes such as Young's Modulus revealed a strong correlation with the density of recorded microseismic events. Prospective areas for future development were then identified based on seismic attributes. Similarly, Rafiq et al. (2016) showed how sets of attributes extracted from microseismic data can be correlated with curvature anomalies from 3D seismic data to partition a reservoir into depositional facies units.

Chopra et al. (2017) conducted a seismic analysis within part of the Duvernay play to show that induced seismicity appears to follow pre-existing basement faults. Schultz et al. (2017) investigated areas within the Duvernay play that are prone to induced seismicity from hydraulic fracturing and identified event hypocenters extending from the Duvernay into the underlying Precambrian basement. This study confirmed a correlation between the presence of basement fault systems and the location of induced seismic events. Igonin et al. (2017) used a passively recorded data set (co-located within this study's 3D/3C seismic survey) to analyze induced seismic and microseismic events.

This study makes use of a 3D/3C multicomponent seismic data set in the Kaybob portion of the Duvernay play, within a region where nearby induced seismic events (felt on the surface as earthquakes) have occurred (Bao and Eaton, 2016). Analysis of this data set includes structural interpretation and mapping, fault detection, and reservoir characterization based on poststack and simultaneous P-P and P-S inversion. Various presentations of the data are used to illustrate how structural and inversion attributes can be employed to identify areas that are most prospective for development, as well as areas where the existing fault architecture may pose a risk for induced seismicity.

The main objective of this study is to present a comprehensive workflow for interpretive processing and inversion of 3D/3C multicomponent seismic data for unconventional reservoir geophysics. I start with observation of the Duvernay/Leduc system in outcrop and use the observations of the outcrop to guide the interpretation. The faulting in the Duvernay Formation can be correlated and interpreted considering basement tectonics. The Gilwood Formation, affected by the same tectonic regime, provides a guide to the tectonic history, giving insight into deep-seated strike-slip and vertical-offset basement faulting. The study area has a history of induced seismicity (Igonin et al., 2017), which can be used independently to spatially identify fault activation. I apply this approach to a data set from the Duvernay play, demonstrating how seismic data can be used to map structural discontinuities and faults, thus providing insights into the tectonic history of the reservoir. I also show how seismic inversion applied to poststack and multicomponent data gathers (P-P and P-S) can be used as a tool to identify facies changes, fault boundaries, and potential geohazards such as basement faults.

**2.3 Geological setting**

The Duvernay Formation, a bituminous/argillaceous carbonate of Late Devonian age in the Western Canadian Sedimentary Basin, is emerging as a major resource play in North America (Hammermaster, 2012; Creaney and Allan, 1990). The Duvernay is rich in organic matter and, depending on thermal maturity and position within the basin, it produces gas, natural gas liquids (NGLs), or oil (Switzer et al., 1994). It is also commonly believed to be the primary source rock for the Devonian Leduc reef, Nisku, and Wabamun carbonate plays (Dunn et al., 2012). With the advent of increasingly widespread horizontal drilling and multistage hydraulic fracturing, the Duvernay is being recognized as a world-class unconventional resource play (Davis, 2013).

The Duvernay Formation was deposited adjacent to several large Leduc reef complexes (Figure 2.2). The Duvernay has an effective porosity of 6 to 7% and an average total organic carbon (TOC) content of up to 4.5% (Chopra et al., 2017). It is correlative with the lower member of the Leduc Formation (Figure 2.2) and is believed to be the source rock for most of the Leduc, Nisku, and Wabamun oil pools in Alberta (Dunn et al., 2012). Leduc reef growth was terminated by sea level rise, during which the reef-building organisms were ultimately unable to keep up with the rising sea level and were drowned (MacKay, 2018). The Leduc and Duvernay Formations are both overlain by the quartz-rich Ireton Formation, which forms a cap and seal to hydrocarbon reservoirs.

The depositional environment of the Duvernay Formation varies depending on where it is situated with respect to the Leduc reef margin. Factors influencing the depositional environment include tides, storms, and sea level changes. Interreef areas have been protected from waves and tides, so sediments in these regimes have been deposited in a low-energy environment. In the subsurface, five lithofacies have been identified from cores (Dunn et al., 2012): argillaceous mudstone, bioturbated limestone, organic-rich siliceous mudstone, siliceous organic-rich mudstone, and mixed siliceous mudstone.

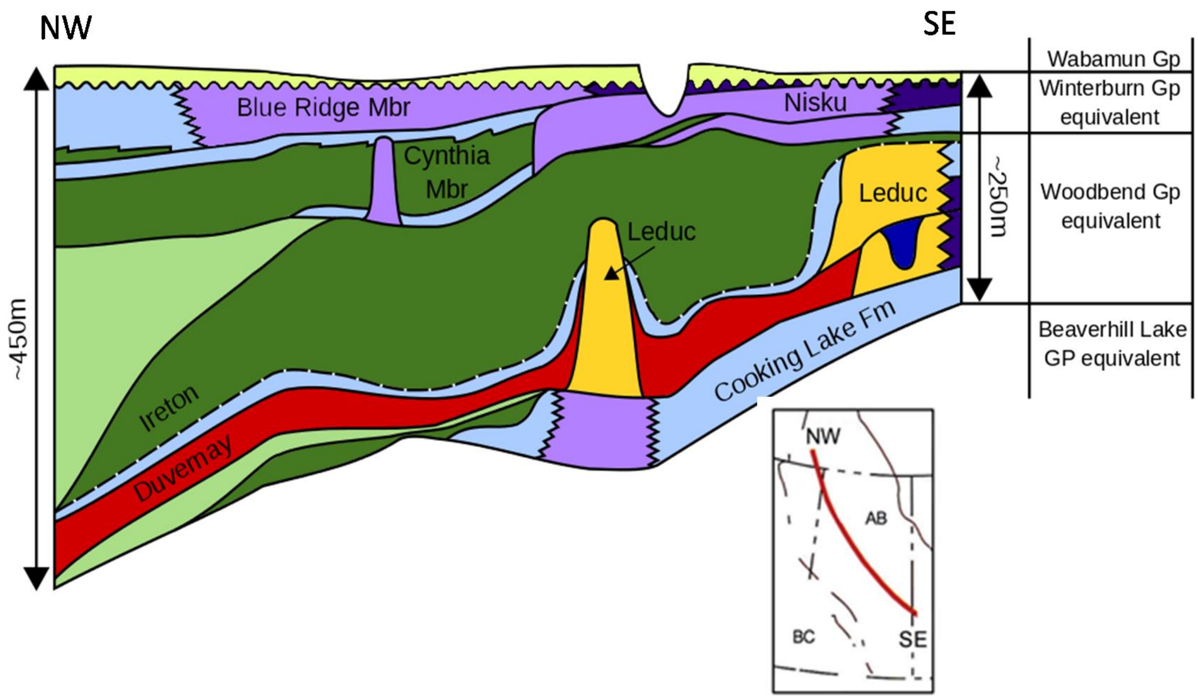


**Figure 2.2.** Generalized regional cross-section showing stratigraphic relationships of the Duvernay Formation with Leduc reef buildups and adjacent Devonian units. Inset shows location of cross-section. Adapted from Switzer et al. (1994).

Variability in depositional setting is evident in Figure 2.3, which shows a Leduc reef (Presqu'ile Formation) outcrop characterized by multiple stages of reef growth, with adjacent Duvernay-equivalent (Perdrix Formation) strata. This outcrop exhibits both lateral and vertical lithofacies variation within the section, including relationships relative to the reef margin. The reef mass visible in this exposure is 100 m thick and 250 m wide in section. The reef exhibits five distinct episodes of growth. To the north, the Perdrix Formation transitions into a quartz-rich shale. The increase in quartz content has an influence on rock properties; quartz-rich areas have a higher Young's Modulus and a lower Poisson's Ratio and may be more brittle than the rocks near the reef (Cho and Perez, 2014). This outcrop shows, at a scale similar to features resolved by seismic images, how the Duvernay Formation lithology varies both laterally and vertically. It follows that reservoir characteristics such as P- and S-wave velocities, density, and Brittleness index exhibit similar lateral and vertical variability in the subsurface.

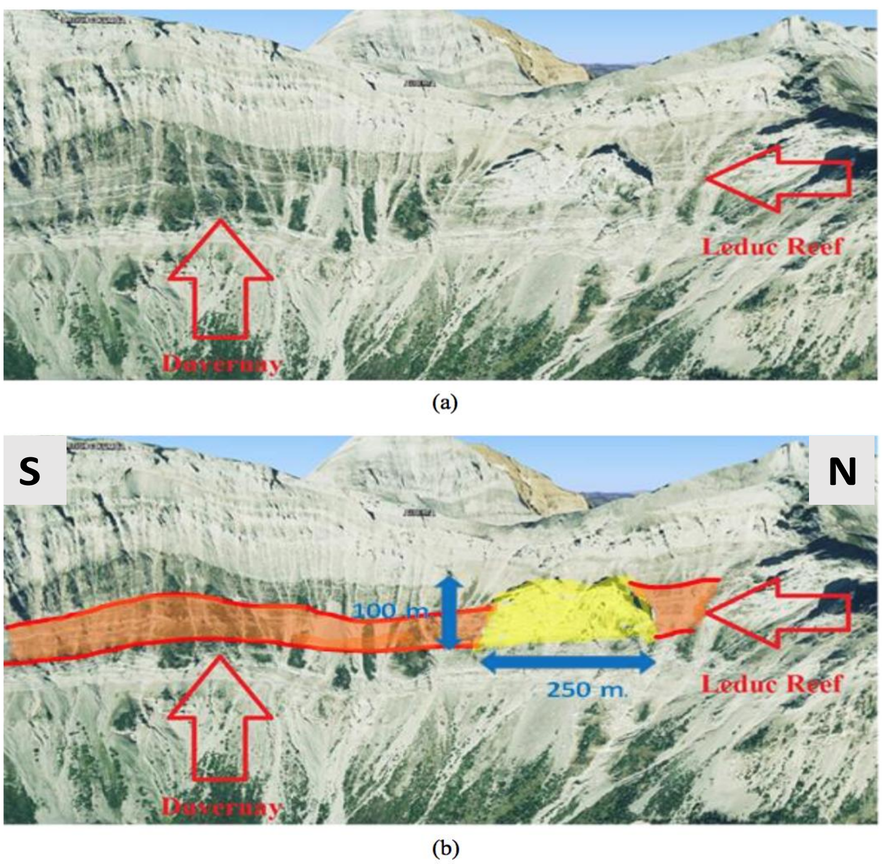


**Figure 2.3.** Outcrop of Perdrix Formation (Duvernay-equivalent) and Presqu'ile (Leduc-equivalent) strata in the Rocky Mountains south of the study area (49.41011162N, and 114.58814773E) (source: Google Earth). (a) Image with Leduc (yellow)- and Duvernay-(orange) equivalent units highlighted. The reef strata are more resistant to erosion. (b) Geological interpretation showing dimensions of the features, which are at a scale compatible with seismic resolution.

Brittleness has been identified as a key indicator of sweet spots in unconventional plays (i.e., areas that are developed with horizontal drilling and completed with hydraulic fracturing) (Cho and Perez, 2014). In general, brittleness is a desirable property that defines which rocks will fracture and yet maintain sufficient strength for the fractures to remain open after placement of proppant. Cui et al. (2017) presented various definitions of brittleness, including how it is derived and how its expressions are relevant to reservoir characterization. In this paper, I use the definition of brittleness proposed by Rickman et al. (2008), which is based on P- and S-wave velocities and density.

A rock with a high Brittleness index will necessarily have a low Poisson's Ratio and a high Young's Modulus. Within an established lithofacies framework, a strong correlation exists between quartz content, TOC, and brittleness of the Duvernay Formation (Dunn et al., 2012). The higher silica content of the Duvernay comes from deposition at distal, low-energy areas. Soltanzadeh (2015) provided evidence that clay content also plays a significant role in the brittleness of the Duvernay and Ireton Formations. Moreover, hydrocarbon generation has changed rock properties such that the high TOC in the Duvernay Formation tends to be more brittle.

## 2.4 Interpretive workflow

### 2.4.1 Amplitude-versus-offset–compliant processing

The 3D multicomponent seismic data used in this study, acquired and processed in 2015, are processed in an AVO-compliant manner (e.g., Lee et al., 1991; Allen and Peddy, 1993) by using processing steps designed to preserve relative amplitudes for both P-P and P-S data sets.

The AVO-compliant processing flow used to generate the P-P data volume is generally similar to a conventional seismic-processing flow, with a few key differences. Spectral balancing is applied in a surface-consistent manner (Taner and Koehler, 1981) by scaling low-amplitude frequency bands using correlated stack equalization. Noise attenuation is then performed in the cross-spread domain (Calvert et al., 2008). Traces with residual anomalous amplitudes (i.e., outliers) are manually edited from the data. Prestack time migration (e.g., Fowler, 1997) is then applied, followed by a radon multiple attenuation (Kelamis et al., 1990). Five-dimensional (5D) interpolation and normalization (Chopra and Marfurt, 2013) is then applied to the data in order to fill in missing traces and to normalize the data to the bin center.

Essentially the same AVO-compliant workflow is applied for P-S data processing, with several adaptations that account for the specific raypath geometry of converted waves (Stewart et al., 2002), in addition to S-wave splitting. In particular, the bin centers are determined using common conversion point binning (Eaton and Lawton, 1992). S-wave–splitting analysis is performed to determine the time shift and rotation angle between the fast and slow $qS$ arrivals. An amplitude compensation is performed using the approach of Jin et al. (2000) that applies corrections that reverse the S-wave–splitting effect along the upgoing raypath. After applying these processing steps, a 5D interpolation and normalization is performed, with the P-S output bins normalized (interpolated) to coincide with the location of the P-P bins. The version of the stacked data used in this study for interpretation and prestack inversion is limited to a maximum 40˚ P-wave incidence angle, based on ray-tracing using a velocity model derived from a control well

(well A) that is discussed below. The corresponding gathers then have residual normal move-out and trim statics (e.g., Hoeber et al., 2005) applied to both the P-P and P-S prestack data volumes.

### 2.4.2 Structural mapping

Sonic and density logs from a control well (well A) are used to generate a synthetic seismogram in order to achieve a precise tie to the seismic data (Figure 2.4). During this process, the source wavelet is also estimated. Well A is logged to the Middle Devonian Gilwood

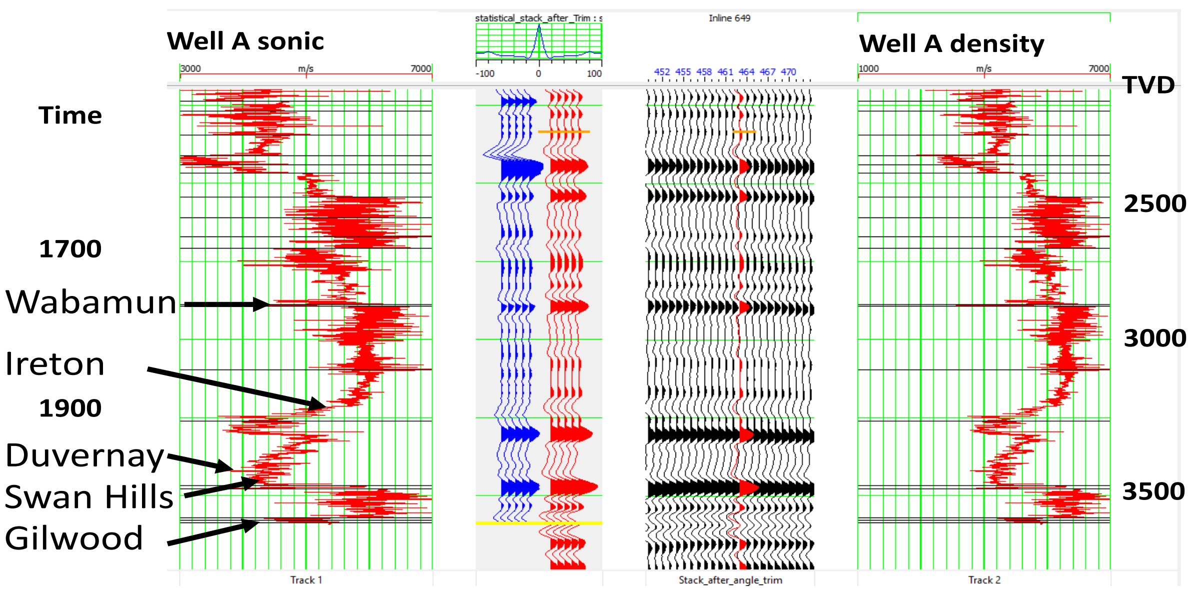


Figure 2.4. P-P synthetic seismogram well tie for the interpretive workflow, showing the extracted source wavelet. The integrated two-way times from the P-wave velocity (VP) log at well A are shifted to match the observed times. Zero-offset synthetic seismograms are duplicated for clarity. Those plotted in blue are from the zero-offset synthetic, while those plotted in red are the actual seismic traces at the wellbore. A good fit for the latter synthetic seismogram is evident by overlaying it onto the P-P data volume at the location of well A, as shown on the right. This correlation provides confidence for the horizon picks and time-depth relationship. The location of well A relative to the seismic survey is indicated in Figure 2.6.

member of the Watt Mountain Formation to a depth of 3607 m. This synthetic seismogram tie establishes a time-depth relationship, which is subsequently used to create angle gathers, perform PP-PS registration, and provide a calibration point for the seismic inversion. Figure 2.5 shows a west-east seismic profile extracted from the P-P stacked data volume. The density and sonic curves from well A are overlaid to illustrate the correlation of these log curves with the seismic profile. The Duvernay, Gilwood, and Precambrian seismic horizon are correlated based on the tie to well A. A horizon marking the top of the Precambrian basement is also picked based on a regional correlation from a deep-crustal seismic profile (Eaton et al., 1999) that passes close to this 3D seismic survey. Structural discontinuities are evident as breaks or sharp bends in the picked horizons.

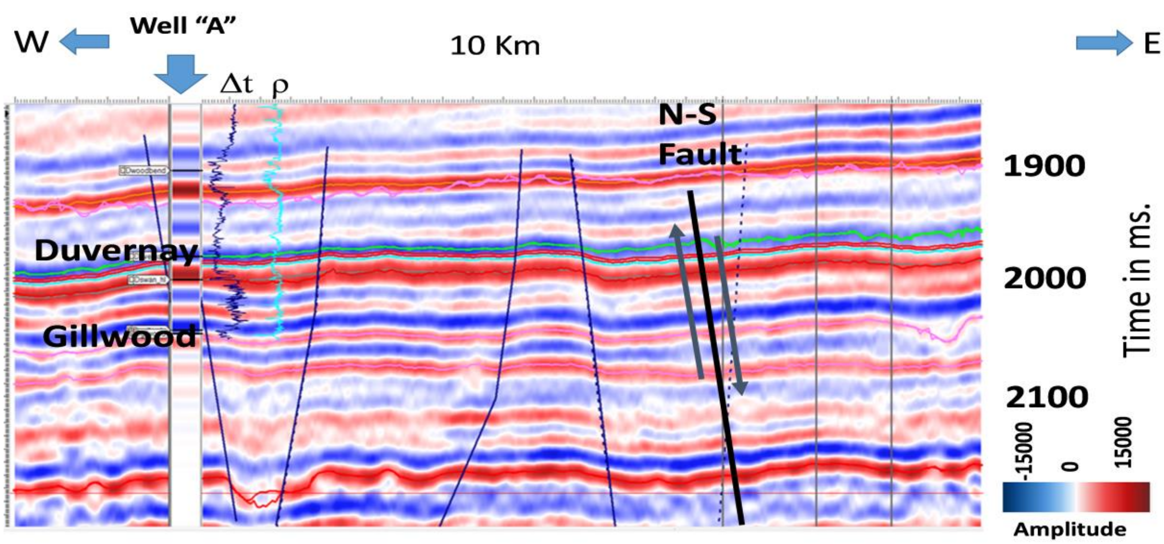


**Figure 2.5.** West-east seismic profile extracted from the P-P data volume, showing the synthetic seismic correlation with the Duvernay and Gilwood horizons. A series of interpreted steeply dipping faults is indicated. At well A, sonic ($\Delta t$) and density ($\rho$) logs are shown. The location of this profile is highlighted in black on Figure 2.6.

Figure 2.6 shows a perspective view of time slices from the P-P data volume intersecting the Duvernay and Precambrian horizons. The location of well A relative to the 3D seismic surface is also shown. Both time slices reveal amplitude trends that define a prominent set of north-south–oriented features. In the case of the shallower time slice, terminations of these prominent features occur along a northeastward trend, defining a secondary set of lineaments.

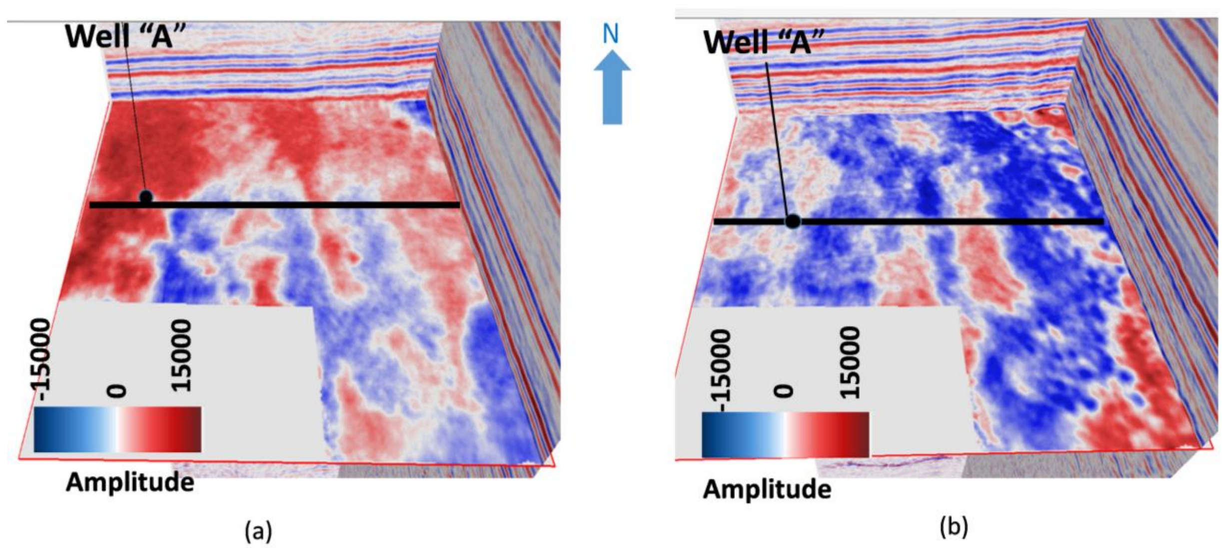


**Figure 2.6.** Perspective view showing amplitude time slices through the P-P seismic volume at (a) 2,000 ms and (b) 2,150 ms. The shallower time slice (a) intersects the Duvernay horizon, while time slice (b) intersects the Precambrian time surface. Both time slices reveal approximately north-south–trending linear topographic features that are interpreted to be associated with fault systems. The black line shows the position of the seismic profile displayed in Figure 2.4.

Time-structure maps are created throughout the data volume for all of the horizons listed above. Representative time-structure maps of the Second White Speckled Shale and Duvernay horizons are shown in Figure 2.7. For all of the Devonian stratigraphic horizons, as well as the top of the Precambrian basement, the overall structural dip is toward the northwest. For the shallower horizons, this trend changes to a regional southwest dip, which is oriented toward the Rocky Mountain deformation front. The Second White Speckled Shale surface also exhibits a distinctive set of northeast-trending lineations. This pattern is also present on the Duvernay horizon, albeit to a lesser extent, whereas the aforementioned north-south structural trend is strongly expressed. This north-south structural fabric is not seen above the Ireton Formation; at greater depth, it extends through the Gilwood and Precambrian horizons.

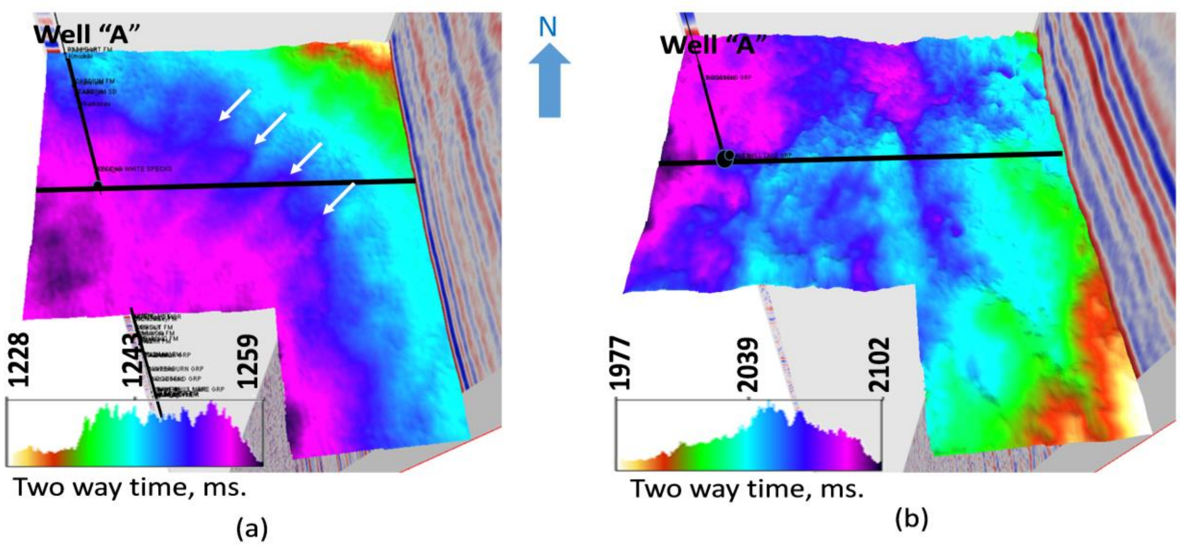


**Figure 2.7.** Perspective view of (a) Second White Speckled Shale and (b) Duvernay time-structure displays, derived from the P-P data volume. The Second White Speckled Shale structural map contains several distinct northeast-southwest lineations, highlighted by the white arrows. The Duvernay time structure shows north-south lineations, in addition to a subtle northeast-southwest fabric. Histograms on the lower left of each panel show color scale, referring to time (ms).

A time-structure map on the Gilwood horizon is shown in Figure 2.8. The Gilwood member of the Watt Mountain Formation is a clastic unit deposited during uplift of the Peace River Arch (O'Connell, 1994). Seismic mapping of this unit reveals a conspicuous feature that is interpreted as a meandering river channel that may represent a drainage system linked to uplift of the Peace River Arch. At the reflection depth of the Gilwood Formation, the seismic data images the edges of the broad channel system, rather than individual channel features. The mapped channel system is in the order of 400 meters wide, comparable to a modern channel system such as the Red Deer River channel. Figure 2.8 also shows images created using a coherence- and curvature-based algorithm for fault detection, followed by an adaptive principal-component analysis. This software delineates and displays lateral discontinuities in the seismic data and highlights several features that are further enhanced by 3D rendering and shading. These features help to elucidate the meandering channel-like feature, which is cross-cut by a prominent north-south linear feature. As discussed below, I interpret this feature as a possible strike-slip fault with left-lateral displacement (sinistral); based on the channel offset, the net displacement along the fault appears to be about 1 km. An important aspect of this fault is that it was active after the time of Gilwood Deposition, and plays an important role in the interpretation of induced seismic events.

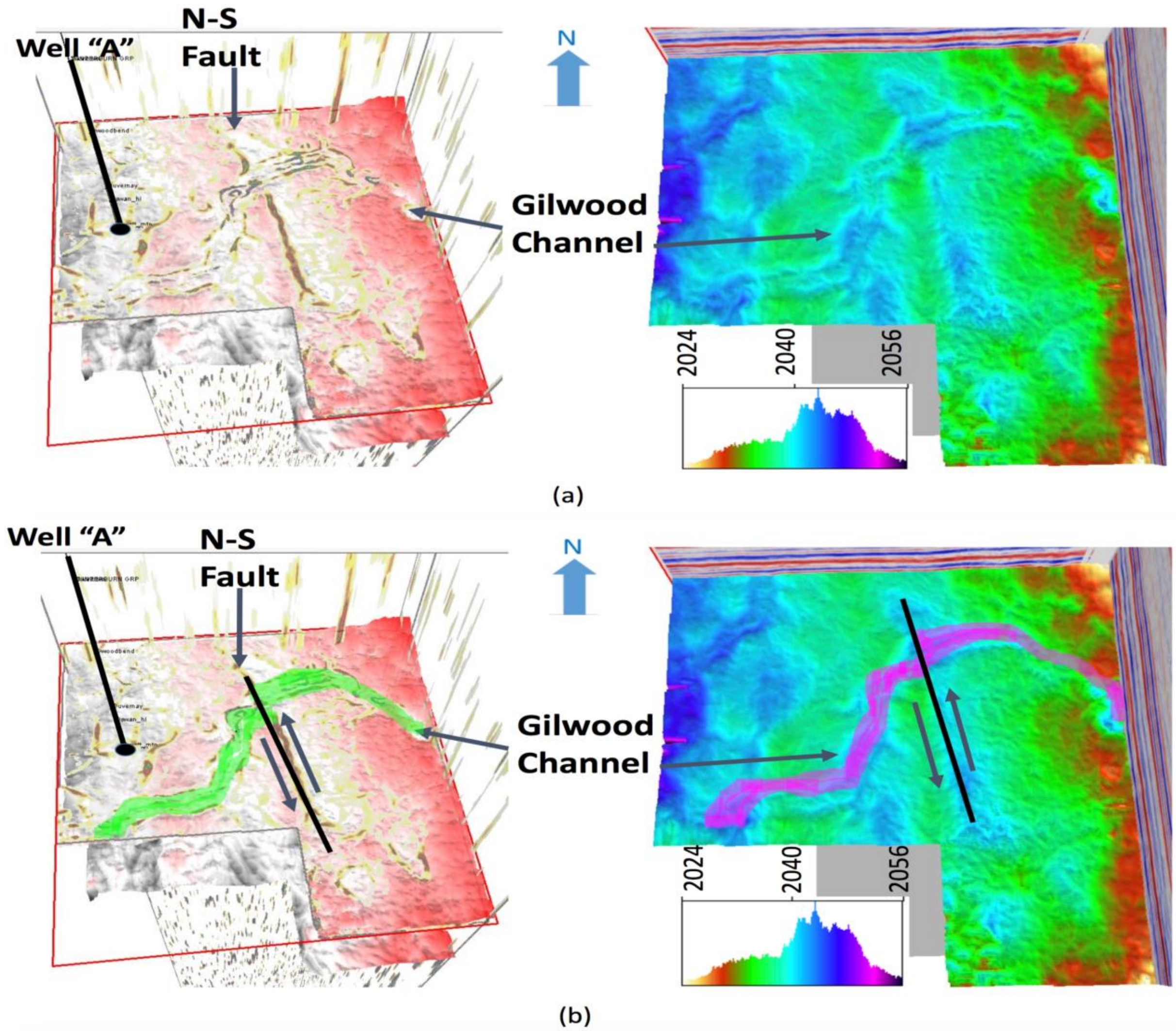


**Figure 2.8.** Gilwood time structure derived from the P-P data volume. Also shown is automatic discontinuity/fault detection (left panels) obtained using a coherence- and curvature-based algorithm with adaptive principal-component analysis. . A meandering channel is evident, cross-cut by a prominent north-south lineament with apparent left-lateral (sinistral) offset. The displacement on the Gilwood indicates post depositional movement after Gilwood erosion and deposition This figure shows both (a) uninterpreted data and (b) data with the channel and fault interpretation overlaid. Histograms indicate time (ms).

## 2.5 Seismic inversion

The seismic horizons, well ties, and structural discontinuities discussed in the previous section are used to guide the inversion process. The theoretical basis for the inversion procedures was presented by Hampson et al. (2005).

### 2.5.1 Poststack inversion

The inversion workflow begins with poststack inversion, in which an initial model of acoustic impedance (i.e., the product of velocity and density) is constructed and then perturbed until a satisfactory maximum-likelihood fit is achieved between predicted and observed stacked seismic traces. Sonic and density logs from well A are used to build a 1D acoustic impedance model, which is then extrapolated and adjusted throughout the data volume by tracking the Precambrian, Gilwood, Swan Hills, Ireton, and Wabamun horizons. This produces the initial-frequency (0 to 12 Hz) components that are absent in the stacked seismic data because of unavoidable bandwidth limitations in the acoustic impedance model, which is illustrated in Figure 2.9(a).

Figure 2.9(b) illustrates the poststack inversion results obtained using poststack seismic inversion. A sample set of input traces from the P-P data volume is shown in Figure 2.9(c). The model-based inversion procedure uses a linear regression method (Russell and Hampson, 1991) with a linear-programming approach in order to obtain a maximum-likelihood waveform fit using the estimated source wavelet from the well tie. The application of poststack inversion increases the resolution of small-scale features, vertically as well as laterally, and also extends the dynamic range of the acoustic impedance (i.e., the difference between maximum and minimum acoustic impedance values).

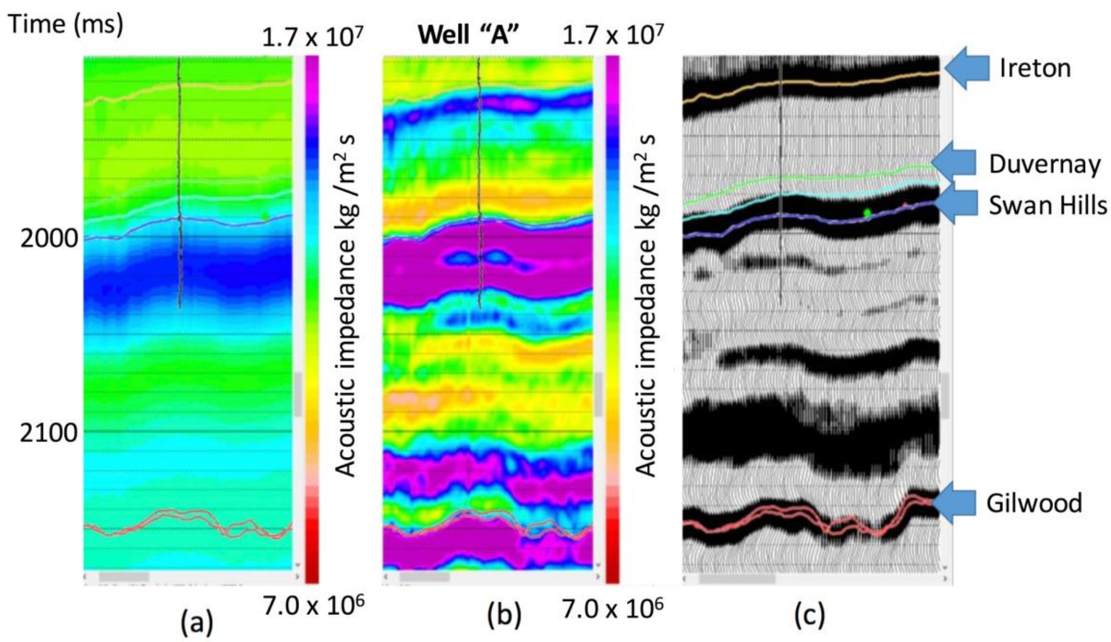


**Figure 2.9.** Small region extracted from poststack inversion of the P-P data volume, obtained using CGG Geoview software. (a) Initial model; (b) inversion output; and (c) input seismic data.

Stratal slices can be used to facilitate geological interpretation for a data volume. This approach is based on extraction of a horizon-parallel slice through the impedance volume, which can then be visualized in map or perspective view. Unlike an image-time slice (e.g., Figure 2.6), amplitude or property variability that is apparent on a stratal slice represents internal variations that occur across a constant geologic-time surface.

An example is shown in Figure 2.10 where a gray-scale rendering is used to accentuate subtle features. This stratal slice, extracted 8 ms (12 meters) above the base of the Duvernay zone, generates an image that reveals features that are broadly representative of the lithologic variability seen in the outcrop image shown in Figure 2.3. This slice shows lateral facies boundaries, two of,

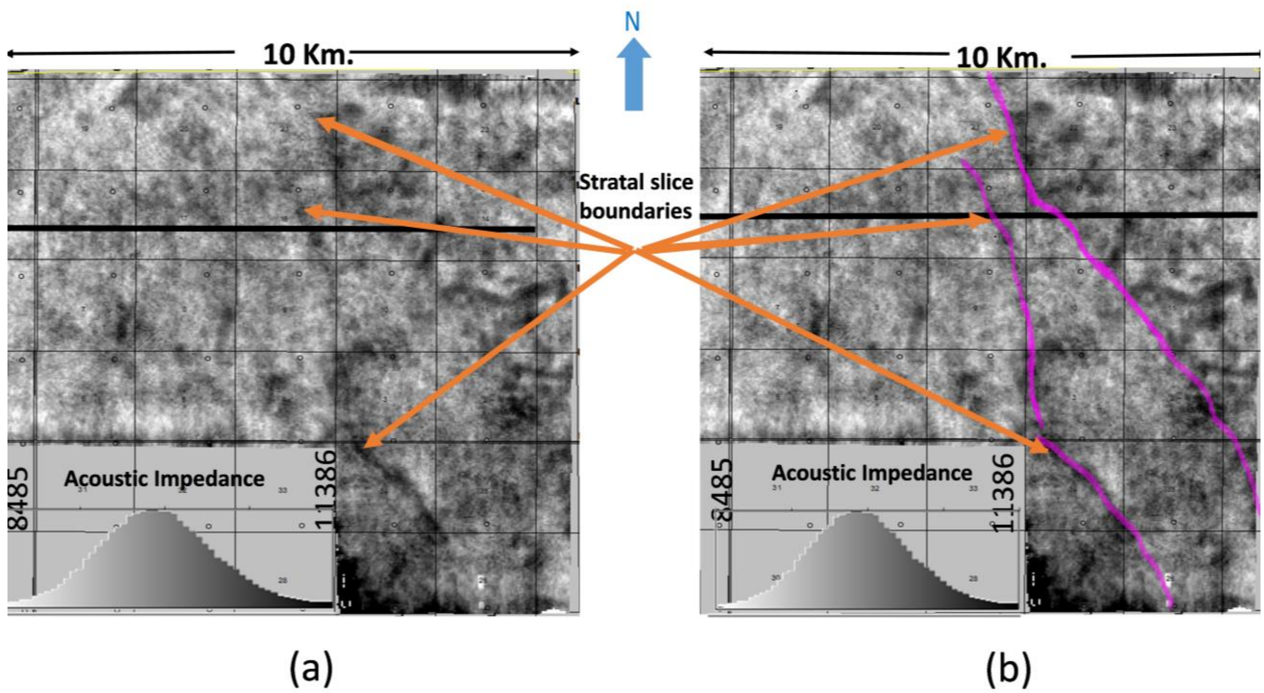


**Figure 2.10.** Stratal slice showing acoustic impedance variations within the Duvernay Formation (a), created using a time horizon 8 ms above the base Duvernay reflector and extracting the amplitude from the poststack inversion volume. Some interpreted trends are highlighted in (b).

which are highlighted in purple. Seismic reflection data is band limited, so these changes are interpreted to represent significant changes in the overall Duvernay Formation lithology. There are two trends observable on the slice, one approximately N-S and the other SW-NE. These trends are likely associated with different stratigraphic levels, and different depositional events. The band limited nature of seismic reflection cannot distinguish these individual events, and superimposes these trends on the individual slice. The main Leduc Formation reef complex is located immediately off of the SE corner of the seismic survey. The NW-SE trends are interpreted as being part of sediments shedding off of the main reef complex, the N-S trends are interpreted to be associated with sea level variation and contourite deposition.

### 2.5.2 Joint inversion of compressional- and converted shear-wave reflection

The next step in my workflow procedure involves PP-PS joint inversion. Figure 2.11 is a small-scale P-P seismic section showing the seismic events used for registration. With no dipole logs available on the seismic survey to calibrate the P- to S-wave velocity ratio ($V_P/V_S$), only one well location has a suitable sonic/density log drilled to the Gilwood Formation (well A). The seismic events correlated for the purpose of registration are Colorado, Second White Speckled Shale, Montney, Wabamun, Ireton, Swan Hills, Gilwood, and Precambrian Formations. The same events are correlated on the P-S data set and are used to perform the PP-PS registration. It is important to keep the registration intervals 100 ms or larger; smaller intervals create conditions where anomalously high or low $Vp/Vs$ ratios can be generated.

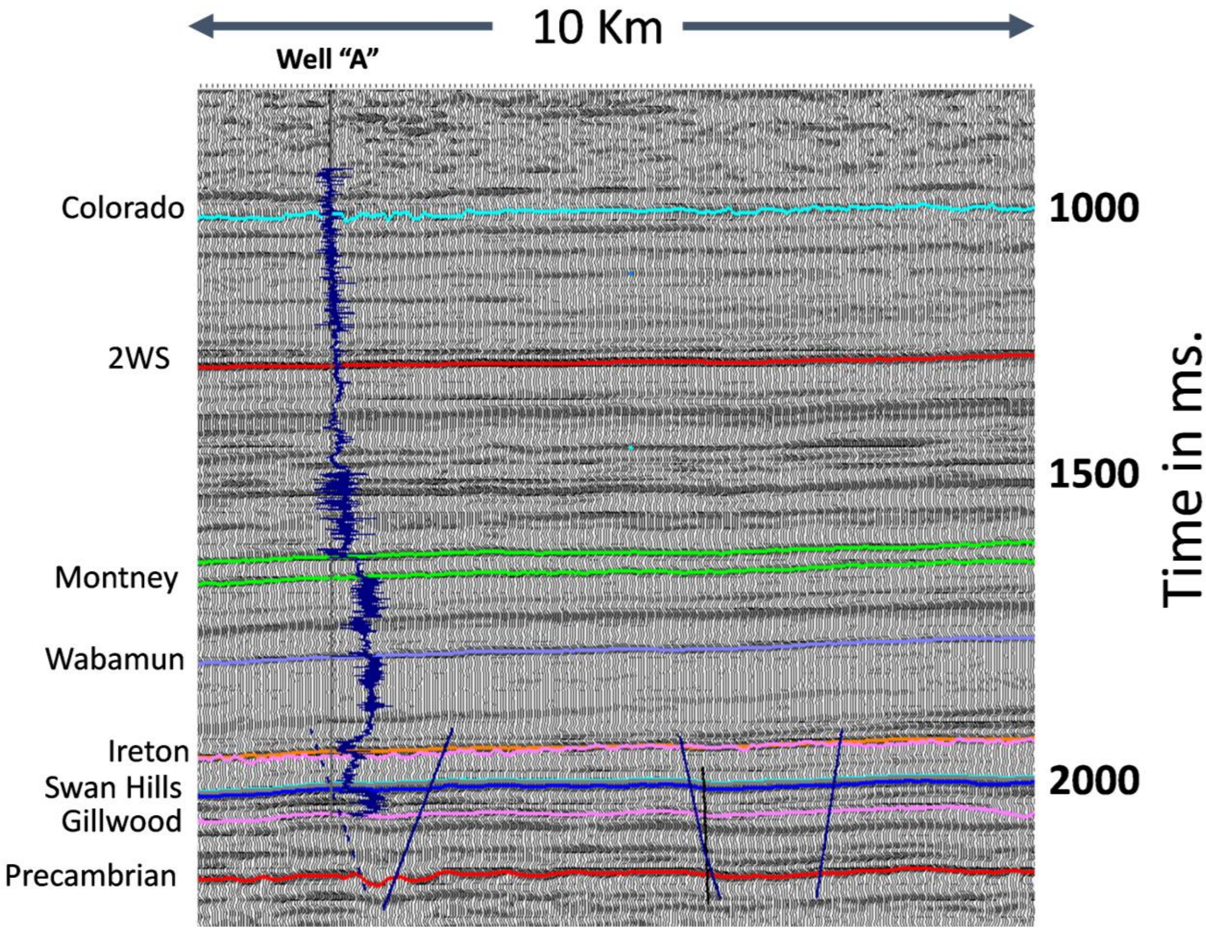


Figure 2.11. Horizon correlation used for registration of P-P and P-S data volumes. This display includes all seismic events used for the PP-PS registration tied to the integrated sonic log.

A crucial step in this process is registration of the P-P to P-S data, which requires correlation of seismic events in the P-P and P-S data sets that correspond to the same geological formation the scale of the P-S data. This simple scaling relationship can be derived easily from the formula for average $V_P/V_S$ for the interval between two horizons (Stewart et al., 2002):).

$$\frac{V_P}{V_S} = 2\left(\frac{\Delta t_{PS}}{\Delta t_{PP}}\right) - 1 \ , \tag{2.1}$$

Figure 2.12 is a synthetic P and PS seismogram generated from a sonic log (well “A”), displaying the results using three *Vp/Vs* ratios,1.8, 2.0and 2.2 The higher the *Vp/Vs* ratio, the greater the time shift required for reflection P-P to P-S data registration. The seismograms in figure 2.12 have a shift of 200 ms added to approximate the seismic processing datum of 1100 meters. The incident angles in the ray trace models range from 0 to 40 degrees, similar to the range used for the amplitude versus offset inversion (38 °).

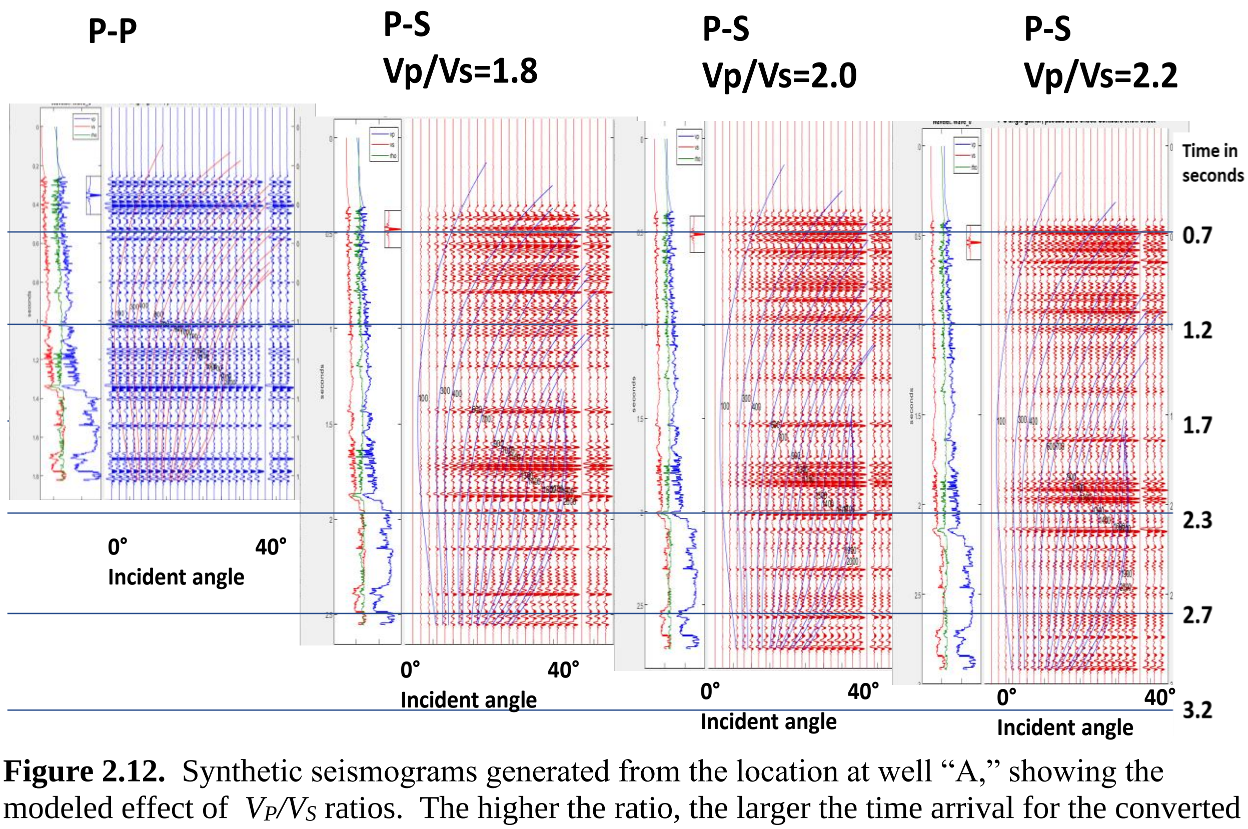


**Figure 2.12.** Synthetic seismograms generated from the location at well “A,” showing the modeled effect of $V_P/V_S$ ratios. The higher the ratio, the larger the time arrival for the converted waves. The models simulate 0 to 40 degrees incident angle, the contours within the figure display offset distance from the shot point.

Figure 2.13 displays the final data P-P/P-S registration, where the P-S data is displayed in P-P time. These data were used to generate the data displayed in table 2.1.

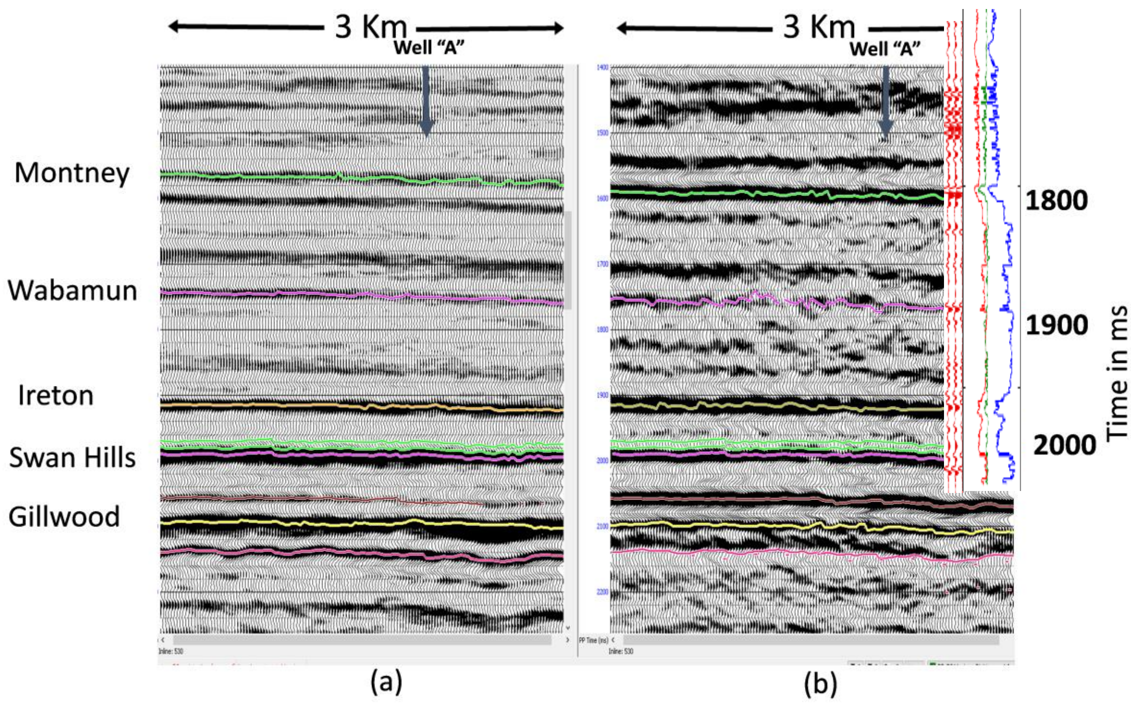


**Figure 2.13.** Horizon correlation used for registration of (a) P-P and (b) P-S data volumes. The time scale for both sections is P-P two-way time. For display purposes, the P-S time scale has been transformed to P-P time assuming $V_P/V_S = 2$. The P-S seismic data has a P-S synthetic seismogram inserted, generated from well "A," and displayed in P-P time.

In practice, if one assumes (for the sake of simplicity) that a constant $Vp/Vs = 2$ is applicable, the P-P and P-S sections can be easily compared by displaying the P-P data at 1.5 times . where ΔtP-P and ΔtP-S are P-P and P-S isochrons (time differences) between horizons that have been correlated between the P-P and P-S sections. On important step in the P-P/P-S registration is the use of a paper plot. Plotting the P-S data at 10”/second, and comparing it with the P-P data at 15”/second is what is used to qualitatively verify the registration.

If the upper horizon is taken as the surface, then it follows from equation (1) that if $V_P/V_S = 2$, then the surface-to-depth isochron ratio is $\Delta t_{PS}/\Delta t_{PP} = 1.5$. Equation (1) is used to determine the interval $V_P/V_S$ for various pairs of horizons, as summarized in Table 2.1.

| *$V_P/V_S$*[1] | *2WS*[2] | *Doe*[3] | *Wab*[4] | *Ireton*[5] | *SWH*[6] | *Gill*[7] | *~Prec*[8] | P-P Time (ms) |
|---|---|---|---|---|---|---|---|---|
| *2WS* | **2.15** | 1.99 | 2.15 | 2.09 | 2.05 | 2.07 | 2.18 | 971 |
| *Doe* | 1.991 | **2.09** | 1.88 | 1.86 | 1.981 | 2.02 | 2.156 | 1,253 |
| *Wab* | 2.148 | 1.88 | **2.03** | 1.80 | 1.78 | 1.94 | 2.06 | 1,766 |
| *Ireton* | 2.088 | 1.88 | 1.80 | **2.03** | 1.814 | 2.09 | 2.06 | 1,933 |
| *SWH* | 2.050 | 1.981 | 1.87 | 1.814 | **2.01** | 2.411 | 2.18 | 2,000 |
| *Gill* | 2.073 | 2.017 | 1.93 | 2.09 | 2.411 | **2.02** | 2.02 | 2,068 |
| *~Prec* | 2.179 | 2.02 | 2.06 | 2.06 | 2.18 | 2.02 | **2.02** | 2,151 |
| P-S time (ms) | 1,484 | 1,950 | 2,674 | 2,909 | 2,994 | 3,110 | 3,298 | ***$V_P/V_S$*** |

[1]P- to S-wave velocity ratio [2]Second White Speckled Shale [3]Definition here [4]Wabamun Formation [5]Ireton Formation [6]Swan Hills Formation [7]Gillwood member, Watt Mountain Formation [8]Precambrian basement, approximation

**Table 2.1.** Interval and surface-to-depth $V_P/V_S$ ratios determined using equation (1). These values were measured from the well A tie on the P-P and P-S reflectivity data. The row in blue is the measured P-S times; the column in green is the measured P-P times.

$$\frac{V_P}{V_S} = 2\left(\frac{\Delta t_{PS}}{\Delta t_{PP}}\right) - 1 \tag{2.1}$$

Table 2.1 calculates $V_P/V_S$ values varying in and around 2.0 for the correlated seismic events, suggesting that the character correlations for registration are reasonable and fall within the theoretical limits for $V_P/V_S$ values (Castagna, 1993). Figure 2.12 is a large-scale plot showing the result of the PP-PS registration, showing the data tie over the zone of interest. Figure 2.12(a) is the P-P seismic data, and Figure 2.12(b) is the P-S data displayed in P-P time.

The approach for simultaneous prestack inversion uses angle gathers for the estimation of P-wave impedance ($Z_P$), S-wave impedance ($Z_S$), and density (ρ). The algorithm is based on the assumption that the linearized approximation for reflectivity is valid. In particular, the Aki-Richards equation (Hampson and Russell, 2005) is used and determines the reflectivity as a function of incidence angle. The P-P and P-S gathers are converted from offset gathers to angle gathers based on the velocity and ray trace tie from well A. The co-registered P-S and P-P angle gather data are used as inputs into the joint inversion. The inclusion of the $V_S$ data means that the S-wave reflectivity and impedance are direct calculations based on the P-S section. The outputs of the joint inversion step are $V_P$, $V_S$, and ρ, from which Young's Modulus (*E*), Poisson's Ratio (*PR*) and Brittleness index (*BRI*) are calculated using:

$$E = 2 * Z_S^2 * \frac{(1+PR)}{\rho} \tag{2.2}$$

and $$PR = \frac{0.5*\left(\frac{V_P}{V_S}\right)^2 - 1}{\left(\frac{v_P}{v_S}\right)^2 - 1} \tag{2.3}$$

where $Z_S$ is the S-wave impedance. *BRI* is a function of *E* and *PR* and is given by

$$BRI = 100 * \left( w * \frac{(PR_{\max} - PR)}{PR_{\max} - PR_{\min}} + (1 - w) * \frac{(E - E_{\min})}{E_{\max} - E_{\min}} \right) \quad , \tag{2.4}$$

where $w$ is a weighting factor that controls the relative importance of $E$ and $PR$. Here, $w = 0.5$ is used. A high Brittleness index is considered to be a desired lithological trait for hydraulic fracture completion (Rickman et al., 2008). The geographical area covered by the 3D/3C survey has very little well control at the Duvernay Formation, with four horizontal wells drilled to date. This area is presently in the process of evaluation and development. As development proceeds, the weighting factor may have to be adjusted to better explain reservoir performance.

Figure 2.14 presents stratal slices that depict Young's Modulus and Poisson's Ratio extracted from the same Duvernay stratal interval as in Figure 2.10. These stratal slices highlight several distinct features. For example, the northeast part of the map is characterized by relatively low Young's Modulus and high Poisson's Ratio; this combination is indicative of relatively lower brittleness, which is less desirable for unconventional reservoir development. Near the central part of the survey, a region with high Young's Modulus values is bounded to the east by an abrupt north-south–trending edge. This edge appears to be aligned with an interpreted deep-seated fault To the west of this edge, the maps of Young's Modulus and Poisson's Ratio exhibit a high degree of variability with pronounced quasilinear features at various orientations. The stratal slices are broadly representative of lithology within the Duvernay Formation, but cannot distinguish individual beds.

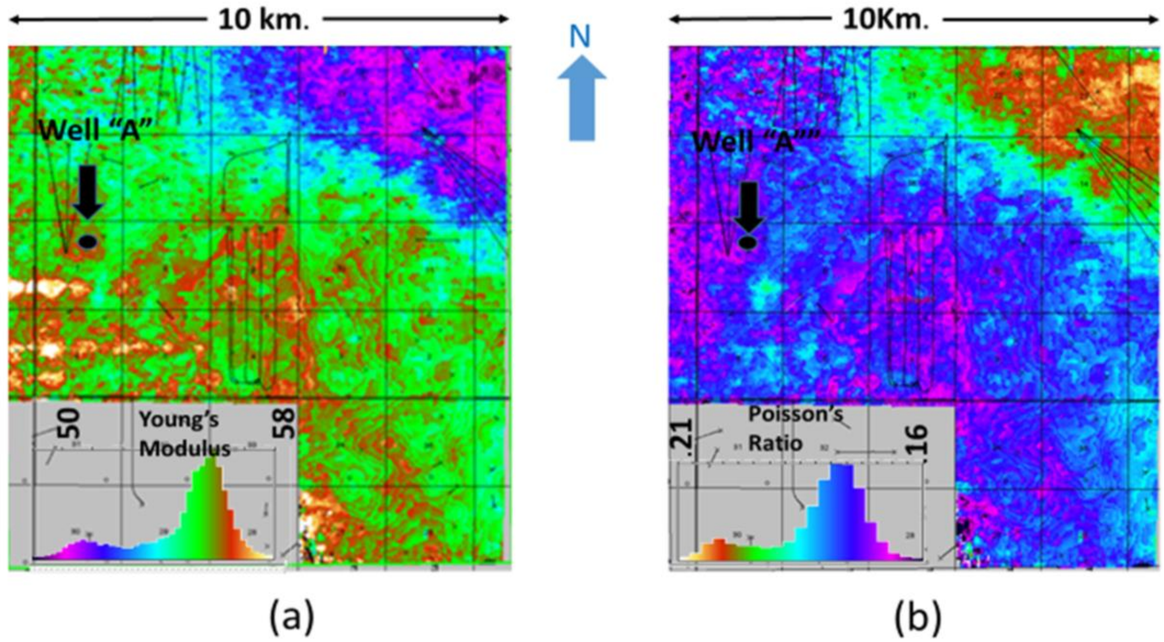


**Figure 2.14.** Stratal slices showing (a) Young's Modulus (*E*, GPa) and (b) Poisson's Ratio (*PR*), from joint PP-PS prestack inversion. The data are extracted from the same stratal slice within the Duvernay interval that is shown in Figure 2.10. East-west lineations in *E* to the south of well A are probably artifacts from an acquisition footprint.

Figure 2.15(a) shows a cross-plot of Young's Modulus versus Poisson's Ratio for the Duvernay interval, including all data values from the joint inversion volume from the top Duvernay horizon to the base Duvernay horizon. For comparison, the points are overlaid onto theoretical values of Young's Modulus versus Poisson's Ratio (Cho and Parez, 2014), as shown in Figure 2.14(b). The Duvernay points cluster within a relatively confined region near the middle of the theoretical values for quartz-clay and quartz-limestone mixtures. The Duvernay values also appear to fall approximately along a trend of constant bulk Modulus, as indicated on the graph by a set of black curves. The cross-plot in Figure 2.15(a) is used to group the data into four distinct seismic lithology zones on the basis of Poisson's Ratio.

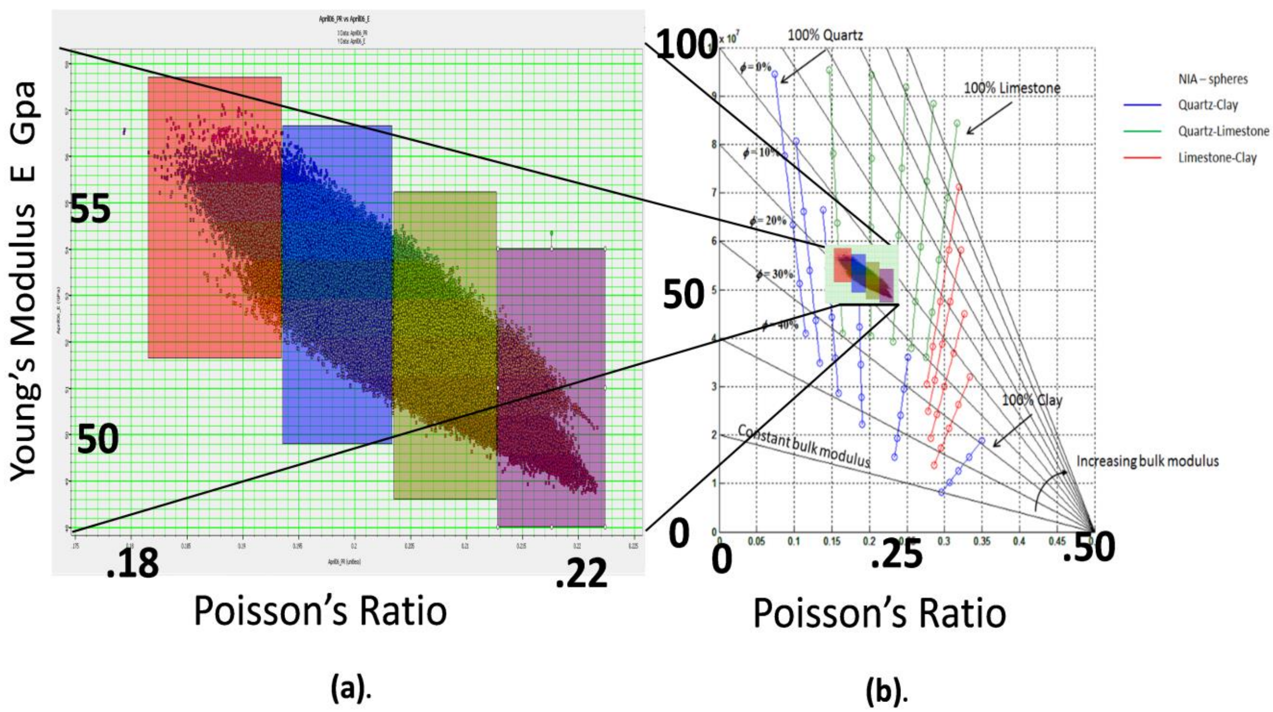


**Figure 2.15.** (a) Cross-plot showing Young's Modulus (*E*) versus Poisson's Ratio (*PR*) from prestack PP-PS inversion for data samples within the Duvernay interval (Figure 2.13). These points are grouped into four seismic lithology zones, which are displayed in Figure 2.15. (b) Cross-plot of theoretical values of *E* and *PR* (Cho and Parez, 2014), showing that the Duvernay points fall approximately along a line of constant bulk Modulus and cluster near the middle of the range for quartz-clay and quartz-limestone mixtures. The highest Brittleness index (*BRI*) corresponds to high *E* and low *PR* and, thus, plots toward the top left corner of the graph.

A seismic cross-section in Figure 2.16 displays the PP-PS inversion results, where each data point is assigned a color according to the parameter ranges of these seismic lithology zones. Although the zones are defined in Figure 2.15 based on the range of Duvernay values, these are applied to data points that fall outside of the Duvernay interval. Along this west-east profile, the Duvernay interval is classified as either zone 3 (blue) or zone 4 (red), where zone 4 may be considered more brittle as it is characterized by a higher Young's Modulus and lower Poisson's

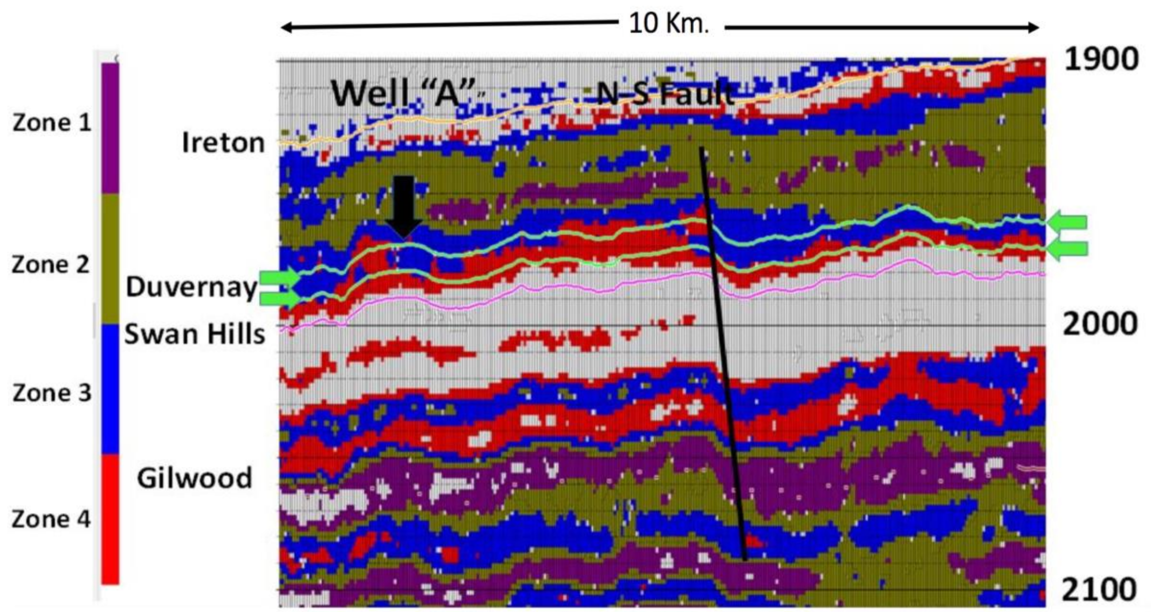


**Figure 2.16.** West-east profile showing data from prestack PP-PS inversion, colored based on the seismic lithology zones in Figure 2.14. The top and base of the Duvernay interval are highlighted with green arrows. Note the red-to-blue contrast across the Duvernay interval, with an abrupt change across the north-south fault. At this location, the fault is 9 ms throw, or 25 meters, and was active during the Deposition of the Upper Ireton Formation.

Ratio. The fault is estimated to have 25 meters displacement, and appears to be marked by a pronounced lateral transition to higher brittleness on the west side. The potential significance of this transition is discussed below. The fault in the central portion of the figure shows displacement from the basement up to the Upper Ireton. This indicates that the fault was active up to the deposition of the upper Ireton carbonate.

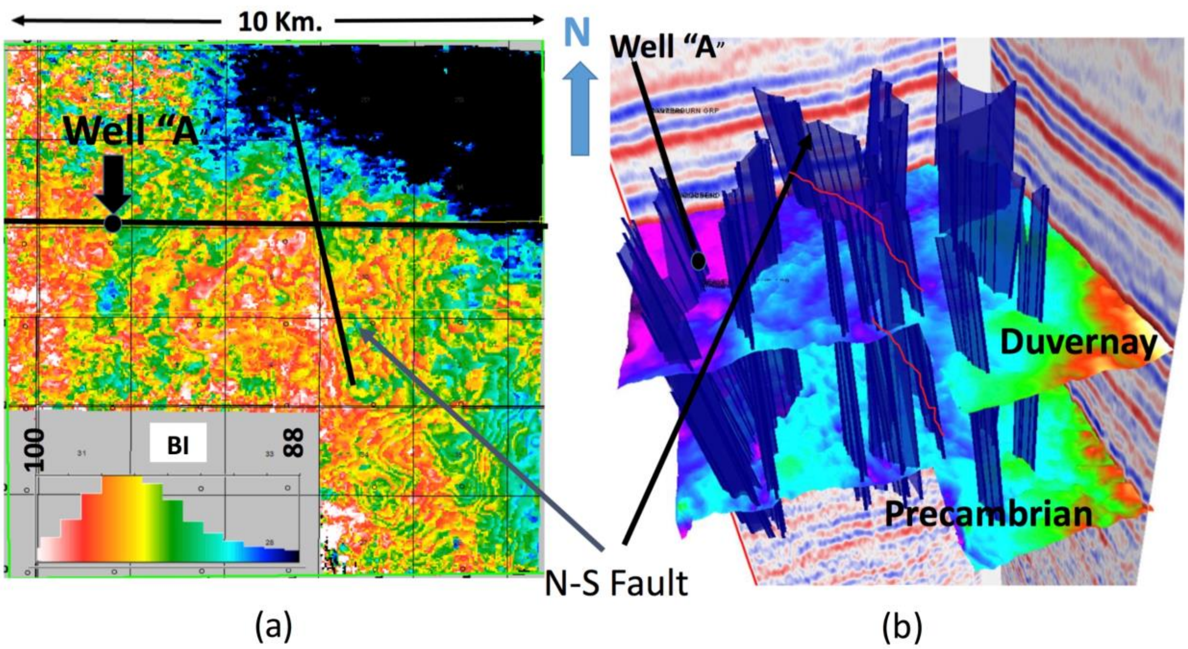


**Figure 2.17.** (a) Stratal slice showing Brittleness index (*BRI*, units percentage) calculated from Young's Modulus (*E*) and Poisson's Ratio (*PR*) within the Duvernay interval. The interpreted north-south fault is marked. (b) Perspective view showing interpreted basement-rooted, steeply dipping faults, as well as Duvernay and Precambrian horizons extracted from the P-P data volume. Red lines highlight where the north-south fault system intersects the Duvernay and Precambrian horizons.

Figure 2.17(a) is a plot of the Brittleness index calculated using equation 4. The major north-south fault is shown, as are the east-west seismic reference line and the tie to well "A." Warm colors are high in Brittleness index, and cold colors are low values. Figure 2.16(b) shows interpreted near-vertical basement-rooted faults seen on all horizons from the Precambrian basement to the Duvernay Formation. This system of faults is picked and correlated based on matching seismic displacements, from the Ireton to the top of Precambrian basement. Combined, these two maps show key elements in evaluating the Duvernay Formation in terms of structural controls and lithologic properties.

**2.6 Discussion**

Although standard resource-play development schemes, such as horizontal drilling on a regular grid and use of uniform completion designs, may be well suited to homogeneous reservoir conditions, they are not optimal for the type of geological complexity that is likely to prevail in the case of the Duvernay play. For example, a uniform pattern of wells may fail because of reservoir heterogeneity and the presence of faults, while uniform perforation intervals may not be suitable, particularly when a wellbore crosses a facies boundary with varying brittleness values. The stratigraphically equivalent Perdrix Formation in the southern Canadian Rockies (Figure 2.3) exemplifies in a spectacular manner how changes in Duvernay lithofacies may be linked to increments of reef growth. Outcrop analysis also reveals how the off-reef depositional environment varies over spatial scales of tens to hundreds of meters, which is compatible with resolution capabilities of seismic data. Stratal slices from 3D seismic inversion volumes, as depicted in Figures 2.10, 2.13, and 2.16, reveal coherent patterns of parameter variability that likely reflect varying reservoir conditions due in part to distinctive lithofacies arising from episodes of Leduc reef building.

The Duvernay Formation is also highly structured, and development of this unconventional play must consider structural controls along with depositional heterogenity. Depending on their present-day permeability structure, faults could represent either a barrier or a pathway for fluids in the subsurface. The presence of faults can thus exert a major influence on reservoir characteristics, even if the accumulated offset is relatively small. The expression of such a fault system in a 3D seismic volume depends, to a large degree, on whether past tectonic activity was syn- or postdepositional. Syn-depositional faulting could lead to some step-like facies change that is localized across a fault; for example, if the TOC content of the Duvernay Formation varies systematically across a fault, this would lead to changes in Young's Modulus, Poisson's Ratio, and Brittleness index (Soltanzadeh et al., 2015). On the other hand, postdepositional faulting could generate seismically detectable linear features that are aligned along a fault. Such linear features could be associated with a damage zone around a seismically invisible fault core or from fluid alteration in proximity to a permeable fault. Hence, there are three pertinent ways in which an active fault system could affect lateral facies distribution: (a) syn-depositional faulting could create a lower-energy depositional environment on the downthrown sides of the fault in a marine setting; (b) postdepositional faulting could be manifested by a damaged or alteration zone; and (c) strike-slip faulting could transport material laterally such that different facies are juxtaposed against each other.

This study highlights various imaging approaches that can be used for identification and cross-validation of putative fault systems based on inversion of multicomponent 3D seismic data. Faults with small vertical offsets can be manifested in profiles as seismically detectable structural discontinuities, or more commonly as fold hinge lines (Figure 2.5). Such features identified on seismic profiles extracted from 3D volumes can be cross-validated on the basis of spatial coherency on time slices or horizon time-structure maps (Figures 2.6 to 2.8). This type of anomaly is also amenable to seismic mapping using curvature attributes (Rafiq et al., 2016; Chopra et al., 2017), as well as automatic discontinuity/fault detection with adaptive principal-component analysis. Lateral offset of paleogeographic features such as a river channel (Figure 2.8) provides a tool to measure lateral fault offset, which is otherwise very difficult to quantify in a horizontally layered medium. In this study, seismic images imply that strike-slip faulting was active during or after formation of a Middle Devonian Gilwood river channel.

As argued above, seismic lithology parameters may provide important clues for distinguishing syn- and postdepositional faulting. For example, a step-like facies change across a fault, as evident from PP-PS inversion results for an inferred north-south feature (Figures 2.15 and 2.16), is interpreted here to indicate that syn-depositional tectonic activity may have taken place during Leduc reef buildup and deposition of the Duvernay. Various linear anomalies that lack such a step-like change are also documented in this study, suggesting that the Duvernay Formation in this area may be transected by a fault system that includes younger (i.e., postdepositional) elements. On the other hand, care in the interpretation of these seismic anomalies is needed because some prominent linear features (Figure 2.13(a)) may be artifacts arising from the acquisition footprint.

Defining the fault architecture is thus crucial to well planning. The objective of a fracture stimulation is to inject proppant into the Duvernay Formation, open up the fracture porosity, and produce hydrocarbons. In the presence of a critically stressed basement fault, the fault may become a thief zone; for example, in a neighboring part of the Duvernay play, Bao and Eaton

(2016) found evidence for fluid loss and associated induced seismicity defining a north-south lineament. Recorded seismic events were reported to have hypocenters extending below the Duvernay into the uppermost part of the basement.

Finally, as noted by Cho and Parez (2014), a desired combination for brittleness is a high Young's Modulus and a low Poisson's Ratio. Hence, a desired reservoir is easy to fracture but sufficiently strong to hold the fractures open long enough for placement of proppant to occur. Attempting to induce a fracture in a rock with a low Young's Modulus would produce poor results, as the rock material would simply collapse back into the induced fracture, sealing it off. Similarly, attempting to induce a fracture at a high Poisson's Ratio is more likely to produce ductile deformation, with less tendency for a fracture to form. In the absence of faults, fracture stimulation should thus be targeted toward areas of high brittleness while avoiding more ductile facies. While straightforward in concept, the use of Brittleness index has many complications and is not straightforward. Nevertheless, the PP-PS seismic inversion in this study shows promise for mapping seismic lithology parameters to aid in development of Duvernay reservoirs.

## 2.7 Conclusions

The Duvernay play is prone to induced seismicity and is likely to exhibit considerable lithologic heterogeneity in the subsurface at scales that are seismically resolvable. Consequently, I recommend that planning for drilling and hydraulic fracturing within well completion programs should consider both reservoir facies and present-day fault structure. In this study, I develop a comprehensive workflow for interpretive inversion of multicomponent 3D seismic data guided by structural analysis. My workflow requires AVO-compliant data processing and makes use of poststack inversion to obtain an acoustic impedance volume, followed by correlation of horizons between P-P and P-S sections and prestack PP-PS AVO inversion. The output parameters from the inversion, consisting of P- and S-wave velocities and density, are used to calculate data volumes containing Young's Modulus, Poisson's Ratio, and Brittleness index (e.g., Rickman et al., 2008). Various presentation formats for the inversion results, including perspective views and stratal slices, provide insights for geological interpretation of the data.

The inversion results reveal spatially coherent patterns of seismic lithology parameter variability that support a number of key interpretations. Lithofacies variations within the Duvernay Formation likely reflect episodes of growth of proximal Leduc reef complexes. These processes lead to variations in Young's Modulus, Poisson's Ratio, and Brittleness index, indicating that some areas within the survey volume are better suited than other areas for hydraulic fracturing. Fault systems characterized by relatively small vertical offsets are expressed by structural discontinuities and, more commonly, curvature anomalies defined by fold hinge lines. The largest fault is a steeply dipping structure with a north-south strike; this fault produced approximately 1 km of left-lateral (sinistral) strike-slip offset based on inferred displacement of a Middle Devonian Gilwood river channel. A step-like discontinuity in Brittleness index, derived from the PP-PS inversion results, provides evidence of syn-depositional motion on this fault. Other seismic anomalies are quasilinear features that lack such a step-like discontinuity; these anomalies are interpreted as damage or alteration zones near postdepositional faults that belong to a complex fault network in this region.

From an economic perspective, basement faulting may produce an undesirable result when fracture stimulation is attempted nearby. The objective of a completion program is for the hydraulic fracture system to remain within the formation. The presence of pre-existing critically stressed faults can produce the undesireable result of induced seismicity. This comprehensive analysis can provide the needed data to effectively develop the Duvernay Formation unconventional play in the Kaybob area of Alberta, Canada.

# Chapter 3[6]

# Application of structural interpretation and simultaneous inversion reservoir characterization of the Duvernay Formation, Bigstone North

## 3.1 Summary

Simultaneous prestack inversion of multicomponent 3D seismic data integrated with structural interpretation can provide an effective workflow to maximize value for unconventional plays. This chapter expands on the previous chapter in an adjoining area using an interpretive seismic workflow. This incorporates multicomponent seismic inversion guided by structural mapping for characterizing low-permeability unconventional reservoirs. I outline an integrated workflow for characterizing the Duvernay play in western Canada, an emerging world-class low-permeability unconventional resource fairway. This workflow includes determination of a time-depth relationship using synthetic seismograms, generation of seismic-derived time- and depth-converted structural maps, and calculation of inversion-based parameters of density and P- and S-wave velocities. The model-based procedure includes poststack (acoustic) inversion, AVO prestack inversion, and joint PP-PS inversion. With these rock properties determined, calculations are made to determine Young's Modulus, Poisson's Ratio, and brittleness. Faults are mapped based on time slices, isochrones, and correlatable vertical displacements of stratigraphic marker

[6] Published in the SEG publication *The Leading Edge* **38**, no. 2 (2019): 151-160. 2018, 6, SE1-SE14.

reflections. Significant strike-slip movements are identified by lateral displacement on interpreted geological features, such as channels and reef edges. Seismic-derived attributes, combined with structural mapping, highlight zones that are conducive to hydraulic fracturing, as well as areas unfavorable for development. Mapping of structural discontinuities provides a framework for identifying zones of pre-existing weakness and induced seismicity hazard.

### 3.2 Introduction

Unconventional plays such as the Duvernay play in western Canada are located in geologically defined fairways and are characterized by low-permeability, organic-rich shales. These plays are not economically viable based on conventional drilling and completion methods. The Duvernay play is currently undergoing development with multiple horizontal wells from single-surface well pad locations and is being completed using hydraulic fracturing. King (2012) provided a general description of the hydraulic fracturing method, which enhances natural permeability and allows hydrocarbons to be produced in an economic manner (Dusseault and McLennan, 2011). In planning an unconventional drilling program, well logs, cores, sequence analysis, and seismic data provide valuable information for horizontal well placement and the design of hydraulic fracture stages. Seismic data can also provide estimates of parameters such as Young's Modulus, Poisson's Ratio, and brittleness.

Goodway et al. (2010) described impedance-based methods built on the use of AVO analysis to differentiate ductile shale reservoirs from brittle reservoirs in the Barnett Shale in Texas. Parameters known as lambda-rho ($\lambda\rho$) and mu-rho ($\mu\rho$) (where $\lambda$ and $\mu$ are the Lamé parameters and $\rho$ is density) were derived from well logs, cross-plotted, and compared with data derived from seismic inversion (LMR analysis). Trends emerging from this approach demonstrated that variations in rock properties, often attributed to the brittle behavior of reservoir rocks, exhibit coherent patterns that reflect reservoir quality. When seismic-derived LMR attributes were back-projected onto the seismic section, trends in brittleness were observed and could be mapped spatially within the seismic volume.

The importance of fault mapping using seismic data was highlighted by Refayee et al. (2016), who used conventional and unconventional seismic attributes to define faults in the Utica Shale. This analysis was extended to examine fracture networks using attributes such as FEF volume. They proposed that sweet spots within the reservoir are defined by areas of dense fracture networks within the seismic volume.

Meek et al. (2013) described the use of a multidisciplinary geophysics approach to reservoir characterization by combining the results obtained from microseismic monitoring, structural attribute analysis, and seismic petrophysics. Comparison of recorded microseismic events with curvature anomalies and other seismic-derived attributes such as Young's Modulus revealed a strong correlation with the density of the recorded microseismic events. A high density of microseismic events suggests an efficiently stimulated reservoir volume; therefore, prospective areas for future development can then be identified based on seismic attributes. Similarly, Rafiq et al. (2016) demonstrated a correlation between microseismic data attributes and curvature anomalies from 3D seismic data, resulting in partitioning of the reservoir into depositional facies units.

Another application of fault mapping from seismic data is to identify faults that may be susceptible to induced seismicity. Several studies have suggested that the hypocenters of hydraulic fracturing–induced seismicity in the Duvernay extend from the injection interval into the Precambrian basement (Bao and Eaton, 2016; Schultz et al., 2015; 2017). Following these findings, Sharma and Chopra (2017) conducted a seismic analysis within part of the Duvernay play to investigate whether induced seismicity appears to follow any pre-existing basement faults that can be identified in the 3D seismic data. This study demonstrated good potential for identifying seismogenic faults, but concluded poor correlation of microseismic clusters with 3D seismic anomalies. A reason for this may be that strike-slip faults generally have small vertical displacement and therefore may not be readily observable on conventionally stacked seismic data.

The main objective of this study is to present a comprehensive workflow for interpretive processing and inversion of 3D multicomponent seismic data for unconventional reservoir geophysics. This study builds on an integrated workflow developed by Weir et al. (2018). Here, I analyze and interpret a different 3D multicomponent seismic data set from the Kaybob portion of the Duvernay play, located within an area where induced seismic events have occurred (Bao and Eaton, 2016; Schultz et al., 2017). Analysis of this data set includes structural interpretation and mapping, fault detection, and reservoir characterization based on poststack and simultaneous P-P and P-S inversion and, thus, provides insights into the tectonic history of the reservoir. I show how seismic inversion applied to poststack and multicomponent data gathers (P-P and P-S) can be used as a tool to identify facies changes, fault boundaries, and potential geohazards such as basement faults. Various presentations of the data are used to illustrate how structural and inversion attributes can be employed to identify areas that are most prospective for development, as well as areas where the existing fault architecture may pose a risk for induced seismicity.

### 3.3 Geological setting

The Duvernay Formation analyzed here is a bituminous/argillaceous carbonate of the Late Devonian age in the Western Canadian Sedimentary Basin. The Duvernay is emerging as a major unconventional resource play in North America (Hammermaster, 2012; Creaney and Allan 1990). The Duvernay is organic-rich and, depending on thermal maturity and position within the basin, produces oil, NGLs, or natural gas (Switzer et al. 1994). Figure 3.1 is an outcrop photograph of the Leduc Formation and Duvernay Formation outcrop equivalents (Perdrix and Presqu'ile reef formations). These outcrops have approximately the same vertical and horizontal scales as the subsurface equivalents in the ToC2ME and Bigstone North project areas. The Duvernay Formation is also commonly believed to be the primary source rock for the Devonian Leduc reef, Nisku, and Wabamun carbonate plays (Dunn et al., 2012). The Duvernay is emerging as a world-class unconventional resource play (Davis, 2013), primarily because of the advent of horizontal drilling and multistage hydraulic fracture technology.

Figure 2.1 in the previous chapter illustrates, in a basin-wide sense, the hydrocarbon maturity setting. The Duvernay Formation was deposited contemporaneously with several large Leduc reef complexes. It typically has an effective porosity of 6 to 7% and an average TOC content of up to 4.5% (Chopra et al., 2017). The mechanism for Duvernay sediment deposition was the combined effect of suspension settling, turbidity currents, and bottomwater currents (Knapp et al., 2017). Growth of the Leduc reef was terminated by rapid sea level rise. The Leduc and Duvernay Formations are both overlain by the quartz-rich Ireton Formation, which forms a cap and seal (MacKay et al., 2018).

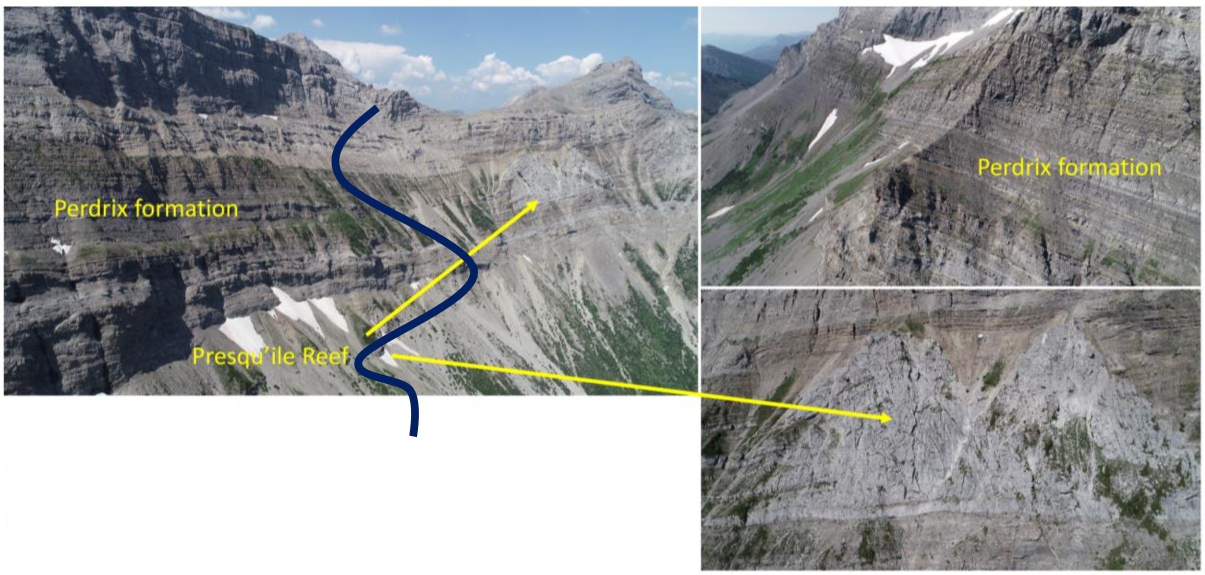


**Figure 3.1.** Drone photographs of the Perdrix and Presqu'ile reef formations. These photographs are at the same location as shown in Figure 2.2 and display the same outcrops. For illustration, a seismic wavelet is plotted on the outcrop to approximate scale (courtesy of Pedersen, University of Calgary).

Analysis of outcrops of equivalent formations in southern Alberta show evident variability in depositional setting. Weir et al. (2018) described a Leduc reef–equivalent outcrop (Presqu'ile Formation) characterized by multiple stages of reef growth, with adjacent Duvernay-equivalent (Perdrix Formation) strata. This outcrop was observed to exhibit both lateral and vertical lithofacies variation within the section, including interfingering relationships relative to the adjacent reef margin.

The composition of the Duvernay Formation was determined by its location in the basin, with factors including proximity to the Leduc reef, pre-existing basin structure, weather patterns, tides, sea level changes, and sediment sources. Using core analysis, Knapp et al. (2017) identified 10 lithofacies in the Duvernay Formation based on core word. He also discussed depositional mechanisms such as contourites, turbidity currents, and in-situ precipitation, as well as how they relate to depositional environments.

A rock with a high Brittleness index is characterized by either a low Poisson's Ratio, a high Young's Modulus, or both. Within an established lithofacies framework, a strong correlation exists between quartz content, TOC, and brittleness of the Duvernay Formation (Dunn et al., 2012). The higher silica content of the Duvernay comes from deposition in more distal, low-energy environments. Soltanzadeh et al. (2015) showed that clay content also plays a significant role in the brittleness of both the Duvernay and Ireton Formations (moreover, hydrocarbon generation has changed the rock properties such that high-TOC Duvernay tends to be more brittle than other facies.

### 3.4 Seismic data processing

This study focuses on a multicomponent 3D seismic survey acquired in January 2015. The objective of the seismic analysis is to define lithologic variations that occur in the Duvernay Formation at depth. Seismic inversion is used to characterize variations in the Duvernay Formation due to deposition and hydrocarbon generation and to generate maps of key reservoir parameters, namely Poisson's Ratio, Young's Modulus, and Brittleness index. My seismic structural analysis includes interpretation and mapping of faulting and the timing of faults; this is used to define induced fracture patterns and to identify any associated seismicity.

The seismic data are processed in an AVO-compliant manner, with the processes designed to preserve relative amplitudes for both P-P and P-S data sets. The AVO-processing flow generally follows a conventional-processing flow such as that described by Allen and Peddy (1993), with a few key differences, as described by Weir et al. (2018). The version of the stacked data used in this study for interpretation and prestack inversion is limited to a maximum 38˚ P-wave incidence angle based on ray tracing using a velocity model derived from a control well (well A), discussed farther on.

### 3.5 Interpretive workflow

Seismic inversion is used to characterize variations in the Duvernay Formation due to deposition and hydrocarbon generation and to generate maps of key reservoir parameters, namely Poisson's Ratio, Young's Modulus, and Brittleness index. My seismic structural analysis includes interpretation and mapping of faulting and the timing of faults; this is used to define induced fracture patterns and to identify any associated seismicity.

Well A located 4 km south of the survey has both sonic and density logs used to generate a synthetic seismogram. Figure 3.2 shows the precise well tie to the seismic data,

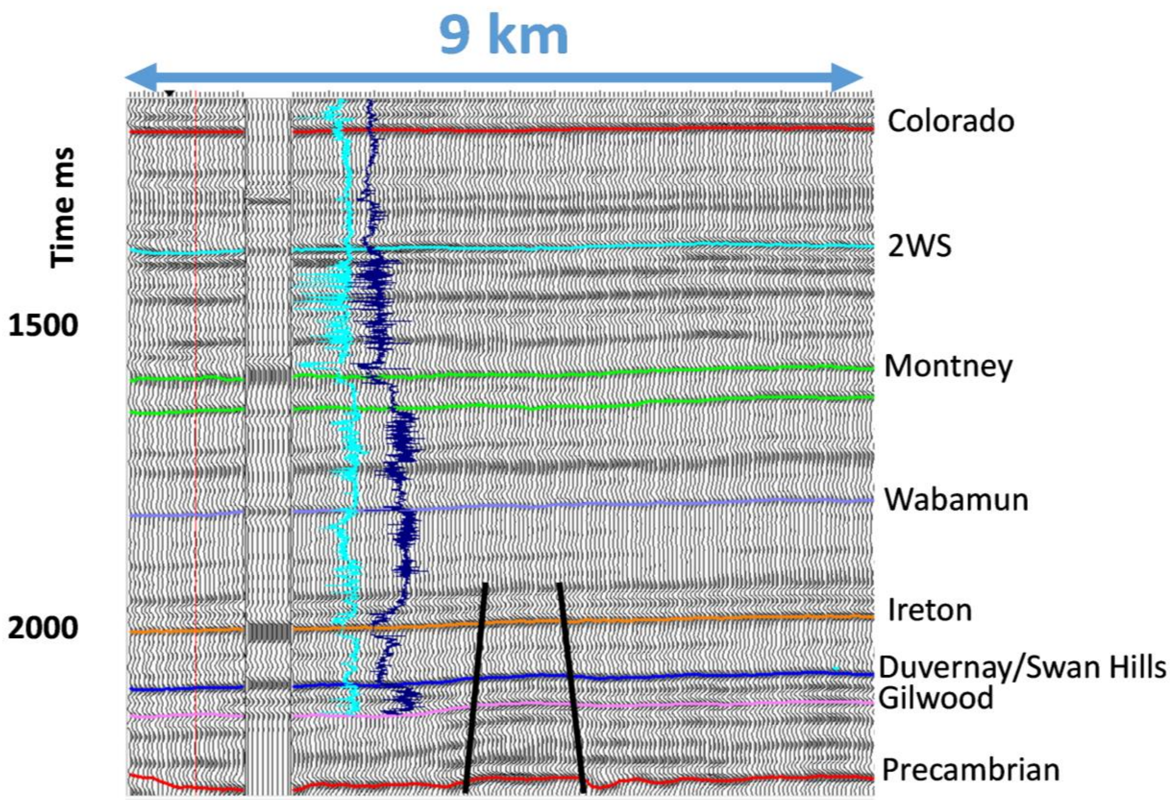


**Figure 3.2.** West-east seismic profile extracted from the P-P data volume, showing the integrated sonic log correlation with the mapped seismic horizons; sonic (*Δt*, blue) and density (ρ, cyan) logs are shown. A synthetic seismogram is inserted to the left of the well logs for comparison. The well is located 4 km southeast of the line along structural strike. Two interpreted basement faults are shown (black).

showing the time-depth correlation down to a depth of 3607 m. This synthetic tie establishes the time-depth relationship, which is subsequently used to create angle gathers (mentioned above), perform PP-PS registration, and provide an initial model for the seismic inversion. A small west-east portion of the stack data is shown in Figure 3.2. The Duvernay, Gilwood, and Precambrian seismic horizons are correlated based on the jump tie to well A. The deep Precambrian pick was interpolated from the Lithoprobe deep-crustal seismic profile (Eaton et al., 1999). The two faults interpreted on Figure 3.2 are seen as breaks or sharp bends in the picked horizons.

A chair plot is shown in Figure 3.3 (a perspective view) of time slices from the P-P data volume. The horizontal slices approximately intersect the Duvernay and Precambrian horizons. Both time slices reveal amplitude trends that define a prominent set of north-south–oriented features. In the case of the shallower time slice (b), a curved surface trending northeast-southwest is seen, as well as the north-south trend observed on the deeper time slice, interpreted to be the edge of a carbonate reef based on structural drape above, Gilwood pull-up below, and an internal character change within the Swan Hills Formation (Lines and Newrek, 2004). This Swan Hills feature is not aligned with the predominant north-south trend observed on the deeper Precambrian time slice and exhibits a possible structural closure to the northeast. There are several north-south and north-northwest–south-southeast lineations evident, with similar orientations to those seen on the chair plot in Figure 3.3. The curved northeast-southwest feature is predominant (highlighted by white arrows), as well as north-south and north-northwest–south-southeast lineations. The deep Precambrian seismic event is correlated and picked based on a correlation from regional deep well control.

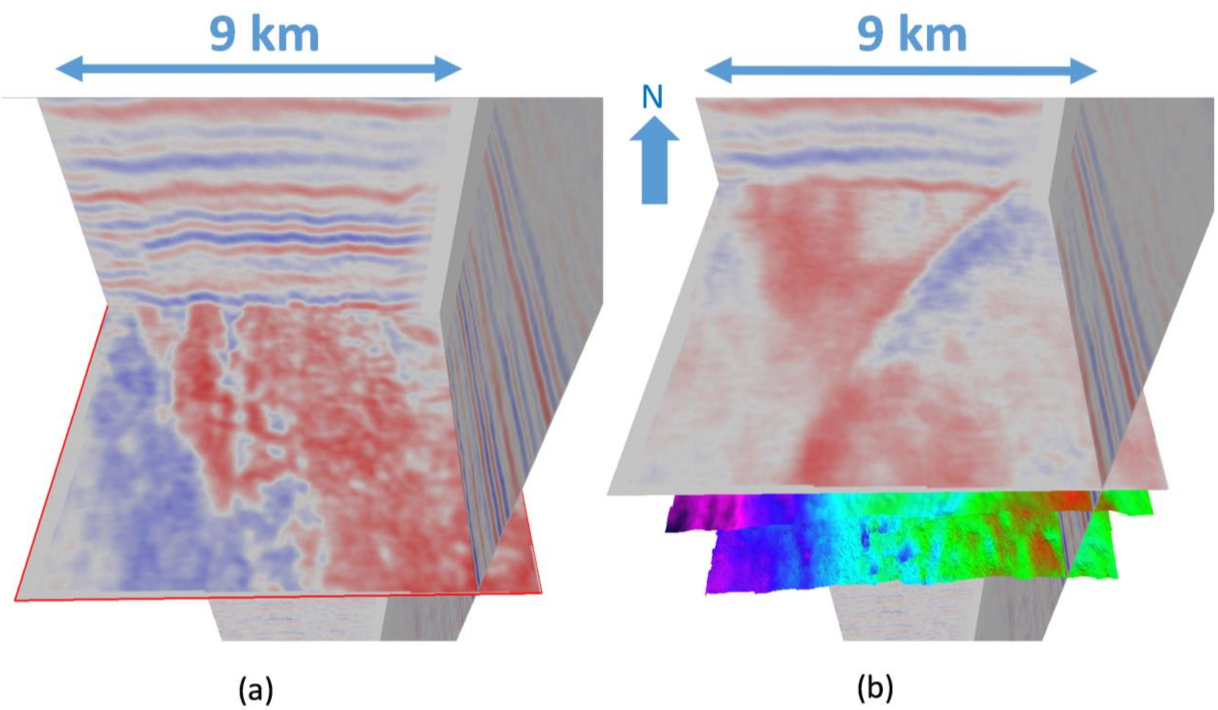


**Figure 3.3.** Perspective view (chair plots) showing time slices through the P-P seismic volume at (a) 2,154 ms and (b) 2,002 ms. The shallower time slice (a) intersects the Precambrian surface, while time slice (b) intersects the Swan Hills horizon. Both time slices reveal approximately north-south–trending linear topographic features that are interpreted to be associated with the north-south basement fault systems. (b) also shows a prominent north-northeast–south-southwest–trending feature. The lower color horizons on (b) are the Gilwood and Precambrian time surfaces.

Several time-structure maps ae created using the identified time surfaces in the seismic volume. A representative time-structure map of the Swan Hills time horizon is shown in Figure 3.4. For this time stratigraphic horizon, the overall structural dip is seen to be toward the southwest. The southwest-northeast–curved feature seen on the Swan Hills map highlighted in Figure 3.4 is interpreted to be the edge of a carbonate reef based on structural drape above, Gilwood pull-up below, and an internal character change within the Swan Hills Formation (Lines and Newrek, 2004).

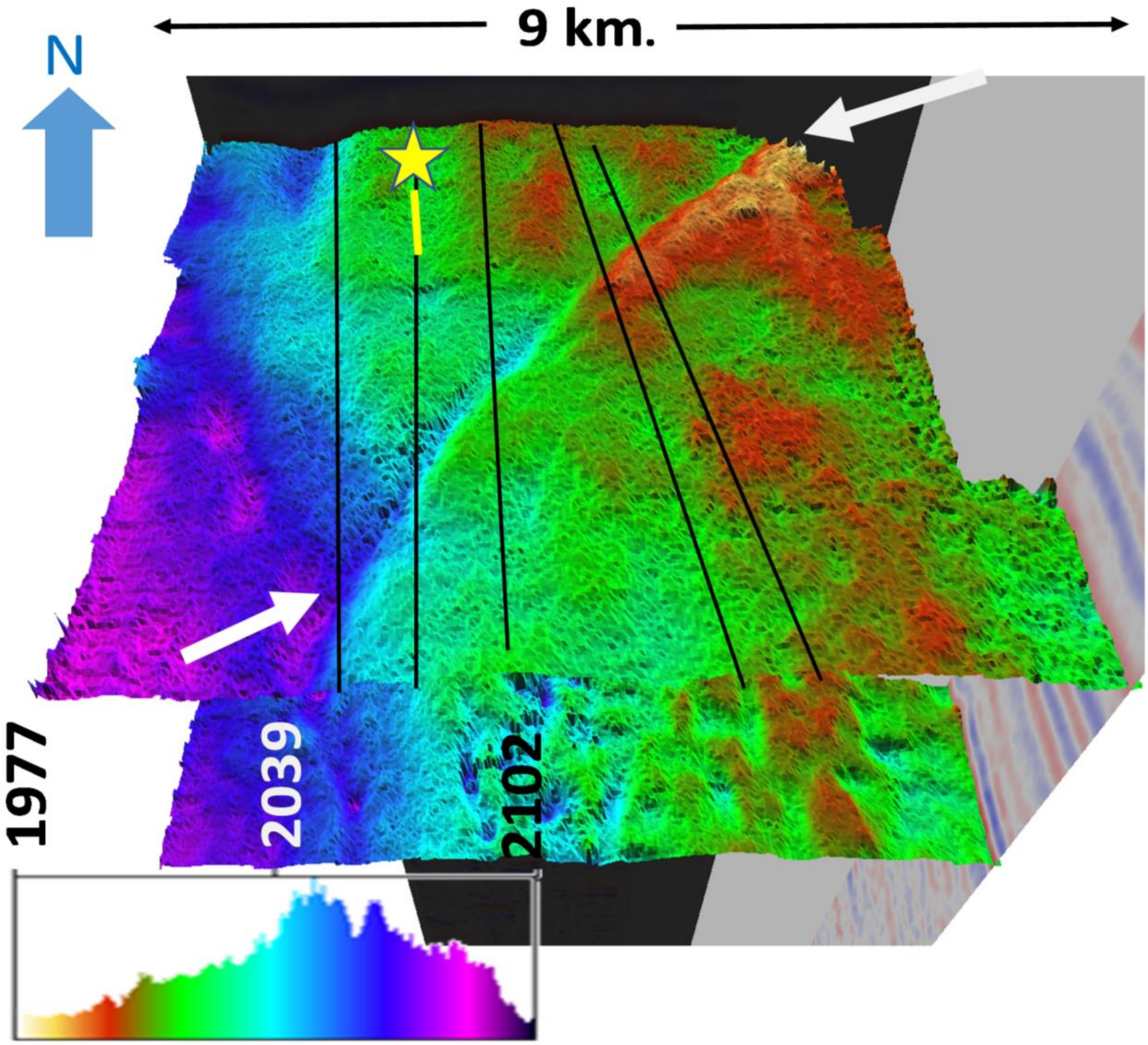


**Figure 3.4.** Perspective view of the Swan Hills Formation time-structure displays, derived from the P-P data volume. There is a prominent northeast-southwest feature on the Swan Hills time structure that shows curvature, starting northeast-southwest and trending to north-south. This feature is highlighted by white arrows. The histogram on the lower left shows the color scale; time is in ms. Black lines show the interpreted strike-slip faults, and the yellow star shows the relative position of the induced seismic event.

This Swan Hills feature is not aligned with the predominant north-south trend observed on the deeper Precambrian time slice and exhibits a possible structural closure to the northeast. There are several north-south and north-northwest–south-southeast lineations evident, with similar orientations to those seen on the chair plot in Figure 3.3. The curved northeast-southwest feature is predominant (highlighted by white arrows), as well as north-south and north-northwest–south-southeast lineations.

The Gilwood time-structure map horizon is shown in Figure 3.5. The deposition of the Gilwood member of the Watt Mountain Formation occurred during the uplift of the Peace River Arch (O'Connell, 1994). The Peace River Arch movement was a regional tectonic event located several hundred km to the north and west of the study area; the Gilwood member channeled into the Watt Mountain Formation as a response to the tectonic uplift. A predominant meandering channel feature is present in the Gilwood time-structure map; this may be the drainage system linked to uplift of the Peace River Arch. This channel feature is cross-cut by a prominent north-south linear feature. As discussed below, I interpret this feature as a possible strike-slip fault with left-lateral (sinistral) displacement occurring after deposition. Based on the channel offset, the net displacement across the fault may be as much as approximately 1 km.

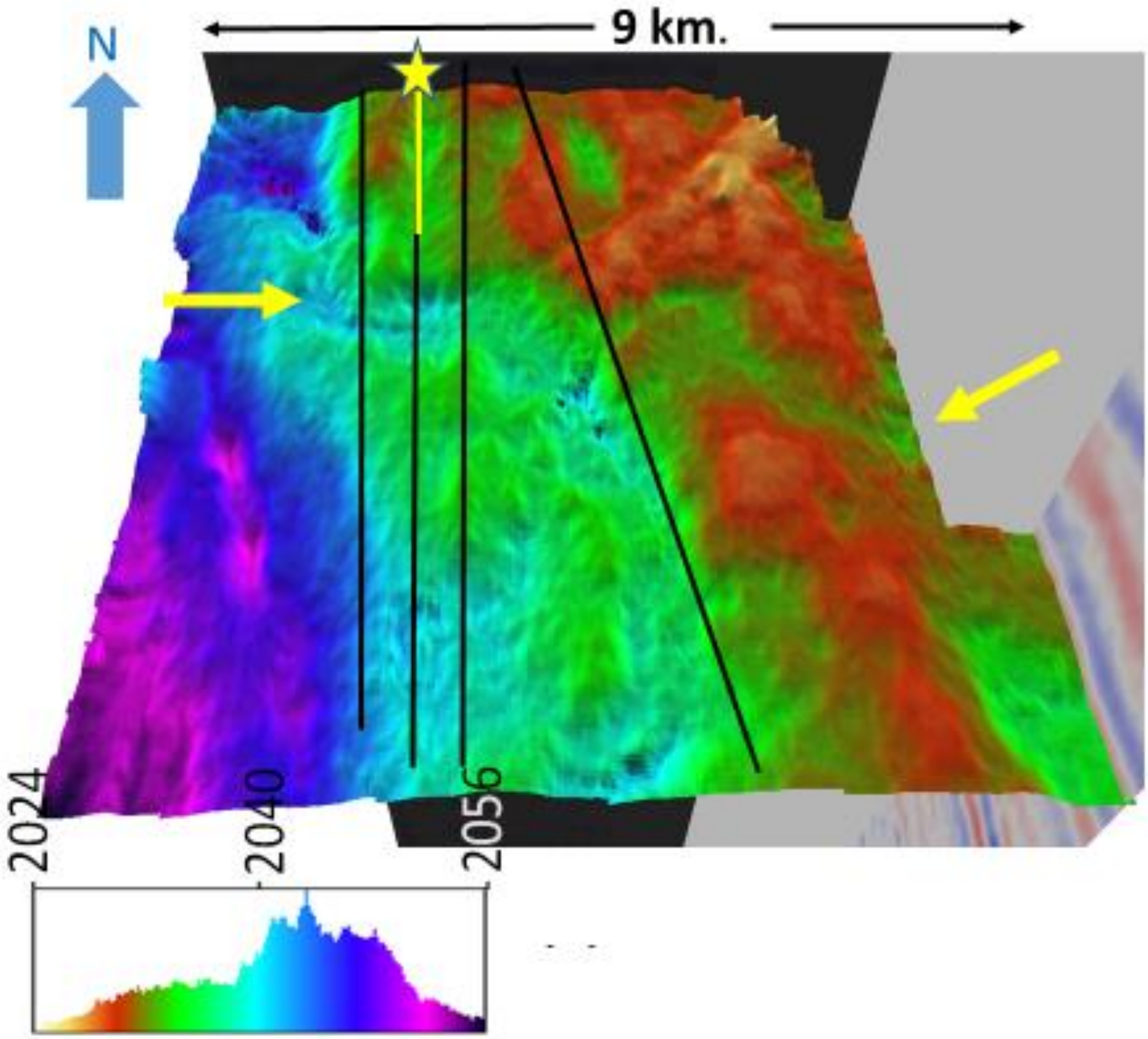


**Figure 3.5.** Gilwood time structure derived from the P-P data volume. The interpreted strike-slip faults are shown in black. Yellow arrows show the position of the Gilwood channel; note the displacement of the channel at the center of the figure. The yellow star indicates the relative position of the induced seismicity, projected from the top of the Ireton Formation area (Bao and Eaton, 2016). The histogram on the lower left shows the color scale; time is in ms.

## 3.6 Seismic inversion

### 3.6.1 Poststack inversion

This section focuses on the seismic inversion components of the interpretive workflow. The inversions processed here are model-based, using seismic horizons, well ties, and structural discontinuities derived from the structural mapping. Hampson and Russell (2005) described the theoretical basis for model-based inversion. A poststack inversion is processed as a first step to derive the acoustic impedance volume (i.e., the product of velocity and density). A blocked model is constructed using well ties constrained with horizon picks and is then perturbed until a satisfactory maximum-likelihood fit is achieved with the stacked traces. The sonic and density logs from control well A are used to build the initial 1D acoustic impedance model, which is then extrapolated and adjusted throughout the data volume by tracking the Precambrian, Gilwood, Swan Hills, Ireton, and Wabamun horizons. This produces the initial acoustic impedance volume model (a portion of which is illustrated in Figure 3.6(a)). Seismic reflection data lack frequency content over the low-frequency band (0 to 12 Hz); the well log data provide this missing low-frequency information. The model-based inversion procedure uses a least-squares optimization based on conjugate gradients (Hampson and Russell, 2005) with a linear-programming approach to obtain a maximum-likelihood waveform fit using the estimated source wavelet from the well tie. The application of poststack inversion increases the resolution of small-scale features, vertically as well as laterally, and extends the dynamic range of the model (i.e., the difference between maximum and minimum acoustic impedance values) by including the 0- to 12-Hz frequency component. The poststack inversion process is used to generate the seismic volume slice illustrated in Figure 3.6(b). The corresponding P-P input traces from the P-P data volume are shown in Figure 3.6(c), as well as the constraining horizons.

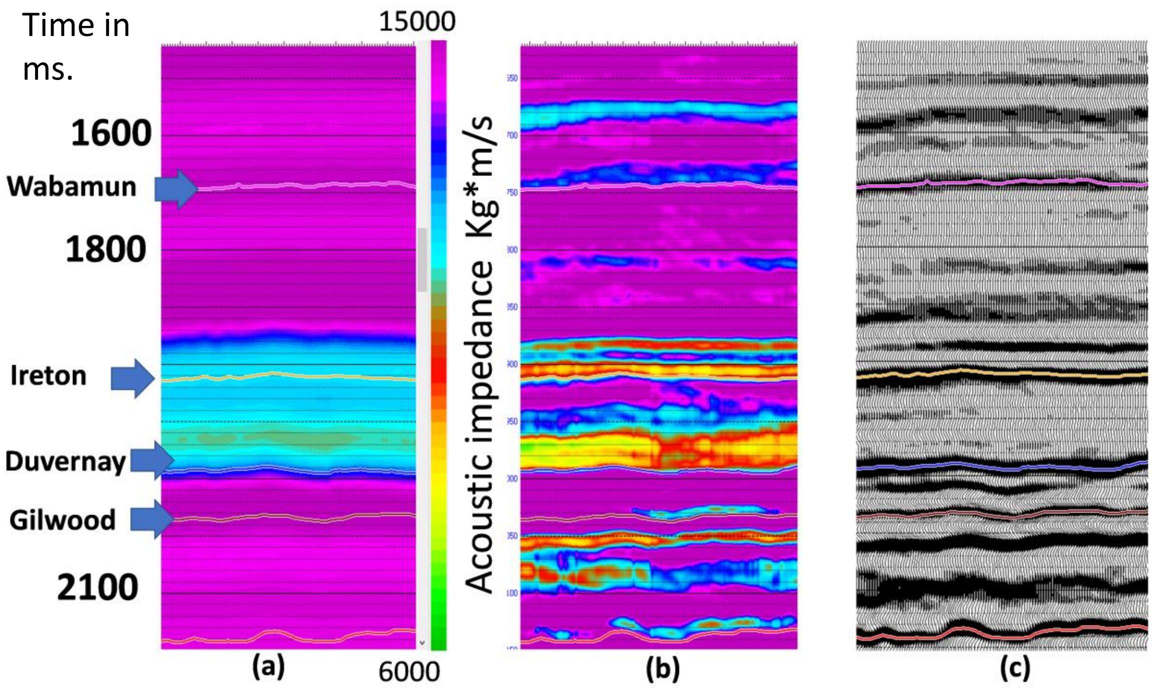


Figure 3.6. Small region extracted from poststack inversion of the P-P data volume: (a) initial model; (b) inversion output; and (c) input seismic data with formation time picks.

The geological interpretation derived here relies on stratal slices calculated at a constant horizon isochron above the correlated Swan Hills surface. This horizon-parallel surface is used to extract the corresponding amplitude information from the inversion volumes. This information can be viewed in perspective or map view. A time slice is generally used as a structural interpretation tool; here, I see lineations interpreted to be faults. By contrast, a stratal slice conforms to a geological surface and represents internal variations occurring within a single geological unit.

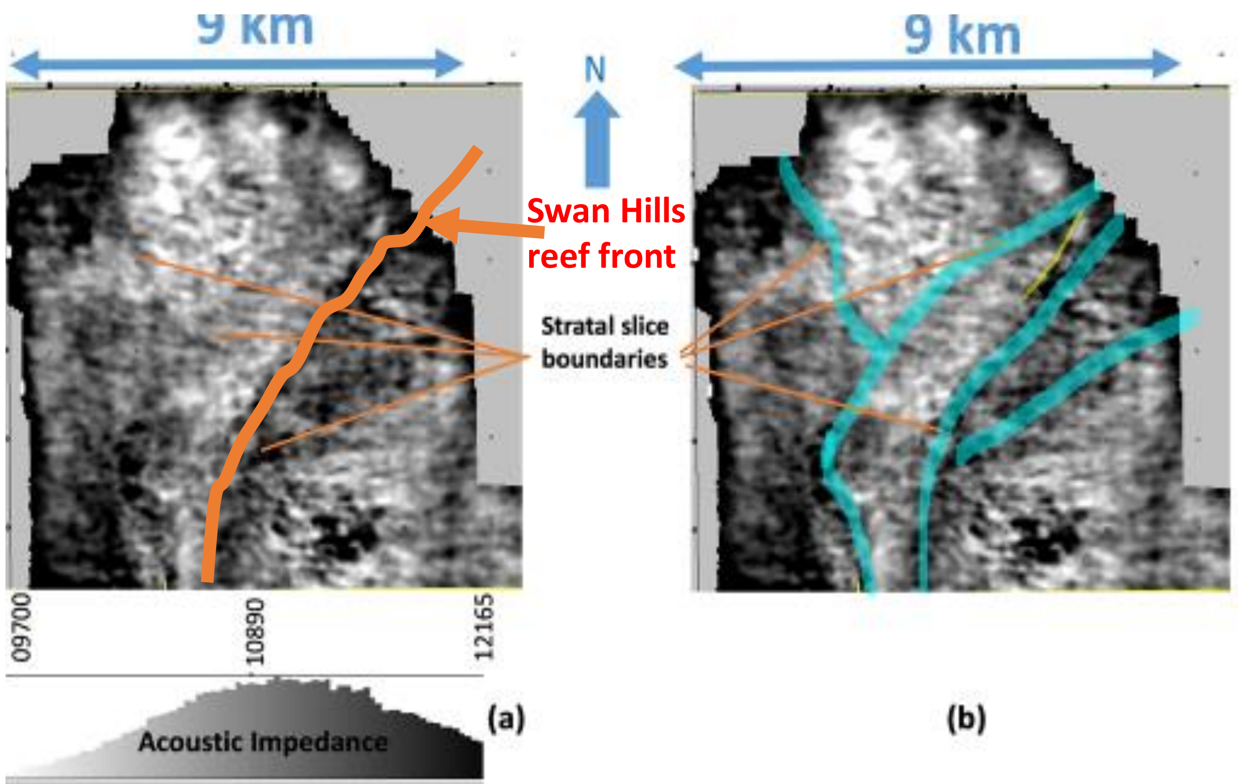


**Figure 3.7.** Stratal slice showing acoustic impedance variations within the Duvernay Formation, created using a time horizon 8 ms above the base Duvernay reflector and extracting the amplitude from the poststack inversion volume. Some interpreted trends are highlighted in blue on the right. (a) is a uninterpreted slice with arrows highlighting prominent features and the Swan Hills reef front;(b) shows an interpretation of four of the stratal boundaries.

Figure 3.7 uses a gray-scale rendering of summed amplitudes extracted 6, 8, and 10 ms above the base of the Duvernay. These slices appear to represent seaward facies variations within the Duvernay Formation (Weir et al., 2018).

### 3.6.2 Joint inversion of compressional- and converted shear-wave reflection

PP-PS joint inversion uses both the P-S converted seismic data as well as the P-P reflection data simultaneously. A crucial step in this process is registration of the P-P to P-S data, which requires correlation of seismic event horizons in the P-P and P-S data sets that correspond to the same geological formation. Figure 3.8 shows the event horizons used for registrations; the seismic events correlated for registration are the Colorado, Second White Speckled Shale, Montney, Wabamun, Ireton, Swan Hills, Gilwood, and Precambrian. To start the registration process, an initial P- to S-wave velocity ratio ($V_P/V_S$) assumption of $V_P/V_S = 2$ is used, and the corresponding seismic sections are displayed such that the P-P vertical display is 1.5 times the P-S vertical display over the same area. Corresponding horizons are correlated by overlaying the P-P sections on the P-S and finding corresponding seismic events. These corresponding horizons are picked in the P-S volume and used to adjust $V_P/V_S$ to the time horizons, thus producing a depth-dependent $V_P/V_S$ field. Stewart et al. (2002) derived a formula to relate P-P reflection times to P-S reflection times as follows:

$$\frac{V_P}{V_S} = 2\left(\frac{\Delta t_{PS}}{\Delta t_{PP}}\right) - 1, \tag{3.1}$$

where $\Delta t_{PP}$ and $\Delta t_{PS}$ are P-P and P-S time differences between isochrons of horizons that have been correlated between P-P and P-S sections. If $Tp/Ts = 1.5$ for the seismic reflections, the corresponding $V_P/V_S$ for any seismic event is 2.0, according to equation (3.1). $V_P/V_S$ is adjusted between various layers with horizon matching; the result is shown in Figure 3.8. A portion of the P-P and P-S data is shown in Figures 3.8(a) and 3.8(b); the P-S data are displayed in P-P time.

The Aki-Richards equation (Hampson et al., 2005) is used to determine P- and S-wave impedance as a function of $V_P$ and $V_S$ and density (ρ) as a function of the incidence angle (θ), the P- and S-wave reflection coefficients, and $V_P/V_S$. The inversion method used here assumes the linear approximation of the Aki-Richards equation (2), with ϒ being $V_P/V_S$ and θ being the incidence angle:

$$R_{PP}(\theta) = c_1 R_P + c_2 R_S + c_3 R_D \quad , \tag{3.2}$$

where

$$c_1 = 1 + \tan^2\theta,\ c_2 = -8\gamma^2\sin^2\theta,\ c_3 = -\frac{1}{2}\tan^2\theta + 2\gamma^2\sin^2\theta \ . \tag{3.3}$$

$$c_1 = 1 + \tan^2\theta,\ c_2 = -8\gamma^2\sin^2\theta,\ c_3 = -\frac{1}{2}\tan^2\theta + 2\gamma^2\sin^2\theta \ . \tag{3.4}$$

The inclusion of the P-S gather data means that the S-wave reflectivity and impedance are a direct calculation from the P-S seismic data. Using the inversion outputs of $V_P$, $V_S$, and ρ, Young's Modulus ($E$) and Poisson's Ratio ($PR$) are calculated using:

$$E = 2 * Z_S^2 * \frac{(1+PR)}{\rho} \tag{3.5}$$

and

$$PR = \frac{0.5*\left(\frac{V_P}{V_S}\right)^2 - 1}{\left(\frac{v_P}{v_S}\right)^2 - 1} \quad , \tag{3.6}$$

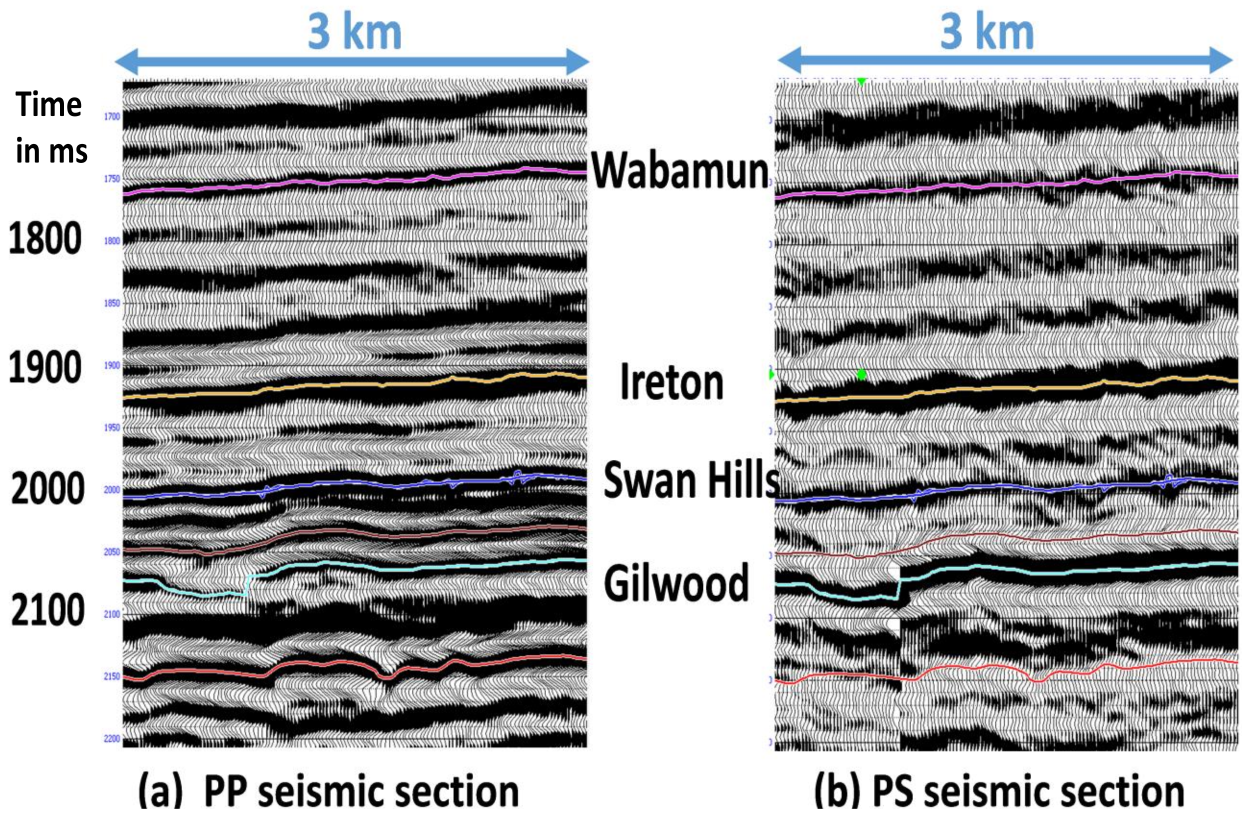


**Figure 3.8.** Horizon correlation and registration of (a) P-P and (b) P-S data volumes. The time scale for both sections is P-P two-way time. P- to S-wave velocity ratio ($V_P/V_S$) is adjusted for the correlated intervals.

where $Z_s$ is the S-wave impedance. Brittleness index (*BRI*) is a calculated function of *E* and *PR* and is given by:

$$BRI = 100 * \left(w * \frac{(PR_{\max} - PR)}{PR_{\max} - PR_{\min}} + (1 - w) * \frac{(E - E_{\min})}{E_{\max} - E_{\min}}\right) \tag{3.7}$$

*BRI* is expressed as a relative value within the zone of interest. *w* can be adjusted to determine the relative weighting of *E* and *PR*. Here, I weight them equally; $w = 0.5$ is used. Cross-plotting *E* versus *PR* yields a spatial representation of the *BRI* in a given zone. For a horizontal well fracture completion program, high *BRI* values are generally desirable, and low *BRI* values are not (Rickman et al., 2008).

### 3.7 Results

Figure 3.9 presents stratal slices that depict Young's Modulus and Poisson's Ratio extracted from the same Duvernay stratal interval as shown in Figure 3.7. These stratal slices highlight several distinct features. For example, a region of high Young's Modulus and low Poisson's Ratio, which follows the Swan Hills structure, shows a distinct southwest-northeast trend. There are also north-south features aligned with the interpreted deep-seated basement faults. The very low Poisson's Ratio values seen in the extreme northernmost portion of the survey may be related to lack of subsurface fold and edge effects.

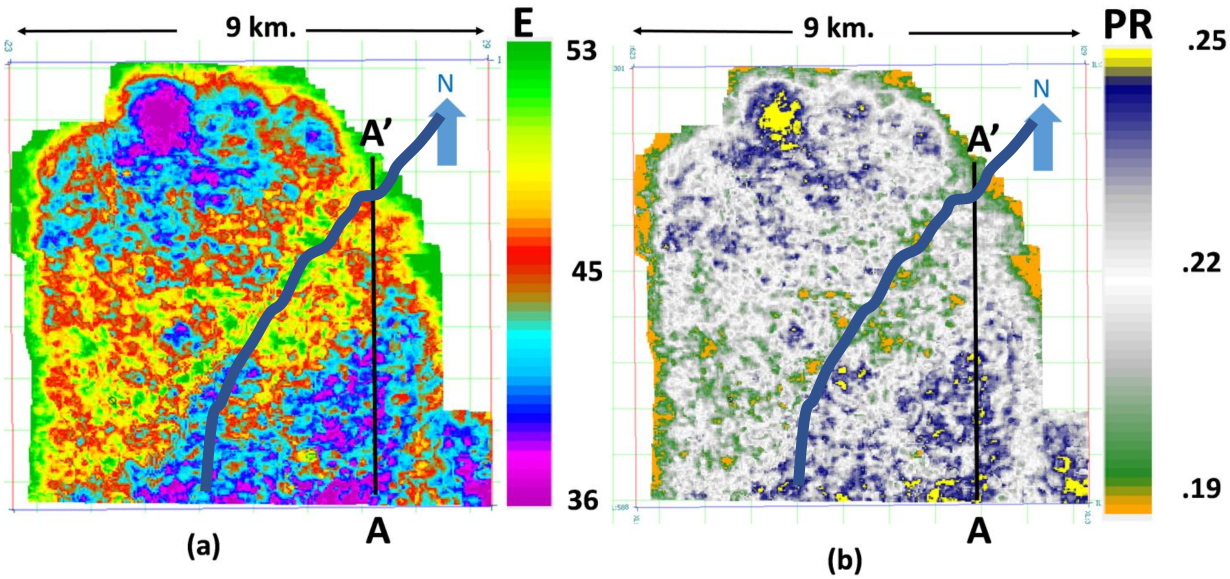


**F igure 3.9.** Stratal slices showing (a) Young's Modulus (*E,* GPa) and (b) Poisson's Ratio (*PR*), from joint PP-PS prestack inversion. The data are extracted from the same stratal slice within the Duvernay interval shown in Figure 3.10. This slice is conformable to the Swan Hills structure, the Swan Hills reef outline is shown in blue. Profile A'-A is indicated for the plot shown in Figure 3.11.

Figure 3.10(a) shows a cross-plot of Young's Modulus versus Poisson's Ratio for the Duvernay interval, including all data values from the simultaneous inversion volume from the top Duvernay horizon to the base Duvernay horizon. For comparison, the points are overlaid onto theoretical values of Young's Modulus versus Poisson's Ratio (Cho and Perez, 2014), as shown in Figure 3.10(b). The Duvernay points cluster within a relatively confined region near the middle of the theoretical values for quartz-clay and quartz-limestone mixtures. The Duvernay values also appear to fall approximately along a constant slope of bulk Modulus versus Poisson's Ratio, as indicated on the graph by a set of black curves. The cross-plot in Figure 3.10(a) is used to group the data into four distinct seismic lithology zones.

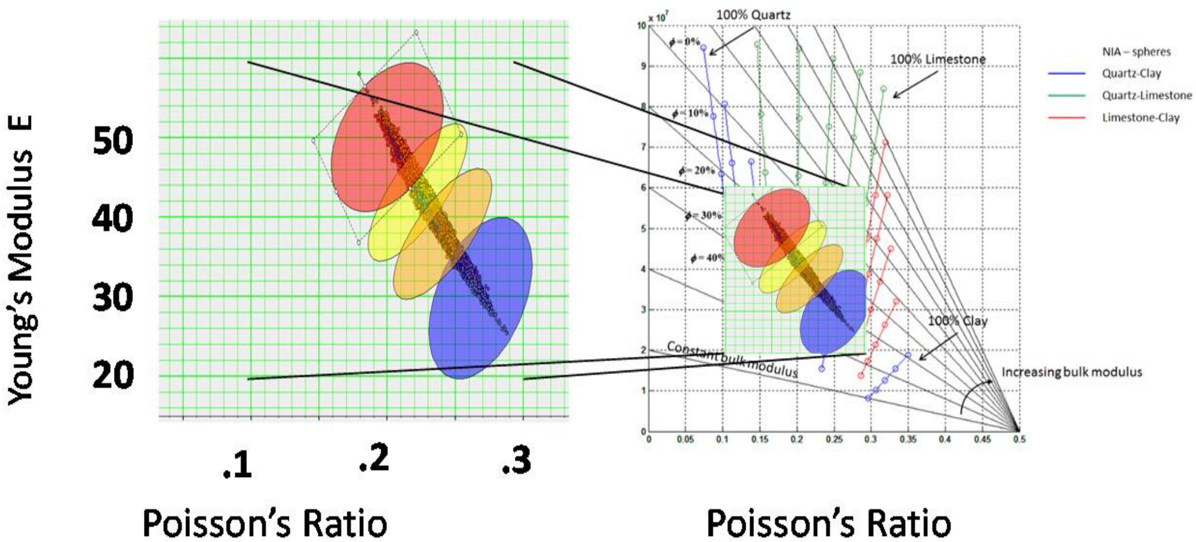


**Figure 3.10.** (a) Cross-plot showing Young's Modulus (*E*) versus Poisson's Ratio (*PR*) from prestack PP-PS inversion for data samples within the Duvernay interval. These points are grouped into four seismic lithology zones, which are displayed in Figure 3.11. (b) Cross-plot of theoretical values of *E* and *PR* (Cho and Parez, 2014), showing that the Duvernay points fall approximately along a line of constant slope of bulk Modulus versus *PR*; these cluster near the middle of the range for quartz-clay and quartz-limestone mixtures. The highest Brittleness index (*BRI*) corresponds to high *E* and low *PR* and, thus, would plot toward the top left corner of the graph (the region highlighted in red).

Although the zones are defined in Figure 3.10 based on the range of Duvernay values, these are applied to data points that fall outside of the Duvernay interval. Along this west-east profile, the Duvernay interval is classified from zones 1 to 4, where zone 1 may be more brittle as it is characterized by a higher Young's Modulus and lower Poisson's Ratio, and zone 4 is the least brittle. The region with north-south faulting and the deeper Swan Hills structure appear to be marked by a pronounced lateral transition from low to higher brittleness. The potential significance of this transition is discussed below.

The seismic cross-section in Figure 3.11 displays the PP-PS inversion results, where each data point is assigned a color according to the parameter ranges of these seismic lithology zones.

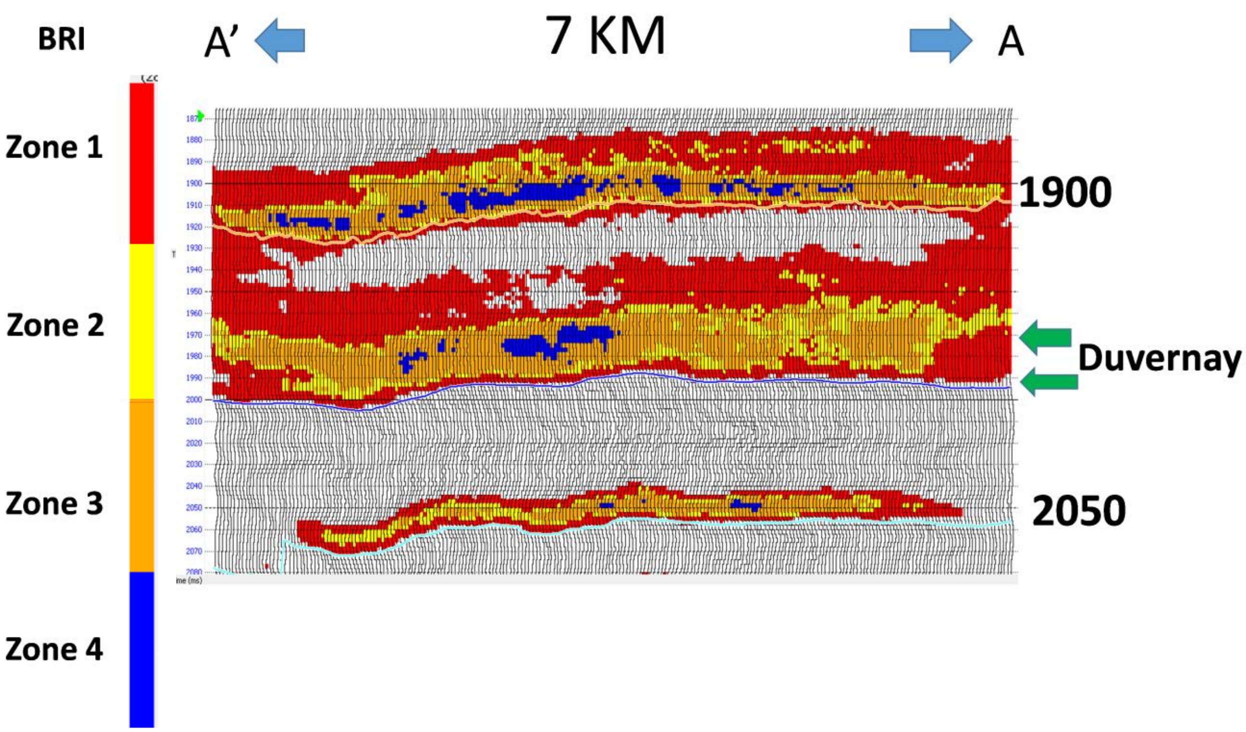


**Figure 3.11.** A north-south profile (A'-A in Figure 3.9) showing Young's Modulus (*E*) versus Poisson's Ratio (*PR*) data from prestack PP-PS inversion, colored based on the seismic lithology zones defined in Figure 3.10. The top and base of the Duvernay interval are highlighted with green arrows. Note the red-to-blue contrast across the Duvernay interval.

Figure 3.12(a) shows interpreted near-vertical basement-rooted faults seen on all horizons from the Precambrian to the Duvernay, including the major north-south fault. Figure 3.12(b) is a plot of the Brittleness index calculated using equation 3.5. Warm colors are high in Brittleness index; cold colors are low values. This system of faults is picked and correlated manually based on matching seismic displacements from the Ireton Formation to the top of Precambrian basement, including small vertical displacements from lineations observed on time slices (e.g., Figure 3.3) and observed lateral displacement of the Gilwood channels, suggesting strike-slip movements. Combined, these two maps show key elements in evaluating the Duvernay: structural controls and lithologic properties. The effects of low fold can be seen along the north and east edges of the survey in Figure 3.12(b). This low fold manifests itself in the form of an anomalously high Brittleness index value along the edge of the survey. Base on the BRI contrast across the Swan

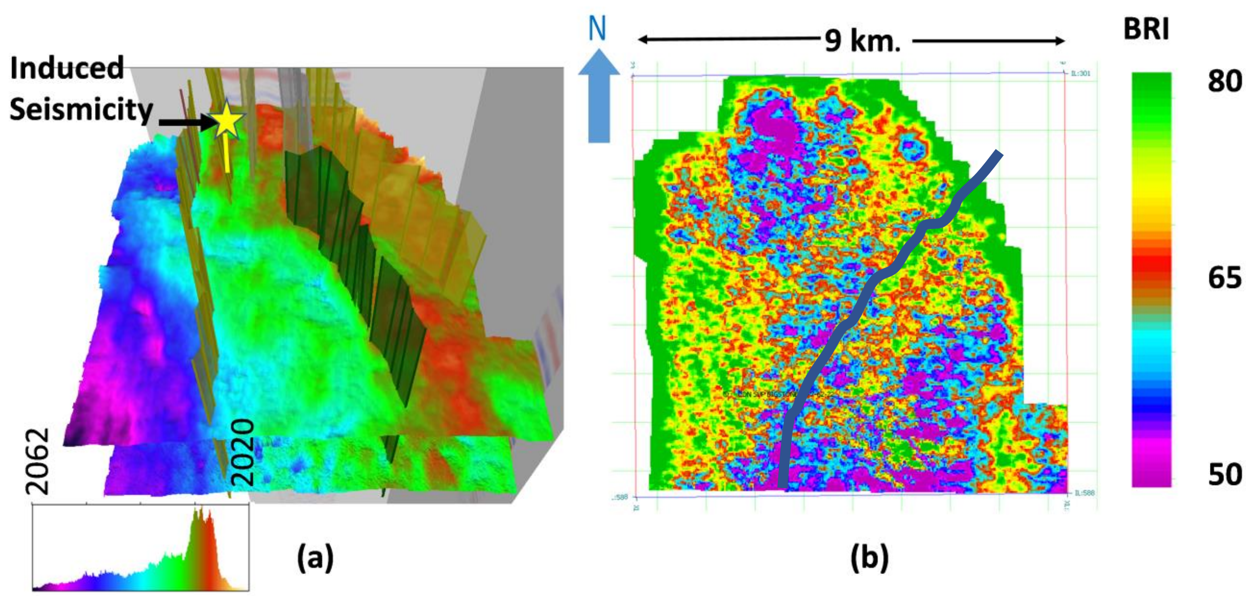


**Figure 3.12.** (a) Perspective view showing interpreted basement-rooted, steeply dipping faults, as well as Gilwood and Precambrian horizons extracted from the P-P data volume. The interpreted north-south vertical faults are marked; these faults also have a strike-slip component. The arrow indicates where induced seismicity has occurred (Wang et al., 2017). (b) Stratal slice showing Brittleness index *(BRI*, units percentage) calculated from Young's Modulus (*E*) and Poisson's Ratio (*PR*) within the Duvernay interval. The Swan Hills reef front is shown as a blue line.

Hills Reef front (dark blue), there is an observable change in brittleness, particularly in the central portion of the map. At the South reef boundary, the change across the reef front is minimal. From these observations, it appears that the Swan Hills reef had an effect on the deposition, more so to the NE portion of the map.

In figure 3.12 there is a

**3.8 Discussion**

Standard resource-play development schemes, such as horizontal drilling on a regular grid and using uniform completion designs, may be well suited to homogeneous reservoir conditions. Evenly spaced boreholes and completion intervals are not optimal for the type of geological complexity one is likely to observe in the Duvernay play. For example, a uniform pattern of wells may fail because of reservoir heterogeneity and the presence of faults, which may cause offsets in the reservoir, while uniform perforation intervals may also not be suitable, particularly when a wellbore crosses a facies boundary with varying brittleness. The stratigraphically equivalent Perdrix Formation in the southern Canadian Rockies (Weir et al., 2018) demonstrates how changes in Duvernay lithofacies may be linked to increments of reef growth. Outcrop analysis also reveals how the off-reef depositional environment varies over spatial scales of tens to hundreds of meters, compatible with the resolution capabilities of seismic data. Stratal slices from 3D seismic inversion volumes, as depicted in Figures 3.7 and 3.9, reveal coherent patterns of parameter variability that likely reflect varying reservoir conditions due, in part, to distinctive lithofacies arising from episodes of Leduc reef building and pre-existing Swan Hills structure.

The structural map of the Duvernay Formation includes regional dip, strike-slip, and vertical faulting. The lithology changes laterally as a function of the local and regional depositional envorrnments. A development program should take into account structural control, as well as reservoir heterogeneity. During a fracture stimulation program, faulting could create either a barrier or a pathway for fluids, depending on their present-day permeability. Faulting can have a significant effect on the architecture of the present-day Duvernay reservoir. The timing of the faulting can be predepositional, syn-depositional, or postdepositional. The type of faulting can be strike-slip, normal, or reverse. If the faulting is predepositional, the marine depositional environment across the fault would be subject to different water depths (e.g., the Swan Hills reef edge), resulting in different organic matter concentrations and sediment content. Abrupt changes to Young's Modulus, Poisson's Ratio, and Brittleness index (Soltanzadeh et al., 2015) across the fault would be the result.

Faulting may have had a significant effect on the Duvernay reservoir (Bao and Eaton, 2016). If vertical faulting were active during deposition, one would expect to see facies changes occurring across the fault boundary. Faulting occurring after deposition would create fractures in the Duvernay Formation, along with zones of weakness (damage zones). Postdepositional strike-slip faulting would create a condition wherein different facies of the Duvernay are juxtaposed across a fault, having been transported from their original depositional setting. For example, Figure 3.2 shows two interpreted near-vertical basement faults seen on the Precambrian to Duvernay reflection events, based on matching seismic displacements from the Ireton Formation to the Precambrian. The Gilwood Formation map and fault display suggest that north-south basement faulting may have been active during formation of the Gilwood channel (O'Connell 1994), leading to a lateral strike-slip fault offset.

The fault-mapping process used here includes observing horizontal time slices, examining lateral displacements on geological features, and matching vertical displacements on vertical time slices. Strike-slip features can be identified by observing displacment on the features such as the observed displacement on the Gilwood channel, even if there is little or no vertical displacement. (Figures 3.6 to 3.8). This type of anomaly is also amenable to seismic mapping using automatic discontinuity/fault detection with adaptive principal-component analysis (Weir et al., 2018). Lateral offset of paleogeographic features such as a river channel (Figure 3.5) provides a tool to measure lateral fault offset, which is otherwise very difficult to quantify in a horizontally layered medium.

As noted above, the simultanious inversion outputs lithology paramaters, which can be used as a tool to differentiate syn- and postdepositional faulting. Figure 3.9 has features that exhibit step-like changes occurring across interpreted fault boundaries, indicating active faults during deposition. Figure 3.9 on both the Poisson's Ratio and Young's Modulus plots contain features that align north-south, consistent with the interpreted north-south strike-slip faults seen in Figure 3.5. This infers that tectonic activity (strike-slip motion) has taken place after the Leduc buildup and deposition of the Duvernay Formation.

Determining fault architecture is crucial to well planning; faults can control depositional boundaries, act as a conduit for fluids, or partition a well by acting as a barrier. For a fracture stimulation program to be succsssful, the proppant must stay in the target zone, stimulate brittle reservoir, and avoid geohazards such as induced seismicity. Basement faulting may leave potentially activated faults in a near-failure condition, to be triggered by hydraulic fracture stimulation. A fracture stimulation program drilled in the proximity of these faults could lead to these faults becoming critically stressed, such as that observed by Bao and Eaton (2016). In well planning, the aim is, of course, to avoid both of these issues: the loss of fluid into thief zones and induced seismicity.

As noted earlier, a desired combination of a high Young's Modulus and low Poisson's Ratio is optimal for hydraulic fracture stimulation (Cho and Parez, 2014). A high Young's Modulus value indicates that the rock material contains the mechanical strength to remain open after stimulation. The material will crack open and remain open with proppant as opposed to deforming in a ductile manner and closing up the fracture. A high Poisson's Ratio value indicates that the rock is relatively incompressable, again indicating that the material will crack under stress rather than deform. Treatment of a well with fracture stimulation should target areas of high brittleness while avoiding low-brittleness areas. The concept of brittleness is seemingly straightforward in concept; however, there may be other factors to consider. According to Cho (2014), the elastic moduli defined by using Poisson's Ratio and Young's Modulus may be only two of many elastic moduli defined by material constitutive relations. Other elastic moduli may influence Poisson's Ratio and Young's Modulus, such as fracture networks and porosity distribution.

More work needs to be done to calibrate brittleness with well performance, fracture propagation, and induced seismicity. Nevertheless, PP-PS seismic inversion in this study shows promise for mapping seismic lithology parameters to aid in the development of Duvernay reservoirs. For example, a pre-existing structure such as the interpreted Swan Hills reef front, will create an environment with varying depositional energy in much the same manner as a pre-existing fault with varying brittleness (Knapp et al., 2017). Figure 3.12(b) shows a marked boundary in the Brittleness index from southwest to northeast. Here, I would expect to see a lower-energy environment, a higher silica content, and, hence, a more brittle Duvernay facies in the lower-structure depositional environment (Cho and Parez, 2014).

### 3.9 Conclusions

The Duvernay play is prone to induced seismicity and is likely to exhibit considerable lithologic heterogeneity in the subsurface at scales that are seismically resolvable. Consequently, I recommend that planning for well completion programs with drilling and hydraulic fracturing should consider reservoir facies, present-day fault structure, and the influence of basement tectonics. In this study, I develop a comprehensive workflow for interpretive inversion of multicomponent 3D seismic data, in conjunction with structural analysis. My workflow requires AVO-compliant data processing and makes use of poststack inversion to obtain an acoustic impedance volume, followed by correlation of horizons between P-P and P-S sections and prestack PP-PS inversion. The output parameters from the inversion, consisting of P- and S-wave velocities and density, are used to calculate data volumes containing Young's Modulus, Poisson's Ratio*,* and Brittleness index. Various presentation formats for the inversion results, including perspective views and stratal slices, provide insights for geological interpretation of the data.

The inversion results reveal spatially coherent patterns of seismic lithology parameter variability that support a number of key interpretations. Lithofacies variations within the Duvernay Formation likely reflect episodes of growth of proximal Leduc reef complexes. These processes lead to variations in Young's Modulus, Poisson's Ratio*,* and Brittleness index, indicating that some areas within the survey volume are better suited than other areas for hydraulic fracturing. Fault systems characterized by relatively small vertical offsets are expressed by structural discontinuities and, more commonly, curvature anomalies defined by fold hinge lines. The largest fault observed here is a steeply dipping structure with a north-south strike; this fault produced approximately 1 km of left-lateral (sisistral) strike-slip offset, based on inferred displacement of a Middle Devonian Gilwood river channel.

The interpreted Swan Hills reef front has produced an abrupt change in brittleness in the Duvernay Formation from the high side to the low side. This change is interpreted to be the result of a lower-energy marine depositional environment caused by pre-existing Swan Hills structures at the time of Duvernay shale deposition. A step-like discontinuity in Brittleness index, derived from the PP-PS inversion results, provides evidence for syn-depositional motion on this fault. Other seismic anomalies are quasilinear features that lack such a step-like discontinuity; these anomalies are interpreted as damage or alteration zones near postdepositional faults that belong to a complex fault network in this region. From an economic perspective, basement faulting may produce an undesirable result when a fracture stimulation is attempted nearby, as the objective of a completion program is for the hydraulic fracture system to remain within the formation. If these pre-existing faults are critically stressed, fluid injection can produce unwanted induced seismicity.

# Chapter 4

## Application of deconvolution to continuously recorded passive seismic data

### 4.1 Summary

The motivation for signal conditioning (processing) of continuously recorded seismic data came about from earlier work in reflection data field testing. The early field processing systems allowed an observer to perform simple processes in the field such as deconvolution, filtering and scaling in the field for testing. The testing would include parameters such as charge size and shot hole depth, with the desired outcome of strong reflections and a high signal to noise ratio. Often, a field shot record during the test sequence would be devoid of observable reflection events, a single pass of deconvolution would bring out these events so they could be easily observed. Applying these processes to continuously recorded (microseismic data) achieved similar results; continuously recorded seismic records seemingly devoid of events in their raw state are observed to have visible seismic events.

### 4.2 Introduction

Passive seismic recording during hydraulic fracturing can be used to detect and locate microseismic events, with the primary goal of mapping and characterizing hydraulic fractures (Eaton, 2018). Some methods used to process microseismic data require picking of the arrival times of P- and S-waves, but this step can be challenging because of low signal-to-noise ratio and complex waveforms. Some parallels exist with seismic reflection data, inasmuch as waves propagate in the same medium and therefore experience similar path effects (e.g., due to attenuation and scattering). These path effects can lead to undesirable waveform characteristics (e.g., complex wave shape, reverberatory signals). To address this issue, deconvolution is routinely used in seismic reflection processing to sharpen the seismic pulse and render the wavelet more suitable for interpretation. For example, zero-phase deconvolution (Margrave, 2005) simplifies interpretation by allowing events to be picked at a peak or trough. The similarity in path effects motivates me to test the use of deconvolution methods for microseismic data, as described in this chapter.

### 4.3 Methodology

In this study, I evaluate the applicability of deconvolution for improving event detection and arrival-time picking in the case of continuously recorded passive seismic data. The test data set comes from ToC2ME, a research-focused program that recorded a four-well hydraulic fracturing program in the Kaybob-Duvernay region of Alberta, Canada (Eaton et al., 2018) using a dense geophone array, with 3C sensors buried at a depth of 27 m. Like most passive (and active) seismic programs, this data set contains noise from wind, power lines, vehicle traffic, pumps, etc. For the testing portion, a number of records are processed using VISTA®; the complete set of data is processed at a commercial processing center using parameters determined during the testing sequence.

Figure 4.1 illustrates the path effect of reflected and direct arrival waves. In the case of the reflection data, S-wave returns through the earth as a result of wave conversion. For passive events (induced seismicity), P- and S-waves are generated as a direct arrival. All of the waveforms pass through the same subsurface media and are recorded using surface (or near-surface) geophones.

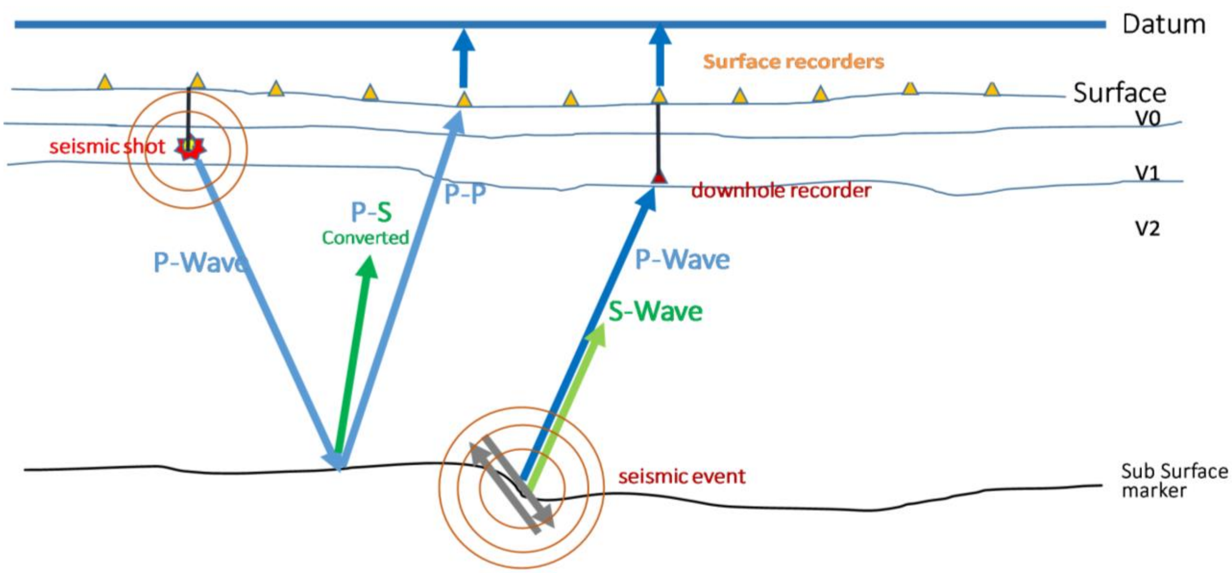


**Figure 4.1.** Raypaths for passive seismic sources and seismic reflections. Both raypaths encounter similar subsurface attenuation effects. The passive and active seismic waves pass through the same media and are subject to the same attenuation effects. Both types of wave are recorded by surface or near-surface geophones.

### 4.4 Passive seismic data testing

Seismic reflection data–processing tools appear to have useful applications in the conditioning of continuously recorded seismic data for microseismic monitoring. Processes such as deconvolution, filtering, and scaling can enhance the signal-to-noise ratio and improve the effectiveness of autopicking algorithms to detect events. Beacuse the frequency spectrum of the processed data is altered, however, deconvolved records may not be suitable for direct calculation of magnitude or moment tensor inversion, as described by Walter and Brune (1994).

Along with the desired signal, passively recorded data contain noise generated from traffic, pipelines, human activity, etc. Figure 4.2 illustrates the convolutional aspect of the seismic-recording system, illustrating the source wavelet, the earth's impedance (Green's function), and the effect of noise. The key differences between the seismic events are that the passive events have a primary P- and S-wave source, whereas the reflected data generate a converted S-wave at the reflection interface. The passive seismic recording uses buried 3C geophones, while the reflection data use surface geophones. The geophones at the surface respond differently to an incoming signal than the buried geophones because of the free surface effect (Aki and Richards, 2002). The surface geophones record a larger amplitude from an incoming wave, but are subject to increased surface noise. positive signals. Here I use deconvolution, filtering, and scaling on continuous data and examine the results using the REDPy[7] software (Hotovec-Ellis and Jeffries (2016)). Preliminary results show a significant increase in the number of detected events. Applying these signal processes to continuous data prior to using earthquake detection software may add significant value to future induced seismic detection work.

---

Repeating Earthquake Detector in python[7]

## Active seismic recording

For P-P reflections:

$T_{pp}(t|\, x_s, x_r\, ,V_{PP})= W_p(t)^{*}\, R_p(t)\, +\, Noise$

For P-S (converted) reflections:

$T_{ps}(t|\, x_s,x_r,V_{PS})= W_p(t)^{*}\, R_{ps}(t)\, +\, Noise$

$W_p(t)$ = *source wavelet*

$R_p(t)$ = *reflection coefficient series*

* *Is the convolution operator and*

$R_p(t) \approx \boldsymbol{G}_p\, ,\, R_s(t) \approx \boldsymbol{G}_s$ (***G*** *is a Green's function)*

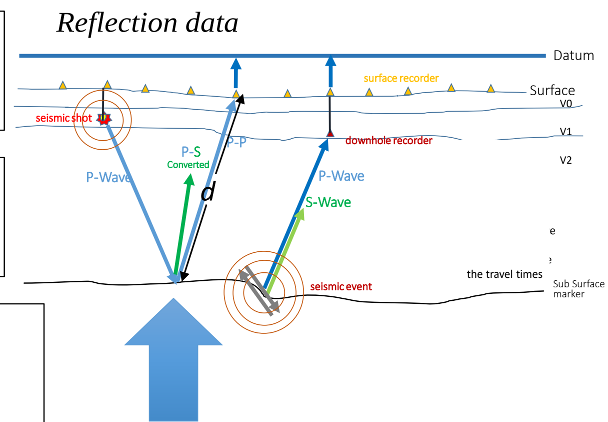


## Passive seismic arrival, induced events

For P arrivals:

$\boldsymbol{T}_p(t \mid x,t_0,V_P) = \boldsymbol{W}_p(t)^{*}\boldsymbol{G}_p + Noise$

For S arrivals:

$\boldsymbol{T}_s(t \mid x,t_0,V_S) = \boldsymbol{W}_s(t)^{*}\boldsymbol{G}_s + Noise$

$\boldsymbol{T}_p(t), \boldsymbol{T}_s(t)$ = *recorded seismic events*

$W_p(t)$ = *source wavelet*

$\boldsymbol{G}_{p,}\, \boldsymbol{G}_s$ = *Green's function*

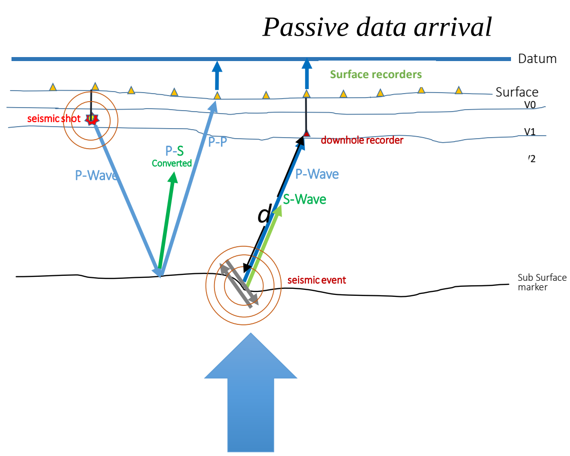


**Figure 4.2.** A comparison of passive and active seismic sources. S-waves are often generated as a primary source for induced events. In reflection data, S-waves are the result of conversion at reflection boundaries.

The raw data contain a high-frequency signal that lies beyond the bandwidth of recorded seismic events. Cross-feed between horizontal and vertical channels may also generate false positive signals. Here I used deconvolution, filtering and scaling on continuous data and examined the result using the REDPy software (Repeating Earthquake Detector, Python code). Preliminary results have shown a significant increase in the number of detected events. Applying these signal processes to continuous data prior to using earthquake detection software may add significant value to future induced seismic event detections.

A number of seismic records are used from the ToC2ME data set to test the applicability of deconvolution, filtering, and scaling on passive seismic recording. Initial data testing is performed on a selection of 60-second records to test specific types of seismic event; a perforation shot and induced seismic event are processed using deconvolution, filtering, and scaling. These are in turn analyzed for their spectral content, comparing the P- and S-wave arrivals. The geophones in the recording array are buried at a depth of 27 m, resulting in significant cross-feed of P- and S-waves on the vertical (V or Z), horizontal (H1), and horizontal-orthogonal to H1 (H2) channels.

Preliminary test analysis demonstrates that the P- and S-wave fields have significant differences in the recorded bandwidth (Weir et al., 2018). Results from the autopicking algorithms demonstrate a significant improvement in the performance of the autopicking program on the V channels, resulting in a greater number of identified events (Paes and Eaton, 2018). The spiking deconvolution has a detrimental effect on the ability of the autopicking test to detect events, so deconvolution is not applied to the horizontal channel data set.

**4.5 Theory**

For continuous seismic data, the origin time ($t_0$) is not known, and the recorded signal is dominated by the direct arrival. I use a simple model for the P-wave arrival and components of the wave field. For non-normal incidence, P-waves are recorded on the H1 and H2 channels (nonzero) incidence. Similarly, S-waves are recorded on the V channel for non-normal incidence.

$$Tp(t) = Wp(t) + N(t) \ ,$$

and the S-wave arrival,

$$Ts(t) = Ws(t) + N(t) \ ,$$

where $W_P(t)$ is the P-wave source wavelet, $W_S(t)$ is the S-wave source wavelet, and $N(t)$ is a noise term. Induced seismic events typically result from a double-couple event, producing significant S-wave energy, whereas explosive events such as perforation shots may only generate P-waves (Cronin et al., 2010). A double-couple event is mathematically represented by orthogonal force couples (Aki and Richards, 2002). The radiated energy from a double-couple event is representative by slip on a fault surface.

The burried array and the surface geophone array differ in one important aspect, as illustrated in Figure 4.3. The near-surface low-velocity layer (Margrave, 2005) acts as a natural P- and S-wave separator due to the effect of the low-velocity layer. The low-velocity layer is approximatly 900 m/s in this area and has the effect of bending nonzero incidence upgoing waves close to vertical. In the extreme case of a 45° incidence angle, the ray will bend to approximately 15° from the vertical. The nonzero incidence components of the P- and S-waves are recorded on the H1, H2,

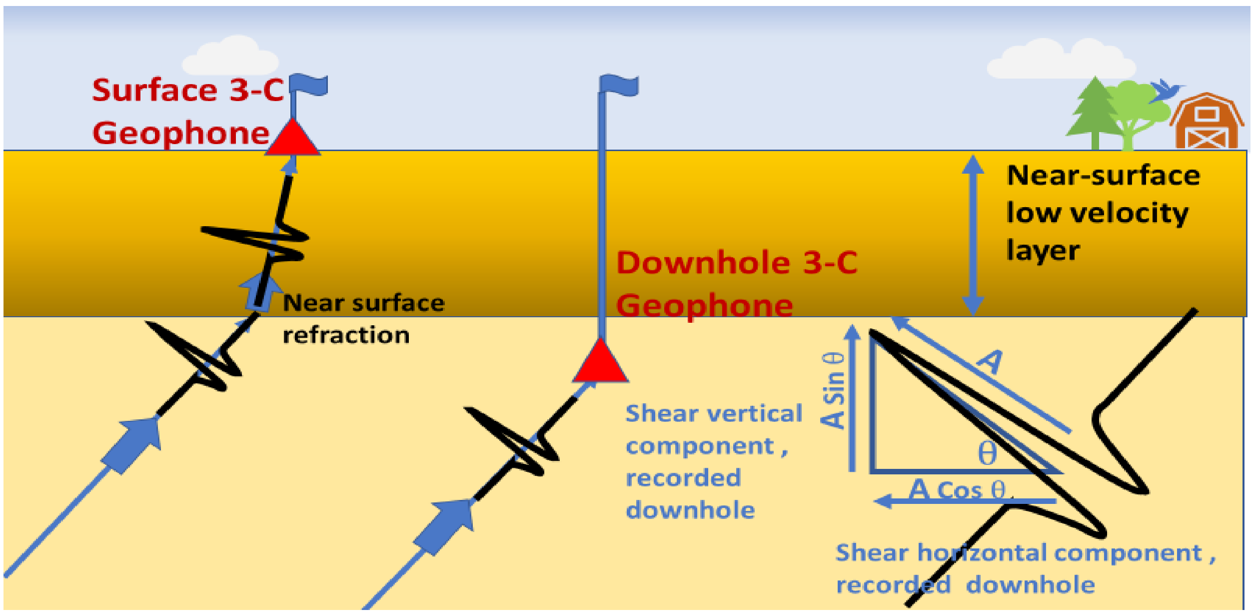


**Figure 4.3.** An illustration of the near-surface effect. The near-surface low-velocity layer acts as a P- and S-wave splitter by refracting the incoming wave to near-vertical incidence. For the burried array, no such seperation occurs, causing the burried array to record the nonzero incidence components.

and V channels, respectively. The ToC2ME array has the 3C geophone set at a depth of 27 m, thereby recording data below the low-velocity layer.

Generally in a seismic reflection survey, the objective of deconvolution in the data-processing stream is to balance the amplitude spectrum over the signal bandwidth and display the final data such that reflection arrivals are band-limited approximations of a delta function. This ensures that a seismic reflector (an event) is a peak or a trough, which corresponds to either a positive or negative reflection coefficient (Robinson and Treitel, 1980). This enables the data to be tied to well log data by means of a synthetic seismogram, enabling the time picks to be accurately be converted to depth. After zero-phase deconvolution is applied, the onset of a seismic reflection event occurs in negative time a few milliseconds in advance of the main event (Figure 4.4). For microseismic events, larger magniduced induced seismic events (anthrophegenic), and natural occuring earthquakes, the onset of the event is marked by an initial deflection of the geophone element as the P- and S-waves arrive from the source. Applying the aforementioned process to passive seismic data has the same effect, as illustrated in Figure 4.4. The event is identified with a peak or trough, depending on the position relative to the source and whether it is a double-couple or explosive source (Walter and Brune, 1993). Seismic event picking then becomes a matter of simply identifying a maximum peak or trough and correlating it with nearby

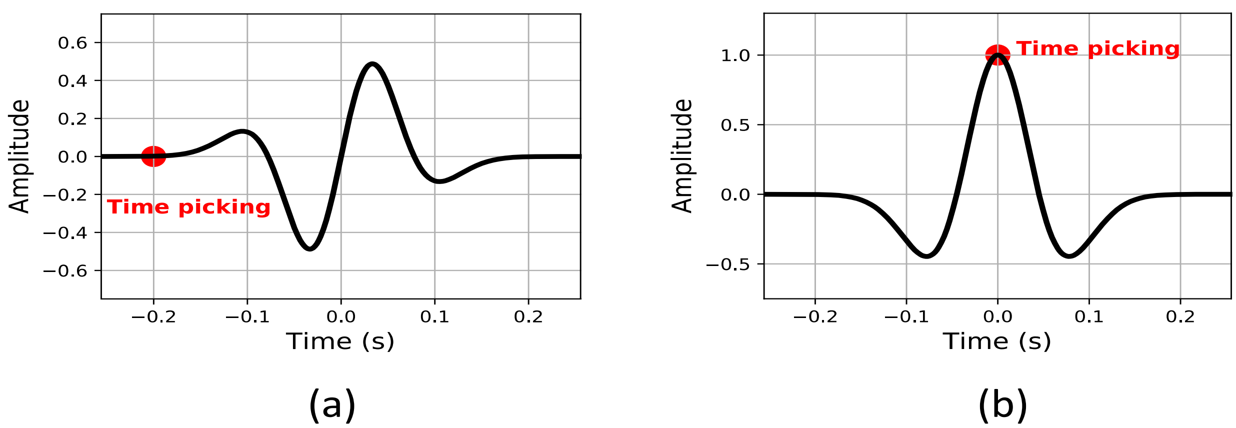


stations, in contrast to identifying the initial onset of the arrival (Eaton, 2018).

**Figure 4.4.** Schematic diagram amplitude spectra showing the effect of deconvolution and how seismic events are picked. The onset of a seismic event on raw data (a) is the first arrival, whereas deconvolution (b) shifts the phase spectrum to zero-phase, such that the event is picked on the maximum amplitude. Note the location of the seismic event picks, denoted by the red circles, before and after processing.

Figure 4.5 displays four individual seismic events seismic recorded at the same station, displaying three components of the passive seismic event. These events have been arbitrarily shifted to a 1-second start time for display purposes, with a gain applied to enable the P- and S-wave arrivals to be seen in the context of noise. From top to bottom, the events range from a seismic moment magnitude ($M_W$) of 1.0 to 0.2. If processing were able to improve the signal-to-noise ratio, then smaller-magnitude events would be easier to identify.

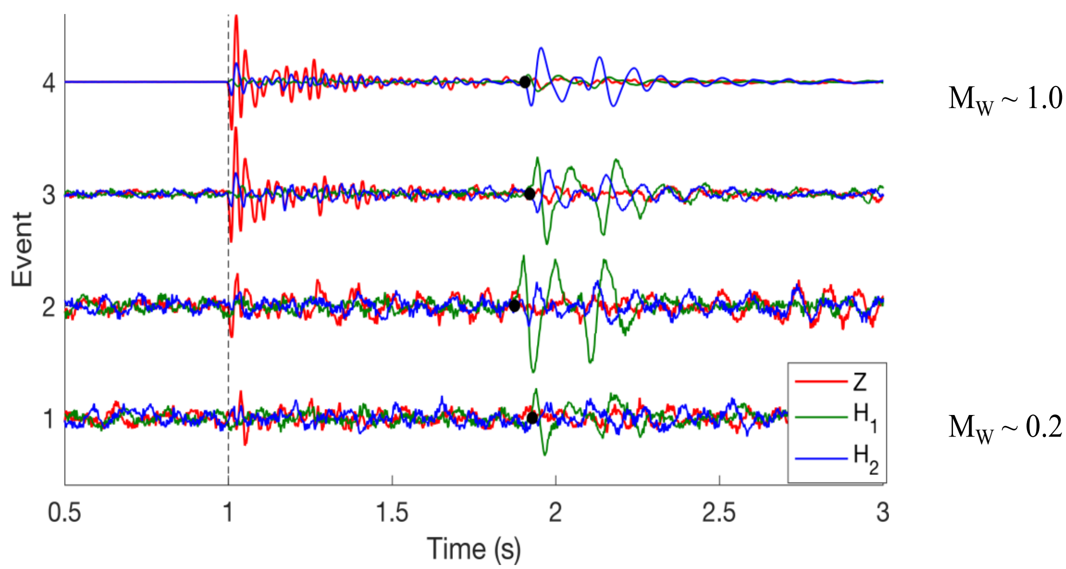


**Figure 4.5.** A display of four individual seismic events recorded at the same station from ToC2ME. The travel times are normalized to the first P-wave arrival. Z, H1, and H2 channels are displayed in red, green, and blue respectively (courtesy of A. Poulin).

## 4.6 Single stream data–processing sequence

In order to process continuously recorded microseismic data, the continuous record is first segmented into 60-second time intervals, after which the recorded data segments are loaded into personal computer (PC)–based commercial processing software. Each record contains Z and H1 and H2 data components. For the data set considered here, the Z channel generally captures the P-wave arrival, whereas the H1 and H2 channels capture two orthogonal horizontal components of the S-wave energy. Seismic records known to have recorded perforation shots and/or detected events from a fracture stimulation are processed to determine the effectiveness of deconvolution.

Several deconvolution operators are tested, 60, 80 , 100, and 120 ms spiking deconvolution operators, all with 1 % pre whitening. A predictive deconvolution operator is included in the test sequence. Differences in the result using spiking deconvolution operators are not readily observable. The predictive deconvolution produces less satisfactory results From these Side-by-side comparisons of raw and processed data are displayed in three examples to demonstrate the effect of filtering and deconvolution. User-defined deconvolution parameters are operator length, design gate, and prewhitening. An operator length of 80 ms is used, similar to that used for surface seismic reflection data. Prewhitening is a stability factor that is introduced, given that there are frequencies where the spectrum of the estimated wavelet is small (Margrave, 2005). Here I apply a prewhitening factor of 1% (or 0.01). The design gate is a time window that contains seismic events. A bandpass filter is chosen on the basis of the spectral output of the deconvolved trace. As a final step, the data are converted to zero-phase.

Figure 4.6 shows the processing flow used for testing the processing. The testing phase consists of two passes; the top row illustrates the process applied to the entire 60-second record, with the objective of identifying a passive seismic event. The deconvolution is designed around the identified seismic event and is then applied to the entire record.

In general terms, a seismic reflection record may contain 20 or more identifiable events in the space of a 4-second window, whereas there are generally comparatively few, if any, microseismic events on a continuous 60-second record. In the case of reflection data, as shown in Figure 4.6, the operator design is typically centered over known reflectors, whereas for the continuous data the operator is applied to the entire trace as a first pass. Once events such as perforation shots and hydraulic fractures are identified, a redesigned operator using a 1,000-ms window is applied, centered on an identified induced event. A basic spiking deconvolution, filter, scaling, and zero-phase conversion are applied to the full 60-second record.

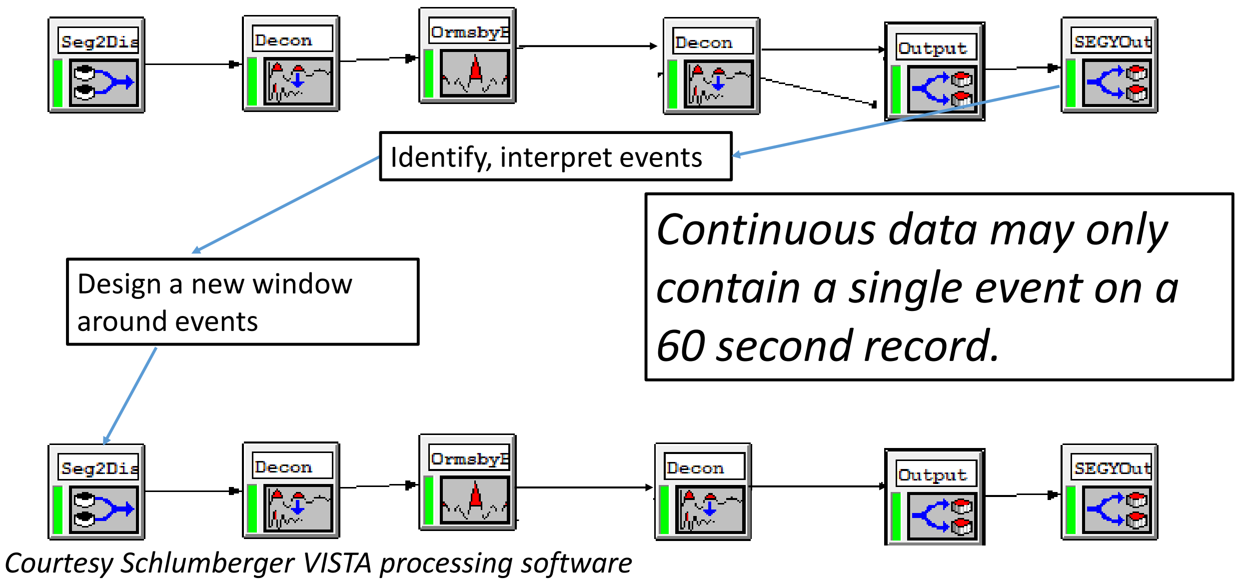


**Figure 4.6.** Passive seismic workflow used to test processing paramaters. The first pass cleans up the record and allows events to be identified. In the second pass, the operators are designed around an identified seismic event. An 80-ms, 1% prewhitening operator is used. The final filter is an 8-12-65-75–Hz bandpass filter.

Records are identified visually on the record, and then the deconvolution design window is rerun centered on an identified seismic event. The process results in a significant improvement in the signal-to-noise ratio.

### 4.7 Testing and analysis

Figure 4.7 shows a P-P seismic reflection section through the treatment area, plotted alongside a spectral plot. The maximum frequency obtained at the target from seismic reflection data is approximately 65 Hz. The two arrows indicate the zone of interest. The observed spectrum from the reflection data is similar in bandwidth to that observed in the continuously recorded data.

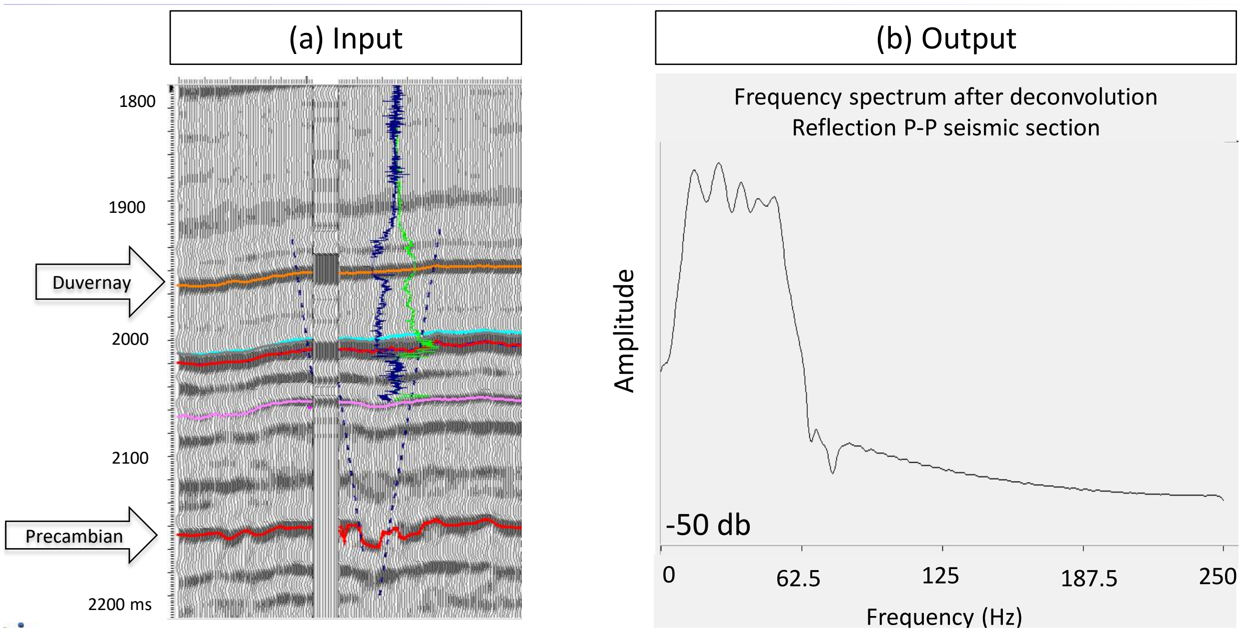


**Figure 4.7.** Spectrum (a) for a representative seismic profile (b). It is worth noting that P-wave bandwidth for seismic reflection data is comparable to that of passive seismic events generated from induced events at similar depths. The majority of the passive seismic events occur in and around the Duvernay Formation time equivalent at 2,000 ms.

For testing purposes, the continuously recorded 60-second SEG Y records are deconvolved with an initial pass of a Wiener (spiking) deconvolution (Leinbach, 1995), applied to the entire record using an 80-ms operator with 1% prewhitening. An Ormsby filter is then applied using a bandpass of 8-12-60-70 Hz; this range is determined to be the estimated usable frequency in the P-wave data. The traces are then amplitude-balanced using a total trace average. Some of the traces have very high overall amplitudes due to noise. Trace balancing brings the amplitude of noisy traces to be consistent with the rest of the data, making the microseismic data easier to interpret. A zero-phase operator is then applied to condition the data. Figure 4.8 is an example of this process, where the perforation shots are not visible in panels (a) and (b); the processing brings them out, so they are observable in panel (c).

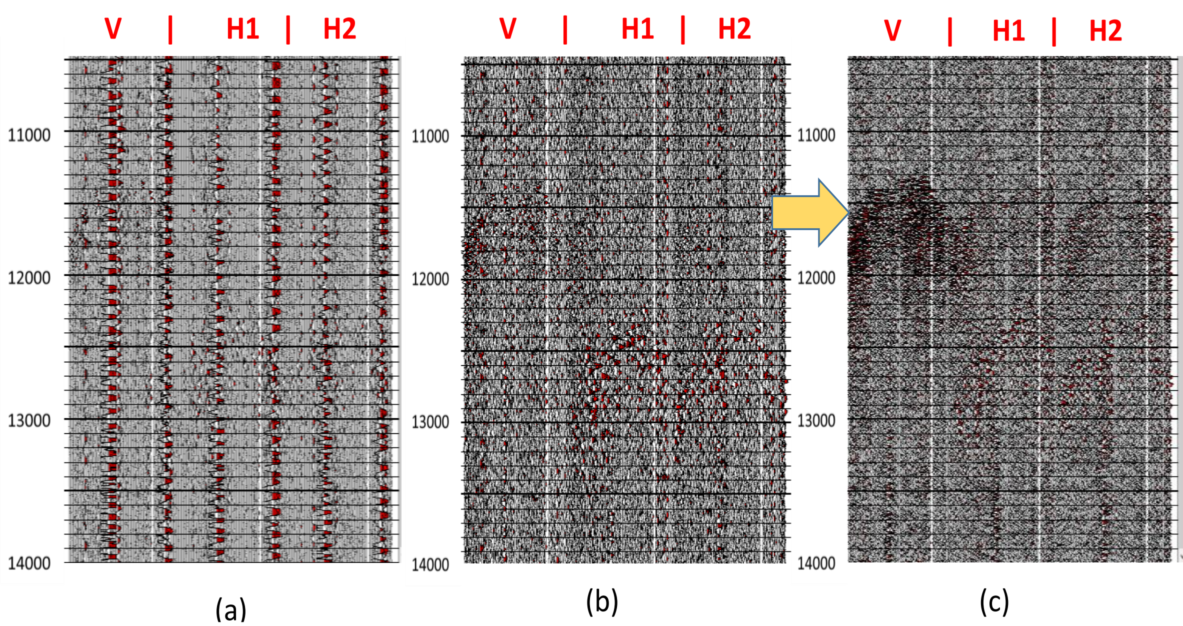


**Figure 4.8.** Example of a continuous seismic record perforation shot (V, H1, and H2 components) (record 61622): (a) raw, (b) filtered and scaled, and (c) deconvolution, scaling, and filtering. Seismic events are visible between 11,000 and 11,500 ms on the processed record (c) after deconvolution.

The first example of seismic processing is the seismic record shown in Figure 4.8. This record is chosen because it contains a perforation shot record that is not observable on the raw data. The deconvolution is centered on 11,500 ms and uses a 1,000-ms design gate. This processing results in an increase in the frequency content of the processed record. The anomalously strong traces on the raw record are scaled to match the rest of the data. For this seismic record, the second pass of deconvolution is centered on 11,500 ms and uses a 1,000-ms design gate. Once again, the anomalously strong traces on the raw record are scaled to match the average trace amplitude. Figure 4.9 shows the amplitude spectra before and after the deconvolution records from Figure 4.8. Deconvolution successfully flattens the frequency spectrum, enhancing frequencies up to 65 Hz. Frequencies greater than 65 Hz are interpreted to be noise and are filtered out using an Ormsby bandpass filter. The result shown here demonstrates the improvement in signal-to-noise ratio resulting from the application of deconvolution. Figure 4.9 shows where seismic events become visible, notably on the Z traces and to a lesser extent on the H1 and H2 traces. These events are not obvious on the Z component of the raw data (Figures 4.8 and 4.9). This processing flow shows promise for the identification of events such as perforation shots, which have, in many instances, been difficult to pick.

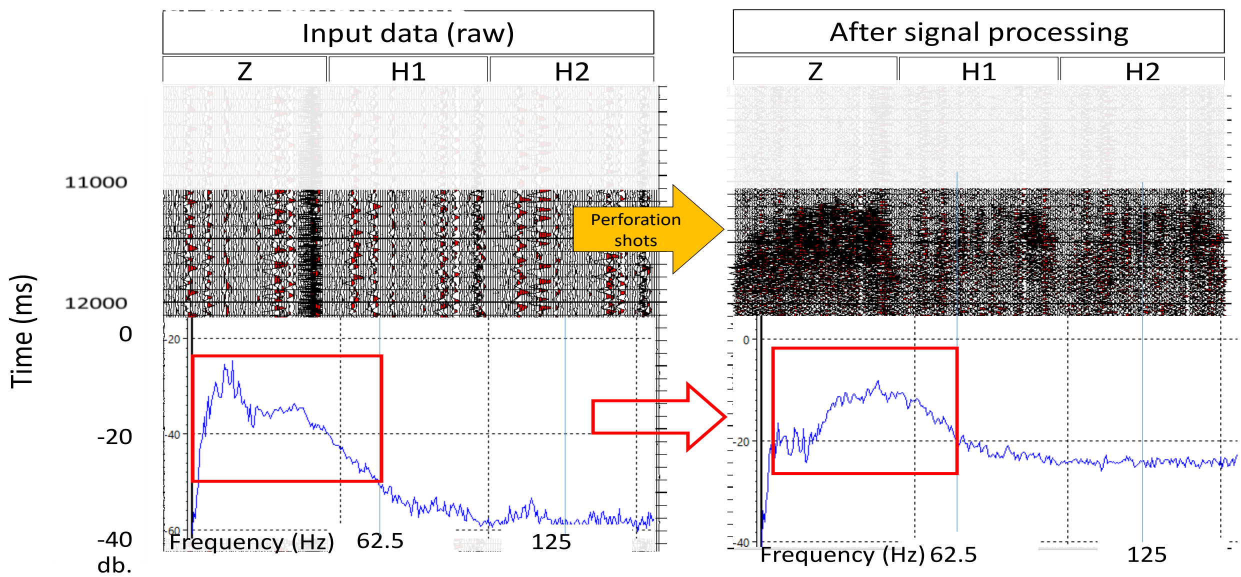


**Figure 4.9.** A spectral analysis of the 60-second record from Figure 4.8 before (a) and after (b) deconvolution. The effect of the spiking (Wiener) deconvolution is to balance the frequency spectra. The recovered frequency spectrum of the continuous data is extended significantly to about 65 Hz. The perforation shots are observable on the deconvolved data, wheras the raw data have no observable events.

A second example of a seismic event is shown in Figure 4.10. This seismic event contains an observable event on the raw data containing both P- and S-wave arrivals. In this example, the seismic records are sorted in absolute offset distance with respect to the calculated hypocenter. The seismic event exhibits normal move-out on both the raw and processed data. The effect of the processing is to sharpen the event and balance the amplitudes in the traces. However, the S-wave arrivals, starting at 13,200 ms, are more obvious on the raw record than on the deconvolved record.

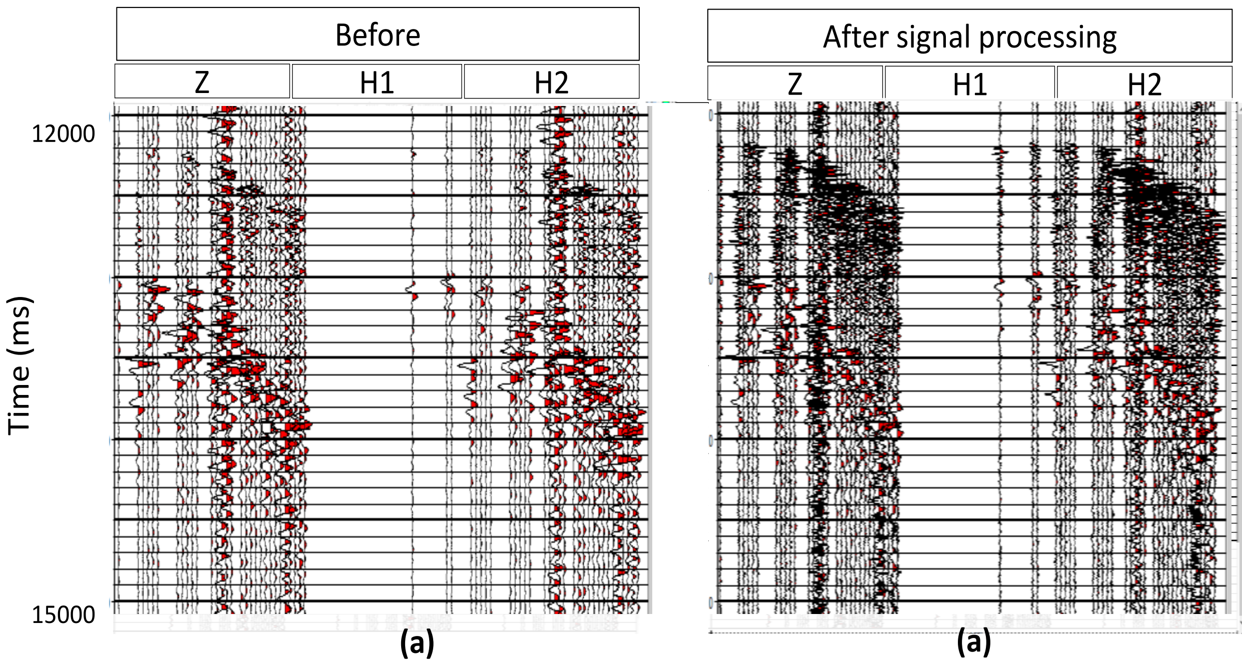


**Figure 4.10.** An example of a raw and processed record, this time sorted in absolute offest from the seismic epicenter. The P-wave reflection is improved by the processing; the S-wave arrival is somewhat degraded.

For the third example (Figure 4.11), events with low signal-to-noise ratios are analyzed using kurtosis and are compared before and after deconvolution. Houstecky (2020) provided a general description of the results of kurtosis applicatin. This analysis illustrates a workflow to retrieve arrival-time picking information using deconvolved passive seismic data in situations where the recorded data have a low signal-to-noise ratio. These data from the third example are analyzed using a newly developed autopicking event detection process based on kurtosis, described by Paes and Eaton (2017). Houstecky (2020) provided a general description of kurtosis.

Figure 4.11 shows a raw trace (top), the results of kukrtosis application (center), and the arrival picking (bottom). The unprocessed data are autopicked using a differential kurtosis algorithm with a characteristic function (CF) (Figure 4.11). In this autopicking process, information from correlatable seismic event picks on adjoining traces are also used to identify seismic event arrivals.

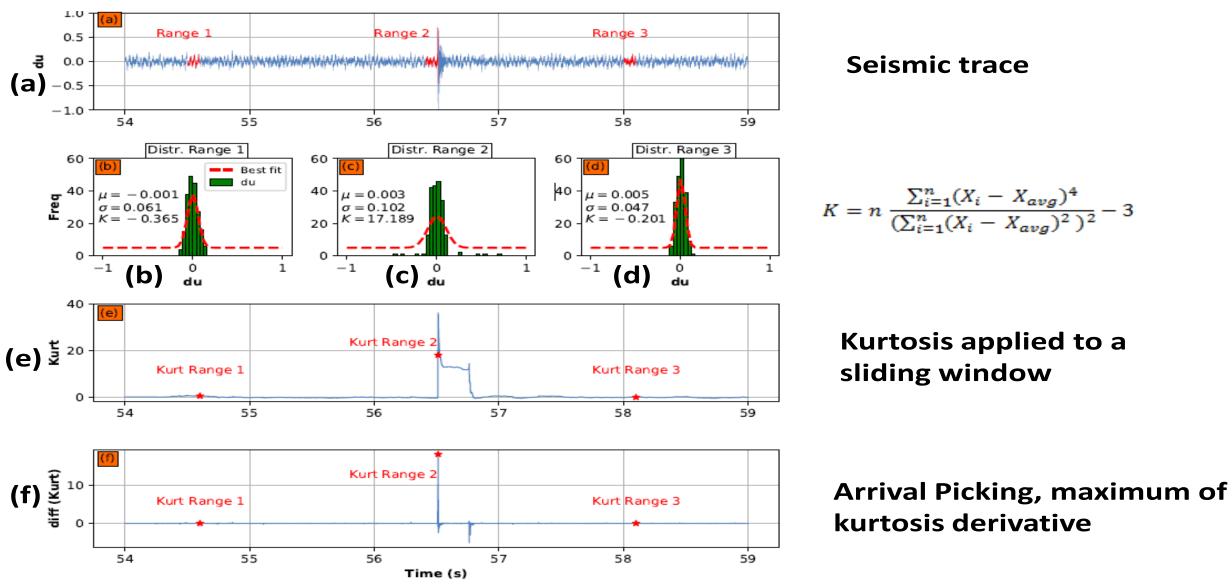


**Figure 4.11.** An example of microseismic signal and calculated CFs over a 5-second noisy interval of the Z component of an event. (a) Seismic trace, bandpass filtered to 15 to 250 Hz. The red plots ranging from 1 to 3 represent three sampled windows (b, c, and d). Histograms are shown of the three evaluated signals, including the mean, variance, and kurtosis, as well as a comparison of the best Gaussian fit of each window. (e) Kurtosis of the seismic trace (calculated over 50 samples. (f) Kurtosis differential CF, with its maximum highlighted by range 2 and used as the seismic wave arrival time (courtesy of Atila da Silva Paes [2019]).

Using the P-wave arrival time, the S-wave is picked as the maximum of a window, set to 0.5 to 2.5 seconds following the P-wave event time pick (on the Z trace).

Following the seismic events identified on the horizontal channels, the S-wave arrivals of the H1 and H2 events are compared. In the case of an outlier (a large difference between times from H1 and H2, > 0.5 seconds), the calculated S-wave arrival time is determined as the one with the pick closest to the S-wave arrival as seen on the neighboring geophones. For the kurtosis based on the autopicking method, (Figures 4.12 and 4.13), cataloging an event is based on the following two conditions: the early maximum peak of each Z-trace is limited to a restricted time window (around 1.0 to 2.0 seconds) (Figure 4.13) and is used as the P-wave onset.

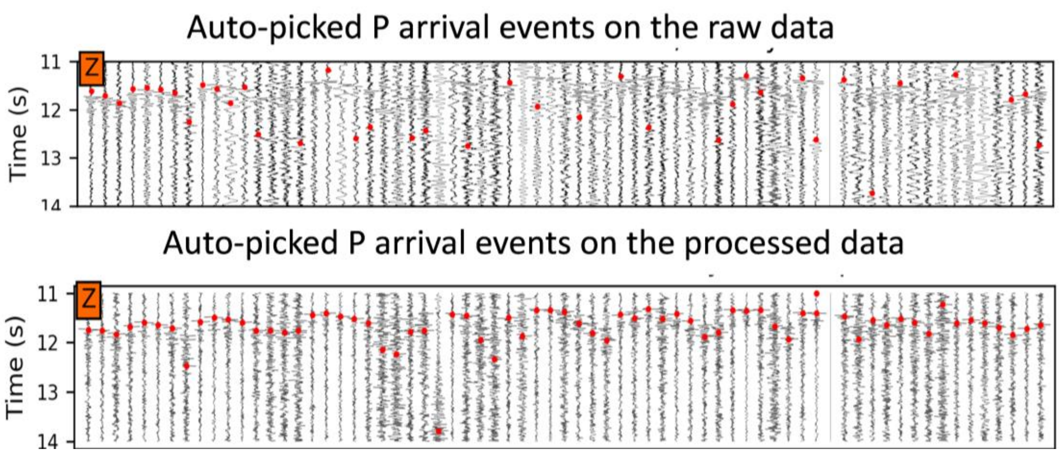


**Figure 4.12.** An example of a raw seismic record vertical component (Z) of the 3-C geophones. The red dots are the arrival picks using differential kurtosis algorithms. There is a significant improvement in the quality and quantity of the post-deconvolution event picks. The CF maximum (value used as arrival-time picking) is shown in red; the top panel is the vertical component. **(**courtesy Atila da Silva Paes)

The displays shown in Figures 4.12 and 4.13 contain identified (autopicked) seismic events before and after deconvolution. Figure 4.12 displays the raw data, with the autopicked events shown in red. Figure 4.13 displays the picked events on the deconvolved data. The conversion of the wavelet to zero-phase and the signal-to-noise ratio improvement significantly improves the autopicking on the V component. The P-wave picks appear to be improved for the deconvolved data in Figure 4.12 when compared with the raw data in Figure 4.13. The event picks are better across the Z time window for the P-waves. For the S-wave picks, the reverse is true; the S-wave picks exhibit more scatter and are less coherent on the processed H1 and H2 channels. The test results here indicate that data conditioning to optimize P-wave data for event detection differs from that for S-wave data, indicating the dual-stream process as being optimal, with differing parameters for the V and H1/H2 components.

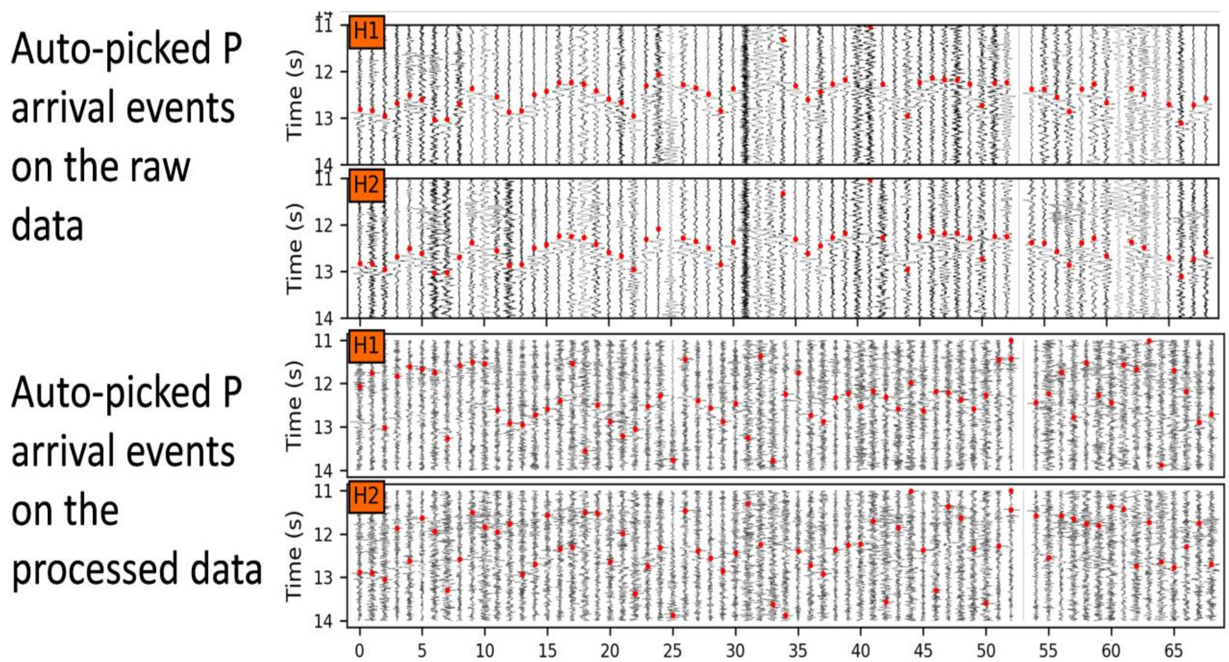


**Figure 4.13.** An example of the corresponding horizontal channels **(**H1 and H2) from Figure 4.12 after processing. This deconvolution based processing flow degrades the data such that the picks are scattered. The top two pannels are the raw data, the lower two pannels are the deconvolved data. This test demonstrates that the processing sequence used here is not suitable for S wave data, as recorded on the H1 and H2 channels.

### 4.8 Dual-stream processing

The test results in the previous sections from the three test examples indicate that the bandwidths of the P- and S-waves are approximately  12-65 hz, and 2 to 15 hz, respectively.  The remainder of this chapter describes the process as applied to the complete ToC2ME data set, as well as the preliminary results.  The objective of this section is to generate a processed data set and use it as input for an automatic earthquake detection program.  In this case, the program used is REDPy, a public-domain program (Hotovec-Ellis and Jeffries, 2016)..  The results are to be compared with the same program run earlier on raw data, having only a bandpass filter applied.  REDPy was initaliay designed to analyze natrually occuring earthquakes caused by volcanic activity, it is used here to detect hydraulic fracturing activity, and induced seismic events.

For the initial data test on the full data set, the batch job is set up to partition the seismic processing into dual streams, one suited for P-wave arrivals and a second for S-wave arrivals.  One-thousand test records are run in a dual-stream manner.  The P-waves are processed by deconvolution, filtering, and scaling; the S-waves are scaled and filtered with a 15-Hz high cut.  Figure 4.14 is an example of a raw seismic record showing a recorded event.  One can observe a significant amount of cross-feed, with S- and P-waves recorded both on the H1/H2 and V channels.  This record shows a number of noisy channels with very high amplitudes.  Cross-feed is also evident, with P- and S-waves from the same initial seismic event arriving on most of the channels.

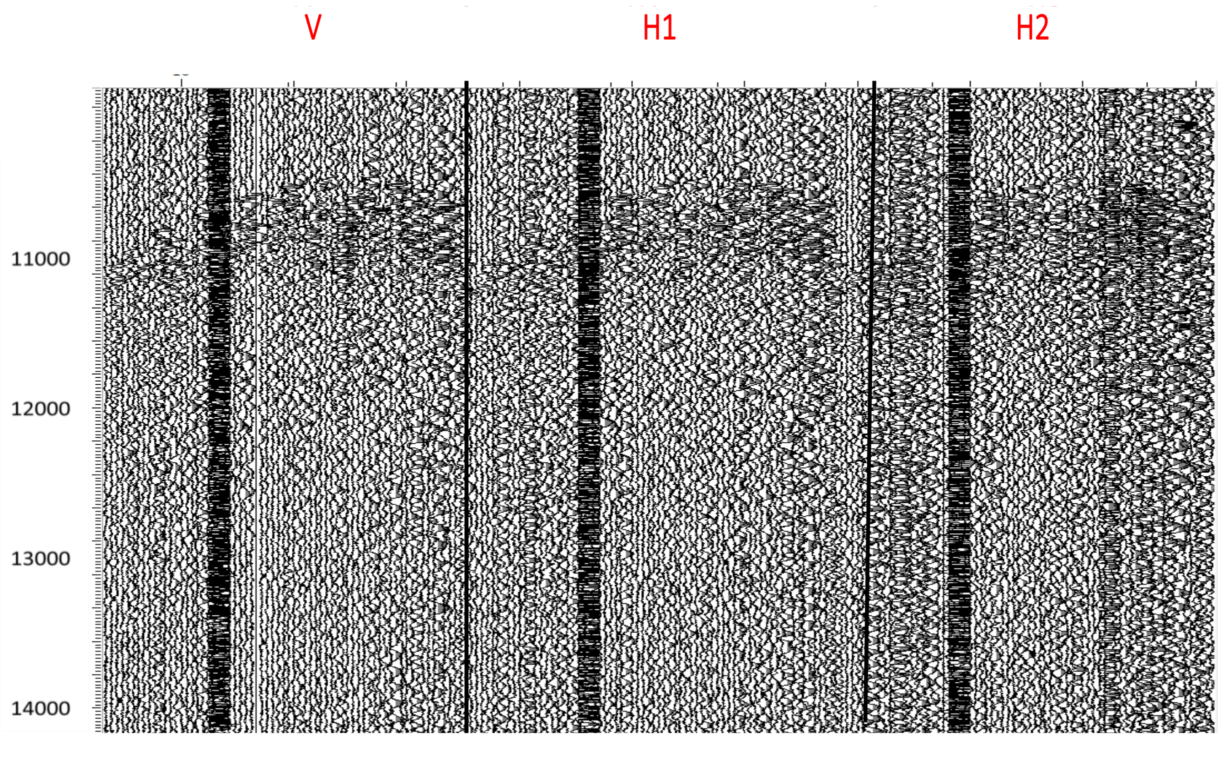


**Figure 4.14.** Raw input data from seismic record 24006 from the ToC2ME recording array. This record shows both P- and S-waves arriving on both H1/H2 and V channels. These geophones are 27 m deep, beneath the low near-surface velocity layer. Nonzero incident P- and S-waves are recorded on both V and H1/H2 channels because of the recording of the vertical and horizontal components of the nonzero incident waves.

There is an observavable seismic event at around 10,500 ms on all three components in Figure 4.14. There is indication of an event at 12,000 ms on the H2 channel, indicative of an S-wave arrival from the same event.

In Figure 4.15, dual-stream processing is applied, and the results show the same event recorded on Figure 4.14. The event arrivals on V are significantly improved, and the S-wave arrivals around 12,000 ms are significantly improved. The cross-feed is significantly reduced, and the frequency content on the V channel is increased.

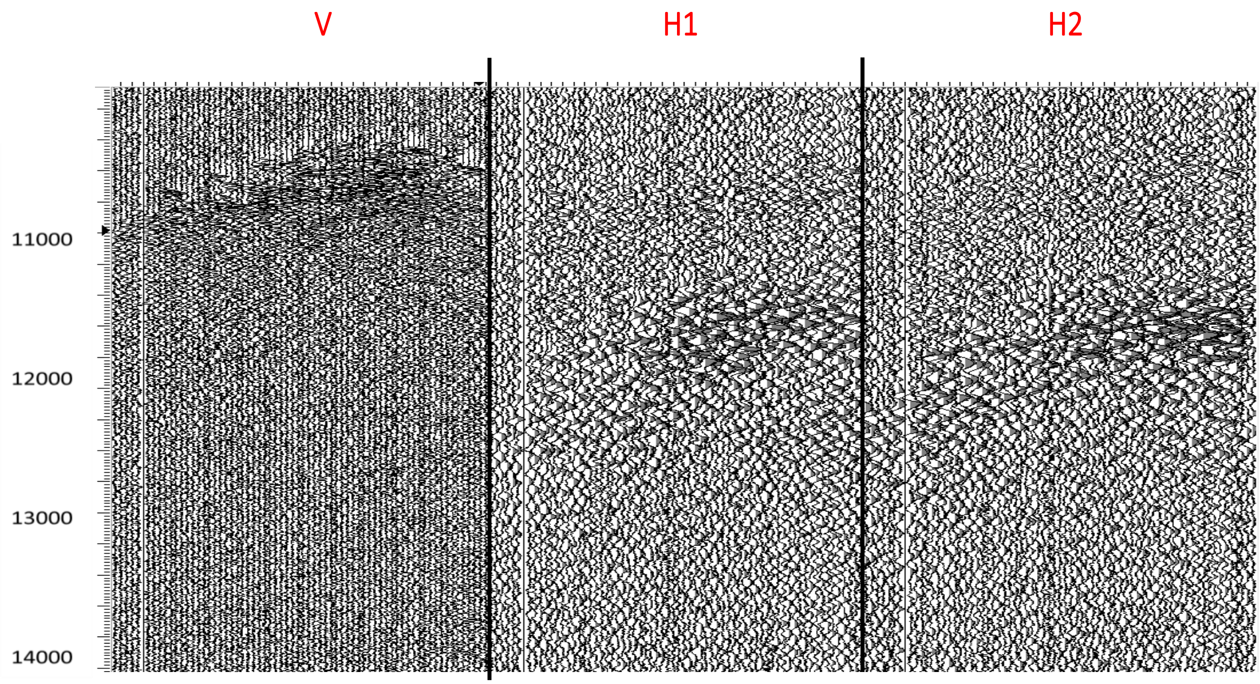


**Figure 4.15.** Record number 24006 processed using deconvolution, filtering, and scaling on V and filtering and scaling on H1 and H2. The P-wave arrivals are visible on the V channel; the S-wave arrivals are visible on the H1 and H2 channels.

Figure 4.16 displays the final test of the field data. In addition to the deconvolution, filtering, and scaling process, random noise attenuation is applied based on the Shearlet transform (Häuser and Steidl, 2014). This record appears to show that the Shearlet transform is reintroducing the cross-feed to the H1 and H2 channels from the incident P-wave. A plausible reason for the appearance of this cross-feed is that the cross-feed is considered to be coherent, not random noise.

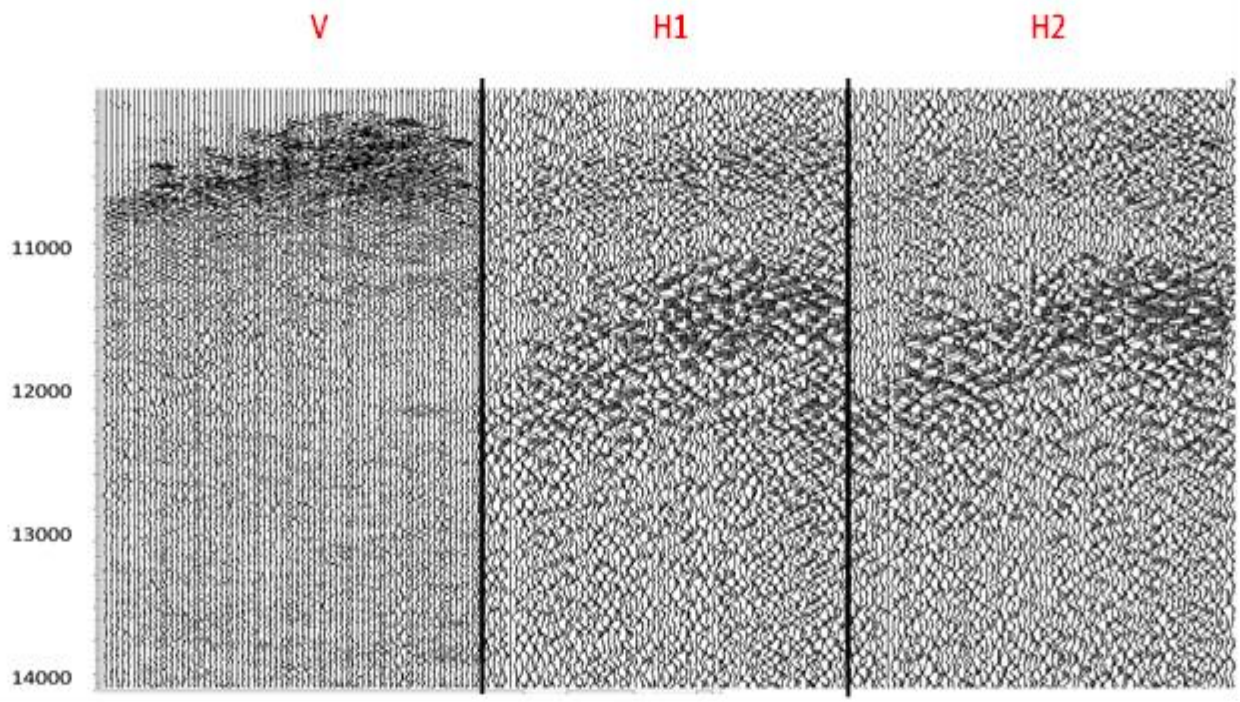


**Figure 4.16.** Record number 24006 processed using deconvolution, filtering, and scaling for V and filtering and scaling for H1 and H2. In attrition, random noise attenuation is applied using the Shearlet transform as described by Häuser and Steidl (2014).

Figure 4.17 is a direct comparison of the raw data to the two test-processing flows, the top being the raw data, the central being the split flow, and the bottom having the random noise attenuation applied. Based on the initial testing, I determine the usable bandwidth of the V channel to be 8 to 65 Hz for the P-wave field. This is compared to P-P reflection data in the same location, which also deliver an 8- to 65-Hz bandwidth.

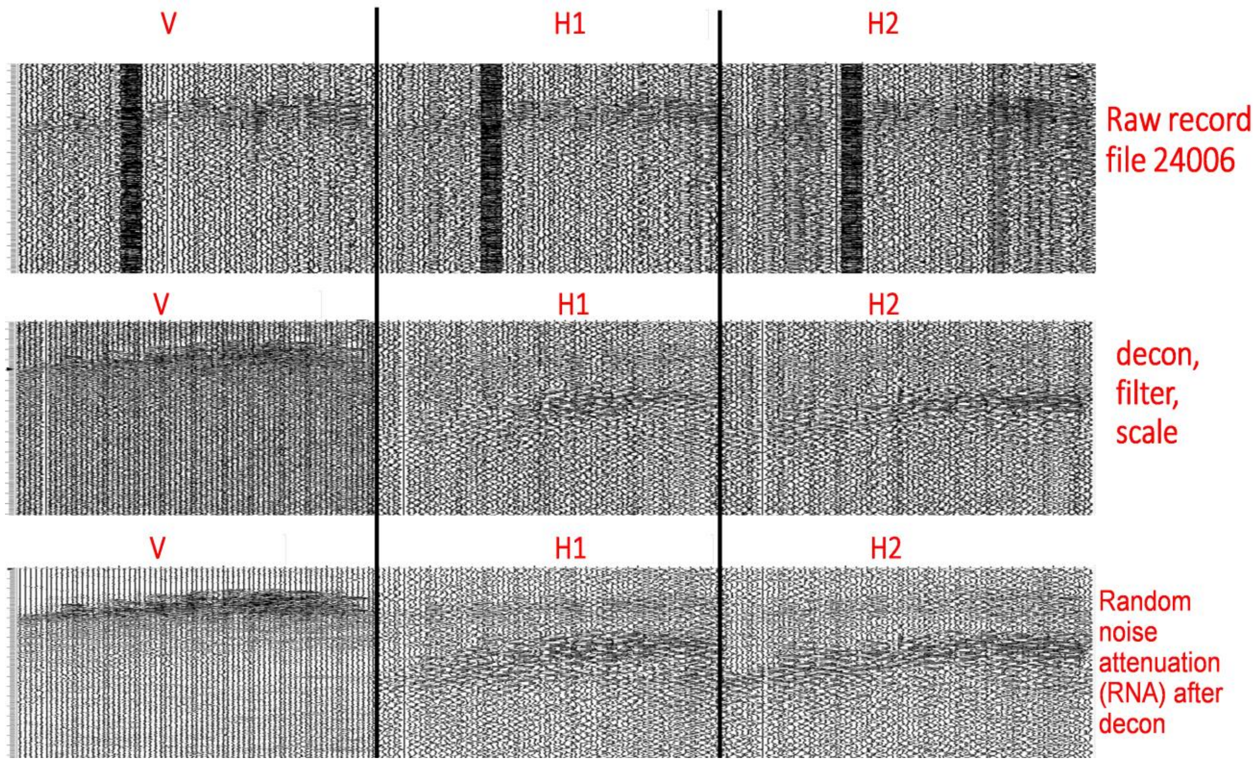


**Figure 4.17.** A comparison of the processing flows tested prior to production processing. The center panel is chosen as a processing flow for the entire data set. The random noise attenuation (bottom panel) leaves some of the cross-feed in the records.

Spectral analysis on the S-wave data indicates most of the signal being contained in the 2- to 12-Hz frequency band. Processes (deconvolution and bandpass filtering) as applied to the P-wave signal are determined to be not applicable to the S-wave data and may actually degrade the S-wave signal. The final filter for the H1 and H2 channels used is 0 to 15 Hz. Figure 4.9 is record 24006 with dual-stream processing applied; the first one-third of the record shows channels 1 to

69, representing the V channel after processing. Channels 70 to 138 are H1, and 139 to 207 are H2 after filtering and scaling.

The processing is split into parallel flows, with deconvolution, filtering, and scaling applied to channels 1 to 69 and with filtering and scaling (no deconvolution) applied to channels 70 to 207. H1 processing includes:

- Deconvolution
- Weiner spiking, 80-ms operator, 1% prewhitening
- Scaling, mean amplitude trace balancing
- Filtering, 8-12-65-75 bandpass

Vertical channel processing includes:

- Scaling, mean amplitude trace balancing
- Filtering, 15-Hz high cut, no low cut applied

This is the processing sequence that is finally used and passed on to the event-picking portion of this project (without the application of any random noise reduction processes). After completion of the testing, the chosen processing flow is run in sequence on the 72 inputs using 80 central processing units (CPUs) and taking approximately 5.5 hours. The results are then restored into their individual files (and names) and output into SEG Y format for review.

This data set is processed on an upgraded IBM server rack using nine nodes. Each node contains two cores, and each core contains six x3650 M4 Intel Xeon multicore processors that support internal processing speeds of up to 3.3 GHz and memory operations up to 1,600 MHz. Each of the 9 nodes has 12 CPUs for a total of 108 CPUs within this configuration. Each of the

9 nodes also has 124 GB of random access memory (RAM) per node and operates on a 10-GHz network switch for faster input/output applications.

### 4.9 Induced seismic event detection

Using a simple amplitude ratio algorithm across a multiple station framework, REDPy detects seismic events from the continuous seismic record and is then able to determine the similarity between events identified using a cross-correlation threshold (Hotovec and Jeffries, 2016). This analysis has already been applied to the ToC2ME data set using the Z component of the 3C station at each borehole (Salvage and Eaton, 2019). Here, I use the same parameters as Salvage and Eaton (2019) to detect seismic events within the ToC2ME data set, but in this case the continuous seismic data undergo a Werner spiking deconvolution (80 ms with 1% prewhitening), filtering (bandpass with corners 8 to 12 and 65 to 75 Hz), and scaling prior to input into REDPy, unlike Salvage and Eaton (2019), who used a simple bandpass filter only.

This chapter focuses on both the events that show similarity between each other in terms of frequency content and waveform shape (repeater events) and events that do not (orphan events), as well as how the events detected compare to those of previous event detection algorithms employed with ToC2ME. The REDPy algorithm for event detection consists of two sliding windows: (1) determining short-term amplitude (STA), which is sensitive to incoming seismic signals, and (2) determining long-term amplitude (LTA) of the signal, which evaluates noise at the given sensor (Withers et al., 1998). Because the trigger is based on the ratio between these two windows, the algorithm is better able to detect weak seismicity compared to a simple amplitude-only trigger mechanism (Trnkoczy et al., 2002).

In order for an event to be detected, the algorithm requires a coincident trigger on at least five stations. This ensures that even small events that may only register on proximal stations are identified, but allows for keeping errors small in the location analysis through a greater number of picks.

**4.10 Results**

Initial results are promising: a total of 17,489 events are identified using the parameters in Table 4.1, compared to 3,711 detected when the only preprocessing is filtering. This represents a five-fold increase in the number of detections using this methodology, a significant improvement over the results using a simple bandpass filter.

| Parameter | Value |
|---|---|
| Stations needed for coincident trigger | 5 |
| Window Length (LTA) | 3 seconds (1500 samples) |
| Window Length (STA) | /*-0.8 seconds (400 samples) |
| Trigger Threshold | 2.5 |
| Trigger Release | 2.3 |

**Table 4.1.** Input parameters for REDPy for event detection using STA/LTA analysis across the entire array.

Figure 4.18 suggests that the number of identified repeating events is similar is each case (maximum of 35 repeating events detected per hour) and that most of the detections within the deconvolved data are orphan events. In fact, the number of repeating events detected is much lower than using a simple filter: the deconvolved data detect 828 repeating events within 31 families over the 28 days analyzed; the filtered data identify 2,033 within 21 families. In both cases, a family of repeating seismicity is defined by having a cross-correlation coefficient of greater than 0.9.

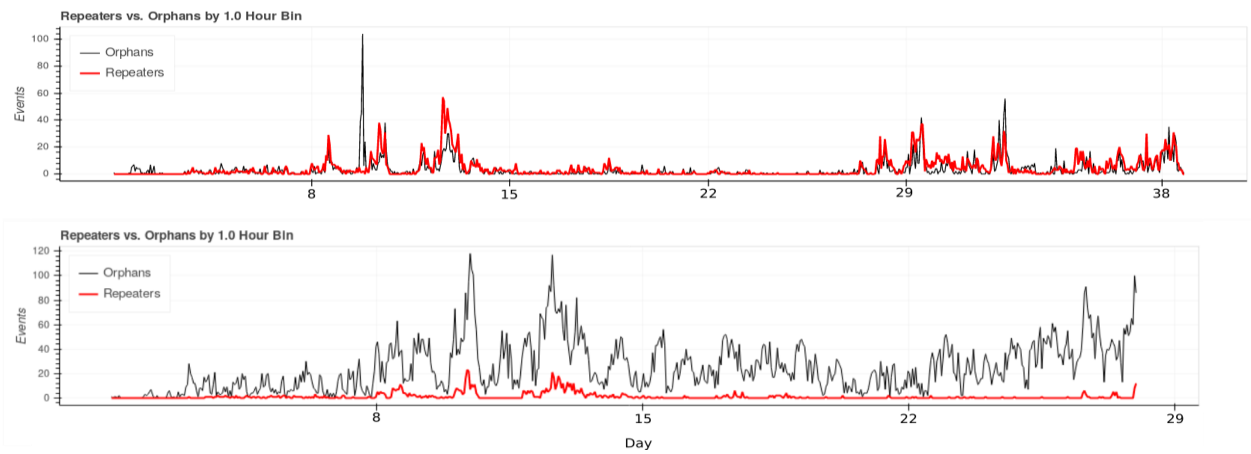


**Figure 4.18.** The number of events per hour detected using REDPy with parameters in Table 4.1, with orphans shown in black and repeaters in red. Upper: data bandpassed filtered between 1 and 70 Hz (see Salvage and Eaton [2019] for further details). Lower: data processed using deconvolution in addition to filtering and scaling. Note that the x-axes are on different scales and so cannot be directly compared.

The evolution of these families with time is shown in Figure 4.19. As expected and as shown by the filtered-only data of Salvage and Eaton (2019), most families have distinctive onsets and cessation points, suggesting that each family occupies a limited location and/or source mechanism and is therefore only “activated” when local stress conditions are optimal for the generation of seismicity.

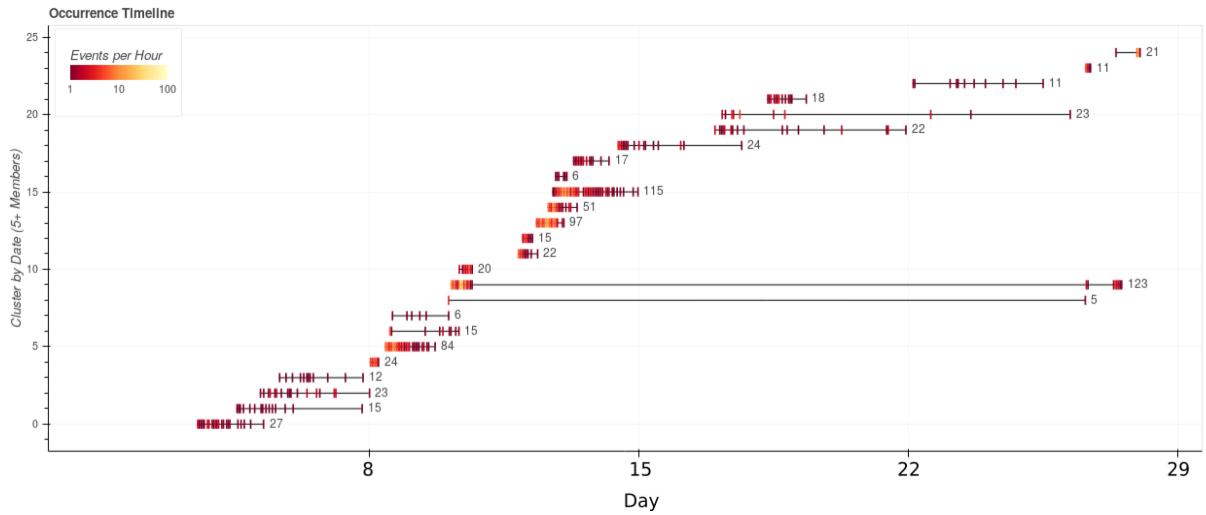


**Figure 4.19.** Temporal evolution of repeating events within the ToC2ME data set using deconvolved data. Each horizontal bar represents one group of repeaters, with events identified on a red-yellow color scale dependent on the number of events occurring per hour (red = few). The number of events per family is shown at the end of the line. Only families with greater than five events per family are shown here.

## 4.11 Conclusions

The results presented in this chapter demonstrate that the use of seismic signal processing can significantly improve the signal-to-noise ratio of continuously recorded seismic data. Processes such as deconvolution and filtering are suitable for data conditioning, and when used with automatic seismic event detection software, show a five-fold increase in the number of detected events. I recommend that these processing steps; deconvolution, filtering, and scaling be routinely applied to enhance seismic event detection. The test here is performed using the REDPy method, based on STA/LTA.. Future work will focus on testing other match-filtering and beam forming methods to see if there are similar results. Another important consideration is to compare the calculated uncertanty in event picking with the processed data (using the RANSAC program), and comparing it with the uncertanty calcaluted on the origional data. The intended goal is a reduceion in the uncertanty, and an improvemt in the accuracy of the hypocenter position.

# Chapter 5[8,9]

## Focal-time estimation: A new method for stratigraphic depth control of induced seismicity

### 5.1 Summary

Focal-time estimation is introduced here as a novel method to obtain robust stratigraphic depth control for induced seismic events or naturally occurring earthquakes. The method requires P- and S-wave-velocity time-depth control from coincident multicomponent seismic reflection data, achieved by registration of correlative P-P and P-S reflections. Event focal depths are initially expressed as the zero-offset focal time (two-way P-P reflection time) and are then converted to depth by leveraging the abundance of data and methods available for time-depth conversion of seismic data. Application of this method requires high-quality P- and S-wave picks, which are extrapolated to zero offset. This approach avoids the necessity to build and calibrate a 3D velocity model for hypocenter location and the determination of accurate absolute origin times. This method also implicitly accounts for factors that are often ill-constrained for most velocity models, such as transverse isotropy of the medium, as these factors similarly affect both the seismic event arrival times and the 3D seismic data. I apply this new method to an induced seismicity data set with events up to a seismic moment magnitude of 3.2, recorded using a shallow borehole monitoring array in Alberta, Canada. Reconciling the seismic-processing data with the

[8] Published in *Expanded Abstracts* 2018, pp. 2977-2981. Society of Exploration Geophysicists, 2018.
[9] Published in *Geophysics* 84, no. 6 (2019): KS173-KS182.

microseismic data is found to be a critical, but not insurmountable, challenge. In contrast to many previous studies of induced seismicity where larger events typically occur in the basement, the inferred foci place induced events stratigraphically above the treatment level.

## 5.2 Introduction

With the increased development in tight oil and shale gas, horizontal well completions using hydraulic fracturing have become commonplace. In specific areas a causal relationship exists between hydraulic fracturing operations and unexpected induced seismicity (Schultz et al., 2017). In order to understand the fault activation process, and for reasons of regulatory compliance, passive recording systems are deployed to monitor hydraulic fracturing programs. These passive rays provide data used for the purposes of estimating stimulated reservoir volume, optimizing completions, and determining best practices for future development.

Focal depth is an important hypocenter parameter that can be helpful to distinguish induced events from natural earthquakes (Zhang et al., 2016). Accurate stratigraphic control on focal depth, such as determining if events are located within the basement, above the injection zone, or within the target zone. Accurate hypocenter determination is also key for interpreting the depth extent of fault zones and/or the extent of the subsurface region affected by stress changes during stimulation (Bao and Eaton, 2016). For regional waveform observations, such detailed inferences are hampered by typical large uncertainties in focal-depth determination using classic travel-time inversion with regional networks (e.g., Schultz et al., 2017).

Detailed interpretations are difficult, given the uncertainties in focal depth, particularly if a surface or near surface sensor array is used (Eisner et al., 2009). Current methods are dependent on the accuracy of the velocity model, which in turn leads to improperly positioned event locations, especially in the areas of strong velocity contrasts (Lomax et al., 2014). Perforation shots can provide time to depth calibration (Maxwell et al., 2010) , however given the noisy environment surrounding a treatment program , perforation shots can be very difficult to detect.

The resolution of focal depth can be significantly improved if near-offset (approximately 1 km or less) microseismic observations are available. In addition, the accuracy of focal depths typically relies on the detection of calibration signals with known locations, such as perforation shots. Calibration data are typically required to develop a velocity model that adequately captures wave propagation effects, including anisotropy.

**5.21 Anisotropy considerations**

Anisotropy is a physical property where the seismic velocity is dependent on the velocity of travel (Lines and Newrick, 2004). Seismic waves generally travel horizontally faster in flat layered sedimentary rocks then vertically (VTI). As a result of this, the CMP stack will generally overestimate the layer velocity, the furthest offsets in the stack being the most affected. As far as the CMP stack is concerned, the derived normal moveout functions used in the stacking process has the combined effect of vertical and horizontal velocities, and is applied in a single moveout correction. Ideally, a walkout VSP could be used to determine which portion of the velocity in the moveout correction is due to the pure vertical component, and which portion is the horizontal velocity component. In our case, the NMO velocity curves are not used for depth conversion; rather, the sonic/density curves from co-located well bores (well “A”) are used to establish the time-depth relationship at the well bore. The microseismic recording arrays deployed here are arranged on the surface as a 3-D array, and are co-located with the 3-D/3-C seismic reflection array. Induced seismic events occurring at depth travel in exactly the same upgoing raypaths as the reflected seismic data. Passive events are subject to the same VTI effects as is seismic reflection data, so a process designed to NMO correct the reflection data are equally valid for induced seismic events at depth. By the same token, the well bore time depth conversion applied to the reflection seismic data are equally applicable to the induced seismic events.

### 5.22 Structural considerations'

Current hypocenter determination methods are dependent on velocity model, which does not take into account variations in subsurface structure, lateral velocity variations, or anisotropy. Areas which have significant structural features such as faults and anticlines create a subsurface profile in which the time-depth field is spatially varying, often quite abruptly. This in turn leads to improperly positioned event locations, which can lead to erroneous interpretations .

## 5.3 Motivation

If a co-located seismic survey is available, a 3-D/3-C volume, then accurately positioned hypocenters for induced[10] seismic events is a powerful seismic interpretation tool. The notion that stratigraphic control on focal depth of induced seismic events is, in many respects, the most important aspect of the event depth. Given coincident seismic control, the ability to position event hypocenters in the seismic image with good resolution and accuracy could represent a powerful interpretive tool. The choice of two-way time as the primary parameter, rather than depth is

---

[10]The term "induced" implies that a seismic event is anthropogenic, triggered by human activity

natural, as wavefields for both microseismic events and seismic reflections propagate within the same medium. Moreover, the intermediate step of accurately positioning hypocenters within time-domain seismic volume enables the use of existing methods for time-depth conversion of the seismic data. Figure 5.1 shows the 3D seismic coverage, the co-located ToC2ME passive seismic array, and the position of the treatment wells.

The focal-time method outlined here is data-driven that does not require calibration shots or the construction of a velocity model. The method requires the joint interpretation of passive seismic, and 3-C/3-D reflection seismic, therefore is limited to where both of these types of data are co-located. It implicitly accounts for factors that are poorly constrained in microseismic processing such as anisotropy and lateral velocity variations due to structure. The following section outlines the basic theory, the application followed by a case study in western Canada over an area of active field development.

**5.4 Theory**

I begin by outlining the basic theory. Next, I describe the workflow and apply this approach to a case study within a region of active drilling, hydraulic fracturing, and induced seismicity near Fox Creek, Alberta. This study makes use of continuous data recorded using a shallow-well microseismic array, with a co-located 3D multicomponent reflection survey (Eaton et al., 2018; Weir et al., 2018). Figure 5.1 outlines the 3-D/3-C seismic array, the co-located microseismic array, and the microseismic array down hole configuration. For display purposes, a time structure map is displayed on the Swan Hills Formation time structure surface; this display also serves to show the extent of the 3-/3-C reflection survey. The microseismic array is plotted with triangles on top of the Swan Hills Formation time structure map.

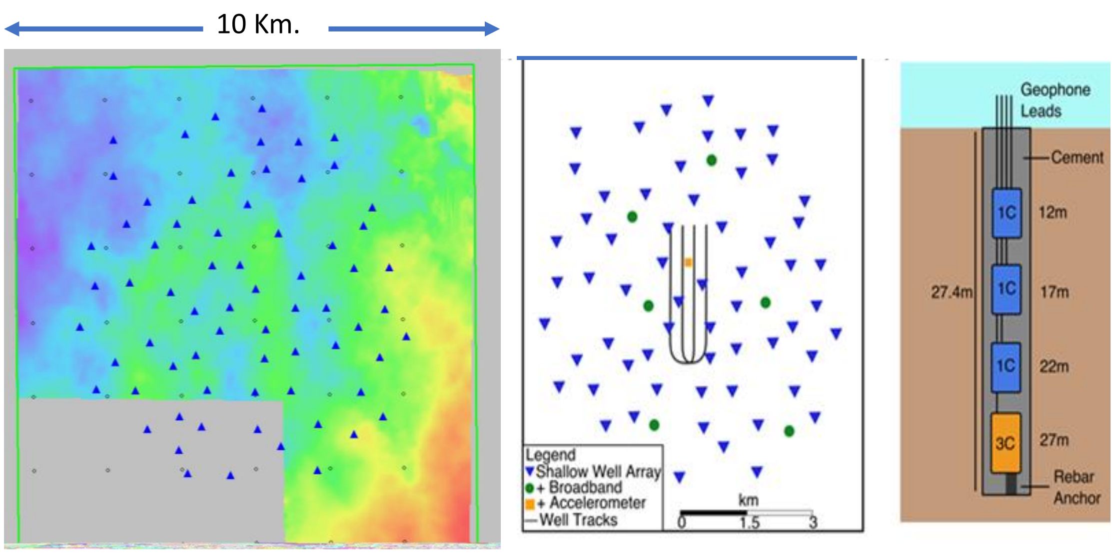


**Figure 5.1.** Left: 3D time-structure map of the Swan Hills Formation, showing the extent of the 3D and the co-located passive seismic array. Center: location of the treatment wells. Right: configuration of the downhole geophones.

Within a continuously recorded data stream, a seismic event (natural, or induced) is generally observed as a compressional wave *(qP)* , followed by a shear wave arrival (*qS*). The *q* prefix denotes quazi-P and quasi-S waves, in that there exists the potentially strong anisotropic effects within unconventional play areas (Ong et al., 2016).

For a microseismic event, the arrival times for *qP* and *qS* waves can be expressed as:

$$t_P(x_S, x_R) = t_0 + \int_{L_P} \frac{dx\prime}{V_P} \quad , \qquad (5.1)$$

and

$$t_S(x_S, x_R) = t_0 + \int_{L_s} \frac{dx\prime}{V_S} \quad , \qquad (5.2)$$

where $x_s$ is the event location, $x_R$ is the receiver location, $t_0$ is the origin time, $V_P$ and $V_S$ are the $qP$ and $qS$ velocities along the path, and $L_P$ and $L_S$ represent the respective raypaths from the source to the receiver. The origin time can be eliminated by taking the travel-time difference,

$$t_S - t_P \approx \frac{|L_S|}{\langle V_S \rangle} - \frac{|L_P|}{\langle V_P \rangle} \quad , \qquad (5.3)$$

where $<V_P>$ and $<V_S>$ denote the average velocities along each path. If I make the approximation that $|L_S| = |L_P| = |L|$, then this can be written as:

$$t_S - t_P \approx \frac{\langle V_P \rangle - \langle V_S \rangle}{\langle V_P \rangle \langle V_S \rangle} |L| \quad . \qquad (5.4)$$

At the event epicenter (i.e., at a surface location vertically above the hypocenter), this is the zero-offset time difference, $\Delta t_M$, which is given by:

$$\Delta t_M(\Delta = 0, z') = \frac{\langle V_P \rangle - \langle V_S \rangle}{\langle V_P \rangle \langle V_S \rangle} z' \quad , \qquad (5.5)$$

Where Δ denotes the offset (distance to the epicenter), the distance, and where *z'* is the focal depth of the event.

Next, I consider the two-way time for a P-P reflection from depth *z*, where *z* is the interface depth. This can be expressed as

$$t_{PP}(z) = \frac{2z}{\langle V_P \rangle} = \frac{2\langle V_S \rangle}{\langle V_P \rangle \langle V_S \rangle} z \quad . \qquad (5.6)$$

Similarly, the P-S reflection time is given by

$$t_{PS}(z) = \frac{z}{\langle V_P \rangle} + \frac{z}{\langle V_S \rangle} = \frac{\langle V_P \rangle + \langle V_S \rangle}{\langle V_P \rangle \langle V_S \rangle} z \quad . \qquad (5.7)$$

I can therefore write the difference between $t_{PP}$ and $t_{PS}$ as:

$$\Delta t_S(z) = \frac{\langle V_P \rangle - \langle V_S \rangle}{\langle V_P \rangle \langle V_S \rangle} z \quad , \qquad (5.8)$$

which has the same form as the expression for $\Delta t_M$. Equations 5.5 and 5.8 can both be regarded as parametric equations that are monotonically increasing functions of the depth parameter *z*. This suggests a simple algorithm for estimation of focal depth by determining the depth at which $\Delta t_M = \Delta t_S$. In practice, it is convenient for the parametric results to be converted back into $t_P$ to enable co-rendering and visualization of the microseismic events with the time-domain seismic data. As described below, this process requires the use of the same datum for both microseismic and seismic travel times. In general terms, it is expedient to deploy this method in terms of a two way P wave travel-time (focal time), as opposed to using depth. Working in terms of travel time facilitates the interpretation of passive and reflection events simultaneously, with no additional errors introduced during the depth conversion process.

**5.5 Method**

The requirements for implementing this method are as follows:

1. A 3-D/3-C reflection survey encompassing the extent of the microseismic recording array. These data are processed as P-P and P-S prestack time migrated volumes.
2. A sonic log, located within the 3-D survey; (preferably density and shear wave (dipole ) logs as well) from surface casing to a depth greater than the target formation. The synthetic seismograms generated from these logs are used to establish time depth relationships for both the P-P and P-S volumes
3 A source fie for induced events, including pick times, event epicenter locations, and receiver coordinates. In order to implement this method, it is necessary to register P-P and P-S reflections (i.e., identify equivalent reflections in both sections) so that $\Delta t_S$ can be computed. The ratio of $V_P/V_S$ emerges as a useful byproduct of this event registration process based on the Garotta equation (Garotta and Grange, 1987):

The workflow used in this study can be summarized as follows:

1. Establish the time-depth relationship in the P-P domain. This can be achieved using various approaches (e.g., using a synthetic well log tie, a vertical seismic profile, or checkshot data).

2. Register P-S reflections by correlating them with stratigraphically equivalent P-P reflections.
3. Use the section registration from step 2 to determine an empirical relationship for $\Delta t_S$ as a function of $t_{PP}$, where $\Delta t_S$ is defined in equation (5.8). If 3D/3C data are available, they can be stored in a spatially varying lookup table.
4. Pick $t_S$ and $t_P$ values for each microseismic event.
5. Determine the zero-offset time difference, $\Delta t_M$. Because the move-out is approximately hyperbolic, a linear regression can be performed based on $t^2 - x^2$ analysis of the pick times. $\Delta t_M$ can then be calculated from the difference between the square roots of the intercept values.
6. Apply time shifts to adjust $\Delta t_M$ to the seismic data.
7. Assign a $t_{PP}$ for each event by interpolating $\Delta t_M$ using the lookup table for $\Delta t_S$.
8. Optionally, convert the calculated focal times into depths by leveraging an existing method for time-depth conversion of seismic data. Figure 5.2 illustrates the first step in the method. The well log is converted to time and generates a synthetic and is then tied to the P-P reflection data. This time-depth relationship is used in the hypocenter calculation.

A preliminary estimate for the registration of P-P and P-S data is established by making assumption as to the *Vp/Vs* ratio. Often, a Vp/Vs ration of 2.0 will serve as an initial estimate, resulting in a *Ts/Tp* ratio of 1.5 (in the time domain), as calculated using equation 5.9.

$$\frac{V_P}{V_S} = 2\left(\frac{t_{PP}}{t_{PS}}\right) - 1 \quad . \qquad (5.9)$$

In a practical sense, plotting the P-P seismic section at 15 inches per second, and the P-S seismic data at 10 inches per second provides a qualitative control (visual) step to the data registration.

A more rigorous method for data registration is to tie the reflection seismic data using P-P and P-S synthetic seismograms generated from a dipole sonic log (Lawton and Howell, 1992). This involves matching the bandwidths of the synthetic seismograms to that observed in the reflection data. Processing converted wave (P-S) and (P-P) data requires the calculation of an explicit velocity model, including NMO corrections and migration (these velocity data are not used to locate microseismic hypocenters). The 3-D velocity models derived from reflection seismic data processing do not provide usable interval velocities therefore are not suitable for calculating hypocenter locations (Cameron et al., 2007).

With the equivalent horizons correlated on the P-P and P-S seismic sections, these events are picked over the entire seismic volume, with $X$,$Y$, and $t$ values (northing, easting, and reflection time) cataloged for multiple horizons. These data are used to build a lookup table comprising $t_{ps}$ – $t_s$ arrivals time and directly relating these to $t_{pp}$ time. A smoothed interpolation is used because the $t_{ps}$ and $t_{pp}$ times are derived from average velocities, and therefore will be smoothed functions in depth. The lookup table uses a spline interpolation to fit data control points between each of the picked horizons ensuring that there is continuous data between horizons. Having picked multiple horizons throughout the entire 3-D volume for both P-P and P-S data, varies with the x and y positions over the entire seismic volume. This method ensures that heterogeneity in velocity (structure) and anisotropy (VTI) are accounted for.

The calculation of $\Delta t_m$ is performed by using an $t^2$-$x^2$ method; x where is the distance to the epicenter *(*$\Delta x$*)* and $t$ is the travel time. As with reflection seismic data in a layered media, the moveout for microseismic events recorded by the surface array is approximately hyperbolic. A plot of $t^2$-$x^2$ will generate a nearly linear relationship for the respective time picks. At $\Delta x = 0$ (the epicenter), the linear uncertainty is calculated based on a regression analysis.

A static and low velocity layer correction is applied to the microseismic hypocenters to reference them to the same datum as the reflection seismic. Land reflection seismic data is referenced to a seismic datum, generally at an elevation higher than the receiver array. A vertical raypath assumption is used to adjust the reflection data to the seismic datum from the surface using an arbitrary replacement velocity; this datum correction puts time “0” at the seismic datum and shifts the P-P and P-S reflections downward in time (a static shift). If the microseismic sensor is located below the surface, the datum correction needs to be applied followed by a correction to account for the depth of the buried geophone.

The two processing streams are combined to obtain a focal time estimate for each event. Here , the $\Delta t_M$ values (with the adjusted time datum) are correlated to the lookup tables at the event epicenters, the $\Delta t_M$ values are mapped to their corresponding $t_{\mathrm{pp}}$ values. Linear regression is used, with a 95 % confidence threshold to establish a valid data point. With the microseismic data and the reflection seismic referenced to the same datum, the location of microseismic events are established within the reflection time framework, and are ready for joint interpretation.

For the case study, the time to depth reationship is established using well control (well "A"), a sunthetic seismogram is tied to the data, providing an accurate time to depth relationship at the wellbore. The same time to depth relationship is applied to the hypocenters as to the reflection seismic data. This ensures that the relationship of hypocenter to seismic reflection in time, is maintend in depth.

### 5.6 Case study

For the case study considered here, the formation of primary interest is the Devonian-age Duvernay Formation. This unit is overlain by the Ireton Formation and overlies Swan Hills Formation. The Duvernay is drilled and completed using horizontal drilling and hydraulic fracturing techniques. Numerous microseismic and induced seismic events are recorded at these depths and are used in this study. The recordings are captured using a 68-station, shallow-buried microseismic array, which covers an area of 60 $km^2$ over the treatment site (Eaton et al., 2018). A 3D multicomponent seismic reflection survey is located above the treatment site as well and encompasses the area of the microseismic array (Weir et al., 2018). The P-P seismic data is tied to a wellbore containing sonic and density data from the surface casing to the Devonian Gilwood Formation, approximately 300 meters deeper than the Duvernay formation target interval. Figure 5.2 shows the synthetic seismogram, the tie to the reflection data, and the time to depth relationship.

The microseismic data are from the Tony Creek dual Microseismic Experiment (ToC2ME) acquired in the fall of 2016 (Eaton et al., 2018). The sensors (geophones ) are comprised of a 3-C 10 Hz geophone at a depth of 27 meters, as well as vertical geophones positioned at 12, 17 and 22 meters. The 68 stations are positioned in a 3-D array around the horizonal treatment wells. Microseismic data was recorded before, during and after the four well horizontal treatment wells were treated with hydraulic fracture stimulation. During the fracture stimulation, anomalous seismic activity (induced seismic events) were detected (Bao and Eaton, 2016; Schultz et al., 2017). There were 13,016 detected induced seismic events, which are used in the analysis presented here. The events were selected (catalogued) based on repeatability, using a criteria of a minimum of 10 stations per event. In addition, the signal to noise ratio was selected to be greater than 3.0. The epicenters are assumed to be located at a position where S-wave arrival has a minimum travel time. The travel time is interpolated between stations to provide finer spatial resolution. The interpolation is designed to be finer than the bin size of the reflection seismic recording (25 meters is used). Efforts were made to resolve perforation shots, but none were readily observable within this data set. Efforts to recover these shots (as described in chapter 4) were unsuccessful. In the absence of perforation shot calibration, depth uncertainties may be unusually large when conventional travel time-based methods (i.e. 1-D velocity models) are used to determine microseismic hypocenters.

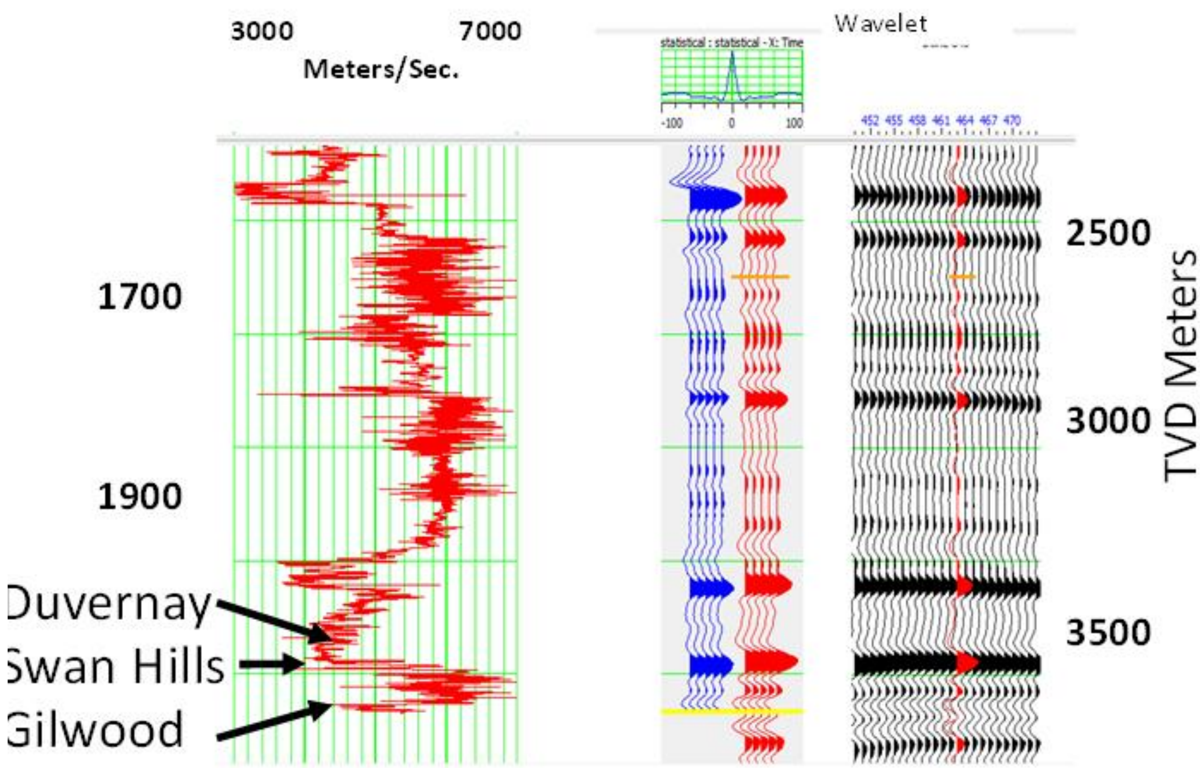


Figure 5.2. Synthetic seismogram correlation. The synthetic seismic trace (blue) is generated and correlated to the seismic reflection data at the well location. The synthetic seismogram is bulk-shifted and stretched to match the reflection data at the wellbore location.

The distribution of receivers used for microseismic monitoring (68 stations) produces a recording geometry with observations at lateral distances (offsets) of hundreds or thousands of meters from the epicenter. For each microseismic event, the location of the epicenter is determined by finding the surface location corresponding to the minimum S-wave travel time. The picked S-wave arrival-time values are interpolated to a fine spatial grid to provide good resolution of the epicenter, with an estimated uncertainty of 25 m in easting and northing. As mentioned earlier, the hypocenter is assumed to lie vertically below the epicenter (which is considered to be reasonable for this area where layers are very close to horizontal). The radial offsets of the stations with respect to the epicenter are then calculated for each event. Offsets greater than 3000 m are removed, as they show evidence of refraction at depth.

Figure 5.3 illustrates step 2 of the methodology, the P-P to P-S registration. This registration provides a $t_{PP}$ -$t_{PS}$ relationship and, in turn, a $V_P$-$V_S$ relationship. $t_P$ and $t_S$ horizons are output to provide a velocity relationship (lookup table) through the entire 3D volume. This registration process used here is described in chapter 2 (2.52) where the data was registered and used for joint inversion . The travel time picks shown in figure 5.3 are used to create the lookup tables as input for the hypocenter depth determination.

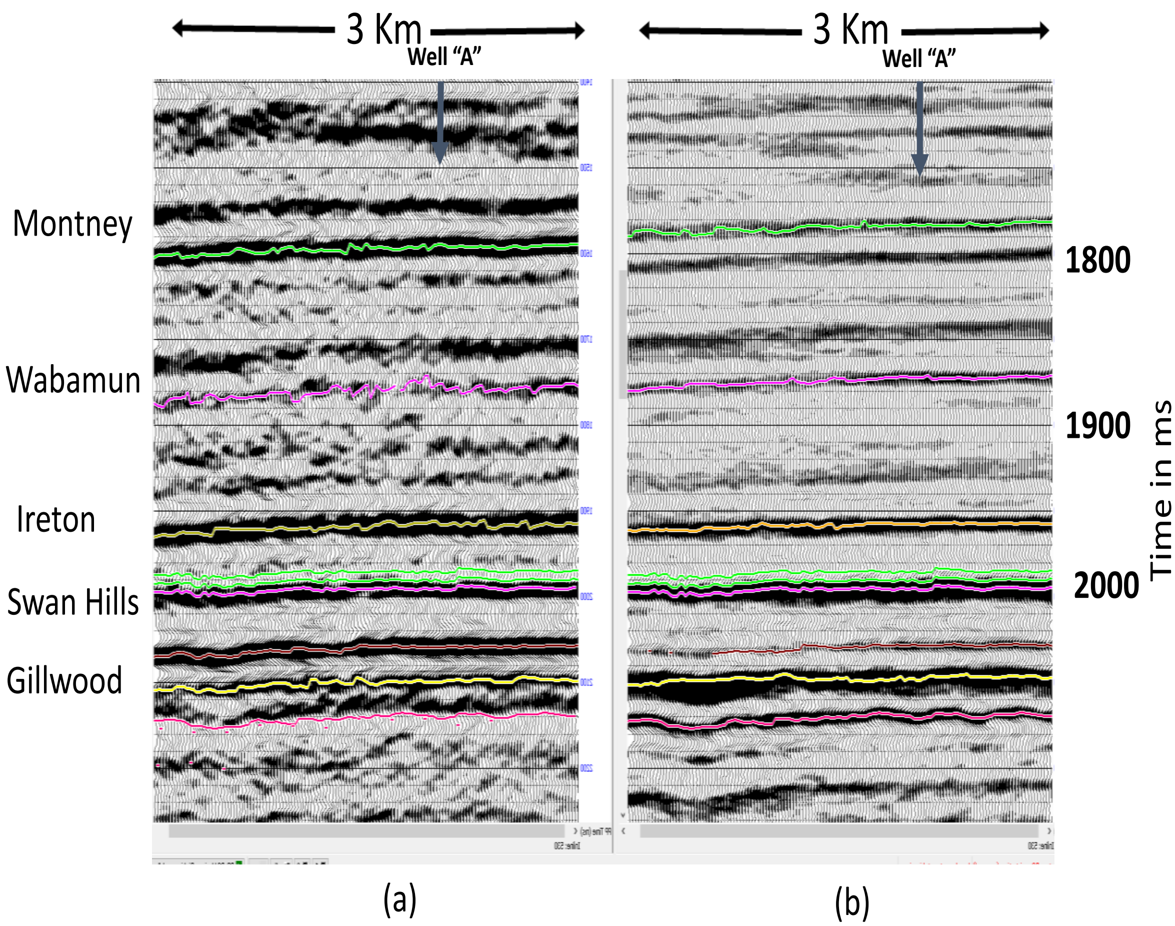


**Figure 5.3.** Registration of P-P and P-S reflections. (a) P-S data, (b) P-P data, showing the horizons used for the calibration. The P-S data (a) is displayed in P-P time.

Figure 5.4 is a seismogram showing four induced seismic events of varying magnitudes, as recorded in a continuous data stream These individual events have been plotted such that the P wave arrival occurs at 1.0 seconds, the S wave occurring just before 2 seconds. The signal to noise ratio is highest for trace 4, and lowest for trace 1. These recorded events are examples of events that are catalogued and output as seismic events. The focal-time method uses these $T_p / T_s$ interval values to calculate the event hypocenter .

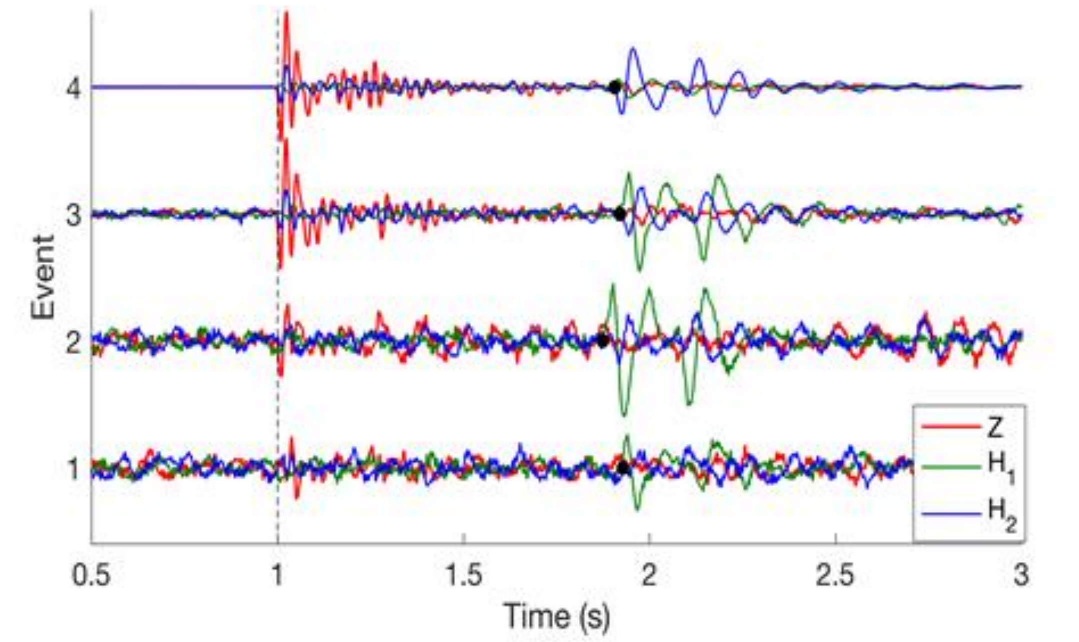


Figure 5.4. Comparison of the raw waveforms and quality of P- and S-wave picks at one station. Traces are approximately aligned on the P-wave (the dashed line), and the S-wave is marked with a black circle. Event 4 represents a high-S/N event (MW ~ 1.0), and event 1 is a low-S/N event (MW ~−0.2). The terms Z, H1, and H2 denote the vertical and unrotated horizontal channels (courtesy, Poulin et al, 2019)

To determine $\Delta t_M$, a linear regression is applied based on $t^2 - x^2$ analysis, as illustrated in Figure 5.5. Because the data contains erroneous $t_P$ and $t_S$ picks, those that deviate from the regression line by more than one standard deviation are discarded, and the regression is repeated. The value for $\Delta t_M$ is then calculated from the difference between the square roots of the intercepts. This value is used to obtain a $t_{PP}$ estimate for each event, as outlined in step 7 in the workflow.

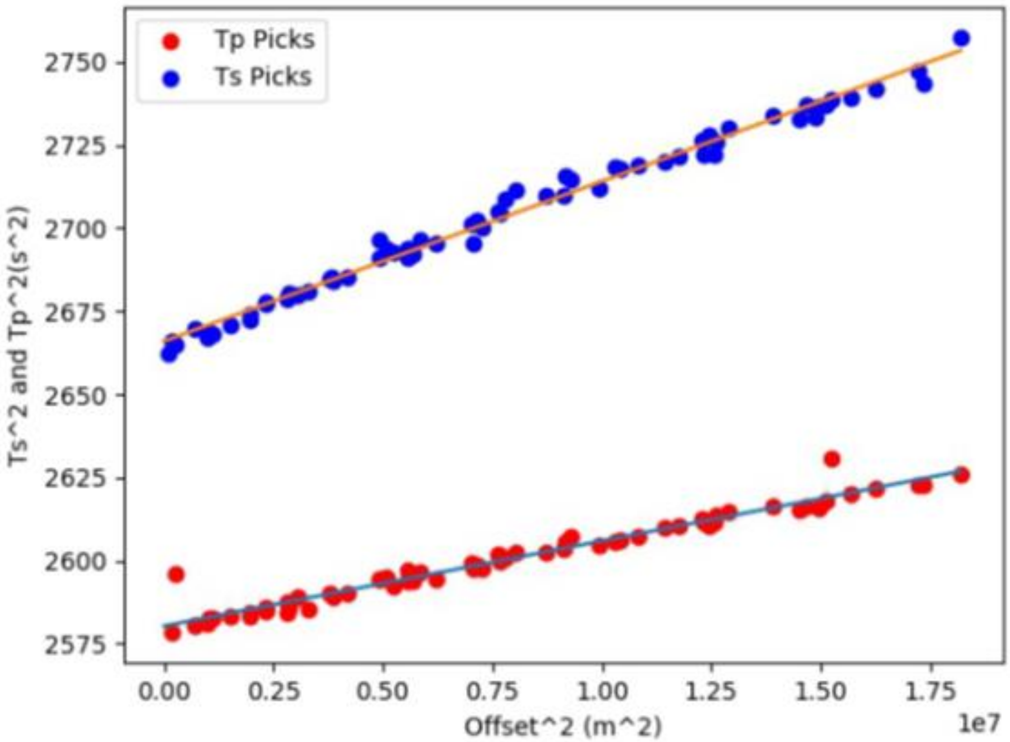


Figure 5.5. Graph showing $t^2 - x^2$ analysis and regression method used to determine $\Delta t_M$. These are the microseismic time picks, the S arrivals are blue, and the P arrivals are red. Outliers beyond 95% are considered to be erroneous picks and discarded.

The Tp and Ts picks in Figure 5.5 shows the linear regression applied to determine zero-offset. The RANSAC algorithm (random sample consensus, Meer et al., 1991) is used to discard statistical outliers in the data. The largest source of uncertainty is from errors in the *qP* and *qS* time picks, therefore it is necessary to perform error analysis on the data. A RANSAC analysis is applied to determine the 95% confidence limit for *qP* and *qS* intercept errors. These errors in the time are calculated to be a mean error in $t_{pp}$ of 36 ms for the entire data set of 13,105 events, equating to an uncertainty in $t_{pp}$ of approximately 25 ms.

An example of the $t_S - t_p$ time grid from the Swan Hills is shown in figure 5.6 shown in a spatial context. These were calculated for several horizons, and used the calibrate the $t_S - t_p$ time picks derived from the microseismic catalogue. What is noteworthy, is the variation in values in $t_S - t_p$ time from SE to NW across the study area

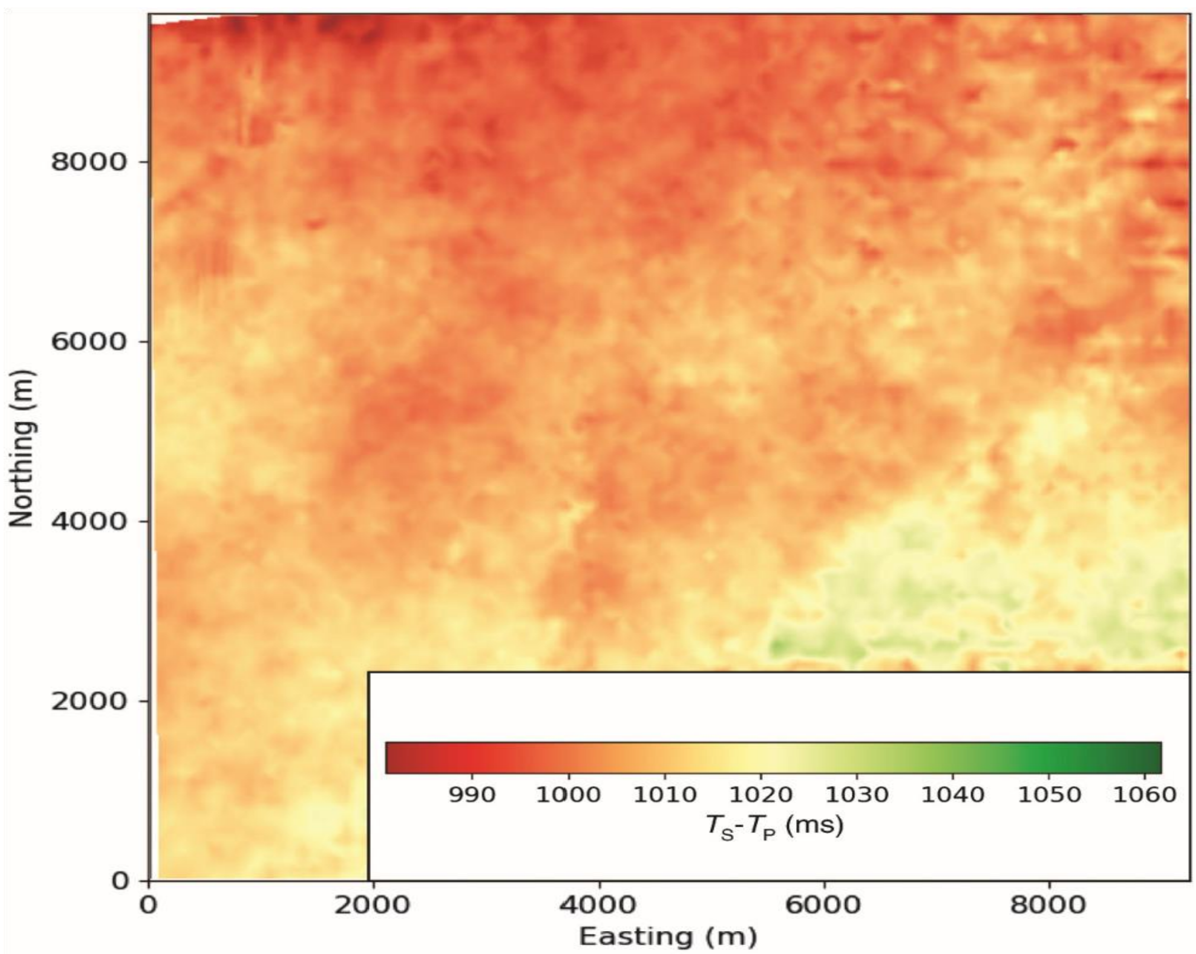


Figure 5.6. Example of a $t_S - t_P$ time grid calculated from the 3D seismic data volumes. The horizon shown is the top of the Swan Hills Formation, which directly underlies the zone of interest (the Duvernay Formation). Spatial coordinates represent relative northing and easting values (courtesy Poulin et al., 2019).

An example of how the lookup table is used is shown in figure 5.7. Two examples of $t_S - t_P$ times are displayed, showing how these detected seismic events convert to depth using our method. This depth calibration method is applied to all 13,016 seismic events in our seismic catalogue.

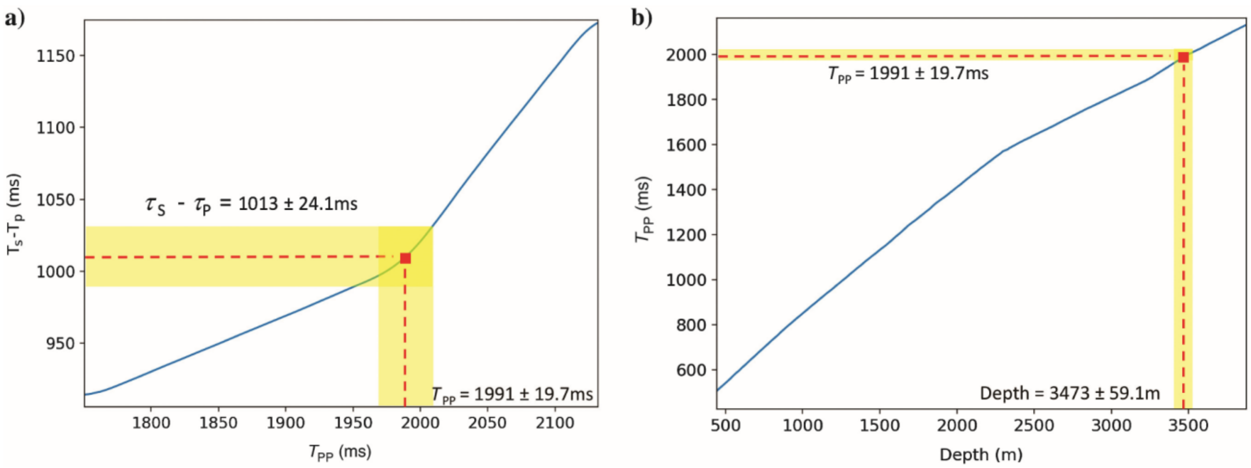


Figure 5.7. (a) Application of a lookup table constructed by spline interpolation of $t_S - t_P$ times measured from 3D multicomponent seismic data. The yellow region shows the 95% confidence interval for $\Delta\tau_M$ ¼ $\tau_S - \tau_P$, based on the linear regression analysis of the microseismic time picks (Figure 5.4). This region is used to obtain corresponding uncertainty estimates for focal time. The graph on (b) illustrates conversion of the P-wave time to depth below the seismic datum. (courtesy Poulin et al, 2019)

To apply data corrections to the $\Delta t_M$ time picks, the corrections for the near-surface layer are made at the epicenter location, which has a known topographic elevation and near-surface-layer thickness. The applied static corrections for P- and S-waves are the same as the receiver statics from the 3D seismic processing. However, because the microseismic geophones are buried to 27 m, a further correction is added based on the calculated one-way S-wave time from 27 m to the surface, based on the near-surface S-wave velocity assumption.

As a basis for comparison, the seismic event catalog is processed using NonLinLoc[11] (Lomax et al, 2014), a probabilistic non-linear global search program. ). Using a systematic grid-search algorithm, NonLinLoc generates a maximum likelihood hypocenter location based on the estimated posterior probability density function for each event. NonLinLoc was applied using a 1D velocity model, derived from smoothing well-log sonic slowness (Δt) curves. The logs used are located 1.5 km southeast of the 3D survey (Well “B”). There were no shear wave logs available within the 3-D volume.

[11] Non linear location determination

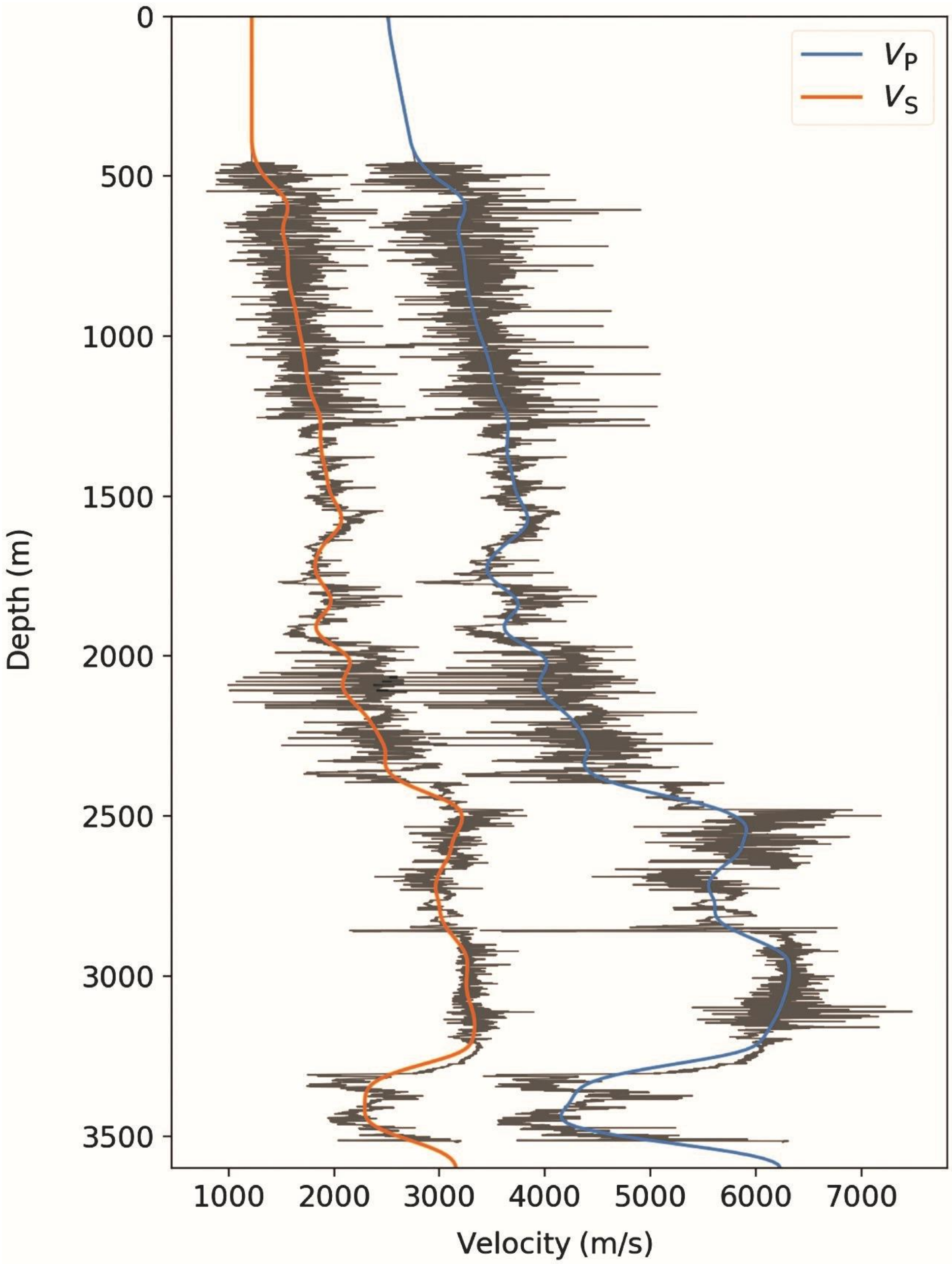


Figure 5.8. Well-log-derived P- and S-wave velocities (from well "B"), showing the smoothed model used to calculate hypocenter locations using NonLinLoc. The velocities were derived by running a median smoothing filter over the sonic slowness curves. The well is located approximately 1.5 km southeast of the 3D seismic survey. A 1D (horizontally layered) model is justified here due to the nearly flat layering in the study area (Weir et al., 2018).

### 5.7 Results

Hypocenter locations derived from focal-time are compared to those derived from NonLinLoc in figure 5.9. The treatment interval is approximately 3540 meters, the calculated event catalog is concentrated in a range from 3200 to 3600 meters. The focal time catalog brackets the treatment interval as seen in Figure 5.9a. The hypocenters derived from NonLinLoc are concentrated above the treatment interval, at approximately 3300 meters (Figure 5.9b).

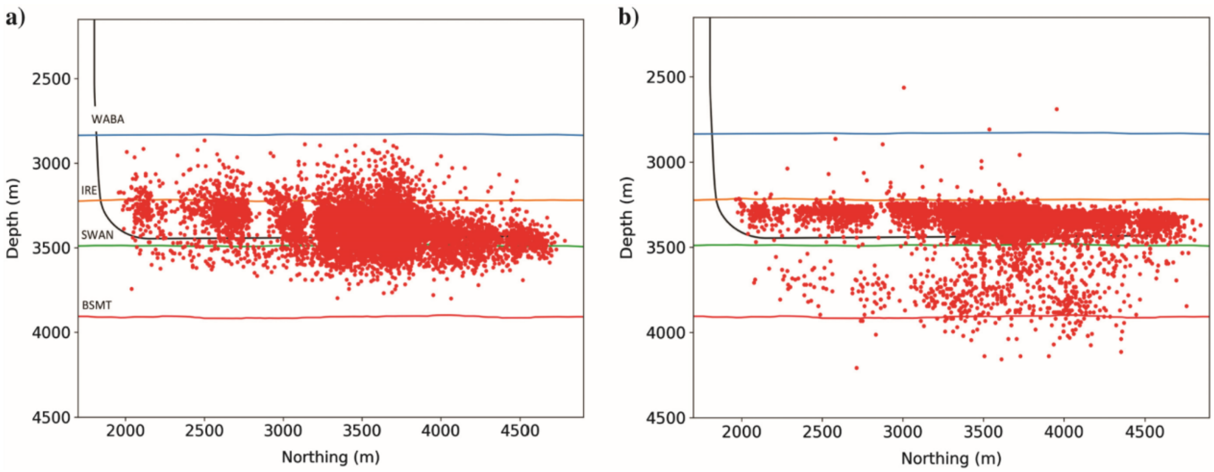


Figure 5.9. Depth distribution of events, with the treatment well and seismic horizons outlined. (a) Depths obtained using the focal-time method. (b) Depths obtained using the NonLinLoc package (Lomax, 2018), for comparison with the focal-time results. The events contained in the current catalog lack operationally induced microseismicity (Eaton et al., 2018), which would have generally lower magnitude and would be expected to cluster at the same depth as the horizontal wellbore. For the focal-time and NonLinLoc results, most of the induced-seismicity hypocenters plot above the treatment level, similar to other programs in this area (Eyre et al., 2019). The NonLinLoc hypocenters were obtained using a 20 m grid with the smooth 1D velocity model shown in Figure 5.8. (courtesy Poulin et al., 2019)

A map view of the hypocentres is shown in figure 5.10, a conspicuous north-south linear trend west of the treatment wells is observed (Cluster 4, blue). These events are linked to a strike slip activation of a pre-existing fault (Zhang et al, 2019).Within this event cluster, a Mw 3.2 induced seismic event was recorded, as well as several events with magnitudes greater than Mw 2.5 (Igonin et al., 2018). Based on the event histograms, these north-south trending events are centered approximately 90 meters above the treatment interval, putting them within the Upper Ireton Carbonate, or the carbonates of the lower Winterburn Group. The green cluster, (4) and the unnumbered grey events show a distinct lineation of approximately 30° W of North, with the histogram centered on the Duvernay Formation treatment zone. These 30° lineations are interpreted to be the result of reactivated Riedel shear faults (transcurrent faults) , associated with deep-seated strike slip movement. Shen, (2019), in a regional study determined that the SHmax in the Duvernay Formation was 43° East of North, which was the expected orientation of hydraulic fracture propagation. This is in stark contrast to the observed orientation of fracture propagation, and leads to the interpretation of Riedel shear fault reactivation as a response to the hydraulic fracture stimulation. Cluster 5, (marked in red) shows a distinct N-S alignment, and is centered on the Duvernay Formation treatment interval. These are aligned with a mapped N-S strike slip fault at the East side of the treatment wells. These observations, from the depth, position, and orientation of the event clusters indicate that the focal-time method generates cluster specific results, that can be incorporated into a comprehensive seismic interpretation of the subsurface.

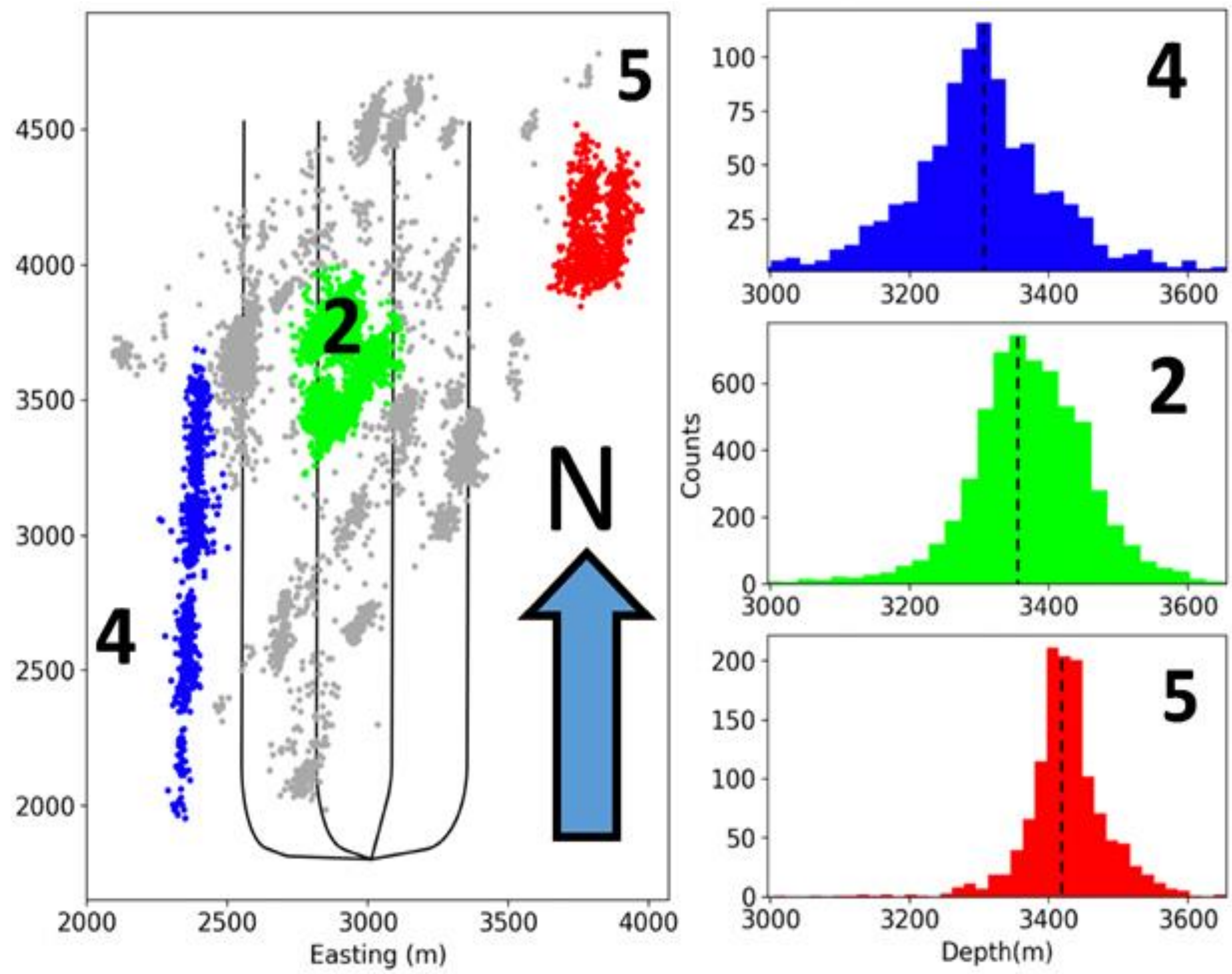


Figure 5.10. (a) Map of epicenters of the 13,105 located events highlighted three clusters. (b) Depth histograms of the highlighted clusters. The dashed black line indicates the mean depth in each cluster. The horizontal treatment well is at approximately 3450 m in depth. fault that crosscuts the Duvernay Formation (Eaton et al., 2018). Although this cluster is approximately 300–400 m east of the nearest treatment well, the focal depths of these events lie close to the depth of the hydraulic-fracturing fluid injections. Taken together, these observations demonstrate that the focal-time algorithm yields coherent, cluster-specific depths. (courtesy Poulin et al., 2019)

**5.9 Discussion**

. Focal time eliminates much of the uncertainty associated with hypocenter determination, however the uncertainty associated with the P and S event picking from the microseismic catalogue is still a factor. An average 95% uncertainty in focal time equates to approximately 89 meters of geological section. The thickness of the Duvernay Formation is in around 50 meters, less than the estimated uncertainty from the hypocenter catalog. . The uncertainty in the zero intercept times arises as a result of the regression analysis, which explains much of the observed scatter in depth distributions. NonLinLoc, used for benchmarking was undoubtably impacted by the accuracy of the velocity model; it was not constrained by calibration shots or any other kind of direct time to depth calibration due to the noisy character of the S wave arrivals. It is also impacted by A 1-D model such as this is derived strictly from well log data, and does not take into account heterogeneity arising from faults, damage zones, reef edges, and a regional dip of several degrees (Weir et al., 2018). As with focal-time, the uncertainty associated with the P and S event picking from the microseismic catalogue is a factor The presence of 3-D Velocity heterogeneity is implicitly incorporated into the focal-time solutions, as is subsurface structure, including lateral variations such as vertical faults. The focal-time solution also benefits from the statics and weathering layer solution derived from the seismic reflection data.

In Figure 5.7, the calculated focal-time hypocenters (the red data points from Figure 5.6) are superimposed onto the migrated 3D P-wave seismic data cube. The tracks of the four

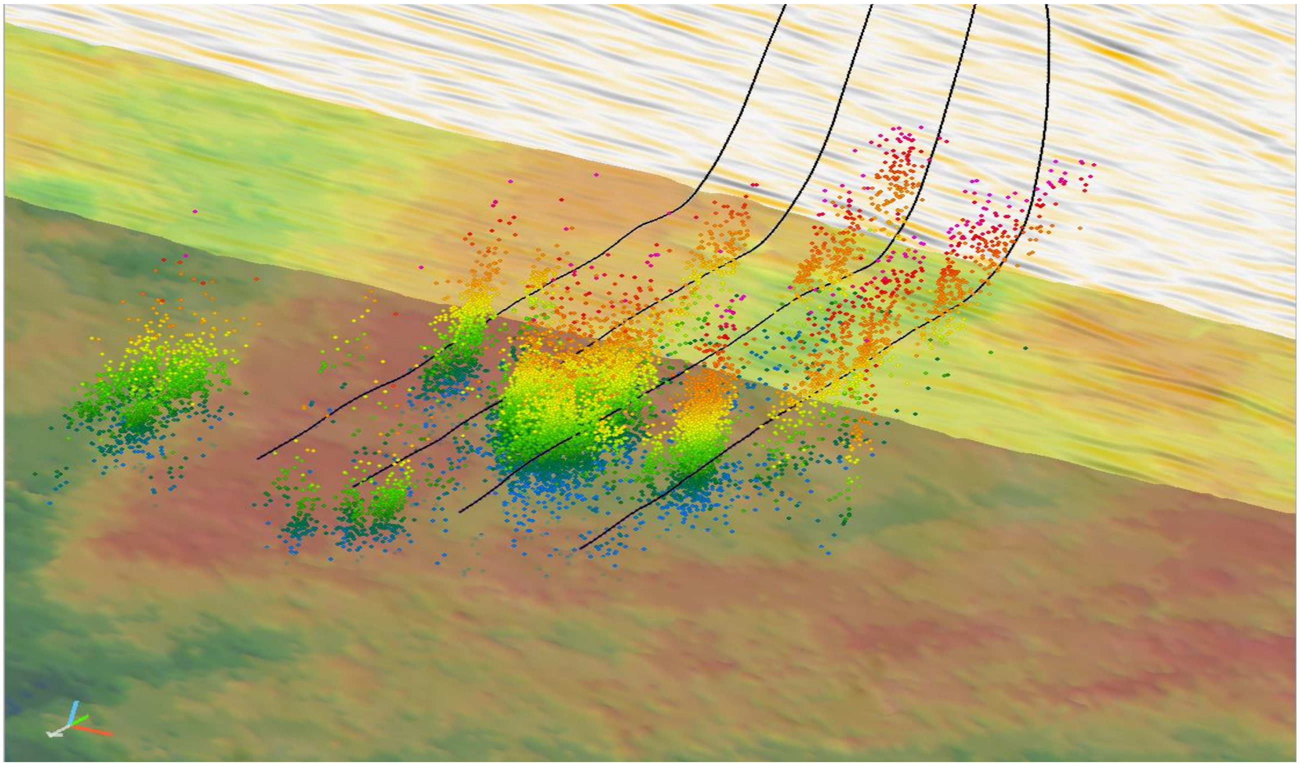

**Figure 5.7.** Microseismic events superimposed onto the 3D seismic depth volume. Well paths are shown for reference. The shaded upper horizon is the Swan Hills Formation depth surface, and the lower surface is the basement (lower).

horizontal treatment wells are plotted in depth with the focal-time processed event catalog. Two seismically defined horizons are also shown: the top of the Swan Hills Formation (a strong seismic reflection that immediately underlies the Duvernay Formation) and the top of the Precambrian basement. Although the depth uncertainty depends on the synthetic seismogram and the method used to convert from P-wave–reflected two-way reflection time to depth, this method results in highly robust stratigraphic correlations for event hypocenters. An unexpected result of this analysis is that the vast majority of induced events are shown to have occurred *above* the treatment zone. This is surprising, as previous induced seismicity studies elsewhere have indicated a strong prevalence for injection-induced seismic events to occur within the

Precambrian basement, where faults are expected to have a considerably greater surface area (Ellsworth, 2013). The geological significance of the hypocenters mapped above the treatment zone is incorporated into chapter 6 of this thesis.

In the course of developing the focal-time method, uncertainties arising from statics corrections applied to the microseismic observations may be problematic. A near-surface *Vp* and *Vs* model can be used to compute the necessary one-way time shifts. With the focal-time method a data-driven method is recommended, rather than a model based one, based on common receiver gathers with only shot statics applied. Seismic reflections identified in stacked common-receiver gathers can be correlated with those in the seismic volume to infer the static shift from the receiver to the seismic datum. Final datum directions can be for shallow buried geophone arrays can be adjusted using observed S-wave uphole travel times (Rodríguez-Pradilla and Eaton(2019)).

### 5.8 Conclusions

This chapter outlines the theory and method for a novel approach to obtain direct focal-time estimates for seismic events, including anomalous induced events. The utility of the method is illustrated by an interpretation and analysis in the Duvernay play of central Alberta, Canada in the following chapter. The method requires co-located, multicomponent surface seismic data so that P-P and P-S reflection times can be correlated. These correlated reflection times are used to construct a lookup table for the difference in the S- and P-arrival times of induced events, extrapolated to zero offset. Care is required to ensure that the microseismic time picks are referenced to the same processing datum as the multicomponent seismic data. Once the focal times of events have been calculated, the stratigraphic levels of the hypocenters can be readily determined through joint interpretation with seismic data. Focal depths can be estimated using existing methods for time to-depth conversion, such as from well ties to seismic data.

This method has several distinct advantages over traditional approaches to focal-depth estimation, which ultimately rely on the accuracy of the velocity model. The same seismic velocities govern wave propagation for seismic reflections and waves radiated by induced events, various poorly constrained parameters, such as anisotropy, are handled implicitly. The use of focal-time analysis results in relatively precise stratigraphic depth control for induced events, which is of considerable importance for interpretation of the results. Our results suggest that there may be considerable value to the industry for P-P and P-S seismic surveys to be more routinely acquired and used in joint processing of hydraulic fracturing data sets.

## 5.9 Future work

This method has possible applications in highly structured environments, such as thrust belts, extensional basins, and sub salt imaging. The travel time from a subsurface seismic event is identical to the one- way return path of a reflected seismic wavefield. It follows that within the boundaries of a 3-D/3-C seismic volume, process such as prestack depth and time migration are applicable to hypocenter positioning.

Incorporating a walk away 3-C VSP with focal-time would be to uniquely determine the horizontal and vertical velocities. Alternatively, if a reflection seismic survey was acquired with surface geophones, and simultaneously recorded by the microseismic array, the two recording systems would be calibrated, and an accurate time correction from subsurface to surface could be obtained.

This technique has applications anywhere there are co-located 3-D/3-C reflection and continuously recorded microseismic data. In areas where there is only vertical 3-D recorded, there may be ways to get the shear wave calibration through indirect methods. One method is to calculate a shear wave impedance volume through simultaneous (AVO) inversion This is not as accurate as a joint inversion (P-P/P-S), but it is worth testing and comparing the results to NonLinLoc..

# Chapter 6

## Integrated interpretation: Using seismic to derisk the Duvernay Formation

### 6.1 Summary

Development of a resource play such as the Duvernay Formation is subject to intrinsic risks. These may include the risk of incurring additional costs due to an induced seismic event or risks associated with unexpected thermal maturity, which can determine the value of the processed hydrocarbons (dry gas versus condensate). These two risks may be related, as the presence of basement faulting may influence heat flow from the basement, causing local variations in thermal maturity. The presence of basement faulting may also increase the risk associated with induced seismicity; whereby pre-existing faults are reactivated during the course of well treatment. Interpretation is complicated by the variable depositional environment for the Duvernay marine shale; an off-reef depositional system includes mechanisms such as contourite deposition, turbidity/mass flow, and in-situ biological carbonate precipitation, thereby creating variances in TOC content. Transtensional faulting caused by deep-seated strike-slip faults may be reactivated during a completion program rather than induced hydraulic fractures. Combining the microseismic and reflection data and displaying the data in depth allows for joint interpretation of seismic reflection and microseismic data. A geological picture is constructed by visualizing microseismic hypocenters in a chair plot with reflection surfaces and depth slices. These can be used to determine best practices for the future location and design of horizontal treatment wells.

## 6.2 Introduction

The Duvernay Formation is an unconventional hydrocarbon play in western Canada and is the object of active horizontal development drilling using hydraulic fracture stimulation. The Fox Creek area is located in the center of a major resource play within the Duvernay Formation (Preston et al., 2016). The map shown in Figure 6.1 displays regional thermal hydrocarbon maturity in the region, highlighting the areas prone to gas, condensate, and oil recovery within the Duvernay Formation. My specific study areas are located near the town of Fox Creek, are covered by two 3D/3C seismic surveys, and are referred to as ToC2ME and Bigstone North. These study areas are contained within the larger condensate (NGL)-prone area, which is the desired target for economic development in this region and is shown by the yellow band in Figure 6.1. The Duvernay oil-prone region is mapped to the northeast, with the dry gas region to the southwest of Fox Creek.

The study area has been mapped regionally to be within the condensate thermal maturity window (Preston et al., 2016). However, the production in the local study area shows that the hydrocarbons produced from the Duvernay Formation vary in composition from dry gas to condensate, to wells with a high water cut. There are several basement-rooted N-S strike-slip faults within this area, several of which are displayed in structural maps. These faults may be a contributing factor to the thermal maturity in the general Fox Creek area.

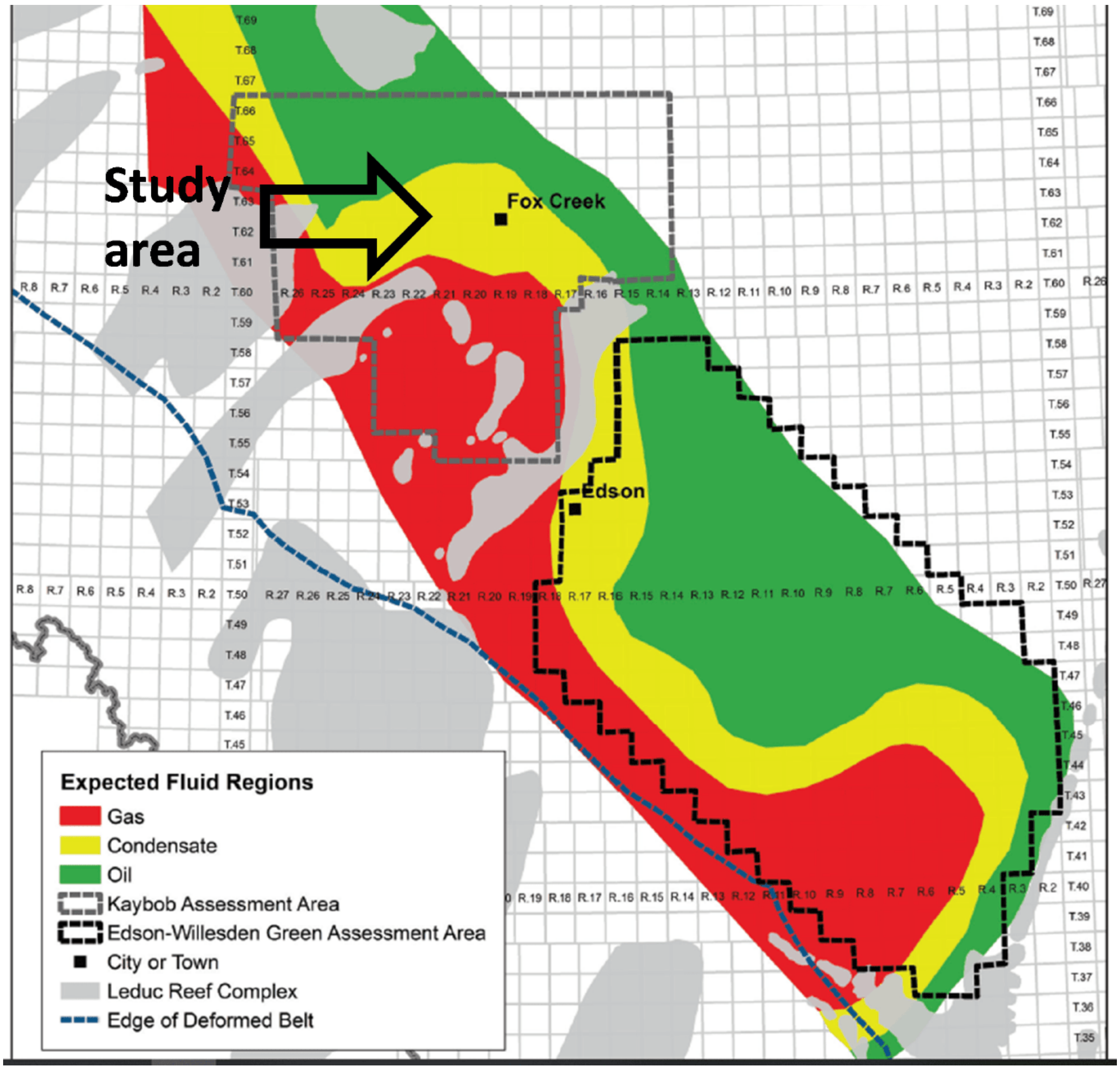


**Figure 6.1.** Expected fluid regions within the Duvernay Formation, given the thermal maturity profiles (modified from Preston et al. (2016). In a regional context, this study area is situated within the condensate fluid region, highlighted by the arrow.

## 6.3. Geology

The formation of interest is the Devonian-age Duvernay Formation, which is overlain by the Ireton Formation shale and sits conformably on the Swan Hills Formation (Switzer et al., 1994). The Duvernay Formation is an organic-rich calcareous shale (Knapp et al., 2017), deposited contemporaneously with the Leduc Formation. In this marine environment, three mechanisms of deposition of the Duvernay were recognized by Knapp et al. (2017): marine snow (in-situ carbonate distribution caused by biological activity), gravity flow (turbidity deposits from the reef and reef edge), and contourite deposition (caused by marine currents running parallel to the existing reef fronts and shelf breaks). Sea level changes, as well as seasonal and climate variations, have affected the deposition of sediments. The Duvernay was classified by Knapp et al. (2017) into 10 geological facies varying in lithology, organic content, and bioturbation. The deposits making up the Duvernay Formation are rich in organic matter, deposited in an oxygen-deprived environment.

After burial and heating, the rich organic matter generated hydrocarbons by the processes of catagenesis and metagenesis (i.e., hydrocarbon generation) (Tissot and Welte, 1984). Petroleum generation in the Duvernay Formation is a function of organic content, temperature, pressure, and time (Tissot and Welte, 1984). Kerogen (solid, insoluble organic matter) is changed to oil, gas, and condensate by a process called catagenesis. Figure 6.2 shows a schematic cross section with the associated stratigraphic table, the Leduc Formation is highlighted in yellow, the Duvernay Formation is highlighted in Red.

The first stage of catagenesis is the formation of oil, generating hydrocarbons with a medium to low molecular weight. With pressure (burial) and a temperature increase, carbon-carbon bonds continue to break, creating the wet gas condition. In the final stage, called metagenesis, most of the available organic matter has previously been consumed through catagenesis. Large amounts of methane are generated from the cracking of the source-rock hydrocarbon and the liquid petroleum reservoir. The methane in the rock is quite stable and is not readily destroyed by high temperatures. Tissot and Welte (1984) stated that methane remains stable up to temperatures as high as 550°C.

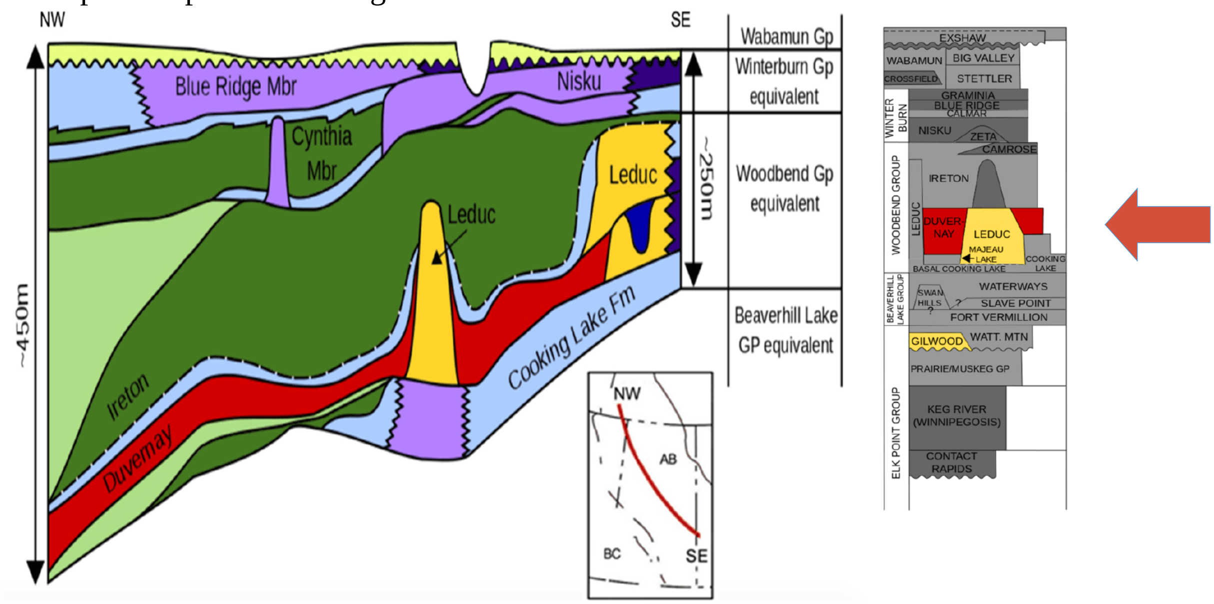


**Figure 6.2.** Schematic cross-section showing the Duvernay Formation with its geological setting (modified from Preston et al. [2016]). The Duvernay Formation (highlighted in red) is the stratigraphic equivalent of the Leduc Formation and is the focus of this study.

Preston et al. (2016) placed the general Kaybob / Fox Creek area within the condensate (NGL) region for the Duvernay Formation. The local project areas, ToC2ME and Bigstone North, are within the regional NGL Duvernay Formation window. They both contain two 3D/3C seismic reflection surveys, two co-located microseismic recording arrays, and well control and production data. The passive microseismic recording arrays were active during drilling and completion operations.

Figure 6.3 displays a smaller area (within the larger condensate region) that encompasses both the seismic reflection and microseismic surveys. The cumulative production data from the Duvernay are displayed as pie charts, with the size of the circle proportional to cumulative production. Red refers to condensate, blue is water, yellow is gas, and green refers to oil. The red stars show the epicenters of the large-magnitude events associated with hydraulic fracturing. Although the area displayed in Figure 6.3 is within the regional condensate window, the production displayed on the map shows reported volumes of dry gas, condensate, and gas/condensate production. The blue areas of the pie charts in Figure 6.3 indicate that some of the wells also have significant reported produced water volumes. Condensate volumes are often underreported, as reporting requirements require condensate (NGL) to be either reported as gas or oil (Alberta Energy Regulator [AER] directive 017 13.2.2). It is up to the operator to report condensate (NGL) volumes on a voluntary basis.

A regional study in the Fox Creek area by Shen et al. (2019) demonstrated that the maximum horizontal stress axis is 43°N within the Duvernay Formation. This study area is 150 × 150 km in size and encompasses both the Bigstone North and ToC2ME areas. The map area

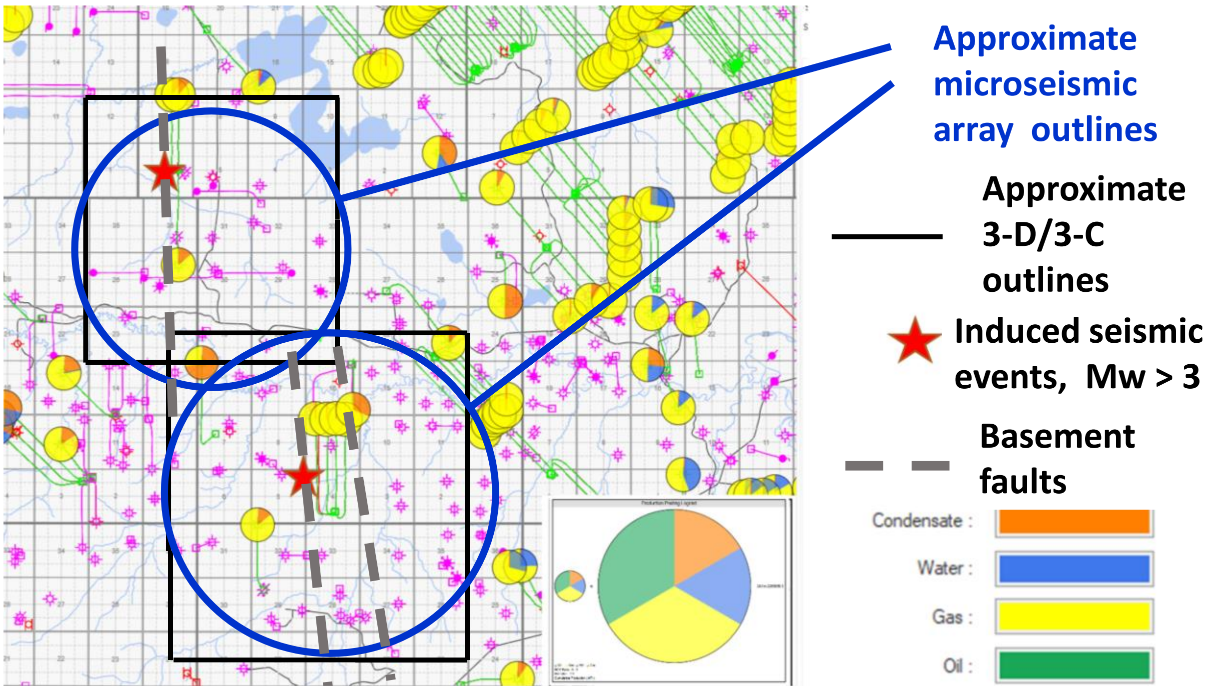


**Figure 6.3.** Local map showing the wells that have been completed in the Duvernay Formation (green lines). The pie chart represents the type of production; red is condensate, yellow is gas, and blue is water. According to the reported data, there is no oil production in this map area (green). Most of the Duvernay wells have been drilled in a northwest-southeast orientation perpendicular to $SH_{max}$. Condensate production reporting is not a requirement; therefore, condensate volumes tend to be underreported (AER directive 017 13.2.2). Pie chart sizes are proportional to the quantity of production to date (October 2019).

displayed in Figure 6.3 is contained within the larger regional study published by Shen et al. (2019), as well as the two seismic volumes incorporated in this chapter. Horizontal wellbore placement in the study area is generally based on the assumption that induced fractures propagate in the direction of maximum horizontal stress ($SH_{max}$), which is 43°N in this area. The assumption made in drill planning is that an orientation orthogonal to *SHmax* allows hydraulic fractures to propagate at a right angle, maximizing the stimulated reservoir volume (Eaton et al., 2018). As can be seen, many of the well locations shown on the map are positioned to be oriented orthogonal to 43° $SH_{max}$. Many of the horizontal treatment wells are oriented north-south because of land ownership constraints.

### 6.4 Reflection data

Two seismic volumes are used in this study, referred to here as ToC2ME and Bigstone North. These are located in adjoining areas and have a small overlap. Detailed structural maps are constructed using geological ties as defined by the synthetic seismogram in. This seismogram is also used to determine the time-depth relationship and depth-convert the seismic volumes. Depth and time scales are shown on the synthetic seismogram with the sonic and density curves.

The first step in the interpretation process is to correlate the seismic data to the geological column. Here, a synthetic seismogram (blue traces, Figure 6.4) is created from a sonic and density log by creating an acoustic impedance series. This acoustic impedance log is in turn convolved with a wavelet and generates the synthetic seismogram. By matching the synthetic seismogram to the actual reflection data (red), reflection horizons are correlated to the well log depths. This correlation establishes the time-depth relationship in the P-P domain and correlates the seismic reflection markers to geological horizons. The target zone, the Duvernay Formation, is highlighted with an arrow, as is the underlying Swan Hills Formation. The full interpretation and inversion workflows used for this data were described by Weir et al. (2018) and Weir et al. (2019), respectively.

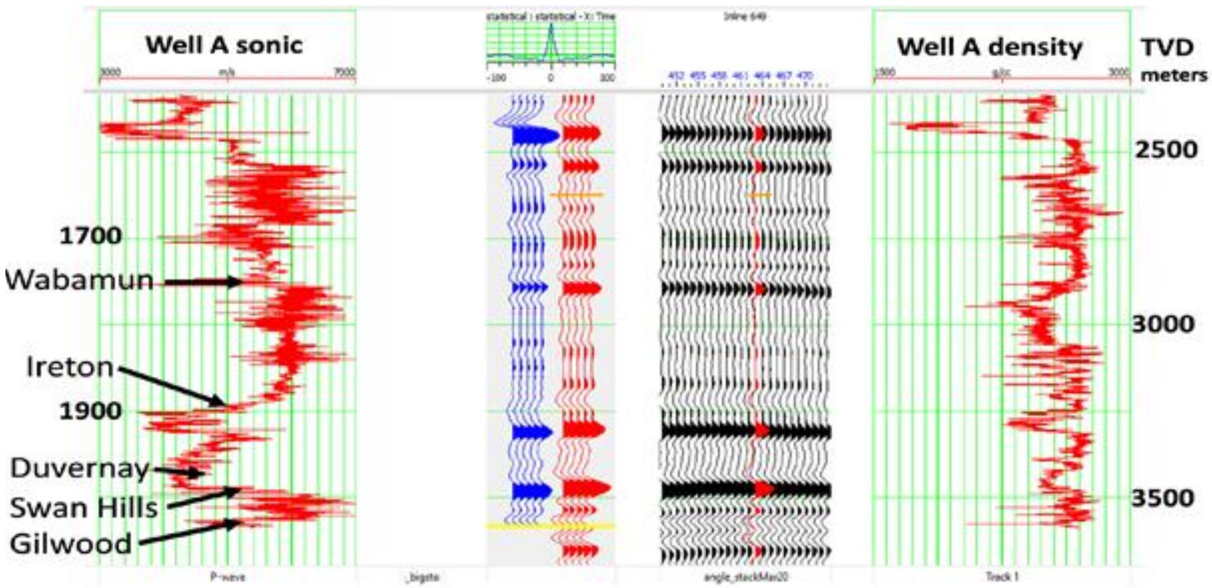


**Figure 6.4.** P-P synthetic well tie. Sonic and density well logs are shown, as well as the synthetic seismogram (blue) and actual reflection data (red, black). The synthetic seismogram tie shows the correlation of the key seismic horizons, as well as the corresponding depths. The treatment zone is the Upper Devonian Duvernay Formation, shown on the well tie. The match between the blue and red traces shows the final correlation.

### 6.5 Seismic reflection data

Time-structure maps created from the 3D volumes enable the visualization of geological features. In the ToC2ME and Bigstone North areas, the seismic reflection surfaces are relatively flat, with vertical breaks in the horizontal reflectors interpreted as faults, channels, or carbonate reefs. Horizontal time slices (chair plots) are quite useful for the interpretation of geological features. Channels are generally sinuous, while vertical and strike-slip faults show linear patterns. Carbonate reef banks observed in Bigstone North are observed as a curved feature, with a localized high on the western edge.

Time-structure maps are generated based on the synthetic seismic traces correlated to the P-P reflection data. For the ToC2ME seismic volume, the top Wabamun (Figure 6.5(a)) (Upper Devonian) and top Swan Hills (Figure 6.5(b)) are shown. The position of well A (the well logs used to construct the synthetic seismogram) is shown in both volumes, with the color bar corresponding to isochron values. With this display, the Swan Hills surface shows two distinct structural lineations: one is approximately north-south, while the other is north-northeast–south-southwest. The Wabamun time surface is structurally high to the east, with north-south trends, some of which correspond to features in the Swan Hills time surface. The structural interpretation incorporates structural geology concepts such as deep-rooted strike-slip faulting, flower structures, and transcurrent faulting (Ekpo et al., 2017). The technique used for fault interpretation is observing matching vertical displacements in reflection horizons and interpolating vertically between them.

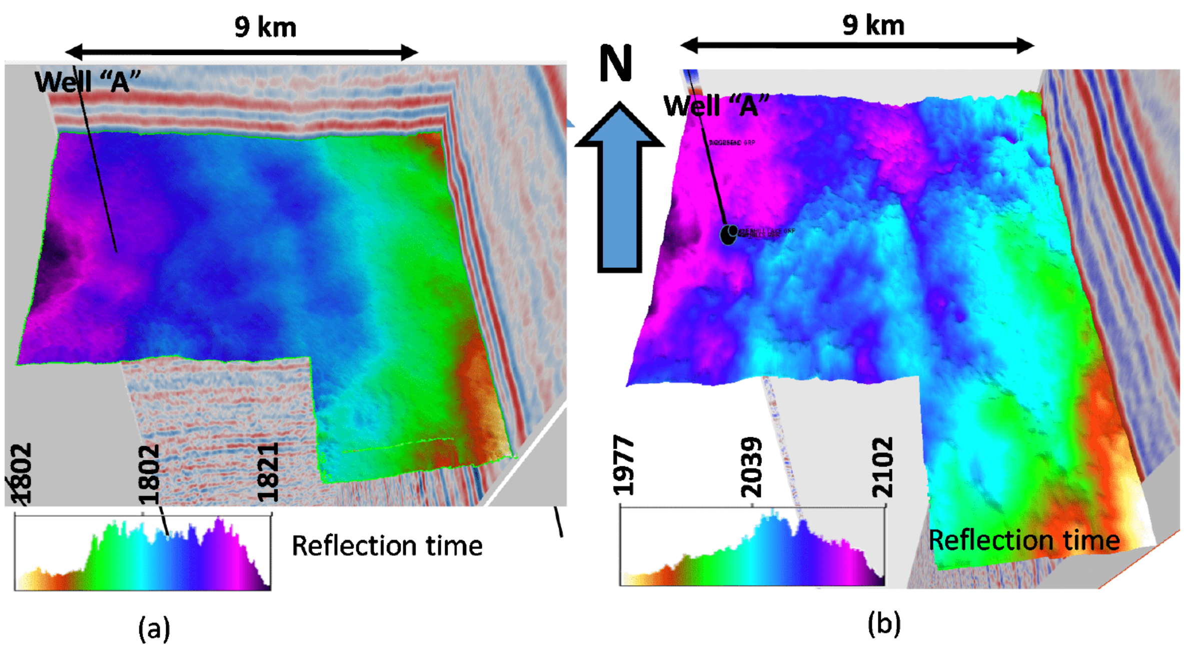


**Figure 6.5.** 3D chair plot views of seismic data from the ToC2ME program. (a) Wabamun and (b) Swan Hills time-structure maps. The treatment zone, the Duvernay, sits conformably above the Swan Hills Formation. The color bar is in two-way travel time (ms). The Swan Hills Formation time-structure map (b) shows a marked north-south lineation. These features are interpreted as faults. These maps are in two-way reflection time.

Within these seismic volumes, channel structures are observed within the Gilwood Formation (within the deeper Elk Point group, as well as a major Swan Hills reef front (Switser et al., 1994). The Gilwood channel is observed to have significant lateral displacement in the seismic volume, as does the Swan Hills reef front. These lateral displacements are herein interpreted as strike-slip faults in the seismic volume. In some instances, there are minimal vertical displacements on the same faults. Figure 6.6 illustrates the basement faulting and how it expresses itself in shallow horizons as transcurrent faulting. The transcurrent faulting is incorporated into this thesis as method to explain the present-day faulting within the Duvernay Formation.

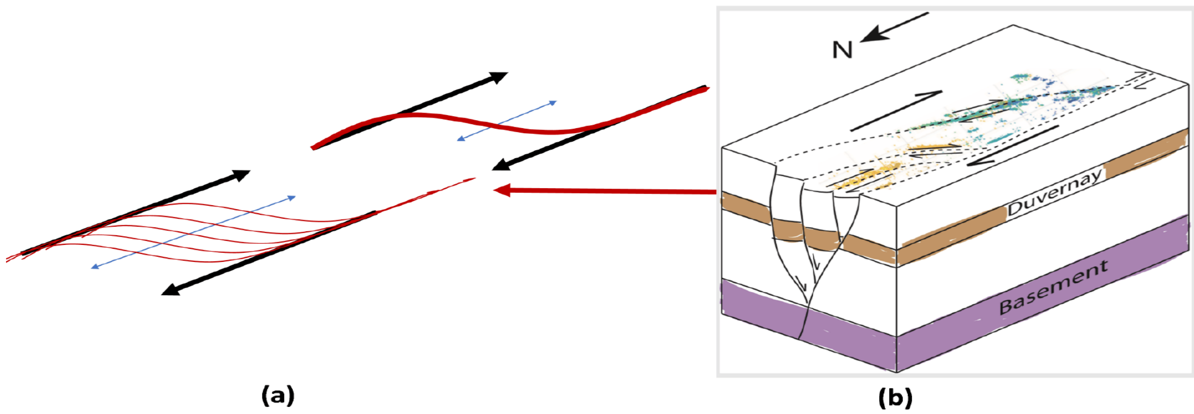


**Figure 6.6.** (a) Schematic diagram of a transtensional fault system in the Duvernay. The movement of the strike-slip fault is transferred to a number of cross-cutting faults. (b) Illustration of a Precambrian fault and the associated flower structure (Eyre et al., 2019). According to this model, the flower structure extends from the basement into the sedimentary section. This diagram represents the structural interpretation of the Duvernay Formation using the seismic data in this report.

### 6.6 Microseismic data

The microseismic hypocenters for the ToC2ME portion of this study are processed using the focal-time method as described by Poulin et al. (2019) and Weir et al. (2018). This method is used to convert the microseismic event time picks to depth. For the Bigstone North area, hypocenters, provided by an industry partner, are determined as described by Eyre et al. (2019). hese hypocenter locations into the seismic workstation provides an independent set of data to be used in the seismic interpretation. For the Bigstone North area, the microseismic hypocenters predominantly align in a north-south direction. For the ToC2ME area, there are two distinct fault lineations: north-south–aligned structures originating in the basement and an approximately 30°N alignment in the Swan Hills Formation structural map.

For the ToC2ME area, moment tensor inversion provides information as to the nature of the fracture or fault deformation of the seismic event clusters (Zhang et al., 2019), displayed in the form of beach ball diagrams. Figure 6.7 illustrates the source mechanisms of two groups of microseismic data; in this area, the source mechanisms are seen to be primarily strike-slip faults. The map displays 4,108 epicenters of the induced events, as well as the locations of the treatment wells. The beach ball diagrams are shown for clusters 4 and 5; cluster 4 indicates a north-south strike-slip motion, which is later used in the fault interpretation. Similar source mechanisms were found by Eyre et al. (2019) for the Bigstone North area. The largest induced event recorded during the ToC2ME treatment program had a seismic moment magnitude ($M_W$) of 3.2, triggering a series of aftershocks in cluster 4. The hypocenters for cluster 4 are approximately 70 to 90 m above the Duvernay Formation treatment interval (Poulin et al., 2019; Weir et al., 2018). The microseismic hypocenters are labeled as clusters 1 to 6. The color bar used for the epicenters in Figure 6.7 is in terms of clock time, displaying events from October to November. Cluster 4 is calculated to have a hypocenter depth centered in the Upper Ireton carbonate, 70 to 90 m above the Duvernay treatment zone (Figure 6.8). It includes the largest induced seismic event caused by the hydraulic fracture treatment ($M_W$-3.2) and the associated aftershocks. The beach ball diagram

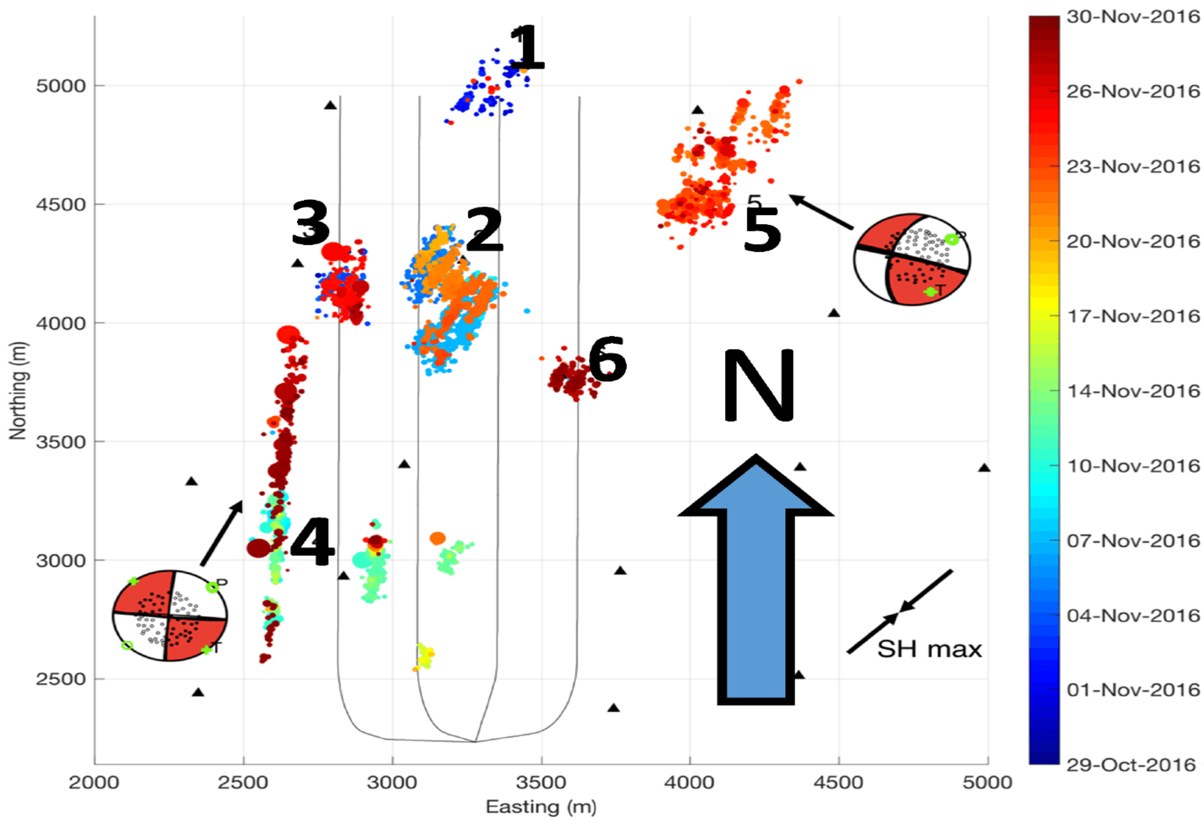


**Figure 6.7.** Epicenter locations of induced events with two examples of focal mechanisms in ToC2ME (modified from Eaton et al. [2018]). Group 4 is an $M_W$-3.2 induced seismic event followed by aftershocks occurring in the Upper Ireton Formation, situated 70 to 90 m above the treatment zone. It shows a north-south lineation, with a strike-slip mechanism derived from moment tensor inversion. The principle stress axis is plotted; $SH_{max}$ is 43°. Cluster 5 shows a predominantly strike-slip motion on the beach ball plot, with a north-northeast–south-southwest orientation and a small vertical component.

shows the calculated average focal mechanism for these events, indicating a north-south strike-slip motion. For clusters 1, 2, 3, 5, and 6, the seismic events are centered on the Duvernay treatment interval. For these clusters, the direction of induced fracture propagation is around 30°N. In contrast, the published maximum horizontal stress ($SH_{max}$) is shown on the lower right corner of Figure 6.7, with a direction of 43°N (Shen et al., 2019).

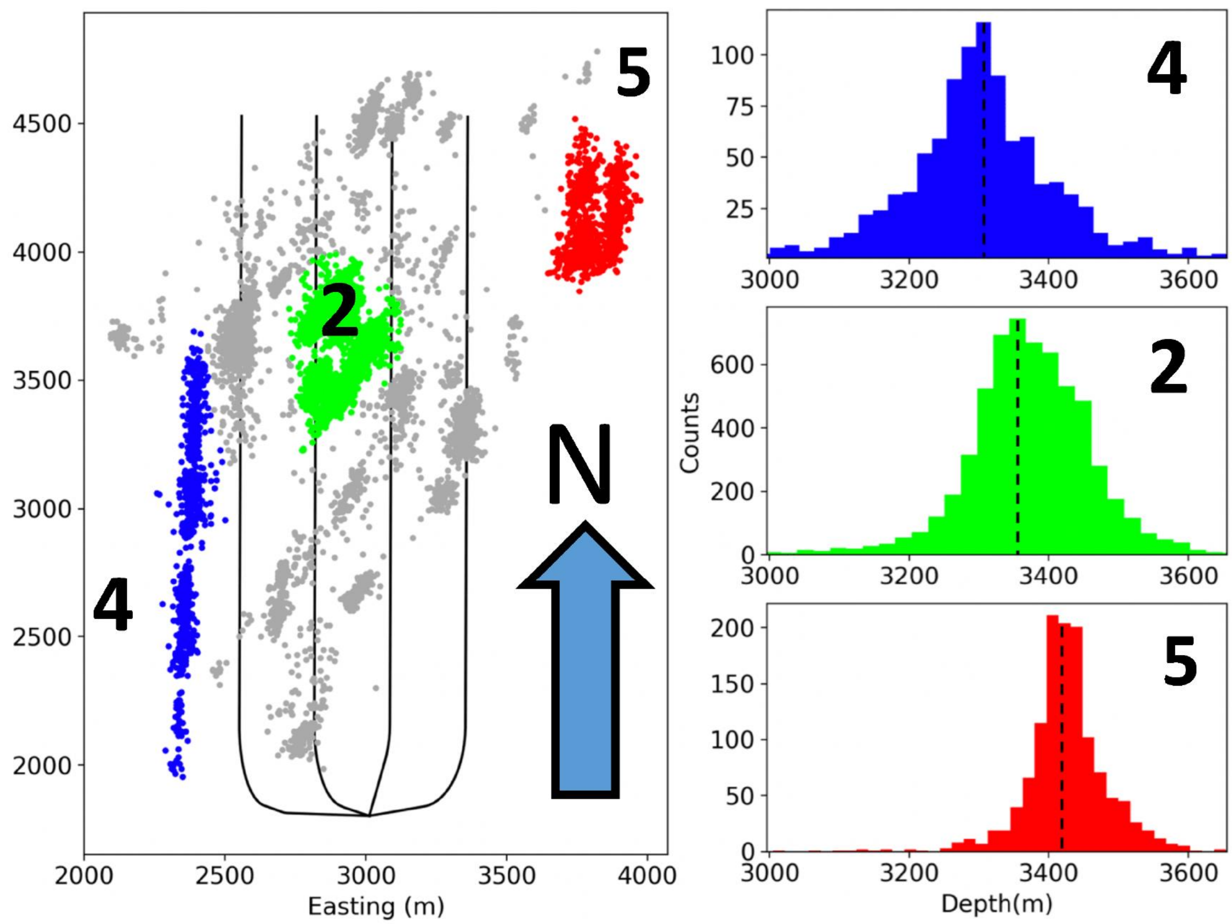


**Figure 6.8.** Hypocenter depths. Depth histograms of the calculated hypocenters for three of the microseismic clusters and map of those clusters (modified from Poulin et al. [2019]). The blue cluster (4) is centered at 3300 m, the green and gray (2) at 3370 m, and the red (5) at 3425 m. The blue events in cluster 4 are associated with the largest induced seismic event in ToC2ME.

### 6.7 Reflection data and microseismic joint interpretation

The fault interpretation performed here is a manual process performed by correlating matching vertical displacements of reflectors and lateral offsets of geological features. A fault detection volume is used in conjunction with the conventional reflectivity seismic volume to highlight lateral discontinuities. The microseismic hypocenters are used as an independent point set combined with the manual fault interpretation. Given the orientations of lineations in the volume and the strike-slip source mechanisms of induced seismicity in the region (Zhang et al., 2019), the fault system is interpreted to be a flower structure (as shown in Figure 6.6), interpreted to be the result of deep-seated strike-slip movement and the resulting displacements in the shallower Middle to Upper Devonian horizons. This matches the findings of other studies in the region (Zhang, 2019; Eyre, 2019). The structural lineation is primarily north-south minor vertical displacement.

Transcurrent faulting, also referred to as transpressional and/or transtensional faulting, forms within deformation zones that deviate from the major strike-slip faults (Fossen and Tikoff, 1998). These faults form complex fault systems running oblique to the main strike-slip motion. Transcurrent faulting can occur when there is a deviation in the linear strike-slip fault direction or as the net displacement of the larger fault system moves laterally from one strike-slip fault to the next in an on-echelon manner. On a local scale, if the adjoining strike-slip faults are converging, a transpressional system results; if they diverge, a transtensional system results. The small structural patterns on the Swan Hills surface occurring between the major strike-slip faults are interpreted to be transpressional faults, later described in the *Interpretation and analysis* section of this chapter.

Combining the microseismic hypocenters with the depth-converted seismic volume results in the chair display shown in Figure 6.9. From the focal-time event catalog, 13,105 hypocenters are loaded, along with the depth-converted seismic P-P volume, into the interpretation software. The directional surveys from the horizontal wellbores are also loaded into the interpretation software, as well as the calculated seismic edge-detect volume. The displayed 3D volume is a co-rendered structural stack combined with an edge-detect volume. The depth slice intersects an interpreted Gilwood channel system, which is observed to meander through the seismic volume from left to right.

The Gilwood member (highlighted by the time slice) contains a fluvial channel cut active during the Peace River Arch uplift (Switzer et al., 1994). It cut into the Muskeg Formation, leaving a distinct seismic signature that is readily identifiable within the 3D seismic volume. There is an observable displacement from north to south along the interpreted strike-slip fault (arrows) of about 2 km. Cluster 4 of the microseismic data appears to align with this fault, situated nearly directly above the strike-slip displacement in the Gilwood member.

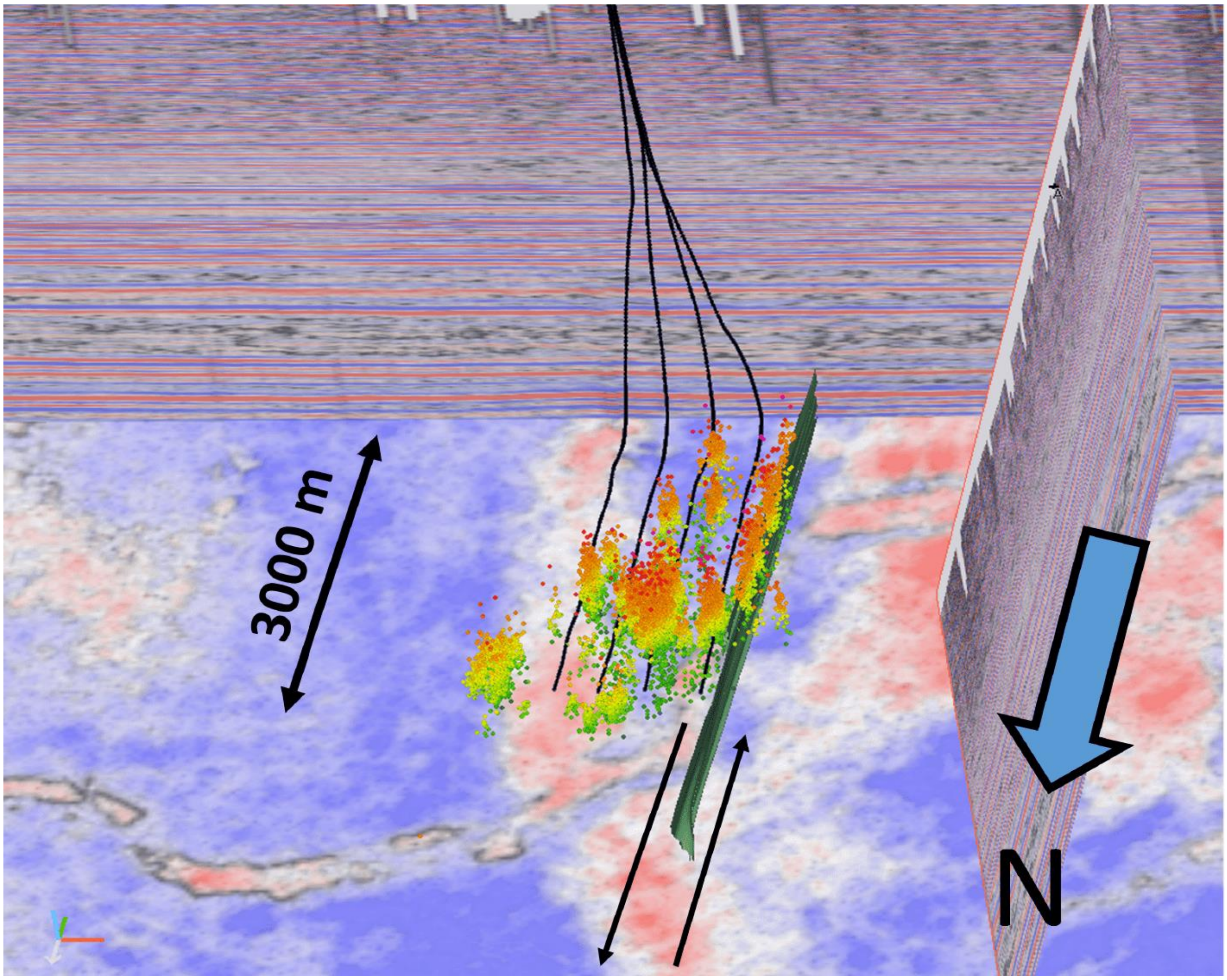


**Figure 6.9.** Combined chair plot showing a Gilwood time slice (viewed from the north), a co-rendered fault detect volume with amplitude (red to blue). The Gilwood channel-like feature appears to be displaced approximately 3000 m across the interpreted left-lateral (sinistral) fault. The microseismic events from cluster 4 are observed to occur approximately 300 m directly above this fault in the Gilwood Formation.

The Swan Hills Formation is a strong seismic reflector directly below the Duvernay Formation. Given that there is not a strong reflection event associated with the Duvernay Formation, the Swan Hills Formation serves as an excellent proxy for the Duvernay structure (Weir et al., 2019).

The Swan Hills structure is presented in Figure 6.10 as a red-to-blue map, calibrated in depth and viewed from the north. There are observable structural lineations in the Swan Hills surface, oriented 30° from the north in the vicinity of the wellbores. Figure 6.10(b) shows the alignment of the induced events with the major Swan Hills structural alignments. However, more minor pre-existing structures can also be observed, as indicated by the arrows in Figure 6.10(a), also appearing to align with many of the lineaments observed in the microseismic data. These are not aligned with the direction of maximum horizontal stress ($SH_{max}$), which is also indicated. This is the same depth-structure map displayed in Figure 6.3(b), but using a different color map and north-view angle. The microseismic events plotted are derived from the focal-time method, described in Chapter 5. The events are color-coded according to depth in the chair plot. Detailed examination of the Swan Hills depth-structure map shows a preponderance of northeast-southwest structural lineations (cluster 2), abruptly terminating against a major north-south fault to the east (cluster 5). What is noteworthy is that the pattern of microseismic activity observed in cluster 2 follows the same northeast-southwest alignment as the interpreted transcurrent faulting within the present-day Swan Hills structure. Cluster 5 terminates abruptly against another north-south deep-seated fault to the northeast of the treatment wells. The alignments of cluster 2 with the structural alignment in the Swan Hills structure suggest that the pre-existing structure dominated by northeast-southwest faults is the primary control mechanism for hydraulic fracture propagation. The abrupt termination of cluster 5 against a deep-seated fault confirms this hypothesis, in that the microseismicity stops at the eastern north-south fault. In the same manner, the large-displacement north-south fault (cluster 4) aligns with the major induced seismic events observed 70 to 90 m above the treatment zone.

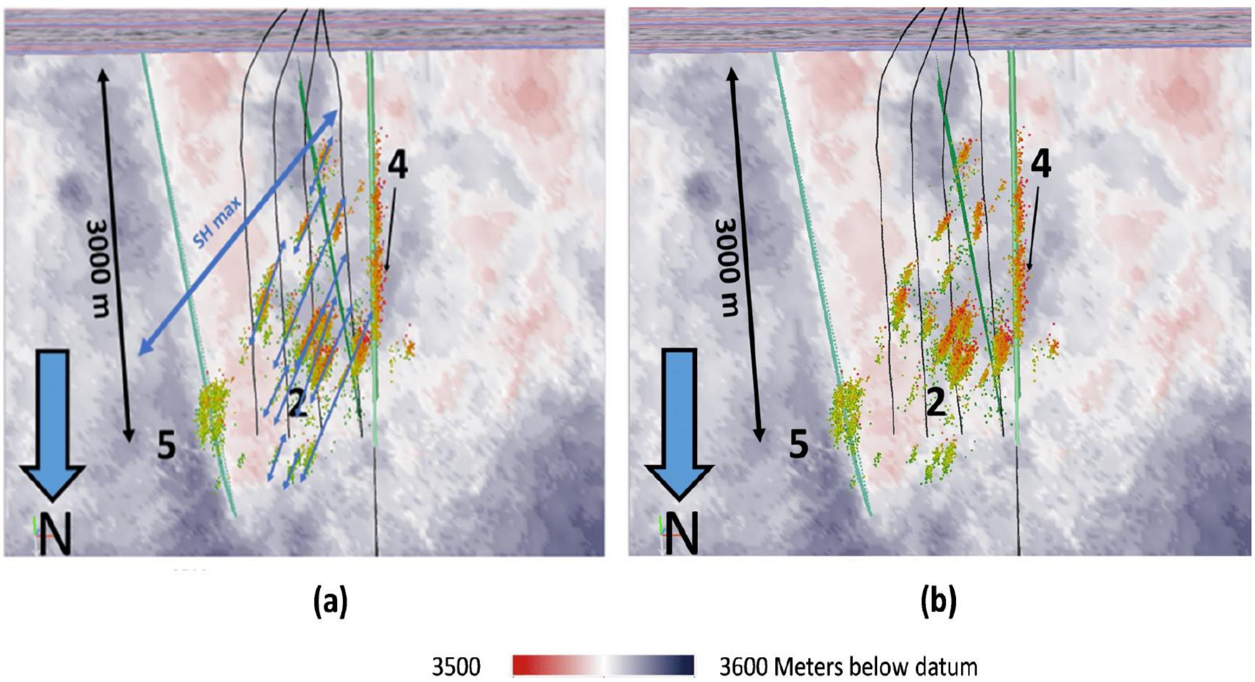


**Figure 6.10.** Combined chair plot showing Swan Hills Formation depth-converted structure viewed from the north. Cluster 2 occurs at the Duvernay Formation treatment depth. There is a pronounced north-northeast–south-southwest structural trend on the underlying Swan Hills Formation, which matches the orientation of cluster 2 events from the microseismic data (a). Because the Duvernay conformably overlies the Swan Hills, this map also approximates the Duvernay depth structure. Cluster 5, occurring at the treatment depth, terminates abruptly in the northeast against an interpreted vertical fault that does not appear to activate (b). Cluster 4 appears to align with the main fault activated by this treatment, which is oriented north-south (b). The structural lineaments that are aligned 30°N are consistent with the interpretation of transtensional tectonics, where strike-slip motion is transferred from one fault to another by a series of intermediate faults.

Eyre et al. (2019) proposed that the triggering mechanism for the large induced seismic event was caused by aseismic creep of the Duvernay/Ireton Formation along a pre-existing north-south deep-seated fault. Hydraulic fracturing is thought to have caused this aseismic creep in a north-south direction within the Duvernay formation along the fault, resulting in an abrupt seismic event due to structural failure in the rigid upper Ireton carbonate.

The large lateral (approximately 2 km) displacement observed on the Gilwood channel is correlated with fault interpretation lines, and a lineation of induced events (cluster 4) is correlated spatially with the fault interpretation lines in the same manner. This proves to be particularity useful in that the fault associated with cluster 4 has very little vertical displacement, but has a clearly defined linear alignment. Interpolating a fault plane between the user-defined interpretation lines gives a 3D fault volume using both reflection and microseismic data. The north-south movement of this fault is independently confirmed by moment tensor analysis of the ToC2ME microseismic data. (Refer to the beach ball plot associated with cluster 4 in Figure 6.7 (Zhang et al., 2019)).

**6.8 Discussion**

The reflection seismic data interpreted is comprised of two distinct project, the Tony Creek area and Bigstone North. The initial interpretation and analysis is described in chapter 2 (Tony Creek), which published in “Interpretation,” one year prior to chapter 3 (Bigstone North) being published in TLE. . The two surveys are 3-D/3-C seismic, with a small overlap in CMP coverage. The seismic coverage in Both areas are co-located with microseismic arrays covering hydraulic fracture stimulation programs. The P-P/P-S data registration, the synthetic tie, and the methodology applied to the seismic inversion are very similar. The seismic work in Toc2ME encompassed detailed structural mapping, seismic inversion, and an integration of microseismic data. Key features in the Toc3ME seismic program is the mapping of a Gilwood channel, and a N-S fault system that is correlatable to the basement. . Another key observation is the 30° E of North of the hydraulic fracture seismic events, which was unexpected given that *SHmax* is 43° in this area (Shen et al., 2019). These hypocenters are in alignment with pre-existing faults, interpreted to be Riedel shear faults within the Duvernay Formation.

When the two seismic surveys are aligned, the basement faults can be seen to continue from Toc2ME into Bigstone, as can the meandering channels of the Gilwood formation. What is conspicuously different, is the presence of a large Swan Hills Reef front running NE-SW in the Bigstone survey, and the complete absence of Ridel shear faults at the Swan Hills level. In Bigstone North, the hydraulic fracture propagation direction was nearly N-S, aligned with a basement rooted fault system that was mapable to the upper Ireton carbonate. In both areas, the high magnitude induced seismic events and associated aftershocks occurred above the treatment zone (Upper Ireton/Lower Winterburn Group), and had a N-S strike slip movement,

**6.81 Tony Creek area**

Previous work on the 3D seismic volume in the ToC2ME area (Weir et al., 2018) has detailed significant structural and compositional variations within the Duvernay Formation. Inversion-derived stratal slices show lateral impedance variations within the Duvernay Formation. Joint inversion–produced maps of Poisson’s Ratio, Young’s Modulus, and Brittleness index indicate faulting to have a significant postdepositional effect on rock properties. Detailed examination of the Swan Hills depth-structure map shows a dominant trend of north-northeast–south-southwest (approximately 30°) structural lineations (cluster 2), abruptly terminating against a major north-south fault to the east (cluster 5). The abrupt termination of cluster 5 against a deep-seated fault appears to confirm the hypothesis that rock properties may play a major role in fracturing.

The results suggest that the location and geometry of induced seismic events within the Duvernay Formation are controlled by pre-existing Riedel shear faults (transcurrent faults) that cut through the Duvernay Formation. Although the expressions of these faults is subtle, many associated strike-slip faults within the Duvernay Formation can be observed, given the visualization techniques available through 3-D rendering. Interpreting the Swan Hills Formation lineations in terms of Riedel shear faulting explains the predominant 30°N direction between the bounding north-south strike-slip faults. The faulting on the Swan Hills Formation is predominantly 30°N in the vicinity of the treatment wells, but this varies throughout the 3D depth structure. What is noteworthy is the alignment of the microseismic events with the Riedel shear faults displayed as group 2. Directly above the Swan Hills Formation are the Duvernay and Ireton Formations. The transtensional faulting may terminate within the shales of the Ireton Formation; these shales tend to deform in a ductile manner rather than via faulting or fracturing (Eyre et al., 2019). This is a possible explanation as to why the transcurrent faulting is not observed in the Upper Ireton carbonate or the Upper Devonian Winterburn group.

In the same manner, the large-displacement north-south fault aligns with the major induced seismic events (cluster 4), observed 70 m above the treatment zone. Eyre et al. (2019) proposed the triggering mechanism for the large induced seismic event to be caused by aseismic creep of the Duvernay/Ireton Formation along a pre-existing north-south deep-seated fault, the induced seismic event having been initiated by pore pressure increase due to fluid injection. The alignment between the deep-seated fault in the Gilwood Formation and the induced seismicity (cluster 4, Figures 6.7, 6.8, and 6.10) confirms the activation of a deep-seated fault during the course of hydraulic fracture treatment of the Duvernay Formation, with events occurring significantly above the reservoir, as observed by Eyre et al. (2019). The north-south event cluster appears to be at the depth of the Upper Ireton carbonate.

### 6.82 Bigstone North area

The Bigstone North area incorporates the northern portion of the 3D/3C seismic reflection survey. It serves as a second case study to examine the relationship between geological structure and microseismic event propagation. This area is covered with the 3D/3C seismic data volume, co-located with a passive microseismic array. As in the ToC2ME data, this area has microseismic events and induced seismicity with aftershocks triggered by the hydraulic well treatment program. Previous work on this data set (Weir et al., 2019) has shown the results of structural interpretation and joint inversion. This work states that there are significant variations in Young’s Modulus, Poisson’s Ratio, and brittleness across the area. These variations may be attributed to the local depositional environment or postdepositional alteration caused by faulting.

The structural lineations on the Swan Hills Formation depth map are predominantly north-south, with a notable absence of observable oblique transcurrent faulting (as observed in ToC2ME). An explanation for this is that the basement faulting displacement is predominantly strike-slip in this local area, with no convergence or divergence to create transtensional faults. The implication of this is that the fault reactivation, occurring as a result of fracture stimulation, would occur in a north-south direction along the path of the pre-existing strike-slip faults.

Figure 6.11 is an east-west seismic cross-section of the seismic volume. The key elements of this seismic section are the Gilwood channel, the Swan Hills reef edge, and the interpreted near-vertical faults. The Duvernay Formation sits directly above the Swan Hills reflector. The Swan Hills, Gilwood, and Precambrian horizons are shown in depth; these same horizons are displayed in north-view map displays in Figures 6.12, 6.13, and 6.14. The seismic line displayed in Figure 6.11 is shown as the cross-section A-A' in the map views in Figure 6.12. The projected depth of the seismic moment magnitude ($M_W$)-4.1 event is shown as the yellow star and is located significantly above the reservoir within the Wabamun carbonate (Eyre et al., 2019).

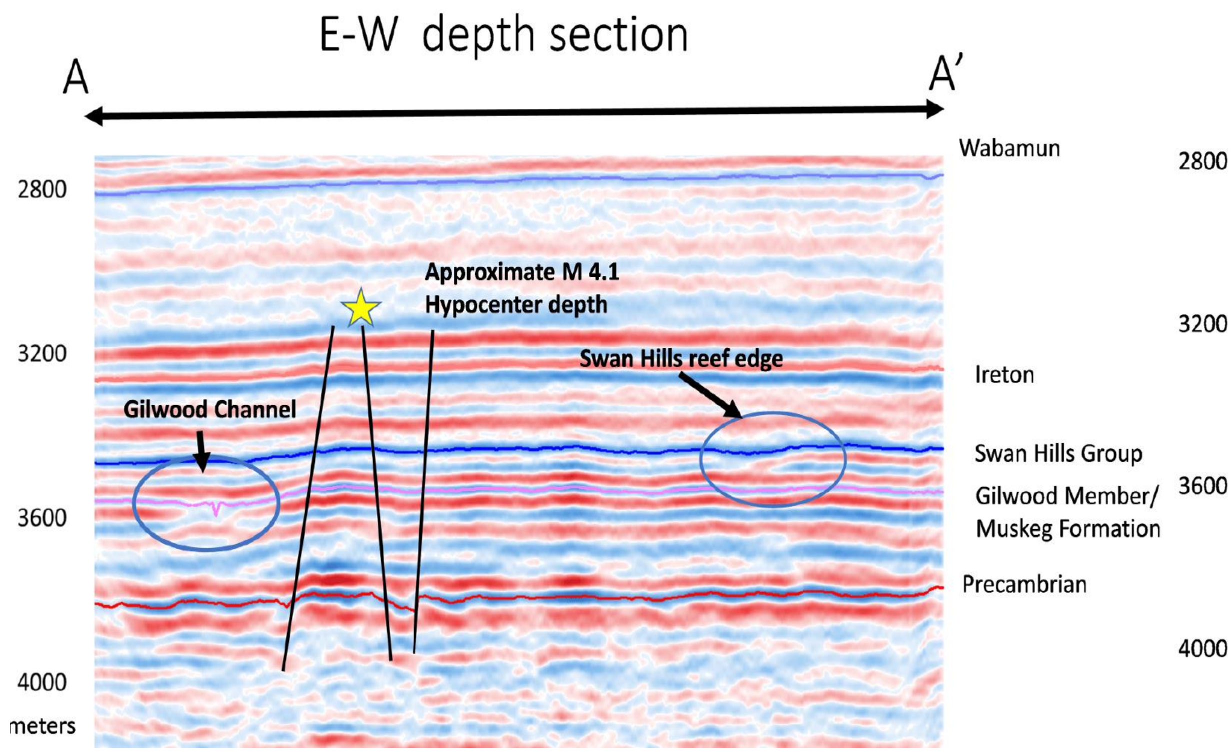


**Figure 6.11.** East-west cross-section showing the key features in the Bigstone North region. The Swan Hills reef edge, a Gilwood channel, and the vertical displacement associated with the basement strike-slip faults are highlighted. The Swan Hills group, Gilwood member, and Precambrian markers are displayed in depth. The projection of the $M_W$-4.1 seismic event is shown as the yellow star. Associated maps and the interpretation of these features are displayed in Figures 6.12, 6.13, and 6.14.

Figure 6.12 displays the depth-converted seismic surfaces on the Swan Hills Formation and the Precambrian basement. The hypocenters are displayed in color, according to the calculated depth. These events are aligned along N-S basement rooted faults. The microseismic events terminate to the South at the Swan Hills reef front.

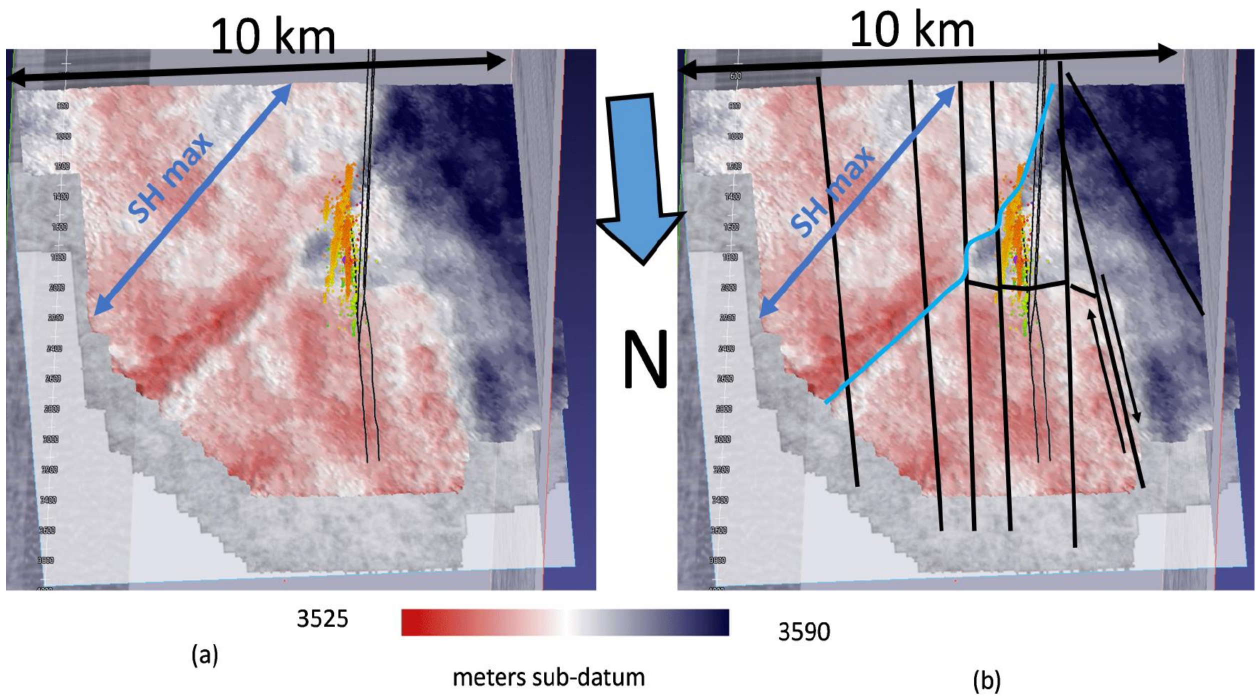


**Figure 6.12.** Depth-converted seismic surfaces on the Swan Hills Formation (a) and the Precambrian basement (b). This chair plot viewed from the north highlights both the north-south faulting and the reef edge. The Swan Hills reef is a prominent northeast-southwest feature displayed in Figure 6.13(a).

Figure 6.13 is a display of the Swan Hills Formation surface. This chair plot viewed from the north highlights both the north-south faulting and the reef edge. The Swan Hills Reef is a prominent northeast-southwest feature displayed in Figure 6.13(a), shown with a blue outline in Figure 6.13(b). Notable north-south displacements can be observed along this reef front. A series of north-south faults are also seen on both the Swan Hills and Precambrian maps; several of these are interpreted and shown in Figure 6.13(b). Although these faults are predominantly strike-slip, in some instances, there is noticeable vertical displacement. The faulting is almost entirely north-south, in contrast with the ToC2ME area, where there is a significant north-northeast–south-southwest component to the faulting. Maximum horizontal stress ($SH_{max}$) is displayed as a blue arrow at 43°N.

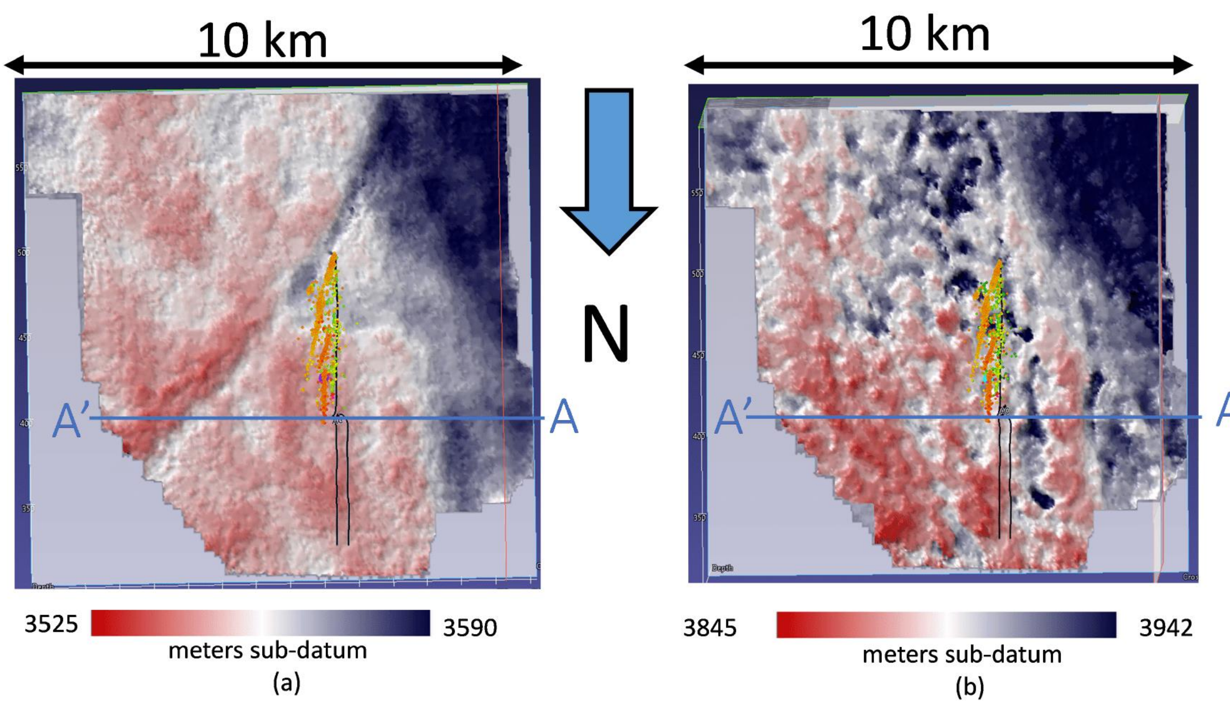


Figure 6.13. Map views of depth-converted structures for the Swan Hills Formation (a) and Precambrian basement (b). The microseismic catalog locations are displayed on top of the structural map, showing a distinct north-south alignment parallel to the observed north-south fault lineaments. The Swan Hills reef front, seen as a northeast-southwest curved line on the Swan Hills surface (a), appears to have acted as a barrier inhibiting microseismic growth to the south and east of the treatment well. Notable north-south displacements can be observed along this reef front. A series of north-south faults are also seen on both the Swan Hills and Precambrian maps; several of these are interpreted and shown in (b). Although these faults are predominantly strike-slip, in some instances, there is noticeable vertical displacement. The faulting is almost entirely north-south, in contrast with the ToC2ME area, where there is a significant north-northeast–south-southwest component to the faulting. $SH_{max}$ is displayed as a blue arrow at 43°N.

Figure 6.14 is a north-view depth map of the Gilwood member of the Muskeg Formation of the Middle Devonian age; Figure 6.14(a) is the depth-structure map, and Figure 6.14(b) shows five of the correlated strike-slip faults. The Gilwood member is highlighted with a blue outline and shows postdepositional displacement along the faults. The Gilwood member is a channel that was active during the uplift of the Peace River Arch (Switzer et al., 1994). The distinct channel-like feature (blue highlighting) is approximately 400 m wide and is seen to meander through the map area. This channel changes direction abruptly as it crosses interpreted strike-slip faults. This matches the observed displacement in the higher Swan Hills reef front (Figure 6.13), presumably caused by postdepositional strike-slip fault movement.

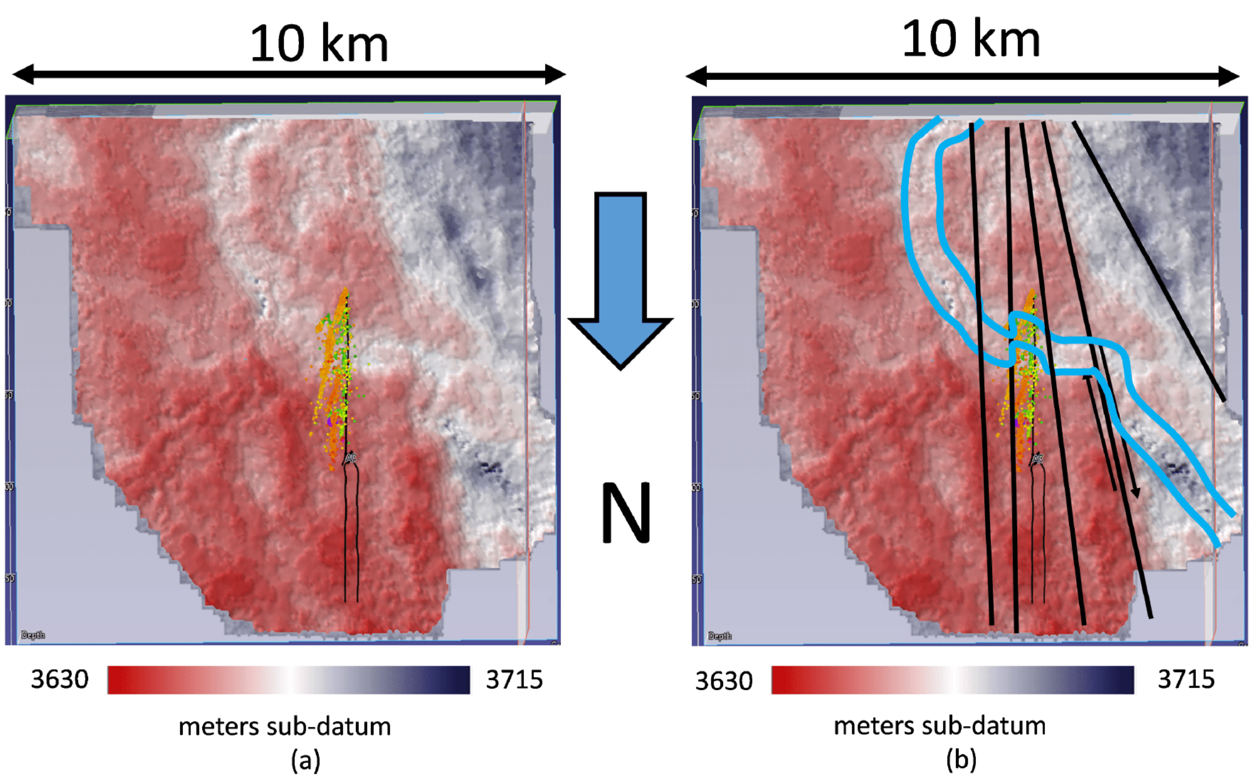


**Figure 6.14.** North-view plot of the Muskeg Formation, Gilwood member. (a) Time structure and (b) three of the interpreted strike-slip faults, with the Gilwood channel highlighted in blue. The microseismic events are shown as points, colored by their corresponding depths.

The microseismic events plotted in Figures 6.12 and 6.13 are color-coded with depth. The catalog comprises more than 10,000 seismic events, many of which are located above the Duvernay reservoir, and including the $M_W$-4.1 induced seismic event with its associated aftershocks. This is the same induced event that Eyre et al. (2019) used to propose the mechanism whereby aseismic creep can produce an induced seismic event at a depth shallower than the treatment formation. The microseismicity shows a distinct north-south trend, aligned to the north-south structural lineaments observed on the depth-converted Swan Hills map, as well as the Gilwood map. The Swan Hills reef also appears to present a barrier to hydraulic fracture propagation, in that where microseismic events come close to the reef front, their orientations rotate to reef-parallel. The significant $M_W$-4.1 event and its aftershocks follow a north-south lineation aligned with a fault mapped to the deep Precambrian (Eyre et al., 2019).

Fault systems play an important role in fluid flow and advective heat transport in sedimentary basins (Bjorlykke, 1993). Given sufficient upward fluid flux within basement-rooted fault systems, large thermal anomalies can be created (Bjorlykke, 1993). Indeed, the effects of basement-derived fluids in the nearby Simonette oil field (Swan Hills) have been well documented with respect to dolomitization (Duggan et al., 2001). Geochemical data indicate the occurrence of both early- and late-stage dolomitization; in the latter case, the fluids are considered to be hydrothermal and basement-sourced along near-vertical faults (Duggan et al., 2001). Further evidence in the Western Canadian Sedimentary Basin is provided by regional deep-crustal two-dimensional (2D) seismic data, which suggest that deep-seated faults could have controlled the fluid circulation patterns in the basin, as well as the orientation of reef foundation during the Devonian age (Eaton et al., 1995). Controls on fluid circulation and advective heat transport within sedimentary basins are also well documented for certain types of ore deposits, such as unconformity-related uranium deposits (Li et al., 2016). In this case, basement faults can localize fluid ingress and egress into the sedimentary units and thus establish stable patterns of convective circulation (Li et al., 2016). Thus, the observed basement-seated faulting is likely to play a key role in the thermal maturity of the Duvernay Formation.

**6.9 Interpretation and analysis**

In order to understand the complexities associated with the development of the Duvernay Formation, one must address several aspects of the present-day Duvernay Formation:

- The organic-rich shale was deposited as a result of organic in-situ precipitation, gravity flows, and contourite currents. Pre-exiting structures such as the Swan Hills reef front, faulted structure present during deposition, and the Leduc reef complex, are important factors influencing reservoir quality. Joint inversion may address this issue by displaying reservoir properties (such as brittleness) over the seismic volume.
- Thermal maturity may be affected, on a local level, by basement faults. The faulting may impact heat flow and, in turn, thermal maturity. The Fox Creek area, regionally mapped as condensate-prone, may have localized areas of dry gas due to high heat flow caused by basement faulting. Given the relatively small areas (in a regional sense) of the 3D/3C seismic surveys, there are not enough data to fully test this hypothesis.

Nevertheless, given the local variations observed in Figure 6.1 in gas, condensate, and water production and the observations of basement-seated faults, local variations in heat flow by basement faulting present a plausible explanation for the production.

Pre-existing faulting and fracturing caused by transtensional tectonics appear to be a significant factor controlling fracture propagation. These structures, created by a releasing step-over within a flower structure, appear to control the direction of induced fracture propagation. The presence of Riedell shear faults in Toc2me is contrasted with the lack of these type of features in Bigstone North. The center of the treatment wells in Toc2ME is only 10 km from the wells in Bigstone North. This contrast over a small geographical area is explained by Davis et al. (2000), where the Riedel shear faults step across from shear zone to shear zone in an oblique manner.

I show here that these features can be mapped using 3D seismic and should be considered when planning a horizontal well treatment program. The alignment of microseismic events with transtensional faults indicates that they are the result of the reactivation of existing faults rather than induced fractures oriented to maximum horizontal stress, and the orientation of the Riedel faults can change over a short distance, or disappear completely.

The deep seated strike-slip faults in the region may be critically stressed, and wellbores running in close proximity and parallel to a fault such as this may trigger an induced seismic event of significant magnitude (Eyre et al., 2019). Aseismic slip in the Duvernay Formation caused by hydraulic fracturing may cause induced seismic events in deeper or shallower formations. The pattern of induced fractures observed in Bigstone North terminates against the underlying reef front (Figure 6.13). Two possible explanations for this are that the reef front itself is a mechanical barrier preventing fracture propagation or that the facies of the Duvernay varies across the reef front because of the differences in water depth due to deposition. In either case, the fracture stimulation does not propagate across the reef front, leaving the hydrocarbon reserves to the south untouched. A similar pattern is observed for cluster 5 in the ToC2ME region. The faulting in Bigstone North is almost entirely north-south or north-northwest–south-southeast, in contrast with the ToC2ME area, find where there is a significant 30°N component in the faulting.

### 6.10 Conclusions

The interpretation methodology deployed here emphasizes the use of combined microseismic event detection and reflection seismic imaging. The depth-dependent patterns observable in the microseismic catalogue were observed to align along faults identified on the reflection seismic data. The North-South patterns of induced seismic events are aligned with pre-existing strike-slip faults, seated within the basement rocks. The alignment of microseismicity (30 degrees east of north) is consistent with a strike slip fault pattern interpreted in the Swan Hills Formation structure map as Ridel shear faulting. A notable feature is that the Swan Hills Reef front in Bigstone North appears to have acted as a barrier to hydraulic fracture stimulation, preventing observable seismicity south of the reef edge. The results presented here indicate the dominant factor in the propagation of induced seismicity to be pre-existing faults within the Duvernay Formation. The ToC2ME data show an alignment of microseismic events with pre-existing Swan Hills structures, as opposed to maximum horizontal stress. In both Bigstone North and ToC2ME areas, the pattern observed for the minor faulting is consistent with Riedel shear related strike-slip faulting. Many of these faults can be mapped in the seismic volume from the basement to several hundred meters above the reservoir. The abrupt termination of induced fractures against a deep seated fault can be explained in terms of geological structure, with major strike-slip faults acting as a barrier to fracture propagation.

The deep-seated faults interpreted from the seismic data may have created areas of increased heat flow, influencing thermal maturity, hence the local variations in condensate production. There is nearby petrographic and geochemical evidence that deep-rooted faults provide conduits for circulation of hydrothermal fluids from the basement (Al-Aasm, 2002). The findings here may be used in future treatment well design to mitigate geohazards and optimize completion programs. From an induced-seismicity risk-management perspective, it is advisable to drill horizontal wells so that they intersect known faults at a high angle, as this approach facilitates mitigation steps during completion such as skipping stages near a fault.

From a drilling, completion, and production perspective, the well treatment objective is to use hydraulic fracturing to open up the formation, inject proppant, and thereby increase the permeability of the reservoir. If minor fault reactivation is the dominant mechanism for reservoir enhancement in the Duvernay Formation, then an optimal completion program would orient the wells orthogonally to the predominant transtensional fault trends. In both Bigstone North and ToC2ME areas, the pattern observed for the minor faulting is consistent with transtensional-related strike-slip faulting. Many of these faults can be mapped in the seismic volume from the basement to several hundred meters above the reservoir. The abrupt termination of induced fractures against a fault can be explained in terms of geological structure, with major strike-slip faults acting as a barrier to fracture propagation.

The orientation of treatment wells with respect to pre-existing faults may be a key factor in causing large-magnitude induced seismic events. In both areas studied here, large-magnitude induced seismic events occurred when hydraulic fracture stimulation was performed in wellbores parallel to, and in close proximity to, basement-rooted faults (Eyre et al., 2019; E et al., 2018). This leads to multiple interactions between fluid injections and the faults. Depending on how the fault is locked, multiple stages of fracture stimulation may cause cumulative aseismic creep over a significant portion of the fault, resulting in sudden failure in the overlying unstable rock. A mitigation strategy may include orienting the wellbores orthogonally (not parallel) to the basement faults and skipping the stages that intersect, or are in close proximity to, the deep seated strike-slip fault.

The minor Riedel shear faulting and fracturing mapped in the Duvernay can change orientation over a relatively short distance, as shown in the seismic structural mapping of the Swan Hills Formation in Toc2ME in contrast to Bigstone orth. adjoining areas. Future drilling and well treatment could be optimized by taking into account pre-existing geological structures. According to the work presented here, the Bigstone North area has a preferred orientation for treatment wells in an east-west direction orthogonal to the pre-existing fault and fracture lineations. This optimized well orientation would improve the treatment program by using the pre-existing fracture network and maximizing the stimulated reservoir volume. In contrast, a wellbore positioned parallel to a pre-existing fracture network would be ineffective in opening up the reservoir. The

Swan Hills reef edge should also be taken into account, as it appears to be a significant barrier to fracture propagation. For the ToC2ME area, the preferred wellbore orientation is southeast-northwest, taking into account the pre-existing Swan Hills structure in the area. This study demonstrates that 3D seismic is a very effective tool for wellbore planning, and in addition to depth control, mapping vertical and strike-slip faulting provides useful information for treatment programs.

# Chapter 7

# Summary, conclusions, and future research

## 7.1 Summary

This thesis integrates new concepts in seismic reflection interpretation, microseismic, signal processing, and a new model for fault interpretation. Prestack inversion highlights variances in the reservoir, the influence of pre-existing structure, and the influence of post depositional faulting. Structural interpretation explains microseismic activity and the nature of induced seismic events. The focal-time method developed here accurately locates hypocenters by using information independently obtained from reflection seismic data and well depth control. A desire for improved seismic event detection is addressed by new applications of signal processing as applied to the continuously recorded seismic data, resulting in a significant improvement in event detection.

It was the initial assumption that seismic inversion could play a key role (added value) in the development of unconventional reservoirs, and that identifying areas of high brittleness would identify a means of reducing economic risk associated with unconventional development. Inversion results in Toc2ME and Bigstone North show that there are significant changes in brittleness across the study areas Indications are the number of wells and fracture stages could be reduced by characterizing the Duvernay formation unconventional reservoir, and strategically planning the location and orientation of the well bore, and planning stages to optimize perforation intervals. The initial assumption with respect to the nature of hydraulic fracture propagation is that *Shmax* is a key parameter in determining the propagation direction.

The interpretation of observed structural features results in a geological model (Riedel shear faulting) that explains the direction if induced fracture propagation, and why it differs from the way fracture propagation is predicted based solely on *$SH_{max}$*. The method proposed for the triggering of induced seismic events, aseismic creep (published in Science Advances), uses the structural interpretation presented here as a basis for the structural deformation that triggers induced seismic events. Finally, a comprehensive risk assessment is presented, including reservoir risk, induced seismic risk, and a hypothesis with respect a mechanism explaining Duvernay Formation thermal maturity. Explaining local variations in the Duvernay Formation thermal maturity may account for dry gas production in an area generally considered to be rich in condensate. This thesis presents factors to be considered for future Duvernay Formation development, as well as technologies applied in a general sense to microseismic analysis, and unconventional reservoir development.

**7.11 Seismic imaging**

Chapters 2 and 3 demonstrate that 3-D/3-C Seismic data can be used for reservoir characterization by calculating petrophysical properties. A multicomponent inversion produces reservoir parameters such as Poisson's Ratio, Youngs Modulus, and Brittleness, and when mapped, identify sweet spots in the reservoir. These parameters show significant variations across the reservoir, indicating the reservoir is not homogeneous. Certain areas of the reservoir may not be conducive to hydraulic fracture stimulation and are identified with a low BRI; in contrast with those that may be more suitable for development (high BRI). Structural mapping identifies fault systems, such as strike-slip faults and transcurrent faulting. The basement faults responsible for induced seismicity are identified by aligning them with the induced seismic events, the associated aftershocks, and how they overlay with those said events.

**7.12 Signal processing**

The signal processing evaluated here demonstrates that there is a significant improvement in seismic event detection by using signal processing on continuously recorded seismic data. To improve the passive raw recorded signal, processes commonly used in seismic exploration are applied, such as deconvolution, filtering, and scaling. Microseismic recording during completion operations typically occurs in a very noisy environment; signal processing technology exists to mitigate the noise problem and high-grade the signal, the benefits of which are demonstrated here. These signal processes, originally designed for reflection data, increase the number and quality of the detected passive seismic events, which are in turn incorporated into the seismic interpretation. The deconvolution operator compresses the wave form and converts it to zero phase. The more accurate time picks are, the less error there will be in the uncertainty analysis, and the more accurate the hypocenter calculation. This will be verified when the processed data is analyzed with the focal-time program.

**7.13 Focal Time Estimation**

The use of the newly developed focal time method shows a significant improvement for hypocenter determination over model-based methods. Using information from the seismic reflection data to locate the hypocenters calculates a more accurate depth solution than a simple 1-D model. The results from chapter 5 show accurately positioned hypocenters, and their relation to seismic events within the seismic depth volume. When these hypocenters are combined with structural mapping, the depths and positions of the seismic hypocenters enable joint microseismic and reflection seismic interpretation.

### 7.13 Integrated interpretation

Combining microseismic hypocenters with structural interpretation, and seismic inversion.  provides a method for comprehensive reservoir evaluation.  A key finding is the role of Riedel shear faulting in hydraulic fracture propagation (in contrast with the assumption of $SH_{max}$ being the dominant factor controlling fracture direction).  The induced seismicity within the Duvernay Formation interval is interpreted to be reactivated Riedel shear faults.  The microseismic events overlay  fault patterns observed on the Duvernay/Swan Hills seismic reflection event.  The induced large magnitude induced seismic events follow mapped  strike-slip basement faults, and have hypocenters occurring above the treatment interval in the overlying carbonates.  Geohazards such as unintended induced seismicity can also be addressed by taking care in the placement of hydraulic fracture stages and borehole direction.  Integrating interpretation using structural mapping, inversion, depth conversion with well control, and microseismic hypocenters adds greatly to the understanding of the Duvernay Formation and the dynamics involved in reservoir treatment.  These findings may  be applied to well planning where hydraulic fracture treatments are planned in the presence of faults, and variable reservoir quality .

## 7.2 Key findings and future work

### 7.21 Reservoir characterization

Seismic inversion is used to calculate reservoir parameters which in turn is used for reservoir development. Converted waves, as well as primary reflections, are used to generate petrophysical properties, which in turn are used to high-grade areas for reservoir development. Many additional seismic attributes can be evaluated, in addition to Young's Modulus and Poisson's Ratio (i.e. λ, μ, shear modulus, bulk modulus, as well as other related attributes) . These mapped attributes can be incorporated into drilling plans to optimize reservoir development by high-grading areas suitable for development while avoiding unsuitable reservoirs.

### 7.22 Signal processing

Signal-processing methods generally used for seismic reflection processing are useful as applied to microseismic data. The number of detetected events is significantly increased, events below the noise threshold became visable after processing. The techniques tested here are trace-to-trace operations designed to reduce noise and improve seismic detection. The geophones used in the burried array have a resonent frequency of 10 hz, and as a result frequencies below 10 hz are attenuated. Future enhancements to the data processing will include applying an inverse Butterworth filter, as described by Margrave et al. (2012) to restore the 2 to 10 hz component of the signal. More advanced options for deconvoloution include specific operaters designed around identified seismic events. Processed microseismc data after deconvolution have a much sharper waveform and a reduced waveform "tail." This will reduce the picking error, the 0 intercept calculated time, and the uncertanty in event location based on a much sharper seismic pick. Additional processes designed on multiple traces, or specific seismic events can be tested as well, such as multi-component deconvolution and surface consistent scaling. The parent events identifed for MFA can also serve to design deconvolution operators specific to these parent events, thereby enhansing the detection of associated child events. There are more advanced deconvolution options to evaluate, such as surface-consistent and multicomponent deconvolution operators (Kendall, 2006). Machine learning is under development in the seismic interpretation field, there may be applications in microseismic event detection whereby an algorithm is "trained" to identify specific events, perforation shots, tensile cracks, induced fault slip movement, to name a few.

The next step for the processing work in this thesis, is to do a hypocenter determination using focal-time on all the new events (as derived in chapter 4), and place them in the vizualization system. The new events will be evaluated in a qualititave sence, to identify if they are associated with pre-existing faults, structures, or *Shmax*. Quantatitive analysis of these data will include an uncertanty analysis, and a direct comparison to the existing Toc2ME catalog, to see if the uncertanty has been reduced.

**7.23 Thermal heat flow**

A new hypothesis presented in this thesis, with respect to enhanced heat flow due to basement faulting and the relationship to thermal maturity may be validated by considering the following as a study:

- Expanding the fault interpretation to adjoining 3D surveys

- Tabulating the downhole temperatures at the Duvernay Formation to investigate how they relate to mapped faults
- Comparing Duvernay Formation production with respect to the position relative to basement faults
- Mapping the thermal maturity with respect to a geochemical analysis to analyze how it relates to basement faulting

If ta relationship between heat flow, basement faulting, and thermal maturity is validated, then the economic uncertainty associated with encountering dry gas when condensate is expected can be mitigated.

**7.24 focal-time**

The focal-time method can be applied to any passive seismic event data set where there is seismic reflection P-P/P-S data available. S wave data can be calculated from the AVO simultaneous inversion if converted data has not been recorded; this is not as accurate as the joint P-P/P-S inversion, but needs to be tested to see if it is a viable alternative to the standard 1-D model. Focal-time has applications in mature areas, lie. central Alberta, where there is an abundance of 3-D P wave data available, and the Duvernay Formation is under active development. They may be applications in the study of naturally occurring earthquakes, where there is reflection seismic data coinciding with natural seismicity, i.e. the San Andreas fault in California.

### 7.25 Geohazard identification

Both areas studied here, Toc2ME and Bigstone North, have encountered unexpected (felt) induced seismic events caused by hydraulic fracturing. These induced seismic events occur above the treatment zone in the carbonates of the Upper Ireton Formation and the Lower Winterburn group. Both of the large magnitude seismic events occurred vertically above deep seated basement faults, as mapped on 3-D seismic data. In both cases, the horizontal wellbore is drilled parallel and in close proximity to a basement fault. These induced seismic events may be avoidable by redesigning wellbore orientation and fracture stage placement. This study may be expanded further, by investigating the relationship between large magnitude induced seismic events, and basement faulting. Most horizontal treatment wells are planned based on depth converted 3-D seismic to guide the depth of the drill bit; this same seismic needs to have an interpretation that includes basement fault mapping to identify potential geohazards. Future development programs, in the due diligence process of well bore planning, need to map these potentially active basement features.

### 7.26 Unexpected fracture behavior

In both study areas, the direction of hydraulic fracture propagation is not aligned with the direction as predicted by maximum horizontal stress (Blackam, 2015). The observed fracture direction in ToC2ME runs in a direction along an interpreted Ridel shear fault trend and not maximum horizontal stress, as predicted by the standard geomechanical model. The same observation holds true in the Bigstone North area, where fracture propagation follows pre-existing faults and terminates against a carbonate (Swan Hills Formation) reef. In ToC2ME, it appears that the observed microseismicity is a pattern of reactivated transcurrent faults rather than a set of newly induced tensile cracks in the direction of maximum horizontal stress. The assumption of a homogeneous reservoir, and the role of Shmax appear to be superseded by the role of pre-existing faults, and geological structures such as reef fronts. Expanding these mapping concepts is recommended where there are co-located microseismic and 3-D reflection surveys. Using these concepts may reduce the number of well bores required, and the number of fracture stages required. Future well bore planning should take into account pre-existing geological structures such as reefs and faults, as these play a crucial role in fracture propagation.

### 7.3 Concluding remarks

The results from technologies developed during the research of this thesis come about from combination of technologies in related fields. Reflection seismic and microseismic come together to produce the focal-time method for hypocentres based on common velocity information. Microseismic signal enhancement comes directly from signal processing technologies applied and proven in the reflection seismic field. The seismic interpretation comes about from using the microseismic hypocenters being interpreted in the same visualization environment as the reflection seismic data. Geological concepts such as Riedel shears and flower structures are incorporated into the seismic interpretation to provide a improved method basis for future resource extraction, and geohazard mitigation. The ultimate finding presented here is to use the geophysical method to enhance reservoir development economics, reduce risk, and present results in terms of recognized geological models. Using existing technologies for simultaneous inversion with new technologies, focal-time, and interpretation techniques incorporating established geological principles accomplishes these objectives.

References

Aki, Keiiti, and Paul G. Richards, 2002, Quantitative seismology, University Science Books.

Akram J. and D. Eaton, 2016, Refinement of arrival-time picking using a cross-correlation based workflow, Journal of Applied Geophysics, **135**, pp 55-66.

Allen, J. L., and C.P. Peddy, 1993, Amplitude variation with offset: Gulf Coast case studies, Allen, J. L., and, C. P. Peddy: Geophysical Developments Series, **4**, 9-22.

Blackam, M, 2015, Geomechanics of hydraulic fracturing, Environmental effects in the Australian context, Coffee.com

Bao, X., and D. W., Eaton, 2016, Fault activation by hydraulic fracturing in western Canada: Science, **354**, 1406-1409.

Bjørlykke, Knut, 1993, Fluid flow in sedimentary basins: Sedimentary Geology **86**, no. 1-2 137-158.

Calvert, A., E**.** Jenner, R. Jefferson, R. Bloor, N. Adams, R. Ramkhelawan, and C. St. Clair, 2008, Preserving azimuthal velocity information: Experiences with cross-spread noise attenuation and offset vector tile pre STM, 78th Annual International Meeting, SEG, Expanded Abstracts, 207-211.

CAPP 2019, Hydraulic fracturing 2019| **11** 2020 from [https://www.capp.ca/explore/hydraulic-fracturing/](https://www.capp.ca/explore/hydraulic-fracturing/)

Caffagni, Enrico, David W. Eaton, Joshua P. Jones, and Mirko van der Baan, 2016, Detection and analysis of microseismic events using a Matched Filtering Algorithm (MFA), Geophysical Journal International **206**, no. 1: 644-658.

Cameron, Maria Kourkina, Sergey B. Fomel, and J. A. Sethian, 1993, Seismic velocity estimation from time migration, Inverse Problems 23, no. 4 , 1329.

Castagna, J. P., Petrophysical imaging using AVO: The Leading Edge, **12**, 172–179.

Chiburis, Edward, Charles Franck, Scott Leaney, Steve McHugo, and Chuck Skidmore, 1993, Hydrocarbon detection with AVO. Oilfield review **5**, no. 1:pp. 42-50.

Cho, D., and M. Perez, 2014, Brittleness revisited: CSPG Conferences Abstract Archive, 2014.

Chopra, S., and K. J. Marfurt, 2013, Preconditioning seismic data with 5D interpolation for computing geometric attributes, The Leading Edge **32** no.12, p 1456-1460

Chopra, S., R. K. Sharma, A. K. Ray, H. Nemati, R. Morin, B. Schulte, and D. D'Amico, 2017, Seismic reservoir characterization of Duvernay shale with quantitative interpretation and induced seismicity considerations – A case study: Interpretation, **5** no.2, T 185 – T 197.

Creaney, S, and J. Allan. 1990, Hydrocarbon Generation and Migration in the Western Canada Sedimentary Basin, Classic Petroleum Provinces, *in* Atlas of the Western Canada Sedimentary Basin.

Cronin, Vince, 2010, A primer on focal mechanism solutions for geologists, Science Education Resource Center, Carleton College.

Cui, Albert, R. Wust, and B. Nassichuk, 2017, A comparison study of existing and new mineralogical, (geo)mechanical, and petrophysical brittleness indices of the Alberta Montney and their applicability for optimizing well Stimulations: Expanded Abstracts CSPG Conferences Abstract Archive

Davis, George H., Alexander P. Bump, Pilar E. García, and Stephen G. Ahlgren, 2000, Conjugate Riedel deformation band shear zones, Journal of Structural Geology **22**, no. 2: 169-190.

Davis, M. K., 2013, A Regional Assessment of the Duvernay Formation; a World-Class Liquids-Rich Shale Play, CSPG Conferences Abstract Archive .

Duggan, J.P., Mountjoy, E.W. and Stasiuk, L.D., 2001, Fault-controlled dolomitization at Swan Hills Simonette oil field (Devonian), deep basin west-central Alberta, Canada. Sedimentology, **48**(2), pp.301-323.

Dunn, L., G. Schmidt, K. Hammermaster, M. Brown, R. Bernard, E. Wen, R. Befus, and S. Gardiner, 2012, The Duvernay Formation (Devonian): sedimentology and reservoir characterization of a shale gas/liquids play in Alberta, Canada: Expanded Abstracts, CSPG Conferences Abstract Archive.

Dommisse, R., 2013, 3-D Geological interpretation examples in unconventional shale reservoirs: Expanded Abstracts. Unconventional Resources Technology Conference.

Dusseault, M. and J. McLennan, 2011, Massive multistage hydraulic fracturing: Where are we? 45 US Rock Mechanics/Geomechanics Symposium.

Eaton, D.W, N Igonin, A. Poulin, R. Weir, H. Zhang, S Pellegrino, and G. Rodriguez-Pradilla. 2018, Induced seismicity characterization during hydraulic fracture monitoring with a shallow-wellbore geophone array and broadband sensors. Seismological Research Letters, **89**(5), 1641,1651.

Eaton, D.W. and D.C. Lawton, 1992, P-SV stacking charts and binning periodicity: Geophysics, **57**, 745-748.

Eaton, David, Mirko van der Baan, Jean-Baptiste Tary, Brad Birkelo, Neil Spriggs, Sarah Cutten, and Kimberly Pike. 2013, Broadband microseismic observations from a Montney hydraulic fracture treatment, northeastern BC, Canada, Ele **1150**, no. (1200): 1250.

Eaton, D. W., B. Milkereit, G. M. Ross, E. R. Kanasewich, W. Geis, D. J. Edwards, L. Kelsch, and J. Varsek, 1995, Lithoprobe basin-scale seismic profiling in central Alberta: Influence of basement on the sedimentary cover, Bulletin of Canadian Petroleum Geology **43**, no. 1: 65-77.

Eaton, D.W., G.M. Ross, and J. Hope, 1999, The rise and fall of a cratonic arch: A regional seismic perspective on the Peace River Arch, Alberta: Bulletin of Canadian Petroleum Geology, **47** no.4, 346-361.

Eaton, D. W., 2018, Passive seismic monitoring of induced seismicity, Fundamental Principles and Application to Energy Technologies, Cambridge University Press.

Eisner, Leo, Peter M. Duncan, Werner M. Heigl, and William R. Keller, 2009, Uncertainties in passive seismic monitoring, The Leading Edge **28**, no. 6: 648-655.

Ekpo, Eneanwan, David Eaton, and Ronald Weir, 2017, Basement Tectonics and Fault Reactivation in Alberta Based on Seismic and Potential Field Data, *in* Geophysics. IntechOpen, 2017.

Ellsworth, W.,2013, Injection-Induced Earthquakes, 2012, Science 12 Jul 2013: Vol. **341**, Issue 6142, 1225942 DOI: 10.1126/science.1225942.

Eyre, T., D. W. S. Eaton, and M. Zecevic, 2019, Observations of long-lived hydraulic-fracturing induced earthquake swarms support driving role of aseismic creep. AGUFM 2019: T31E-0333.

Eyre, Thomas S. , David W. Eaton1, Dmitry I. Garagash, Marco Venieri, Megan Zecevic ,Ronald Weir, and Donald C. Lawton, 2019, The role of aseismic slip in hydraulic-fracturing induced seismicity, Science Advances **28** Aug 2019: Vol. 5, no. 8, eaav7172DOI: 10.1126/sciadv.

Fatti, Jan L., George C. Smith, Peter J. Vail, Peter J. Strauss, and Philip R. Levitt, 1994, Detection of gas in sandstone reservoirs using AVO analysis: A 3-D seismic case history using the Geostack technique, Geophysics **59**, no. 9. pp 1362-1376.

Fossen, Haakon, and Basil Tikoff, 1998, Extended models of transpression and transtension, and application to tectonic settings, , Geological Society, London, Special Publications **135**, no. 1, pp 15-33.

Fowler, P.J., 1997, A comparative overview of prestack time migration methods: 78th Annual International Meeting, SEG, Expanded Technical Abstracts, 207 - 211.

Garotta, R. J., and Grange, P. Y., 1987, Comparison of responses of compressional and converted waves on a gas sand, 57th Annual International Meeting, SEG, Expanded Abstracts, pp, 627–630.

Goodway, B., M. Perez, J. Varsek, and C. Abasco, 2010, Seismic petrophysics and isotropic anisotropic AVO methods for unconventional gas exploration, The Leading Edge, **29**, 1500-1508.

Häuser, S., and G. Steidl∗, 2014, Fast Finite Shearlet Transform: a tutorial. arXiv:1202.1773v2.

Gray, David. PS converted-wave AVO, 2003, 73rd Annual International Meeting, 83nd Annual International Meeting, SEG, Expanded Abstracts, pp. 165-168.

Hammermaster, K., 2012, The Duvernay Formation (Devonian): An emerging shale liquids play in Alberta, Canada: Expanded Abstracts, CSPG Conferences Abstract Archive (2012).

Hampson D., B. Russell, and B. Bankhead, 2005, Simultaneous inversion of pre-stack seismic data: 75th Annual International Meeting, SEG Expanded abstracts, 2668.

Häuser,S and G Steidl, 2014, Fast Finite Shearlet Transform: a tutorial. Fachbereich für Mathematik, Technische Universität Kaiserslautern, Paul-Ehrlich-Str. **31**, 67663 Kaiserslautern, Germany, {haeuser,steidl}@mathematik.uni-kl.de1.

Hobro, James, Michael Williams, and Joel Le Calvez, 2016, The finite-difference method in microseismic modeling: Fundamentals, implementation, and applications, The Leading Edge **35**, no. 4: 362-366.

Hoeber, H., S. Butt, D. Davies, S. Campbell, and T. Ricketts, 2005, Improved 4D seismic processing: Foinaven case study: 75th Annual International Meeting, SEG, Expanded Abstracts, 207-211.

Hotovec-Ellis, AJ and C Jeffries, 2016, Near real-time detection, clustering, and analysis of repeating earthquakes: Application to Mount St. Helens and Redoubt volcanoes, Seismological Society of America Annual Meeting, 2016

Houstecky, P. , Macrooption, 2020, https://www.macroption.com/kurtosis-formula/.

Igonin, N., A. Poulin, and D. Eaton, 2017, A comparison of surface and near surface acquisition techniques for induced seismicity and microseismic monitoring, 79th EAGE Conference and Exhibition.

Igonin, Nadine, Megan Zecevic, and David W. Eaton, 2018, Bilinear Magnitude-Frequency Distributions and Characteristic Earthquakes During Hydraulic Fracturing, Geophysical Research Letters **45**, no. 23, pp 12-866.

Inamdar, Abhijeet Ashok, Tolulope Mobereola Ogundare, Raj Malpani, William Keith Atwood, Keith Brook, Abdunnaser M. Erwemi, and Dave Purcell, 2010, Evaluation of stimulation techniques using microseismic mapping in the Eagle Ford Shale, Tight Gas Completions Conference, Society of Petroleum Engineers, 2010.

Jin, S., G. Cambois, and C. Vuillermoz, 2000, Shear-wave velocity and density estimation from PS-wave AVO analysis: Application to an OBS dataset from the North Sea.: Geophysics, **65**, no.5, 1446-1454.

Kelamis, P.G., E.F. Chiburis, and S. Shahryar, 1990, Radon multiple elimination, a practical methodology for land data: 60th Annual International Meeting, SEG, Expanded Abstracts, 1611-1613.

Kendall, R. Advances in land multicomponent seismic: acquisition, processing and interpretation, 2006, CSEG recorder **31**: 65-75.

King, Hobart, 2011, Hydraulic fracturing of oil & gas wells drilled in shale, Geology.com.

King, G, 2012, Hydraulic Fracturing 101: What Every Representative, Environmentalist, Regulator, Reporter, Investor, University Researcher, Neighbor an Engineer Should Know About Estimating Frac Risk and Improving Frac Performance in Unconventional Gas and Oil Wells, SPE 152596, Society of Petroleum Engineers.

Knapp, L.J., J. M .McMillan, N. B. Harris, 2017, A depositional model for organic-rich Duvernay Formation mudstones, Sedimentary Geology, Volume **347**, 1 January 2017, Pages 160-182.

Knopoff, Leon, and Michael John Randall, 1970, The compensated linear-vector dipole: A possible mechanism for deep earthquakes, Journal of Geophysical Research **75**, no. 26, 4957-4963.

Lee, S., M.S. Ho, and G.W. Purnell, 1991, Preprocessing for amplitude-versus-angle (AVA) analysis of land seismic data: 61st Annual International Meeting, Society of Exploration Geophysicists, Expanded Abstracts, 1070-1071.

Leinbach, J., 1995, Wiener spiking deconvolution and minimum phase wavelets: A tutorial.: The Leading Edge, **14**, no. 3, 189–192.

Lawton, D. C., and T. C. Howell, 1992, PP and P-SV synthetic stacks, 62nd Annual International Meeting, SEG Expanded Abstracts, October, pp. 25-29.

Leinbach, J., 1995, Wiener spiking deconvolution and minimum phase wavelets: A tutorial, The Leading Edge, **14**, no. 3, 189–192.

Li, Z., G. Chi, and K. M. Bethune, 2016, The effects of basement faults on thermal convection and implications for the formation of unconformity-related uranium deposits in the Athabasca Basin, Canada,  Geofluids **16**, no. 4: 729-751.

Lindseth, R., Synthetic sonic logs-a process for stratragraphic interpretation, 1979, Geophysics, volume **44** Issue one, pp 3-26.

Lines, L., Newrick, Geophysical Monograph Series 2004, SEG number **13,** Fundamentals of geophysical interpretation.

Lomax, A., 2018, NonLinLoc, probabilistic global-search earthquake location in 3D media, Lomax Scientific.

Lomax, A., J. Virieux, P. Volant and C. Berge, 2000, Probabilistic earthquake location in 3D and layered models: Introduction of a Metropolis-Gibbs method and comparison with linear locations, *in* Advances in Seismic Event Location Thurber, C.H., and N. Rabinowitz (eds.), Kluwer, Amsterdam, 101-134.

Lomax, A., Michelini, A., and Curtis, A., 2014, Earthquake location, direct, global-search methods: Encyclopedia of Complexity and Systems Science, 1–33.

Lomax, A., A. Michelini, A. Curtis, 2009, Earthquake Location, Direct, Global-Search Methods, in Complexity In Encyclopedia of Complexity and System Science, Part 5, Springer, New York, pp. 2449-2473, doi:10.1007/978-0-387-30440-3.

MacKay, M, D. Eaton, C. Clarkson, 2018, The Geomechanical system of the Duvernay Formation: part 1. Outcrop, core, and microseismic interpretation. Interpretation, Interpretation **6**, no. 4: T919-T936.

Margrave, G. F., 2005, Methods of seismic Data Processing Geophysics 557/657 Course Lecture Notes.: The CREWES project, Department of Geology and Geophysics, The University of Calgary.

Margrave, GF, MB Bertram, KL Bertram ,KW Hall, KAH Innanen, DC Lawton, LE Mewhort, and TM Phillips , 2012, A low-frequency seismic field experiment, 82nd Annual International Meeting, SEG, Expanded Abstracts, pp 1–5.

Maxwell, Shawn C., Jim Rutledge, Robert Jones, and Michael Fehler, 2010, Petroleum reservoir characterization using downhole microseismic monitoring, Geophysics **75**, no. 5: 75A129-75A137.

Meek, R., B. Suliman, R. Hull, H. Bello, and D. Portis, 2013, What Broke? Microseismic analysis using seismic derived rock properties and structural attributes in the Eagle Ford play: Expanded Abstracts, Unconventional Resources Technology Conference.

Meer, Peter, Doron Mintz, Azriel Rosenfeld, and Dong Yoon Kim, 1991, Robust regression methods for computer vision: A review, International journal of computer vision **6**, no. 1, : 59-70.

O'Connell, S.C., 1994, Geological history of the Peace River Arch, in Mossop, G.D. and Shetsen, *in*, Atlas of the Western Canada Sedimentary Basin, Chapter 28.

Ogiesoba, Christopher O., James E. Gaiser, and Robert R. Stewart, 2003, Velocity and VTI anisotropy scanning in multicomponent seismic data, CREWES Research Report – Volume 15.

Ong, Oliver N., Douglas R. Schmitt, Randolph S. Kofman, and Kristine Haug, 2016. Static and dynamic pressure sensitivity anisotropy of a calcareous shale. Geophysical Prospecting **64**, Advances in Rock Physics (2016): 875-897.

Ostrander, W. J., 1984, Plane wave reflection coefficients for gas sands as non-normal angles of incidence, Geophysics, **54**, 680-688.

Paes, A., and Eaton, D., 2017, Energy-stack and Kurtosis: the dynamic duo for microseismic event identification: 9th annual Microseismic Industry Consortium Annual research report.

Paes, A and David W Eaton , 2018, Energy-stack and Kurtosis: the dynamic duo for microseismic event identification, 9th annual Microseismic Industry Consortium research report.

Perez, R. and Kurt Marfurt , 2015, Identification of brittle/ductile areas in unconventional reservoirs using seismic and microseismic data: Application to the Barnett Shale, Interpretation, 2015, Vol.3(4), p.T233-T243.

Pennington, W.D.,2001, Reservoir geophysics: Geophysics, **66**, no.1, 25-30.

Phillips, W. S., T. D. Fairbanks, J. T. Rutledge, and D. W. Anderson, 1998, Induced microearthquake patterns and oil-producing fracture systems in the Austin chalk, Tectonophysics 289, no. 1-3 (1998): 153-169.

Poulin, Andrew, Ron Weir, David Eaton, Nadine Igonin, Yukuan Chen, Laurence Lines, and Donald Lawton, 2019, Focal-time analysis: A new method for stratigraphic depth control of microseismicity and induced seismic events, Geophysics **84**, no. 6: KS173-KS182.

Power, D.V., Schuster, C. L., Hay, R. and Twombly, J. ,1976, Detection of hydraulic fracture orientation in dimensions in cased wells. Journal of Petroleum Technology, **28**(09), 1-116.

Preston, A., G. Garner, K. Beavis, O. Sadiq, and S. Stricker, 2016, Duvernay reserves and resources report: A comprehensive analysis of Alberta's foremost liquids-rich shale resource, Alberta Energy Regulator, Calgary (2016): 83.

Rafiq, A., D.W. Eaton, A. McDougall, and P.K. Pedersen, 2016, Reservoir characterization using microseismic facies analysis integrated with surface seismic attributes: Interpretation, **4**,no. 2, T167-T181.

.

Refayee, H., H. Jaglan, and S. Adcock, 2016, Fault and Fracture Detection in Unconventional Reservoirs: A Utica Shale Study: Expanded Abstracts, Unconventional Resources Technology Conference (URTEC) 2016.

Rickman, R., M. J. Mullen, J.E. Petre, W.V. Grieser, and D. Kundert, 2008, A practical use of shale petrophysics for stimulation design optimization: All shale plays are not clones of the Barnett Shale: SPE Annual Technical Conference and Exhibition, Society of Petroleum Engineers.

Russell, B. and D. Hampson, 1991, Comparison of poststack seismic inversion methods, 61st annual international meeting, SEG expanded abstracts, 876-879.

Robinson, E. A., and Treitel, S., 1980, Geophysical Signal Analysis: Prentice-Hall Inc, Englewood Cliffs, N.J. 219.

Rodríguez-Pradilla, Germán, and David W. Eaton, 2019, The application of coda and energy methods for magnitude estimation of microseismic events, Seismological Research Letters **90**, no. 3 (2019): 1296-1307.

Salvage, Rebecca O and David W Eaton ,2019, Investigating the evolution of microseismicity associated with the Tony Creek Dual Microseismic Experiment, Alberta, Canada 10th annual Microseismic Industry Consortium Research Report.

Schultz, R., R. Wang, Y. Gu, J. Haug, and G. Atkinson, G., 2017, A seismological overview of the induced earthquakes in the Duvernay play near Fox Creek, Alberta: Journal of Geophysical Research: Solid Earth, **122** no.1, 492-505.

Schultz ,R., V. Stern, M. Novakovic, G. Atkinson, Y. Gu, 2015, Hydraulic fracturing and the Crooked Lake Sequences: Insights gleaned from regional seismic network, Geophysical Research Letters, **10**.1002/2015GL063455.

Sharma, R., S. Chopra, 2017, Thin Sweet Spots Identification in the Duvernay Formation of North Central Alberta, Search and discovery Article #10902, AAPG.

Shen, L W., D. R. Schmitt, K. Haug, 2019, Quantitative constraints to the complete state of stress from the combined borehole and focal mechanism inversions: Fox Creek, Alberta, Tectonophysics **764**, pp 110-123.

Soltanzadeh, M., A. Fox, and N. Rahim, 2015, Application of an Integrated Approach for the Characterization of Mechanical Rock Properties in the Duvernay Formation: Expanded Abstracts, CSPG Conferences Abstract Archive.

Stewart, R.R., J.E. Gaiser, R.J. Brown, and D.C. Lawton, 2002, Converted-wave seismic exploration methods: Geophysics, **67** no. 5, 1348-1363.

Switzer, S.B., Holland, W.G., Christie, D. S.,Graf, G.C..,Hedinger, A.S., McAuley, R.J.,Wierzbicki, R.A.and Packard, J.J., 1994, Devonian Woodbend-Winterburn Strata of the Western Canada Sedimentary Basin *in*: Geological Atlas of the Western Canada Sedimentary Basin. G..D. .Mossop and I. Shtsen (comps.) Calgary, CSPG and ARC, chapter 12.

Taner, M., and Fulton Koehler, 1981, Surface consistent corrections, Geophysics Volume **46** Issue 1 Jan 1981 Pages: 2-92 ISSN (print):0016-8033 ISSN (online):1942-2156.

Tissot, B. P., and D. H. Welte, 1984, Petroleum Formation and Occurrence, 2nd edition, 1984.

Trad, D, 2009, Five-dimensional interpolation: Recovering from acquisitional constraints, Geophysics volume **74** No. 6 p 123-132.

Trad, Daniel, 2007, A strategy for wide-azimuth land interpolation, 77nd Annual International Meeting, SEG, Expanded Abstracts, pp. 946–950.

Trnkoczy, Amadej, Peter Bormann, Winfried Hanka, L Gary Holcomb, Robert L Nigbor, Masanao Shinohara, Hajime Shiobara, and Kiyoshi Suyehiro, 2002, Site selection, preparation and installation of seismic stations, *in*: In New Manual of Seismological Observatory Practice (NMSOP), pp. 1-108. Deutsches GeoForschungsZentrum GFZ, 2009.

Walter, W., and Brune, J., 1993, Spectra of seismic radiation form a tensile crack, Journal of Geophysical Research: solid earth, **98**, no. 4, 159–164.

Verdon, James P., J-Michael Kendall, Stephen P. Hicks, and Philip Hill, 2017, Using beamforming to maximize the detection capability of small, sparse seismometer arrays deployed to monitor oil field activities, Geophysical Prospecting **65**, no. 6, pp 1582-1596.

Wang, R., Y J. Gu, R. Schultz, M. Zhang, and A. Kim, 2017, Source Characteristics and Geological Implications of the January 2016 Induced Earthquake Swarm near Crooked Lake, Alberta, Geophysics Journal. International, **210**, 979-988.

Weir, R, A Poulin, and D Eaton , 2018, Can continuously recorded seismic data be improved with signal processing? GeoConvention expanded abstracts Pages 1-4.

.Weir, R.M., Eaton, D.W., Lines, L.R., Lawton, D.C. and Ekpo, E., 2018. Inversion and interpretation of seismic-derived rock properties in the Duvernay play. Interpretation, **6**, SE1-SE14.

Weir, Ronald, Don Lawton, Laurence Lines, Thomas Eyre, and David Eaton, 2019, Application of structural interpretation and simultaneous inversion to reservoir characterization of the Duvernay Formation, Fox Creek, Alberta, Canada, The Leading Edge **38**, no. 2: 151-160.

Weir, Ronald, Andrew Poulin, Nadine Igonin, David W. Eaton, Larry Lines, and Don Lawton, 2018, Focal-time estimation: A new method for stratigraphic depth control of induced seismicity, 88th Annual International Meeting, SEG, Expanded Abstracts pp. 2977-2981.

Weir, Ronald, L. Lines, D. Lawton, D. Eaton, and A. Poulin, 2019, Can continuously recorded seismic data be improved with signal processing? The application of deconvolution to microseismic data, GeoConvention 2019 abstracts.

Whetten, John T., Bert R. Dennis, Donald S. Dreesen, Leigh S. House, Hugh D. Murphy, Bruce A. Robinson, and Morton C. Smith, 1987, The US hot dry rock project." Geothermics 16, no. **4**, pp 331-339.

Widess, M. B.,1973, How thin is a thin bed?, Geophysics **38**, no. 6: 1176-1180.

Withers, Mitchell, Richard Aster, Christopher Young, Judy Beiriger, Mark Harris, Susan Moore, and Julian Trujillo, 1998, A comparison of select trigger algorithms for automated global seismic phase and event detection, Bulletin of the Seismological Society of America **88**, no. 1, pp 95-106.

Wu, Yinghui, X. P. Zhao, R. J. Zinno, H. Y. Wu, V. P. Vaidya, Mei Yang, and J. S. Qin, 2016, The application of microseismic monitoring in unconventional reservoirs. *in* Unconventional Oil and Gas Resources Handbook, pp. 243-287. Gulf Professional Publishing, 2016.

Zhang, Fanchang, and Ronghuo Dai, 2016, Nonlinear inversion of pre-stack seismic data using variable metric method,  Journal of Applied Geophysics **129**, 111-125.

Zhang, H., Eaton, D. W., Li, G., Liu, Y., and Harrington, R. M., 2016, Discriminating induced seismicity from natural earthquakes using moment tensors and source spectra: Journal of Geophysical Research: Solid Earth, **121**, no. 2, 972–993. 9.

Zhang, Hongliang, D.W. Eaton, German Rodriguez, and Suzie Qing Jia, 2019, Source-Mechanism Analysis and Stress Inversion for Hydraulic Fracturing-Induced Event Sequences near Fox Creek, Alberta.  Bulletin of the Seismological Society of America, Vol **109**, No 2, doi 10.1785/0120180275.

Zinno, R. J, A Brief History of Microseismic Mapping in Unconventional Reservoirs, 2011, Borehole Geophysics Workshop-Emphasis on 3D VSP, 16-19, Istanbul Turkey.

Zoeppritz, K., 1919, On the reflection and propagation of seismic waves, 1919.  Gottinger Nachrichten 1, no**. 5**,pp 66-84.